Autoionisation einfacher atomarer Systeme nach Folienanregung

Inaugural - Dissertation
zur Erlangung der Doktorwürde
des Fachbereichs Physik
der Freien Universität Berlin

vorgelegt von
Reinhard Bruch
aus Hannover

Juli 1976

To my mother Ruth Bruch

and

my father Prof. Dr.Ing. E.h. Walter Bruch

Autoionisation einfacher atomarer Systeme nach Folienanregung

Inaugural - Dissertation

zur Erlangung der Doktorwürde
des Fachbereichs Physik
der Freien Universität Berlin

vorgelegt von

Reinhard Bruch

aus Hannover

Juli 1976

UNIV.
LEIDEN
BIBL.

AUTOIONIZATION OF SIMPLE ATOMIC SYSTEMS AFTER FOIL EXCITATION

by

Reinhard Bruch

A thesis presented to the Faculty of Physics in the Free University of Berlin. In partial fulfillment of requirements for the degree of

Doktor der Naturwissenschaften
Dr. rer. nat.
University of Berlin

July 1976

1. Referent: Prof. Dr. J. Andrä

2. Referent: Prof. Dr. K. H. Lindenberger

Tag der mündlichen Prüfung: 10. 11. 1976

Nicht von Beginn an enthüllten die Götter den Sterblichen alles;
Aber im Laufe der Zeit finden wir suchend das Bess're.
Sichere Wahrheit erkannte kein Mensch und wird keiner erkennen
Über die Götter und alle die Dinge, von denen ich spreche.
Sollte einer auch einst die vollkommenste Wahrheit verkünden,
Wüsste er selbst es doch nicht: es ist alles durchwebt von Vermutung.

Xenophanes (Pop 73)

TABLE OF CONTENTS

	Page
ZUSAMMENFASSUNG (ABSTRACT)	i
ACKNOWLEDGEMENTS	iii
LIST OF FIGURES	iv
LIST OF TABLES	xv
I. INTRODUCTION	1
1. Historical Background	4
2. The Physical Problem	8
II. SURVEY OF AUTOIONIZATION PHENOMENA	10
1. Autoionizing Levels	10
2. Selection Rules	15
3. Autoionization Widths and Decay Rates	27
4. Mean Free Decay Length / Mean Free Path Length for K-Shell Vacancy Production	31
5. The Experimental Problem	35
III. ELECTRON ENERGY ANALYZER	38
1. General Description of the CMA	38
2. Basic Construction	42
3. Magnetic and Electric Stray Field Reduction	45
4. Electron Detection	46
IV. PERFORMANCE TEST OF THE ANALYZER	49
1. Calibration of the Analyzer	49
2. Transmission Function	52
3. Line Width and Energy Resolution	55
V. EXPERIMENTAL APPARATUS	58
1. Ion Accelerator and Target Chamber	58
2. Ion Beam Collimation	62
3. The Target	62
4. Faraday Cup and Beam Integration	64
5. Data Acquisition System	66

Page

VI. CHARACTERISTIC FEATURES OF BEAM-FOIL ELECTRON SPECTROSCOPY 70

1. Foil Interaction Processes 70
   a) Charge Distribution 70
   b) Energy Straggling and Angle Scattering 74

2. Kinematics of Electron Ejection 76
   a) Relationship between Center-of-Mass and Laboratory Energies 76
   b) Kinematical Broadening Effects 84
   c) Experimental Line Profiles 89

VII. EXPERIMENTAL RESULTS 95

1. Electron Energy Measurements 95
   a) Effect of Continuum 95
   b) Energy Calibration 97
   c) Prompt Spectra 101
   d) Delayed Spectra 111

2. Intensity Measurements 111
   a) Relative Cross Sections and Yields 111
   b) Effect of Finite Time Window 126

3. Decay Curves 126

VIII. THEORETICAL CONSIDERATIONS FOR THE INTERPRETATION OF THE DATA 143

1. Autoionization Energies 143
   a) Quantum Defect and Screening Method 143
   b) The Effect of Electron Correlation on Autoionization Energies 147

2. Autoionization Decay Channels 154

IX. DISCUSSION OF EXPERIMENTAL RESULTS 160

1. Lithium Autoionization Lines 160
   a) Prompt Spectra 160
   b) Delayed Spectra 171

2. Beryllium Autoionization Lines 178
   a) Prompt Spectra 178
   b) Delayed Spectra 189

3. Boron- and Carbon Autoionization Lines 201
   a) Prompt Spectra 201
   b) Delayed Spectra 208

4. Concluding Remarks 224
   a) Triply Excited Terms 224
   b) Quartet-, Quintet-, and Sextet Terms 226
   c) Satellite Structures 228

		Page
X.	CONCLUSION	231
	1. Comments on the Beam-Foil Interaction Process	231
	2. Cascading via Autoionization and Transfer of Alignment	232
	3. Stark Quenching	236
XI.	APPENDICES	238
	I. Some Core-Excited Configurations of 2-, 3-, 4-, 5-, and 6-Electron Atomic Systems for $Z \leq 6$	238
	II. The Most Prominent Metastable Autoionizing 2-, 3-, 4-, 5-, and 6-Electron Terms (LS Coupling)	239
	III. Magnetic Autoionization of the Lowest Quartet-, Quintet-, Sextet, and Septet Terms for $Z \leq 6$	241
	IV. Autoionization of some Triply Excited States	243
	V. Coulomb Autoionization of some State Configurations with 4 Electrons	244
	VI. Coulomb Autoionization of some State Configurations with 5 Electrons	246
	VII. Energy Values Below Total Ionization Estimated by the Application of the Quantum Defect Method (QDM)	248
	VIII. Hartree-Fock Energy Values Below Total Ionization	249
	IX. Energy Values Below Total Ionization as Deduced from the Work of Safronova et al.	250
	X. Matrix Elements (A.U.) for some State Configurations with 3 Electrons as Deduced from Goldsmith	252
	XI. Energy Values Below Total Ionization as Deduced from the Work of Holøien and Geltman	256
	XII. Additional Rules Concerning Transfer of Orbital Angular Momentum	257

Page

a) Coulomb Autoionization 257
b) Magnetic Autoionization due to Spin-Other-Orbit Coupling 258
c) Magnetic Autoionization due to Spin-Spin Coupling 259

XIII. Determination of the (1s2s2p) $^4P^o$ Wave Functions 261
a) Break-Down of LS Coupling 262
b) Break-Down of IJ Coupling 263

XIV. Autoionization Rates 267

XV. Autoionization of Foil-Excited States in LiI and LiII (Phys. Rev. A 12 (1975) 1808) 270

XII. BIBLIOGRAPHY 287

XIII. LEBENSLAUF (VITA) 301

ZUSAMMENFASSUNG (ABSTRACT)

Über den Zerfall hochangeregter autoionisierender 2-, 3-, 4-, 5- und 6-Elektronenatome gibt es mit Ausnahme von Messungen an den Systemen H^-, He, He^-, Li und einigen hochgestrippten Ionen bisher kaum befriedigende experimentelle Daten. Deshalb wurde in Analogie zur optischen Ionenstrahlspektroskopie die Elektronenemission zeitdifferentiell durch Abtasten der Flugstrecke mit dem Fokus eines elektrostatischen Analysators untersucht. Diese Beobachtungstechnik gestattet es, die prompt zerfallenden Coulomb autoionisierenden Zustände von den zeitverzögert zerfallenden magnetisch autoionisierenden Zuständen durch Verschieben der Folie aus dem Fokus eines Elektronenspektrometers abzutrennen. Während in Oak Ridge (Sellin und Mitarbeiter) vorwiegend hohe Ladungszustände, die zu Li isoelektronisch sind, untersucht wurden, lag der Schwerpunkt dieser Experimente auf einfachen atomaren Systemen mit kleiner Kernladungszahl. Die Analyse von Projektil-Elektronenspektren für kleine Z hat den Vorteil, daß wegen der geringen Zahl von Hüllelektronen die möglichen Ladungszustände und die erlaubten Zerfallskanäle stark beschränkt sind.

Mit dieser Arbeit soll an Hand von Messungen an 300 keV H^+-, He^+-, Li^+-, Be^+-, B^+-, C^+-, Ne^+- und Ar^+ Ionenstrahlen demonstriert werden, daß es im Prinzip möglich ist, Autoionisations-Elektronenspektren nach Folienwechselwirkung zu beobachten und auch zu klassifizieren. Exemplarisch werden hier erstmalig Elektronenspektren von rumpfangeregten Li-, Be-, B- und C-Atom- und Ionenzuständen vorgestellt. Dabei wird der Schwerpunkt auf die Analyse und Interpretation der gemessenen Spektren gelegt. Entscheidend zur eindeutigen Identifizierung der zumeist unbekannten Autoionisations-Übergänge trägt die zusätzliche Zeitinformation in Form von zeitverzögerten Spektren und Lebensdauerkurven bei. So wurden die prompten Li-, Be- und B-Autoionisations-Strukturen teilweise interpretiert. Dabei konnten erstmalig Übergänge von (a) doppeltangeregten LiII $3lnl'$ ($n \geq 3$) und (b) dreifachangeregten LiI, BeII und BIII $2lnl'n'l''$ ($n, n' \geq 2$)

Atomkomplexen experimentell nachgewiesen werden. Außerdem ist es gelungen, die zeitverzögerten Li-, Be-, B- und C-Spektren eindeutig zuzuordnen. Mit Hilfe von Lebensdauermessungen konnte der Zerfall des tiefsten Quintett-Terms $(1s2s2p^2)\ ^5P$ in BeI verifiziert werden. Die Lebensdauer dieses Terms wurde zu 132 nsec abgeschätzt. Zusätzlich wurde der dominierende BeII $(1s2p^2)\ ^4P \rightarrow (1s2s2p)\ ^4P^o$ (E1) Übergang über den Autoionisations-Zerfallskanal beobachtet. Die zeitverzögerten B-, und C-Spektren zeigen charakteristische Linien, die sich nicht durch Autoionisation von BIII und CIV Quartettzuständen allein erklären lassen. Es lag daher nahe, diese Strukturen Autoionisationsübergängen von BII und CIII $(1s2s2p^2)\ ^5P$ und BI und CII $(1s2s2p^3)\ ^6S^o$ Termen zuzuordnen. Diese Interpretation wird gestützt durch die beobachteten Intensitätsverhältnisse als auch durch die auftretenden relativen Linienabstände.

ACKNOWLEDGEMENTS

The author is indebted to Prof. Dr. E. Matthias for suggesting the thesis and for his support throughout its completion. I am especially grateful to Prof. Dr. J. Andrä for his valuable advice, for his helpful criticisms, and for his continued interest during the course of the work. Special acknowledgement is due to Dipl. Phys. G. Paul who shared in the experiments. In addition I wish to thank Dipl. Phys. W. Wittmann for his capable assistance and his repeatedly given encouragement at the start of my dissertation research. Furthermore I am grateful to the technical staff and the members of the beam-foil group for help and advice in performing the measurements.

I gratefully acknowledge helpful discussions with Dr. N. Stolterfoht, Dr. P. Ziem and Dipl. Phys. D. Ridder from the HMI. I owe a great debt of gratitude for enlightening discussions with Professor J. Macek from the University of Nebraska/USA. Professor B. Fricke from the Gesamthochschule Kassel is to be thanked for performing Hartree-Fock calculations. The author wishes to express his gratitude to Professor L. Lipsky from the University of Nebraska/USA for making available to me his energy values prior to publication and for his collaboration in the interpretation of the data. Thanks are also due to Dr. H.D. Betz from the Universität München for providing me with a Hartree-Fock program. I would further like to thank Professor J.O. Stoner Jr. from the University of Arizona/USA for critical reading of a manuscript. Furthermore I am indebted to Drs. W.D. Brewer, D. Salomon and W. Randolph for critical comments concerning parts of the manuscript. I gratefully acknowledge discussions with the members of the Sonderforschungsbereich 161 für Hyperfeinstruktur. The assistance of Dipl. Ing. Friese from the HMI in providing me with a ADC 7 is appreciated. Mrs. G. Sedatis and Mr. S. Lemma devoted much time and energy in preparing various figures and pictures. Finally I am grateful to Mrs. E. Praetorius for the careful preparation of the typescript.

This research was supported by the Sonderforschungsbereich 161 der Deutschen Forschungsgemeinschaft.

LIST OF FIGURES

Figure		Page
1.	Schematic energy level diagram illustrating process of autoionization	12
2.	Schematic representation for autoionization processes	14
3.	Decay rates of the Li-like (1s2s2p) $^4P^o$ terms plotted as a function of nuclear charge	30
4.	Schematic diagram representing beam-foil excitation	32
5.	Competing deexcitation processes in the foil, in its vicinity and far away from it	33
6.	Comparison of the mean free path length λ_K for K-shell vacancy production with the mean free decay lengths L_r for Coulomb autoionization as a function of the incident ion energy	34
7.	Dependence of projectile K-shell vacancy production as a function of foil thickness	35
8.	Schematic of cylindrical mirror analyzer	36
9.	Cross-sectional view of the entrance slit geometry	40
10.	Layout of the electrostatic electron spectrometer	43
11.	Magnetic field along the target chamber axis	45
12.	a) Channeltron connection for pulse counting mode	47
	b) Signal pulse-rate as a function of operating voltage using a constant test electron source of ∿100 eV electrons	47

Figure		Page
	c) Signal pulse-rate as a function of discriminator threshold	47
13.	Dimensional drawing of the monochromatic electron source	50
14.	Energy distributions for point source of electrons at different kinetic energies	51
15.	Transmission functions of the analyzer for several fixed kinetic electron energies and constant electron flux	53
16.	Acceptance angular spread of the electron spectrometer	54
17.	Calculated shape of the transmission function for the electron analyzer with equal slit widths ($w_1 = w_2 = 0.5$ mm)	55
18.	FWHM as a function of electron energy for the CMA	56
19.	Schematic drawing of experimental arrangement used for electron energy and time-of-flight measurements	59
20.	Photo of the electron spectrometer, the foil wheel, the ion beam collimation system, the target rotation mechanism and the foil translation device	60
21.	The measuring system on its mounting	61
22.	Defining apertures of the ion beam	63
23.	Cross section of the Faraday cup	65

Figure		Page
24.	Schematic drawing of the electronics for control of the electron spectrometer and the data acquisition system	67
25.	Block diagram of the electronics for lifetime data measurement system	68
26.	Velocity dependence of the charge state distribution for lithium ions penetrating through carbon foils (Mar 68)	71
27.	Velocity dependence of the charge state distribution for beryllium ions penetrating through carbon foils (Mar 68)	72
28.	Velocity dependence of the charge state distribution for boron ions penetrating through carbon foils (Mar 68)	72
29.	Velocity dependence of the charge state distribution for carbon ions penetrating through carbon foils (Mar 68)	73
30.	Variation of mean energy loss, mean energy spread and mean angular spread versus foil thickness as deduced from the work of Biersack (Bier 75)	74
31.	Energy profiles of lithium ions transmitted through a carbon foil (Wit 75)	75
32.	Velocity vector diagrams illustrating the relation between laboratory and center-of-mass velocities and emission angles (β=0)	77
33.	Polar diagram indicating the LAB-frame energy E_{LAB} as a function of the emission angle Θ_{LAB} for fixed rest-frame energy E_{CM} and variable beam energy E_{BEAM}	80

Figure		Page
34.	Polar diagram indicating the LAB frame energy E_{LAB} as a function of the emission angle Θ_{LAB} for fixed beam energy E_{BEAM} and variable rest-frame energy E_{CM}	81
35.	Kinematics for observation of autoionization electrons emitted from moving projectiles	83
36.	Kinematic broadening factor as a function of beam energy	87
37.	Kinematic broadening factor as a function of beam energy (β=0)	88
38.	Kinematic broadening factor as a function of beam energy (β=0)	88
39.	The variations of peak width with foil thickness for Be^+ ions incident on three different carbon foils	90
40.	Variations of peak position and peak intensity for 300 keV C^+ and 600 keV C^{2+} ions incident on a 7 $\mu g/cm^2$ thick carbon foil	91
41.	The beryllium (1s2s2p) $^4P^o$ autoionization line obtained with slit widths $w_1=w_2=w_1'=w_2'=0.5$ mm	92
42.	Variation of the FWHM-resolution in the laboratory and center-of-mass frame as a function of the acceptance angular spread $\Delta\Theta_L$	93
43.	Prompt electron energy spectrum produced by Li^+ → C-foil excitation	96
44.	Linear scaling procedure for a lithium and a beryllium spectrum	97

Figure | Page

45. Prompt and 3.7 nsec delayed lithium electron energy spectrum scaled both in the laboratory frame (E_{LAB}) and in the rest frame of the emitting projectiles (E_{CM}) 99

46. Electron energy spectrum for He^+ → C-foil collisions 100

47. Beryllium electron energy spectrum with the foil in view of the CMA 101

48. Prompt boron electron energy spectrum 102

49. Prompt carbon electron spectrum (LAB-frame) 103

50. Variation of $(v_i/v_e)^2$ as a function of the projectile nuclear charge ($Z_1 \leq 6$) 105

51. Correlation diagrams for the C+C and Li+C systems 106

52. Prompt neon electron spectrum in the range 0 - 250 eV 107

53. Ar electron spectrum between 0 and 450 eV observed with 300 keV Ar^+ on carbon 108

54. Ar electron spectrum between 0 and 450 eV observed with 600 keV Ar^{2+} on carbon 110

55. Electron spectra above 130 eV recorded at various positions slightly downstream from the foil 112

56. Delayed spectra of electrons emitted by 285 keV boron and 281 keV carbon beams 113

57. Carbon electron spectra with the viewing area centered directly at the foil and at several downstream positions 117

Figure		Page
58.	Schematic drawing of a cross section experiment	118
59.	Energy distribution of electrons ejected from a 7 $\mu g/cm^2$ carbon foil by 310 keV H^+ → C-foil bombardment	121
60.	Energy distribution of electrons ejected from a 7 $\mu g/cm^2$ carbon foil by 285 keV Be^+ → C-foil bombardment	122
61.	Energy distribution of electrons ejected from a 7 $\mu g/cm^2$ carbon foil by 285 keV B^+ → C-foil bombardment	123
62.	Energy distribution of electrons ejected from a 7 $\mu g/cm^2$ carbon foil by 285 keV C^+ → C-foil bombardment	124
63.	Time-window factor versus beam energy for various autoionization rates	127
64.	Time window of the analyzer versus beam energy for various beam segments	128
65.	Prompt electron energy spectrum produced by 285 keV beryllium ions. The arrows indicate the energy positions where decay profiles were recorded	129
66.	Intensity profile versus distance from the foil for $E_{CM} \simeq 92.2$ eV	130
67.	Intensity profile versus distance from the foil for peak 1 centered at $E_{CM} \simeq 96.75$ eV (linear plot)	131
68.	Decay profile for the (1s2s2p) $^4P^o$ state in BeII (linear scale)	132

Figure		Page
69.	Intensity profile versus distance from the foil for shoulder 2 centered at $E_{CM} \simeq 101.1$ eV (linear scale)	133
70.	Semilog plot of the intensity versus distance from the foil (shoulder 2).	134
71.	Semilog plot of the intensity versus foil position for shoulder 2 at $E_{CM} \simeq 101.1$ eV	135
72.	Intensity as a function of foil-to-spectrometer distance	136
73.	Decay in flight of the BeII $(1s2p^2)\ ^4P$ state, obtained at a beam energy of about 284 keV	137
74.	Counts versus foil position for peak 3 centered at $E_{CM} \simeq 104.6$ eV (linear plot)	138
75.	Semilog plot of counts versus foil position for peak 3 at $E_{CM} \simeq 104.6$ eV	139
76.	Semilog plot of counts for peak 3 at $E_{CM} \simeq$ 104.6 eV	140
77.	Semilog plot of counts versus foil position for peak 4 centered at about 109.6 eV	141
78.	Theoretical and experimental term energies in lithium	153
79.	Competing decay channels of the LiI $[1s(3, 3A)\ ^3P^o]\ ^2P^o$ term	155
80.	Term scheme for the LiI quartet system	159
81.	LiI autoionization spectrum between 40 and 60 eV (background subtracted)	163
82.	Energy level diagram for the LiI doublet system	164

Figure		Page
83.	Lithium autoionization structures between 60 and 110 eV (background subtracted) in comparison with predicted line energies	166
84.	Schematic diagram of computed energy levels from triply excited states in LiI and doubly excited states in LiII	167
85.	Segment of the prompt lithium spectrum in comparison with predicted transition energies	168
86.	Segment of the prompt lithium spectrum (peak 7)	169
87.	Energy level diagram for the LiI quartet system	173
88.	Electron decay-in-flight spectrum from metastable autoionizing quartet states in ^{7}LiI	175
89.	Energy level diagram for doubly excited states in LiII below the n = 2 ionization threshold	178
90.	Electron decay-in-flight spectra from autoionizing states of 284 keV beryllium ions plotted in the laboratory and in the rest frame of the emitting projectiles	180
91.	Prompt beryllium spectrum between 80 and 170 eV (E_{CM}) for 300 keV Be^{+} + C-foil collisions	181
92.	Decay scheme for some triply excited states in BeII	182
93.	Partial energy level diagram illustrating the autoionizing decay of the $(1s2s2p^{2})\ ^{5}P$	

Figure		Page
	term in BeI and the (1s2s2p) $^4P^o$ term in BeII	187
94.	Partial energy level diagram showing competing autoionization transitions for some 1s2s2p($^4P^o$)nl configurations in BeI	188
95a.	Electron energy spectrum from a 284 keV beryllium beam viewed 2 mm downstream from the exciting foil	191
95b.	Electron energy spectrum from a 284 keV beryllium beam viewed 2.5 mm downstream from the exciting foil	192
95c	Electron energy spectrum from a 284 keV beryllium beam viewed 3 mm downstream from the exciting foil	193
95d.	Electron energy spectrum from a 284 keV beryllium beam viewed 3.5 mm downstream from the exciting foil	194
96.	Spectrum of autoionization electrons from the decay in flight of metastable beryllium ions	195
97.	Decay curve for blend of BeI and BeII autoionization lines at E_{CM} = 105.5 eV	197
98.	Decay curve of the (1s2s2p) $^4P^o_{1/2,3/2,5/2}$ states in BeII	201
99.	High energy portion of the prompt boron spectrum produced by 300 keV B^+ → C-foil excitation	202

Figure		Page
100.	Energy level diagram of the lowest core-excited states in BI, BII and BIII as measured from the BI ($1s^2 2s^2 2p$) ground state	204
101.	Electron spectrum from boron beam, as observed with the foil in view of the spectrometer (intensity scale logarithmic)	206
102.	Segment of boron electron energy spectrum (linear scale) plotted in the projectile rest frame	207
103.	Partial energy level diagram representing autoionizing decays of the $^4P^o(1)$, $^5P(1)$ and $^6S^o(1)$ terms in boron	209
104.	High energy portion of the prompt and delayed spectra of autoionization electrons emitted in flight by 285 keV boron ions	210
105.	4.5 nsec delayed electron energy spectrum due to decays of metastable autoionizing states in BI, BII and BIII	212
106.	Semilog plot of the 4.5 nsec delayed boron spectrum	214
107.	Energy level diagram for boron showing autoionizing transitions from the ($1s2s2p^2$) ^5P level in BII	215
108.	Partial energy level diagram representing autoionizing decays of the $^4P^o(1)$, $^5P(1)$, $^6S^o(1)$ and $^7S^o(1)$ terms in carbon	218
109.	Spectrum of electrons from highly excited carbon projectiles undergoing decay in flight	219

Figure		Page
110.	Prompt and 2.6 nsec delayed electron spectrum of beam-foil excited carbon ions, plotted in the rest frame of the emitting ion	220
111.	Spectrum of electrons emitted by 275 keV carbon ions undergoing decay in flight	221
112.	Decay curve at $E_{CM} \simeq 238.5$ eV for a carbon beam of about 281 keV	223
113.	Formation of beam-foil excited states with K-shell vacancies	232
114.	Deexcitation of the $(3p^2)\ ^1D$ state through a succession of an autoionization and E1 transition	234
115.	Cascade scheme for the lithium-like $(2s2p^2)\ ^1D$ state	235

LIST OF TABLES

Table		Page
1.	Characteristic properties of the beam-foil source for a 350 keV ion accelerator	7
2.	Atomic systems with few electrons ($Z \leq 6$)	9
3.	Selection rules for autoionization	23
4.	Configuration mixing of prompt and metastable autoionizing ($1s2s2p^2$) states of the beryllium isoelectronic series for I = 0	25
5.	Metastable autoionization of the beryllium-like ($1s2s2p^2$) $^5P_{3,2,1}$ states	26
6.	K-shell fluorescence yields for light atoms	28
7.	Variation of significant spectrometer properties as a function of $w_1=w_2$ for fixed $\theta_L=42.3^\circ$, k=1.3098, n=0.881, $\rho \simeq 1.5$ mm, $\tau=1$, and D=165.31 mm	42
8.	Geometrical parameters for the cylindrical mirror analyzer	44
9.	Summary of information about the CMA	57
10.	Physical quantities defined in the laboratory and center-of-mass frames	78
11.	Effective line width and energy resolution for the $(1s2s2p)\ ^4P^o_{5/2} \rightarrow (1s^2\varepsilon f)\ ^2F^o_{5/2}$ autoionization line	88
12.	Measured width and energy resolution for the $(1s2s2p)\ ^4P^o$ autoionizing decay of the lithium isoelectronic sequence up to Z=6	93

Table		Page
13.	Comparison of (1s2s2p) $^4P^o$ yield measurements for beryllium, boron, carbon, nitrogen and oxygen	120
14.	Position of the binary encounter peak as a function of the projectile mass for $\theta_L = 42.3^o$ and $E_B = 300$ keV	125
15.	Effective quantum numbers for some resonances in BeIII** (Lip 75)	145
16.	Excitation energies of some LiI (1s3131') states above the LiI ($1s^2 2s$) ground state	147
17.	Computed excitation energies above the LiI ($1s^2 2s$) ground state of some prominent lithium states in comparison with experimental data	149
18.	Computed LiII (2s2p) $^{3,1}P^o$ excitation energies above the LiII ($1s^2$) ground state in comparison with experimental data	153
19.	Energy values of some triply excited states in LiI	162
20.	Relative cross sections and cross section ratios for Li^+ → C-foil excitation ($E_B \simeq 300$ keV; $\theta_L \simeq 42.3^o$)	171
22.	Fine structure splitting and fine and hyperfine constants for (1s2s2p) $^4P^o$ state of lithium (in mK)	174
23.	Nuclear spins, magnetic dipole and quadrupole moments for $Z \leq 6$ (Mat 68)	176
24.	Relative excitation cross sections for Be^+ → C-foil bombardment ($E_B \simeq 300$ keV; $\theta_L \simeq 42.3^o$)	184

Table		Page
25.	Cascade scheme for decay of double K-vacancies in beryllium	185
26.	Cascade scheme for three electron autoionization transitions in BeI	186
27.	Transition energies (eV ion rest frame) for metastable autoionizing transitions involving initial core-excited ($1s2s2p^2$) ^5P states in beryllium	199
28.	Comparison of lifetimes obtained in this work with other experimental values	199
29.	Comparison of relative vacancy production cross sections for 300 keV Li^+, Be^+ and B^+ ions on carbon foils	225
30.	Experimental and theoretical values for the energies of some metastable autoionizing states in beryllium, boron and carbon (energies in eV)	227
31.	Predicted line energies for some three electron autoionization transitions in LiI, BeII, BIII and CIV	230

I. INTRODUCTION

If two, three or more electrons are simultaneously excited relative to an atomic (ionic) ground state configuration then the atom (ion) is said to be in a doubly, triply or multiply excited state. More specifically, highly excited state configurations are formed by (i) core excitation, where one or more inner shell electrons are raised to open outer shells, (ii) multiple excitation due to transfer of two or more valence shell electrons to unoccupied orbits, and (iii) core excitation accompanied by simultaneous excitation of valence shell electrons. The simplest atomic systems where double excitation can be studied are the helium-like atoms, while lithium and its isoelectronic analogues are the simplest atoms where core-excited and multiply excited states can occur. Such highly excited states having energy in excess of the first ionization potential subsequently decay by two competing processes, radiatively via multipole transitions and/or radiationless via autoionization to one or more adjacent continuum states. For instance, the $1s2lnl'$ ($n \geq 2$) core-excited states in LiI are more than 50 electron volts (eV) above the $1s^2$ ionization limit and are therefore degenerate in energy with the adjacent $(1s^2\varepsilon l)^2L$ ($L = l$) doublet continuum. The autoionization process can simply be described as a non-radiative readjustment of the atom where in general one electron undergoes a transition to a lower lying open shell and another electron is transferred to an adjacent continuum. The result of this process are a free autoionization electron and the formation of a residual atom corresponding to the next higher ionization stage.

Such core- or multiply excited configurations with unsaturated electrons and/or holes are usually classified according to the independent particle model. Assuming LS coupling the unpaired electrons and/or holes are coupled to give the allowed ^{2S+1}L terms. Here L and S are the total orbital and spin angular momenta of the entire atomic system. If more than two unpaired electrons and/or holes are present in the atomic

(ionic) configuration, high total angular momentum and spin may result. Due to specific selection rules such states are often metastable with respect to Coulomb autoionization, electric dipole transitions or a combination of both processes. In the limit of non-relativistic theory autoionization is caused by the Coulomb interaction, whereas in the relativistic theory the electron-electron interaction has electrostatic and magnetic character. The decay rates of radiationless transitions depend sensitively on the strength of configuration interaction with the adjacent continua. Hence autoionizing states may be characterized according to their decay modes as (a) Coulomb autoionizing terms, which are strongly coupled with the neighbouring continua through electrostatic interactions and (b) magnetic autoionizing terms, which are only weakly coupled with these continua via the relativistic part of the Hamiltonian (Fel 67). Because of the weakness of relativistic interactions in light atoms, magnetic autoionizing states ($Z \leq 6$) are expected to have lifetimes in the range 10^{-8} - 10^{-4} sec, whereas Coulomb autoionization typically occurs in 10^{-15} - 10^{-10} sec.

Whenever there is more than one series for a given S, L, J and parity π, the mixing of different configurations can become quite strong, so that traditional classification based on the independent orbital picture is not valid. The theoretical understanding of configuration interaction in atomic systems with few electrons is most advanced for doubly excited states (Co 63, Fa 75) but seems to be very difficult for N-tuply excited atoms (Ke 75), where two-, three-, and even higher order electron correlations might be significant. Despite the fundamental importance of electron correlation in highly excited atoms and ions, very few data exist for autoionizing states isoelectronic with He, Li, Be, B and C (Sev 72).

This thesis is concerned primarily with the experimental study of electron emission from 300 keV H^+, He^+, Li^+, Be^+, B^+,

C^+, Ne^+ and Ar^+ ion beams, which were passed through 7 $\mu g/cm^2$ thick carbon foils. Prompt and time-delayed autoionization electron spectra on the downstream side of the foil were observed along with the emerging ion beam. In some cases also decay curves from metastable autoionizing states were studied.

In the following section, the historical background of ion-atom and ion-foil interactions is reviewed. Section I.1 also contains a brief description of the characteristic properties of the beam-foil source, and the physical problem is defined in Section I.2. Chapter II gives a survey of autoionization phenomena, including the nature of autoionizing levels, the selection rules for Coulomb- and magnetic autoionization and widths and decay rates. The following three chapters III, IV and V are devoted to the experimental apparatus. In Chapter III, the electron spectrometer is described, and the performance test of the electron analyzer is given in Chapter IV. The description of the ion accelerator, target chamber, beam integration, ion beam collimation and data acquisition system is presented in Chapter V. Chapter VI is concerned with characteristic features of beam-foil autoionization electron spectroscopy, such as ionic charge state distribution, energy straggling and angle scattering in foils, the kinematics of electron ejection and kinematic broadening effects. The experimental results are presented in Chapter VII. This chapter consists of three parts. In the first part, graphs of numerous prompt- and delayed electron energy spectra are displayed. In addition the continuous part of the electron spectra and the absolute energy scale calibration are discussed. In the second part, relative cross sections and yields are estimated, while in the third part decay profiles are indicated. For proper interpretation of the data theoretical calculations and estimates were performed, which are briefly reviewed in Chapter VIII. A comparison of the experimental results with existing theoretical data is given in Chapter IX. The discussion of the results concentrates mainly on the interpretation of (i) Coulomb autoionizing transitions associated with

core-, doubly-, and triply-excited states and (ii) magnetic autoionizing transitions arising from quartet-, quintet-, sextet-, and septet states. In the conclusion, some comments on the beam-foil excitation process are made. Finally the Appendix presents tables concerning highly excited states, their configurations, terms and autoionizing decay modes for atomic systems with less then seven electrons. The Appendix also lists eigenvalues below the ionization threshold of the corresponding H-like ion (total ionization) of various core- and multiply excited states for $Z \leq 6$.

1. Historical Background

The first observation of highly excited levels lying above the lowest continuum threshold was made by Auger (Au 25). In 1927 Wentzel (We 27) and Fues (Fu 27) attempted a non-relativistic theoretical description of autoionization. Further experimental studies which indicated the presence of autoionizing energy levels adjacent to the continuum were made by Compton and Boyce (Com 28) and Kruger (Kru 30). They observed ultra violet (uv)-emission lines in the arc spectrum of helium. These lines were ascribed to transitions from doubly excited states in HeI. In 1931, Shenstone (She 31) found optical transitions which were considerably broadened due to autoionization of the upper level. Atomic resonances were also observed by Beutler (Beu 35). The first resonant states measured by means of inelastic electron scattering were reported by Whiddington and Priestly (Whi 34, 35). Auger electrons were not applied for analytical purposes until 1953, when Lander (Lan 53) demonstrated that Auger electron spectroscopy could be used as a surface analysis technique.

Autoionizing states may also be formed by ion impact on vapour, gaseous and solid targets. Data on the excitation of fast moving particles were provided some 60 years ago in experiments on canal rays (Wie 16). One of the first experimental results on electron ejection after beam-foil collisions were obtained as early as 1930 by Gerthsen (Ger 30) and Schnei-

der (Schn 31), who passed H^+ ions through thin self-supporting foils. The electron emission from the backsurface of the foil was measured in forward direction with a uniform magnetic field electron spectrometer. However, it was not until recently that the study of electron energy distributions following ion-atom collisions was continued. Blauth (Blau 57) measured electron spectra produced by proton impact on atomic and molecular gas targets. The emitted electrons were recorded with an electrostatic cylindrical mirror analyzer (CMA) which was initially proposed by Gerthsen, while Gremmelsmaier (Gre 51) was the first to construct and use one. The first autoionization electron structures subsequent to ion-atom and atom-atom collisions were observed by Berry (Ber 62). In 1964, Rudd (Ru 64) reported autoionization electron spectra resulting from doubly excited states in HeI which were populated by H^+ and H_2^+ ion impact on a helium gas target. The first optical observations of core-excited states using the beam-foil technique where two independent measurements in the LiI spectrum by Bickel et al. (Bick 68) and Buchet et al. (Buch 68). These initial measurements in LiI indicated increased populations of core-excited quartet states relative to normal doublet states when compared with the lithium spectrum produced in a hollow cathode discharge by Herzberg and Moore (Her 59). The beam-foil (BF) technique (Kay 63, Bash 64, Bash 68, Bick 68) consists of passing fast moving ion beams of known velocity through about 3-10 $\mu g/cm^2$ thick carbon foils. By this method atomic particles in different stages of ionization and in various excited states are created. Since the density in foils is about 10^5 times greater than in gaseous light sources or gaseous targets, the condition for multiple collisions is satisfied. Due to a large number of collisions with successive foil atoms the foil excitation process may be described in terms of an excitation temperature corresponding to a streaming plasma (Gar 73). Thus during ion-foil interaction several excitation processes (multiple excitation) including inner-shell vacancy production can occur before the projectiles have time to relax. Further characteristic properties of the

beam foil source are: (a) High chemical and isotopic purity except for minor transmission sputtering, (b) high time resolution, which allows to measure decay rates of excited states, (c) perturbation free deexcitation of atomic states, (d) coherent excitation of atoms in terms of linear superposition of eigenstates, (e) population of optically inaccessable terms and (f) non-statistical excitation of magnetic substates (An 70). Some of these important features of the beam-foil source are specified in more detail in Table 1. Up to 1970 the beam-foil method was extensively used but was limitated to observation of those states decaying predominantly by photon emission. However, the foil excitation technique may also provide a promising method to study the ejection of autoionization electrons of fast moving beam particles. In this connection Dmitriev et al. (Dmi 67, Dmi 68, Dmi 72) reported lifetime measurements of metastable (1s2s2p) $^4P^o_{5/2,\ 3/2,\ 1/2}$ states in Be II, B III, C IV, N V and O VI after passage through a thin celluloid foil. These time-of-flight measurements consisted in measuring the increase of charge i+1 produced in a collision chamber from ions of charge i due to autoionization as a function of the distance between the target and a mass-monochromator. Dmitriev and coworkers have assumed that the total contribution is from decays of the lowest $^4P^o_{5/2,\ 3/2,\ 1/2}$ states. This is a possible source of errors in the lifetime determination of such states. The first direct measurements of the electron spectra of beam-foil excited quartet states were by Donnally et al. and Sellin et al. (Don 71, Sel 71) on oxygen and fluorine beams at Tandem energies. They observed electrons emitted from metastable ions downstream from an exciter-foil. Sellin et al. (Sel 71, Sel 72) also reported the observation of delayed autoionizing decays which probably arise from four-electron systems. No quantitative results concerning autoionization of core-excited beryllium-like and boron-like systems have been reported, however. Velocity spectra of electrons ejected in the forward direction from the backsurface of carbon foils were obtained (Har 71, Luc 72) for the ions H^+, H_2^+, He^+ and also for N^+ and N_2^+. For helium and

Table 1: Characteristic properties of the beam-foil source for a 350 keV ion accelerator

Incident beam energy E_B: 30 - 350 keV
Beam current I: 1 nA - 50 $\mu A/mm^2$
Particle velocity v_B: $v_B \simeq 0.43928 \times (qE_B/M)^{1/2}$ mm/nsec with q = charge state of the ion, M = ion mass, E_B (keV), For example 300 keV $^9Be^+$ ions have the velocity $v_B \simeq 2.5$ mm/nsec
Time-of-flight t: $t = z/v_B \simeq 0$ to $\sim$100 nsec
Time window Δt: $\Delta t = \Delta z/v_B \simeq 100$ psec to $\sim$1nsec
Collision time t_c: $t_c = d/v_B \simeq 10^{-14}$ sec with d = foil thickness
Bandwidth of excitation ΔE: $\Delta E = \hbar/t_c \simeq 100$ meV with $\hbar$ = Planck constant
Coherence: $\|\Psi(t = 0)\rangle = \sum_i \alpha_i \|\Psi_i\rangle$
Alignment: $\sigma(\|M_J\|) \neq \sigma(\|M_{J'}\|)$ for $J > 1/2$ with $\sigma(M_J)$ = excitation cross sections
Plasma temperature T: $T = 2\varepsilon/k$ with $\varepsilon = (m_e/M)E_B$ = reduced beam energy and k = Boltzmann constant Example: $^9Be^+ \rightarrow$ C-foil, E_B = 300 keV $T \simeq 4.2 \times 10^5$ ^oK

nitrogen small peaks were seen, superimposed on a large cusp-shaped continuous electron background. It was suggested that these small peaks might originate from autoionization of transmitted atoms and ions. However, the analysis of these discrete electron spectra have not been done in any detail so that further beam-foil work concerning autoionization transitions for two-, three-, four-, five-, and six-electron systems is strongly needed.

2. The Physical Problem

In the present work, the beam-foil technique is applied to autoionizing decays of the emitting projectiles with $Z < 6$. The possible charge states, atomic state configurations, spectroscopic terms (with LS coupling notation) of beam particles with $Z \leq 6$ can be appreciated from Table 2 and from Appendix I. The beam-foil method concerning observation of electrons emitted in flight is called here beam-foil autoionization electron spectroscopy (BFAES) or generally if solids or gaseous targets are involved projectile autoionization electron spectroscopy (PAES). BFAES is to measure autoionization electrons created by foil transmitted beams of known velocity with some type of electron spectrometer. This kind of time-of-flight measurement permits electron energy spectra and decay curves versus the foil distance z to be recorded. In general, the data which can be obtained in BFAES are excitation energies, spectroscopic character, decay modes, decay rates, branching ratios and excitation cross sections of Coulomb- and magnetic autoionizing levels. These data are useful to test and improve present atomic structure theories and wave functions (Co 63, Bu 63, Fa 65, Al 65, Bu 65, Ma 65, Gar 65, Mac 66, Lip 66, Tem 66, Hol 67, Bha 67, Co 67, Al 67, Or 67, Per 68, Mac 68, Co 70, Sin 70, Hol 71, Das 73). They are also important for the determination of the electron temperature and constitution in astrophysical and laboratory plasmas (Tem 66, Pea 69, Ga 72). For instance in astrophysical sour-

Table 2: Atomic systems with few electrons ($Z \leq 6$)

Isoelectronic Series	Number of Electrons	Charge State	Spectroscopic Assignment	Possible Terms (LS Coupling)
Helium-like	2	He, Li^{+}, Be^{2+} B^{3+}, C^{4+}	He I, Li II, Be III, B IV, C V	^{3}L, ^{1}L
Lithium-like	3	Li, Be^{+}, B^{2+}, C^{3+}	Li I, Be II, B III, C IV	^{4}L, ^{2}L
Beryllium-like	4	Be, B^{+}, C^{2+}	Be I, B II, C III	^{5}L, ^{3}L, ^{1}L
Boron-like	5	B, C^{+}	B I, C II	^{6}L, ^{4}L, ^{2}L
Carbon-like	6	C	C I	^{7}L, ^{5}L, ^{3}L, ^{1}L

ces such as the solar corona (Wa 71) or in a laser generated plasma (Su 72) recombination can take place as a two-stage process, in which an electron and ion form a resonant intermediate state, which then decays to a real bound state via photon emission. This process, called dielectronic recombination (Gab 72), can considerably enhance radiative recombination rates. Further studies which are of interest are the direct Coulomb ejection of electrons emitted from the backsurface of the foil, which may be investigated to yield information on electron production cross sections in multiple ion-atom collisions (Ru 74); and another area where the ejection of electrons due to ion-atom interactions in matter may be of great importance is in biological objects (Der 69, Stre 69, Kob 70, Stol 71) and in medical physics. Finally autoionization (Auger) electrons liberated within the escape depth $\Delta d \sim 10$ Å (Ja 71, Tra 72) of the target can be utilized as a tool to study the elemental composition of the last monolayers of the foil surface (Mus 72, Ben 72, Bu 72).

II. SURVEY OF AUTOIONIZATION PHENOMENA

1. Autoionizing Levels

Using the beam-foil interaction mechanism atoms and ions may be frequently excited to core- or multiply excited states which in turn can spontaneously decay by electron emission. These highly excited states lying above the lowest ionization limit are energetically degenerate with a continuum of the same energy. That continuum may be considered to be composed of a set of continua corresponding to an extension of ordinary term sequences. Thus ordinary quantum numbers of Rydberg series below ionization threshold are retained for the continuum, e.g. for LS coupling the numbers L, S, J and parity π. As depicted in Fig. 1, discrete states $|\Psi_E\rangle_D = |\Psi_i\rangle$ and continuum states $|\Psi_E\rangle_C = |\Psi_f\rangle$ are mixed due to mutual interactions of electrons participating in the radiationless deexcitation process. Such quasi-stationary states lying in the continuum are usually called Auger-, autoionizing-, compound- or resonant states. Holøien has divided these states (Ho 70) into two general classes:

a) weakly quantized states which are subject to Coulomb autoionization with lifetimes less than 10^{-11} sec and
b) strongly quantized states which cannot autoionize by pure Coulomb interactions.

Autoionizing states are decaying states and therefore correspond to a pole of the S-matrix (Smi 71). This dual nature of highly excited states as decaying autoionizing states and resonant scattering states has been brought out by Fano (Fa 61, Fa 65). Accordingly Auger and autoionizing states are mostly considered as quasi-stationary states implying the bound-state character, whereas compound and resonance states imply the scattering point of view. In the following the decay of autoionizing (Auger) states will be studied. Usually the more intense lines that appear in the autoionization spectrum are the result of normal autoionization processes (Fig. 2a) and are referred to normal lines. Ordinarily Coulomb autoionization may be

characterized as

$$(\ldots\ nln'l'n''l'') \rightarrow (\ldots\ n'''\,l'''\,n'l'\varepsilon l^{iv}) \qquad \text{(II-1a)}$$

where one nl electron fills an inner-shell vacancy, e.g. $nl \rightarrow n'''\,l'''$, a second electron is emitted, namely, $n''l'' \rightarrow \varepsilon l^{iv}$, while a third n'l' electron is not involved in the autoionization process, but acts as spectator. However, there is a finite probability for the occurence of three electron transitions causing lower intensity satellite autoionization lines. Three electron autoionization (Fig. 2b, c, d) of the type

$$(\ldots\ nln'l'n''l'') \rightarrow (\ldots\ n'''\,l'''\,n^{v}l^{v}\varepsilon l^{iv}) \qquad \text{(II-2)}$$

involves non-radiative readjustment of three electrons, e.g., $nl \rightarrow n'''\,l'''$ $(n > n''')$, $n'l' \rightarrow n^{v}l^{v}$ $(n' > n^{v}$ or $n' < n^{v})$ and $n''l'' \rightarrow \varepsilon l^{iv}$, respectively. Using the above nomenclature three electron transitions can be subdivided into two groups: (a) Satellite lines arising from those autoionization processes where one electron fills an inner-shell vacancy accompanied by the excitation of a second electron $(n > n'''$, $n' < n^{v})$ and the energy of these two transitions is transferred to a third electron (see Fig. 2b, c). The spectral lines associated with these transitions are shifted to lower energies with respect to the "diagram" lines. (b) Three electron transitions where two electrons are deexcited simultaneously $(n > n'''$, $n' < n^{v})$ and a third electron is emitted (see Fig. 2d). Satellite transitions of this type are shifted to higher energies with respect to the corresponding normal lines. We further note that many-fold excited states with N electrons can also autoionize in a two step (Fig. 2e) or generally in a (N-1) step multi-stage autoionization process via cascading

$$(\ldots nln'l'n''l'') \rightarrow (\ldots n'''\,l'''\,n'l'\varepsilon l^{iv}) \rightarrow (\ldots n^{v}l^{v}\varepsilon l^{vi}\varepsilon l^{iv})\ldots \qquad \text{(II-3)}$$

Additional autoionization electrons may occur from states that can autoionize into the double-electron continuum as characterized by the following type of process

$$(\ldots nln'l'n''l'') \rightarrow (\ldots n'''\,l'''\,\varepsilon l^{iv}\varepsilon l^{v}) \qquad \text{(II-4)}$$

In this manner, two electrons, e.g. εl^{iv} and εl^{v} are simult-

aneously emitted (Fig. 2f, g). Generally speaking N-tuply excited atoms may be embedded in single-, double-, ...(N-1)-tuple electron continua and hence can eject one, two, up to (N-1) autoionization electrons simultaneously. Also characteristic of radiationless processes is the charge state m on the resulting ion following autoionization. Normal autoionization may be represented by the reaction process

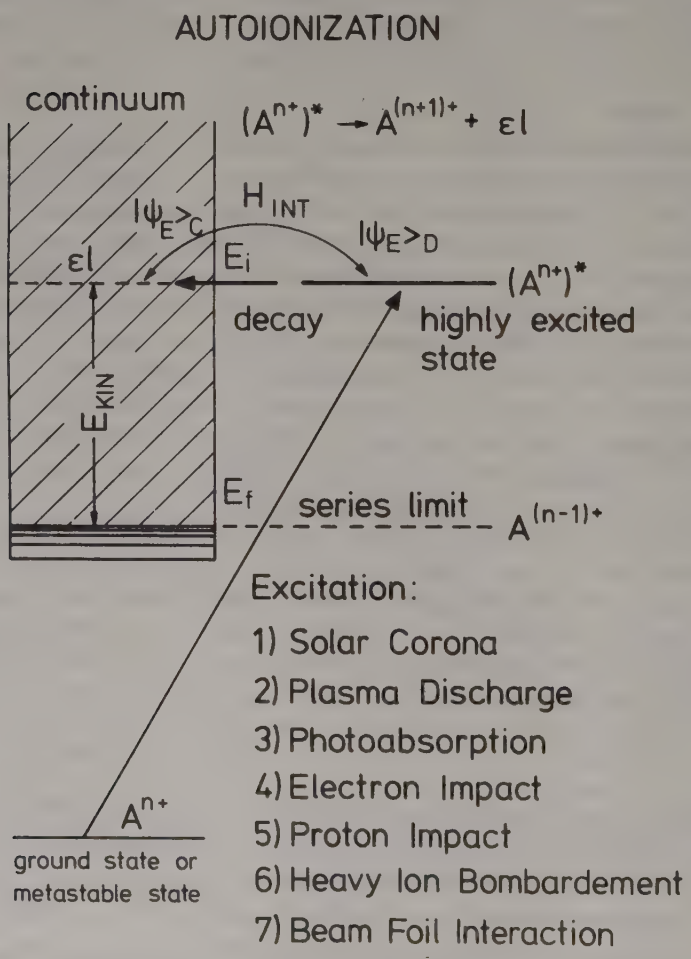

Fig. 1: Schematic energy level diagram illustrating process of autoionization

a) NORMAL TRANSITION

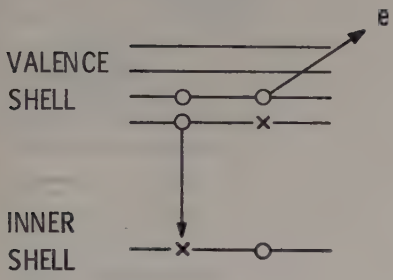

b) THREE ELECTRON TRANSITION

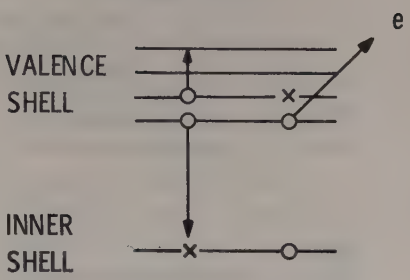

c) THREE ELECTRON TRANSITION

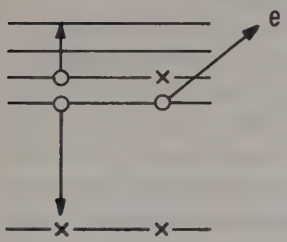

d) THREE ELECTRON TRANSITION

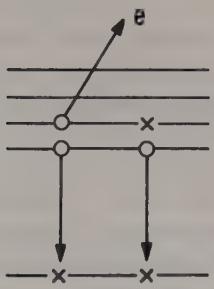

e) TWO STEP TRANSITION

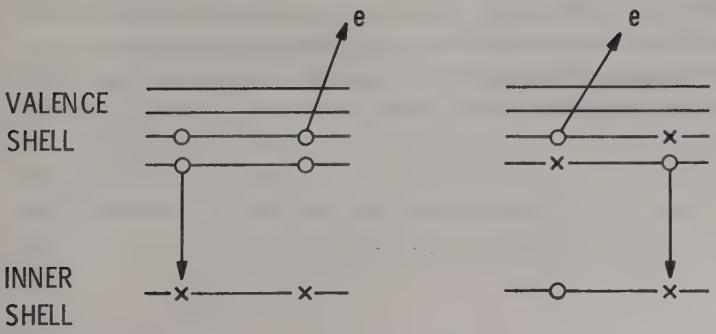

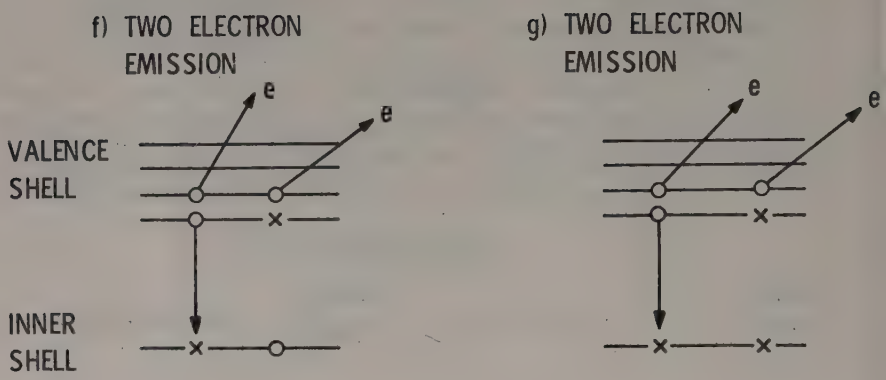

Fig. 2: Schematic representation for autoionization processes.
x = inner or valence shell vacancy

$$(A^{n+})^{**} \rightarrow A^{(n+1)+} + \varepsilon l \qquad \text{(II-1b)}$$

where n is the charge state of the initial state, m = n+1 represents the next higher ionization stage and εl refers to the emitted electron (see Fig. 1). For radiationless processes resulting from two step autoionization (cascading) or decays to the double-electron continuum the residual ionic state is m = n+2, etc. To display autoionizing transitions, commonly two different types of energy level diagrams are used: The autoionization transitions are either represented by horizontal arrows from the initial discrete states to the final continua as indicated in Fig. 1 or as Rudd has suggested (Ru 70) by arrows connecting the initial discrete states with the residual final ionic states. Since the total energy is conserved in autoionizing transitions the kinetic energy transferred to the ejected autoionization (Auger) electrons is equal to the difference between the energy of the initial state E_i and the energy of the residual ion E_f

$$E_{KIN} = E_i - E_f \qquad \text{(II-5)}$$

where E_f can often be determined from optically measured energy levels such as those tabulated by Moore (Mo 46).

2. Selection Rules

Intensities of autoionization lines obtainable in BFAES are generally governed by specific selection rules. The probability amplitudes resulting from a non-radiative readjustment of a highly excited state can be expressed in terms of matrix elements of the kind $\langle \Psi i | H_{INT} | \Psi_f \rangle$. Ψi describes the eigenfunction of the initial electronic state derived from a given coupling scheme (LS, jj, etc.) and Ψ_f describes the final residual ion plus the autoionization electron, again coupled. H_{INT} is the interaction operator related to the coordinates, spins and angular momenta of the initial and final states. We consider an atomic beam particle of N electrons with a nucleus of charge Z. The total Hamiltonian of such a system, H, is approximately given by

$$H = H^{O} + H_{RL} + H_{HF} \qquad \text{(II-6)}$$

where H^{O} is the non-relativistic Hamiltonian

$$H^{O} = \sum_{i=1}^{N} \left(\frac{p_i^2}{2m} - \frac{Ze^2}{r_i} \right) + \sum_{i<j} \frac{e^2}{r_{ij}} \qquad \text{(II-7)}$$

and

$$H_{RL} = H_{SO} + H_{SOO} + H_{SS} + H_{DC} \qquad \text{(II-8)}$$

describes the relativistic corrections to H^{O} due to spin-orbit (SO), spin-other-orbit (SOO) and spin-spin (SS) coupling and H_{DC} is the Darwin contact term according to the (SS) interaction. Finally

$$H_{HF} = H_{M} + H_{Q} \qquad \text{(II-9)}$$

is the hyperfine (HF) Hamiltonian, which can be written as the sum of two terms: the magnetic dipole interaction (M), and the electric quadrupole interaction (Q). The magnetic fine structure operator H_{RL} has been analyzed by Blume and Watson (Bl. 62). It has been shown that the leading terms of these magnetic interactions (Man 66, Man 71) are

$$H_{SO} = \sum_i{}' \zeta(r_i) \vec{l}_i \cdot \vec{s}_i$$

$$H_{SOO} = -\frac{\alpha^2}{2} \sum_{i \neq j}{}' \left(\frac{\vec{r}_{ij}}{r_{ij}^3} \times \vec{p}_i\right) \cdot (\vec{s}_i + 2\vec{s}_j) \qquad \text{(II-10)}$$

$$H_{SS} = \frac{\alpha^2}{2} \sum_{i \neq j}{}' \frac{1}{r_{ij}^3} \left[\vec{s}_i \cdot \vec{s}_j - 3(\vec{s}_i \cdot \vec{r}_{ij}) \frac{(\vec{s}_i \cdot \vec{r}_{ij})}{r_{ij}^2}\right]$$

where α is the fine-structure constant and $\vec{r}_{ij} = \vec{r}_i - \vec{r}_j$. The Darwin contact term $-8\pi \times 3(\vec{s}_i \cdot \vec{s}_j)\delta(\vec{r}_{ij})$ of the (SS) interaction does not affect the multiplet splitting and is therefore ignored. The primes on the summations in equation (II-10) indicate that the sums are to be carried out over the unpaired electrons. The term H_{SO} represents the perturbation between the spin of each electron and the orbital angular momentum. In the absence of any shielding $\xi(r_i)$ would have the value $(Z\alpha^2/2)\langle 1/r_i^3 \rangle$ where $\langle 1/r_i^3 \rangle$ is the expectation value of $1/r_i^3$. The term H_{SOO} describes the spin-other-orbit interactions, that is, the coupling between the electron spin and the orbital magnetic moment of other electron. H_{SS} is the spin-spin interaction term representing the spin-spin dipolar interaction among the electron spins (Fel 67, Bal 67, Fel 68, Est 68, Est 70, Bl 70, Lev 71, Das 73). The selection rules of autoionizing states can now be deduced by calculating matrix elements. Firstly we express the electrostatic interaction in tensor-operator form. We write (Sho 68)

$$H_C = e^2 \sum \frac{r_<^k}{r_>^{k+1}} (C_i^{(k)} \cdot C_j^{(k)}) \qquad \text{(II-11)}$$

The Coulomb matrix elements to calculate in the $[\gamma S M_S L M_L]$ basis are of the form

$$\langle \gamma S M_S L M_L | C_i^{(k)} \cdot C_j^{(k)} | \gamma' S' M_S' L' M_L' \rangle$$

As Judd (Ju 63) has shown these matrix elements are proportional to $\delta(S, S')\ \delta(M_S, M_S')\ \delta(L, L')\ \delta(M_L, M_L')$, i.e. all matrix elements nondiagonal in S and L vanish. Let us now con-

sider matrix elements of the Coulomb operator in the $[\gamma SLJM_J]$ representation. Apart from numerical factors (Sho 68) $H_C \sim T^{(o)}$ is a tensor operator of rank k = o. As a consequence of the Wigner-Eckart theorem (So 72) we can write

$$\langle \gamma SLJM_J | T_o^{(o)} | \gamma' S'L'J'M_J' \rangle = (-1)^{J-M_J} \langle \gamma SLJ || T^{(o)} || \gamma S'L'J' \rangle \times \begin{pmatrix} J & O & J' \\ -M_J & O & M_J' \end{pmatrix}$$

The 3-j symbol if not to vanish must satisfy the condition $\Delta J = O$. Therefore the selection rules for Coulomb autoionization are $\Delta S = O$, $\Delta L = O$ and $\Delta J = O$, respectively. Secondly, we consider spin-orbit matrix elements. Fortunately H_{SO} is already in tensor-operator form. For $\sum_i \zeta(\vec{r}_i)\vec{s}_i \cdot \vec{i}_i$ we have (Ju 63, So 72):

$$\langle \gamma SLJM_J | \sum_i \zeta(r_i)\vec{s}_i \cdot \vec{l}_i | \gamma' S'L'J'M_J' \rangle \sim \delta(J, J')\delta(M_J, M_J') \times \begin{Bmatrix} S & S' & 1 \\ L' & L & J \end{Bmatrix}$$

Using the following two triangular conditions for the nonvanishing of the 6-j symbol we obtain:

$\Delta S = O, \pm 1$

$\Delta L = O, \pm 1$

Therefore the selection rules for autoionization due to spin-orbit coupling are $\Delta J = O$, $\Delta S = O, \pm 1$ and $\Delta L = O, \pm 1$. Let us now deduce the selection rules for the magnetic spin-spin interaction. H_{SS} can be written in tensor operator form (Bl 62, Ju 62, Ju 63, Arm 71)

$$H_{SS} = -2(5)^{-1/2}\beta^2 \sum_k (-1)^k \left\{\frac{2k+5)!}{(2k)!}\right\}^{1/2} \times \sum_{i>j} \frac{r_j^k}{r_i^{k+3}} \{C_i^{(k+2)} \times C_j^{(k)}\}^{(2)} \cdot \{s_i^{(1)} \times s_j^{(1)}\}^{(2)}$$

$$+ \frac{r_i^k}{r_j^{k+2}} \{C_i^{(k)} \times C_j^{(k+2)}\}^{(2)} \cdot \{s_i^{(1)} \times s_j^{(1)}\}^{(2)} \qquad \text{(II-12)}$$

where $\beta = he/2mc$. The first term in the bracket of Eq. (II-12) is taken for $r_j < r_i$ and the second term for $r_i < r_j$. For a particular term of this expansion we derive (Ju 63)

$$\langle \gamma SLJM | \{C_i^{(k)} \times C_j^{(k+2)}\}^{(2)} \cdot \{s_i^{(1)} \times s_j^{(1)}\}^{(2)} | \gamma' S' L' J' M_J' \rangle$$

$$\sim \delta(J, J')\, \delta(M_J, M_J') \begin{Bmatrix} S' & L' & J \\ L & S & 2 \end{Bmatrix}$$

By inspecting the 6-j symbol we find:

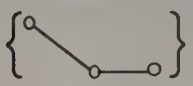

$\Delta S = 0, \pm 1, \pm 2$

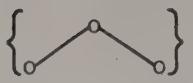

$\Delta L = 0, \pm 1, \pm 2$

Thus the matrix elements for H_{SS} are non zero if

$$\Delta J = 0, \Delta S, \Delta L = 0, \pm 1, \pm 2.$$

We must also consider the effect of hyperfine coupling, especially for core-excited states with unpaired s electrons. The hyperfine interaction mixes levels of different electronic angular momentum J, which is no longer a good quantum number. This effect of hyperfine mixing is to produce states of total angular momentum $\vec{F} = \vec{I} + \vec{J}$ having differing autoionization rates. The magnetic hyperfine Hamiltonian H_{HF}, is composed of three terms, namely the Fermi contact, the magnetic orbital, and the dipole-dipole terms (Jet 74). These three terms are given by

$$H_{FC} = \frac{16\pi}{3} \frac{\mu_B \mu_N}{I a_B^3} \vec{I} \cdot \sum_i \vec{s}_i \, \delta(\vec{r}_i)/r_i^3 \qquad \text{(II-13a)}$$

$$H_O = 2 \frac{\mu_B \mu_N}{I a_B^3} \vec{I} \cdot \sum_i \vec{l}_i / r_i^3 \qquad \text{(II-13b)}$$

$$H_D = 2 \frac{\mu_B \mu_N}{I a_B^3} \vec{I} \cdot \sum_i [3(\vec{r}_i \cdot \vec{s}_i)/r_i^5 - \vec{s}_i / r_i^3] \qquad \text{(II-13c)}$$

For core excited states with unsaturated s electrons such as (1s2snl), (1s2pnl), (1s2s2pnl), ($1s2p^2nl$), etc. the Fermi contact interaction is expected to be of comparable order as the fine structure splitting. To study the nature of matrix elements of H_{FC} we use the [I(LS)JFM$_F$] representation. Thus

$$\langle \gamma I J F M_F | \sum_i s_i^{(1)} \cdot I^{(1)} | \gamma' I' J' F' M_F' \rangle$$

$$\sim \delta(F, F') \, \delta(M_F, M_F') \begin{Bmatrix} I' & J' & F \\ J & I & 1 \end{Bmatrix}$$

$$\times \sum_{\gamma''} \langle \gamma I || I^{(1)} || \gamma'' I' \rangle \langle \gamma'' J || S^{(1)} || \gamma' J' \rangle$$

The 6-j symbol is non-vanishing if the triangular condition $\Delta J = 0, \pm 1$ is fulfilled. The reduced matrix element $\langle \gamma J || S^{(1)} || \gamma' J' \rangle$, expressed in terms of L S and J, can be written as

$$\langle \gamma LSJ || S^{(1)} || \gamma' L' S' J' \rangle$$

$$\sim \delta(L, L') \begin{Bmatrix} J & 1 & J' \\ S' & L & S \end{Bmatrix} \langle S || S^{(1)} || S' \rangle$$

where $\langle S || S^{(1)} || S' \rangle$ is given by (Arm 71)

$$\langle S || S^{(1)} || S' \rangle = [S(S+1) \cdot (2S+1)]^{1/2} \, \delta(S, S')$$

It follows that the matrix elements of H_{FC} vanish unless $\Delta S = 0$, $\Delta L = 0$, $\Delta J = 0, \pm 1$, $\Delta F = 0$, and $\Delta M_F = 0$. Consequently the Fermi contact interaction can couple states differing in J by 1. We further note that for non-s states ($l \neq 0$), the radial matrix elements $\langle R_{nl} | \delta(\vec{r}) | R_{nl} \rangle$ vanish. Hence the Fermi contact term does not contribute for p, d, f, g, etc. electrons.

Next, we turn our attention to the hyperfine terms H_O and H_D. Thus matrix elements of H_O in the $[I(LS)JFM_F]$ representation can be expressed as follows

$$\langle \gamma I(LS)JFM_F | \vec{I} \cdot \sum_i \vec{I}_i | \gamma' I'(L'S')J'F'M_F' \rangle$$

$$\sim \delta(F, F')\, \delta(M_F, M_F') \begin{Bmatrix} I' & J' & F \\ J & I & 1 \end{Bmatrix}$$

$$\times \sum_{\gamma''} \langle \gamma I || I^{(1)} || \gamma'' I' \rangle \langle \gamma'' J || L^{(1)} || \gamma' J' \rangle$$

where $\langle \gamma LSJ || L^{(1)} || \gamma' J' \rangle \sim \delta(S, S') \begin{Bmatrix} J & 1 & J' \\ L' & S & L \end{Bmatrix}$

$$\times \langle L || L^{(1)} || L' \rangle$$

By inspecting these expressions we find that the conditions $\Delta S = 0$, $\Delta L = 0$, $\Delta J = 0, \pm 1$, $\Delta F = 0$, and $\Delta M_F = 0$ must be satisfied. In order to calculate matrix elements for H_D it is convenient to express H_D in tensor operator form. The expression for H_D is

$$H_D = 2 \frac{\mu_B \mu_N}{I a_B^3} \vec{I} \cdot \sum_i \sqrt{10}\, \{s^{(1)} \times C^{(2)}\}_i^{(1)} / r_i^3$$

The procedure for deriving selection rules for H_D is

$$\langle \gamma IJFM_F | \sum_i \{s^{(1)} \times C^{(2)}\}_i^{(1)} \cdot I^{(1)} | \gamma' I'J'F'M_F' \rangle$$

$$\sim \delta(F, F')\, \delta(M_F, M_F') \begin{Bmatrix} S & S' & 1 \\ L & L' & 2 \\ J & J' & 1 \end{Bmatrix}$$

Making use of the triangular conditions of the 9j symbol (Ju 62, Ju 63, Arm 71) we find

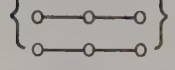

$\Delta S = 0, \pm 1$
$\Delta L = 0, \pm 1, \pm 2$
$\Delta J = 0, \pm 1$

Therefore nonzero matrix elements for H_D exist for $\Delta S = 0, \pm 1$, $\Delta L = 0, \pm 1, \pm 2$, $\Delta J = 0, \pm 1$, $\Delta F = 0$, $\Delta M_F = 0$.

The quadrupole interaction is generally much weaker than H_{FC} and H_O. It has been shown (Ju 62, Ju 63, Arm 71, Das 73) that H_Q is given as a scalar product involving the components of the nuclear quadrupole moment tensor and of the field-gradient tensor of the electrons. Thus

$$H_Q = Q^{(2)} \cdot (\nabla E)^{(2)} \qquad \text{(II-14)}$$

Using Eq. (II-14) matrix elements of H_Q in the $[I(LS)JFM_F]$ representation can be expressed as

$$\langle \gamma I J F M_F | Q^{(2)} \cdot (\nabla E)^{(2)} | \gamma' I' J' F' M_F' \rangle$$

$$\sim \delta(F, F') \, \delta(M_F, M_F') \begin{Bmatrix} I' & J' & F \\ J & I & 2 \end{Bmatrix}$$

$$\times \sum_{\gamma''} \langle \gamma I || Q^{(2)} || \gamma'' I' \rangle \langle \gamma'' J || (\nabla E)^{(2)} || \gamma' J' \rangle$$

The triangular conditions for the non-vanishing of the 6j symbol indicate that H_Q mixes fine structure levels differing in J by 1 and 2, i.e., $\Delta J = 0, \pm 1, \pm 2$. Substituting for the field-gradient tensor

$$(\nabla E)^{(2)}_q \sim \sum_j r_j^{-3} \, C^2_q(j)$$

in the above equation we obtain

$$\langle LSJ || C^{(2)} || L'S'J' \rangle \sim \delta(S, S') \begin{Bmatrix} J & 2 & J' \\ L' & S & L \end{Bmatrix}$$

$$\times \langle L || C^{(2)} || L \rangle$$

By inspecting the 6j symbol we find that the triangular condition $\Delta L = 0, \pm 1, \pm 2$ must be satisfied. To summarize the selection rules for H_Q are $\Delta L = 0, \pm 1, \pm 2$, $\Delta S = 0$, $\Delta J = 0, \pm 1, \pm 2$, $\Delta F = 0$, and $\Delta M_F = 0$.

Another interaction which may affect autoionizing transitions is represented by

$$H_{SM} = \frac{1}{M} \sum_{i<j} \vec{p}_i \cdot \vec{p}_j \qquad \text{(II-15)}$$

where M is the nuclear mass. The presence of the cross terms $\vec{p}_i \cdot \vec{p}_j$ reflects the possibility of correlated motion of the electrons and hence can induce autoionizing transitions. H_{SM} also produces energy shifts (Br 68, Br 69, Br 70). For light atoms the correlated motion (specific mass effect) can be comparable to the normal reduced mass effect (Ko 56, Br 69). We further note that the specific mass Hamiltonian has the same angular matrix elements as the orbit-orbit interaction, which is given by (Lev 71)

$$H_{OO} = \sum_{i<j} (\xi(r_i)/2)\ \vec{I}_i \cdot \vec{I}_j \qquad \text{(II-16)}$$

Using the Wigner-Eckart theorem, one can immediately write

$$\langle \gamma LSJ | \sum_{i<j} C_i^{(1)} \cdot C_j^{(1)} | L'S'J'\gamma' \rangle$$

$$\sim \delta(J, J')\ \delta(M_J, M_J')\ \langle \gamma LS || \sum_{i<j} C_i^{(1)} \cdot C_j^{(1)} || \gamma'L'S' \rangle$$

The latter expression requires that the angular matrix elements for H_{SM} and H_{OO} vanish unless $\Delta J = 0$ and $\Delta M_J = 0$, i.e. the specific mass and the orbit-orbit interaction are independend of J and are zero for atomic configurations with none or only one $l \neq 0$ electron present. Since H_{SM} and H_{OO} are supposed to be very weak, these interactions are omitted throughout the remainder of this work.

Finally parity violating interactions in atoms due to a neutral current (Brod 76) would also affect autoionization (Auger) decays. According to Feinberg and Chen (Fein 74) the parity-violating potential between the electrons and the nucleus should be of the order

$$H_{PV} \sim \sum_i G_F [\vec{\sigma}_i \cdot \vec{p}_i \delta(\vec{r}_i) + \delta(\vec{r}_i)\ \vec{\sigma}_i \cdot \vec{p}_i] \qquad \text{(II-17)}$$

where $G_F \sim 10^{-5}/M_p^2$ (M_p = proton mass) is the weak coupling constant, introduced by Fermi, $\vec{\sigma}/2$ is the electron spin, $\vec{p}$ is the momentum of the electron and $\vec{r}$ its position. Owing to the Coulomb repulsion the electron-electron neutral current inter-

Table 3: Selection rules for autoionization

Term	Interaction	ΔL	ΔS	ΔJ	ΔF	Parity Change	Relative Transition Rate	Range in τ(sec)
H_C	Coulomb	0	0	0	0	No	1	10^{-15} - 10^{-10}
H_{SO}	Spin-Orbit	0, ±1	0, ±1	0	0	No	$\alpha^4 Z^6$	10^{-9} - 10^{-4}
H_{SOO}	Spin-Other Orbit	0, ±1	0, ±1	0	0	No	$\alpha^4 Z^4$	10^{-8} - 10^{-4}
H_{SS}	Spin-Spin	0, ±1, 2	0, ±1, 2	0	0	No	$\alpha^4 Z^4$	10^{-8} - 10^{-3}
H_{FC}	Fermi Contact	0	0	0, ±1	0	No	$\alpha^4 Z^4 (m_e/M_p)^2$	≥ 10^{-7}
H_O	Orbital	0	0	0, ±1	0	No	$\alpha^4 Z^4 (m_e/M_p)^2$	≥ 10^{-3}
H_D	Dipole-Dipole	0, ±1, ±2	0, ±1	0, ±1	0	No	$\alpha^4 Z^4 (m_e/M_p)^2$	≥ 10^{-3}
H_Q	Quadrupole	0, ±1, ±2	0	0, ±1, ±2	0	No	$\alpha^4 Z^4 (m_e/M_p)^2$	≥ 10^{-3}
H_{VP}	Neutral Current	0, ±1	0, ±1	0	0	Yes	G_F^2	?

Table footnote: In the table, Z is the effective nuclear charge, α is the Sommerfeld fine-structure constant, m_e is the electron mass, M_p is the proton mass, and G_F is the weak coupling constant. $\langle H_C \rangle \sim Z$ (Sev. 72); $\langle H_{SO} \rangle \sim \alpha^2 Z^4$ (So 72, Erm 72, Das 73, Gol 74); $\langle H_{SOO} + H_{SS} \rangle \sim \alpha^2 Z^3$ (So 72, Erm 72, Das 73, Gol 74); $\langle H_{FC} + H_O + H_D \rangle \sim \alpha^2 Z^3 (m_e/M_p)$ (Ko 56, Arm 71, So 72); $\langle H_Q \rangle \sim \alpha^2 Z^3 (m_e/M_p)$ (Ko 56, Arm 71, So 72); the hyperfine splitting due to the orbital and dipole-dipole interactions together is about 1 % of the Fermi contact contribution (Wit 73, Jet 74, Be 74, Gau 75, Wit 76). For more details the reader is referred to Appendix XIV.

action should be less effective (Bouch 74) than the electron-nucleus one. On the other hand, parity mixing of high orbitals with $l \neq 0$ would be only sensitive to the electron-electron interaction.

It is well known that autoionizing decays generally proceed close to the nucleus (Mac 67, Mac 68). Thus in doubly excited states the probability for both electrons to penetrate close to the nucleus simultaneously is largest when the electrons are in + states (Co 63). We also note that core-excited and multiply excited states are frequently degenerate in energy with continuum states of opposite parity and equal J. To give a specific example the lithium-like state $(1s2s2p)\ ^4P^o_{5/2}$ is adjacent to the $(1s^2\varepsilon d)\ ^2D_{5/2}$ continuum. Under the action of the parity violating term H_{VP} the unperturbed function $|(1s2s2p)\ ^4P^o_{5/2}\rangle$ might be slightly modified to become $|\Psi\rangle$ where

$$|\Psi\rangle \simeq |(1s2s2p)\ ^4P^o_{5/2}\rangle + \beta|(1s^2\varepsilon d)\ ^2D_{5/2}\rangle$$

However, we suppose that the electromagnetic interactions such as H_C, H_{SO}, H_{SOO}, H_{SS} and H_{FC} are several orders of magnitude stronger than H_{VP}. Therefore parity violating interactions due to a neutral current were neglected.

The selection rules for autoionization are summarized in Table 3. In this table we have also indicated some relative transition rates (Fel 67, Sev 72). If the matrix elements of the electrostatic interaction vanish in first order then the state is said to be metastable with respect to Coulomb autoionization. Such states may decay (a) via E1 transitions, (b) via magnetic coupling with the continuum, e.g. due to magnetic autoionization and (c) by second order processes due to mixing of metastable states with short-lived Coulomb autoionizing states via spin-orbit interaction and/or hyperfine coupling. This last process is referred to as breakdown of LS (IJ) coupling, since the purity of LS(IJ) states is destroyed

by admixtures of other LS(IJ) states. As J(F) and parity continue to be good quantum numbers in the presence of fine structure (hyperfine structure) effects, only LS(IJ) states corresponding to the same value of J(F) and equal parity can mix with each other. Thus, considering the $1s2s2p^2$ state configuration, for example, the lowest energy LS term is ^5P. However, there are other terms $^{1,3}D$, $^{1,3}S$, that can arise from the $1s2s2p^2$ configuration, which may have the same J value and can thus be admixed to ^5P as indicated in Table 4. For example, the matrix element $\langle ^5P_3|H_{SO}|^3D_3\rangle$ of the spin-orbit Hamiltonian leads to a mixing of the $^5P_3$ and $^3D_3$ states. For I = 0, the perturbed function incorporating the mixing is then

$$|(1s2s2p^2)J = 3\rangle \simeq |^5P_3\rangle - \frac{\langle ^3D_3|H_{SO}|^5P_3\rangle}{E(^3D_3)-E(^5P_3)}\,|^3D_3\rangle$$

The energy difference $E(^3D_3) - E(^5P_3)$ involves exchange interactions between electrons in the open shells. For light atoms the denominator in the above expression is substantially larger than the numerator, and perturbation theory is justified. The $(1s2s2p^2)$ ^5P terms are also mixed directly with the adjacent $(1s^2ns\varepsilon l)$ and $(1s^2np\varepsilon l')$ continua through spin-orbit, spin-other orbit and spin-spin coupling. The dominating decay

Table 4: Configuration mixing of prompt and metastable autoionizing $(1s2s2p^2)$ states of the beryllium isoelectronic series for I = 0.

$(1s2s2p^2)$ ^5P	$(1s2s2p^2)$ $^{1,3}S, ^{1,3}P, ^{1,3}D$
$^5P_3$	$^3D_3$
$^5P_2$	^3_1P, $^3_2P_2$, $^1D_2$, $^3D_2$
$^5P_1$	$^3S_1$, $^1P_1$, $^3_1P_1$, $^3_2P_2$, $^3D_1$

Table 5: Metastable autoionization of the beryllium-like $(1s2s2p^2)\ ^5P_{3,2,1}$ states

Initial state	Final state
$(1s2s2p^2)\ ^5P$	$(1s^2 2p\varepsilon p)$ $^{1,3}D,\ ^{1,3}P,\ ^{1,3}S$
$^5P_3$	$^3D_3$ $\Delta S=1$ $\Delta L=1$ (SO/SOO)
$^5P_2$	$^3P_2$ $\Delta S=1$ $\Delta L=0$ (SO/SOO)
	$^3D_2$ $\Delta S=1$ $\Delta L=1$ (SO/SOO)
	$^1D_2$ $\Delta S=2$ $\Delta L=1$ (SS)
$^5P_1$	$^3S_1$ $\Delta S=1$ $\Delta L=1$ (SO/SOO)
	$^3P_1$ $\Delta S=1$ $\Delta L=0$ (SO/SOO)
	$^3D_1$ $\Delta S=1$ $\Delta L=1$ (SO/SOO)
	$^1P_1$ $\Delta S=2$ $\Delta L=1$ (SS)
$(1s2s2p^2)\ ^5P$	$(1s^2 2s\varepsilon s)$ $^{1,3}S$
	$(1s^2 2s\varepsilon d)$ $^{1,3}D$
$^5P_3$	$^3D_3$ $\Delta S=1$ $\Delta L=1$ (SO/SOO)
$^5P_2$	$^3D_2$ $\Delta S=1$ $\Delta L=1$ (SO/SOO)
	$^1D_2$ $\Delta S=2$ $\Delta L=1$ (SS)
$^5P_1$	$^3S_1$ $\Delta S=1$ $\Delta L=1$ (SO/SOO)
	$^3D_1$ $\Delta S=1$ $\Delta L=1$ (SO/SOO)

SO = Spin-Orbit Coupling; SOO = Spin-Other Orbit Coupling;

SS = Spin-Spin Coupling

channels of the $^5P_{3,2,1}$ states resulting from magnetic autoionization are presented in Table 5. Additional tables concerning Coulomb and magnetic autoionizing states are included in the Appendix. These tables are intended to provide a quick survey of nonradiative decay modes of 2-, 3-, 4-, 5-, and 6-electron systems. In particular the $(1s2s2p)\ ^4P^o = {}^4P^o(1)$, $(1s2s2p^2)\ ^5P = {}^5P\ (1)$, $(1s2s2p^3)\ ^6S^o = {}^6S^o\ (1)$ and $(1s2s2p^3 3s)\ ^7S^o\ (1)$ terms are both metastable with respect to E1 decays and Coulomb autoionization, whereas the higher lying ^4L, ^5L, ^6L and ^7L terms should preferentially decay via photon emission or even via Coulomb autoionization.

3. Autoionization Widths and Decay Rates

Collisional excitation processes, such as those used in beam-foil interaction can serve to produce very short-lived and very long-lived levels. The natural line with Γ of such levels are related to the mean live τ by the Heisenberg uncertainty principle, namely

$$\Gamma = \hbar/\tau \simeq 6.582\text{x}10^{-16}\ \text{eV}\cdot\text{sec}/\tau \qquad \text{(II-18)}$$

The autoionization rate (decay probability per unit time) is therefore

$$W_A = 1/\tau_A = \Gamma_A/\hbar \qquad \text{(II-19)}$$

and

$$\Sigma W_i = \frac{1}{\hbar}\,\Sigma\Gamma_i \qquad \text{(II-20)}$$

where Γ_i is the partial width corresponding to autoionization and radiative transitions that compete in the deexcitation process. For a level lying in the continuum the total natural width Γ is given by

$$\Gamma = \Gamma_R + \Gamma_A \qquad \text{(II-21)}$$

where Γ_R is the radiative width and Γ_A the autoionization

width. In general Γ_R and Γ_A are the sum of many partial widths. Yields for radiative and radiationless processes are defined as follows:

$$\omega = \Gamma_R/\Gamma \quad \text{and} \quad a = \Gamma_A/\Gamma \qquad \text{(II-22)}$$

where ω is the radiative (fluorescence) yield and a the autoionization yield. According to Equation (II-22), we have $\omega+a = 1$. For the lightest elements Bambyneck et al. (Ba 72) and Harrison et al. (Har 72) have reported data upon ω, which are presented in Table 6. It is obvious from this table that autoionization is the most probable deexcitation process for low Z elements. This is of course not necessarily true for metastable autoionizing states, where optical decay channels frequently dominate.

There is a definite lack of both experimental and theoretical data on total natural widths and their component partial widths for highly excited states with $Z \lesssim 6$. Propin (Pro 61) has estimated the probability of autoionization in Be^+ ions. Furthermore Manson (Ma 66, Ma 71) has calculated autoionization rates for some helium-like and lithium-like states. Natural width for some doubly excited states of the helium isoelectronic series may be also obtained from the work of Perrott et al. (Per 68) and Balashov et al. (Bal 69). Recently Ziem, Bruch and Stolterfoht (Zie 75) have studied widths of core-excited states in Li I and doubly excited states in Li II. They have determined the full width at half maximum (FWHM) of the $(2s^2)\ ^1S$ state in Li II to be $\Gamma = (100\pm20)$ meV. For the $(1s2s^2)\ ^2S$ state in Li I a width $\Gamma = (50\pm30)$ meV has been

Table 6: K-shell fluorescence yields for light atoms

Z	Atom		References
4	Be	3.04×10^{-4}	(Ba 72)
5	B	7.1×10^{-4}	(Ba 72)
6	C	2.69×10^{-3}	(Har 72)

estimated. The widths of the other Coulomb autoionizing levels in Li I have been found to be less than 30 meV. Levels which are metastable with respect to Coulomb autoionization, must either photodecay, or decay via one of L, S, J and parity violating perturbations such as the spin-orbit interactions. These levels are very narrow. Unlike E1 transitions, autoionization decay rates due to magnetic interactions depend sensitively on the total angular momentum J within a given term (differential metastability with respect to J). Thus for instance the lowest quartet state, $(1s2s2p)\ ^4P^o_{5/2}$ can autoionize to the adjacent $(1s^2\varepsilon f)\ ^2F^o_{5/2}$ continuum through spin-spin interaction, while the $(1s2s2p)\ ^4P^o_{3/2,1/2}$ states are connected to the $(1s^2\varepsilon p)\ ^2P^o_{3/2,1/2}$ continua via spin-orbit plus spin-other-orbit plus spin-spin interactions. In addition, the lifetimes of the $(1s2s2p)\ ^4P^o_{3/2,1/2}$ states are shortened due to admixtures of the $1s(2s2p\ ^3P)\ ^2P^o_{3/2,1/2}$ and the $1s(2s2p\ ^1P)\ ^2P^o_{3/2,1/2}$ rapid autoionizing states. Consequently, the "pure" $^4P^o_{5/2}$ state has a longer lifetime than the corresponding J = 3/2 and J = 1/2 ones. Levitt et al. (Lev 71) have suggested semi-empirical scaling laws for the autoionization rates of the $(1s2s2p)\ ^4P^o$ term. The Z-dependence of the $(1s2s2p)\ ^4P^o_{5/2,3/2,1/2}$ autoionization rates for $Z \leq 6$ approximately goes as:

$$W_A(^4P^o_{5/2}) \simeq (1.13 \times 10^5)\ (Z - 1.75)^3\ \text{sec}^{-1}$$

$$W_A(^4P^o_{3/2}) \simeq (6.75 \times 10^3)\ (Z - 0.4\ )^6\ \text{sec}^{-1} \qquad \text{(II-23)}$$

$$W_A(^4P^o_{1/2}) \simeq (1.1\ \times 10^5)\ (Z - 1.0\ )^6\ \text{sec}^{-1}$$

In Fig. 3 we present a plot of the $(1s2s2p)\ ^4P^o_{5/2,3/2,1/2}$ autoionization rates versus Z as deduced from Equation (II-23). In addition forbidden radiative decays can occur as magnetic quadrupole transitions of the kind $(1s2s2p)\ ^4P^o_{5/2} \rightarrow (1s^22s)\ ^2S_{1/2}$. As Onello et al. (On 75) and Cheng et al. (Che 74) have shown the decay probability for this relativistically induced effect is negligible for low Z, but increases rapidly

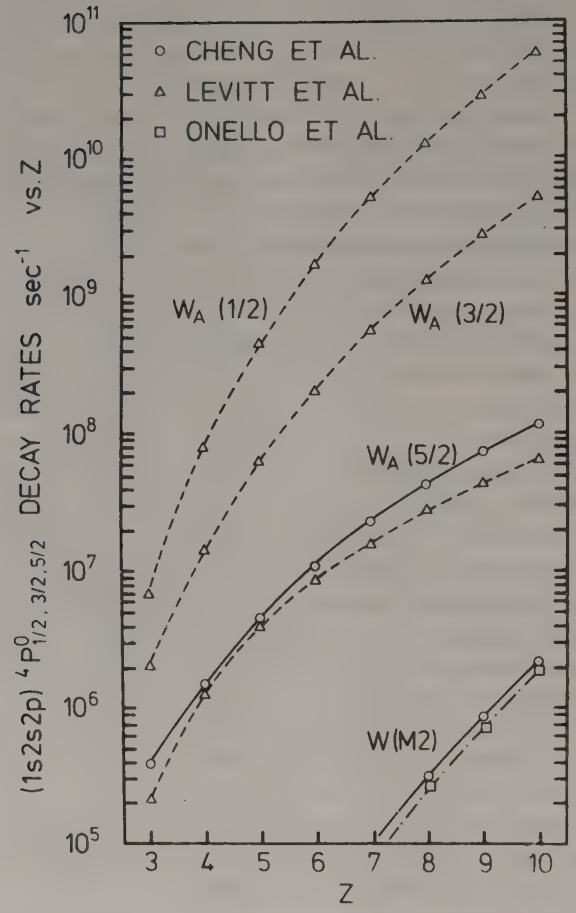

Fig. 3: Decay rates of the Li-like $(1s2s2p)\ ^4P^o$ terms plotted as a function of nuclear charge. $W_A(1/2)$, $W_A(3/2)$ and $W_A(5/2)$ represent the autoionization rates and W(M2) is the M2 radiative decay rate.

with Z (see Fig. 3). Experimental evidence for these kinds of M2 decays have been found in the x-ray spectra of Cocke et al.

(Cock 74). In highly excited state configurations of the type $1s2s2p$, $1s2s2p^2$, $1s2s2p^3$, and $1s2s2p^3 3s$ with unpaired s electrons the Fermi contact term of the hyperfine Hamiltonian can become quite large, so that the hyperfine splitting may have comparable order of magnitude as the fine structure separation. Then different J states are strongly mixed to form hyperfine states F. Due to this mixing hyperfine states have different amounts of J character. That means differing hyperfine components F in general produce differing lifetimes (differential metastability with respect to F). Thus Manson has shown (Ma 71) that the lifetimes of the $(1s2s2p)\ ^4P^o$ terms in ^{6}Li I and ^{7}Li I are different. The hyperfine coupling will be discussed in more detail in Chapter IX.

4. Mean Free Decay Length / Mean Free Path Length for K-Shell Vacancy Production

When He^+, Li^+, Be^+, B^+ and C^+ ion beams with a velocity v_B of about $(2\text{-}3)\times10^8$ cm/sec (∿300 keV) are passed through (7 ± 2) $\mu g/cm^2$ thick carbon foils a relatively large fraction of core excited atoms and ions may emerge from the backsurface of the foil. The foil excitation process is schematically illustrated in Fig. 4. According to Section II.2 and Section II.3, the relaxation times of highly excited beam particles are expected to vary by about eleven orders of magnitude from $\sim10^{-4}$ to $\sim10^{-15}$ sec, corresponding to relaxation distances

$$L_r = v_B \times \tau \qquad \text{(II-24)}$$

ranging from $\sim(20\text{-}30)\times10^{-8}$ cm to $\sim(20\text{-}30)\times10^4$ cm at 300 keV beam energy. Information on the time behaviour and the competing decay modes of highly excited states may be also obtained from Fig. 5. As can be seen from this figure, Coulomb autoionizing states typically have mean lives of $\sim10^{-14}$ sec and therefore decay within (200-300) Å path length. Thus in a foil excitation experiment (foil thickness d ∿ 385 Å) there is a certain probability for the unperturbed observation of such

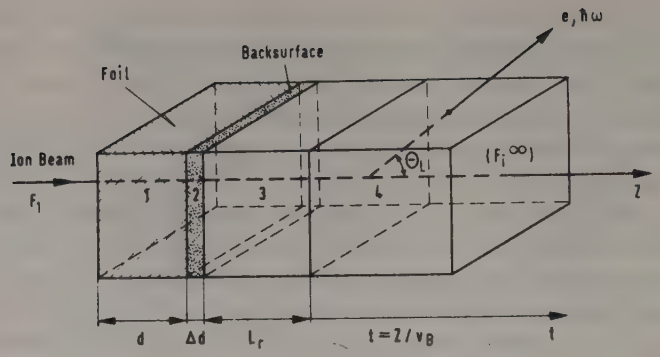

Foil Excitation

Fig. 4: Schematic diagram representing beam-foil excitation. d = foil thickness, Δd∿3Å), L_r = relaxation length for Coulomb autoionization and X-ray transitions, Z = beam axis, v_B = beam velocity, F_i^∞ charge fractions in the far downstream region.

short lived ions in flight after the particles leave the foil. On the other hand atomic systems with few electrons can also exist with lifetimes sufficiently long (τ: $\sim 10^{-10}$ to $\sim 10^{-7}$ sec) to allow time-of-flight measurements. No precise cutoff exists between transitions arising from prompt ($\tau < 10^{-10}$ sec) and time-delayed ($\tau > 10^{-10}$ sec) decaying states.

In order to estimate the probability for K-shell vacancy production in beam-foil experiments a knowledge of the mean free path length λ_K (Gar 70) for K-shell electron removal in solids is required. This quantity is simply given by

$$\lambda_K = 1/(N_C \cdot \sigma_K) \qquad \text{(II-25)}$$

where N_C is the target atom density in carbon foils ($N_C \sim 9$ x

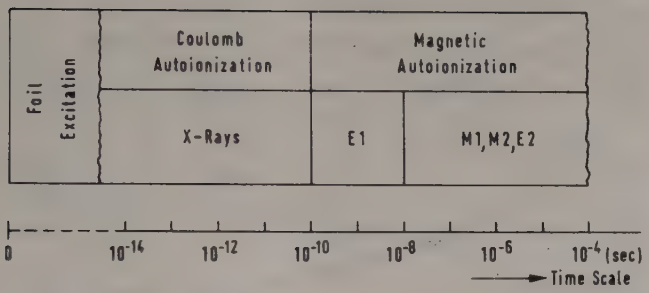

Fig. 5: Competing deexcitation processes in the foil, in its vicinity and far away from it. E1 = electric dipole transitions, M1 = magnetic dipole-, M2 = magnetic quadrupole-, and E2 = electric quadrupole transitions.

10^{22} atoms/cm^3) and σ_K is the cross section for K-shell vacancy production. Now the fraction of ions with one K-shell electron removed can be derived from

$$1 - \exp(-d/\lambda_K) \qquad \text{(II-26)}$$

where d is the foil thickness (1 µg/cm^2: ∿55 Å for C-foils). In Fig. 6 the mean free path length λ_K for C^+ ions incident on C-foils, as a function of the beam energy (range: 0.1 - 1.2 MeV), is compared with the decay length L_r for Coulomb autoionization. To calculate λ_K, observed cross sections σ_K (Gar 73) are used. It is evident from Fig. 6 that λ_K and L_r are of comparable order at 300 keV beam energy. The foil thickness dependence for K-shell vacancy production is shown in the next graph. It can be seen from Fig. 7 that the fraction of ions with one K-shell electron removed is about 78 % for 7 µg/cm^2 thick foils, e.g. only 22 % of the beam particles cannot undergo autoionization (Auger) transitions. In summary it is concluded that beam-foil excitation in the 300 keV ener-

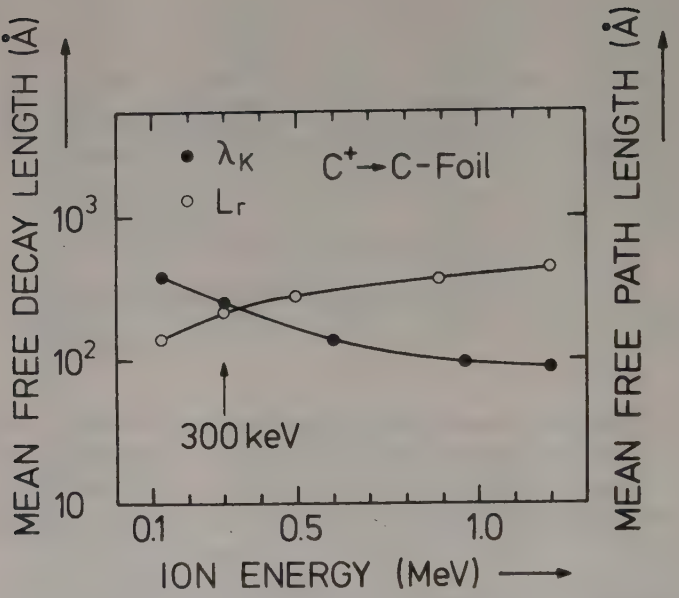

Fig. 6: Comparison of the mean free path length λ_K for K-shell vacancy production with the mean free decay lengths L_r for Coulomb autoionization as a function of the incident ion energy.

gy regime produces considerable fractions of core excited states. In the following section the experimental problem is discussed.

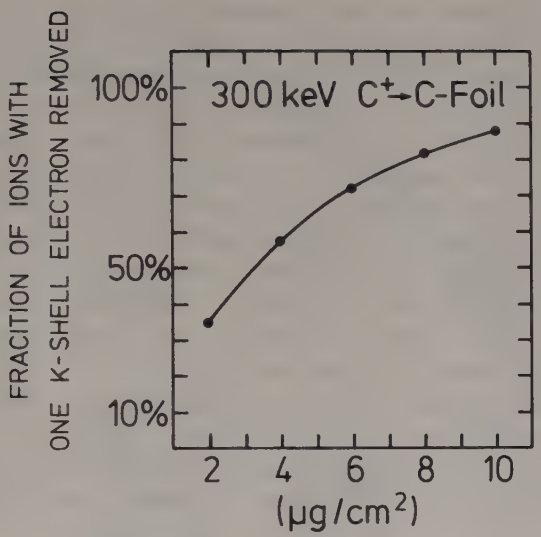

Fig. 7: Dependence of projectile K-shell vacancy production as a function of foil thickness.

5. The Experimental Problem

An experimental apparatus suitable for use in BFAES should fulfill certain requirements. The most important are: (i) High time resolution capability to separate prompt and delayed electron energy spectra, (ii) adequate energy resolution for the separation of prominent autoionization peaks, and (iii) high luminosity for detecting low intensity autoionization lines. In order to measure decay curves a foil drive device is required for moving the exciter-foil along the beam axis in and out of the focus of the electron spectrometer. In addition the maximum delay time should be of the order $\sim$50 nsec or larger to account for metastable states having mean lives in the range $\sim 10^{-9}$ to $\sim 10^{-7}$ sec. To select electrons

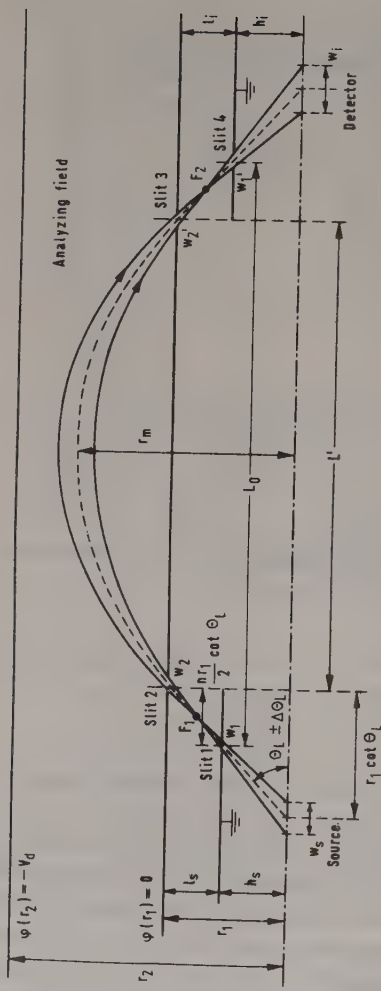

Cylindrical Mirror Analyzer

Fig. 8: Schematic of cylindrical mirror analyzer

according to energy an electrostatic cylindrical mirror analyzer (CMA) was used. The arrangement of a cylindrical mirror analyzer is shown schematically in Fig. 8. Basically the CMA consists of a coaxial double cylinder with two annular slits (slit 2, slit 3). The inner cylinder is grounded, and a negative voltage is applied to the outer cylinder. Electrons which are injected into the condenser field under an angle $\Theta_L \pm \Delta\Theta_L$ are deflected and focused back towards the axis through slit 3. The CMA has a finite energy resolution or window of energies that it will transmit. Owing to the axial symmetry the CMA is capable of collecting electrons from nearly all azimuthal angles $\Phi(\Phi \leq 2\pi)$ at a fixed laboratory cone angle Θ_L with respect to the ion beam axis. In this manner entrance apertures up to several percent of 4π can be achieved. Therefore an electron energy spectrum with a given signal-to-noise ratio (S/N) can be obtained as much as 100 times faster with the CMA than with other common deflection type analyzers such as the parallel-plate-, spherical-, and cylindrical analyzer (Sev 72). Extremely high transmission and luminosity is of particular importance, when weakly autoionizing spin and angular-momentum forbidden decays are studied. Gremmelmaier (Gre 51) and Blauth (Blau 57) were the first to use a CMA design that analyzed electrons which were ejected at 54.5° from the axis and Mehlhorn et al. (Me 60, Me 65, Kör 66, Me 68, Cle 69) used a similar analyzer for extensive Auger spectroscopy studies. Since then the CMA was subjected to detailed theoretical and experimental studies to optimize the energy resolution, dispersion, luminosity and imaging properties. A general description of the CMA is given in the next section.

III. ELECTRON ENERGY ANALYZER

1. General Description of the CMA

The focusing properties of the cylindrical mirror analyzer were extensively described by Zashkvara et al. (Za 66, Za 69, Za 70, Za 71), Sar-El (Sar 67, Sar 71), Aksela et al. (Ak 70) and Risley (Ris 72). It was shown that the CMA can be operated in two different modes of imaging: (i) the axial focus mode, in which a point source on the symmetry axis is imaged back to a focal point on the same axis and (ii) the ring-focus mode, in which the slits are the loci of object and image. The ring-focus mode is illustrated schematically in Fig. 8. In the ring-focus mode the CMA is operated with one pair of entrance slits (slit 1, slit 2) and one pair of excit slits (slit 3, slit 4) having the form of annular rings with widths w_1, w_2, w_1', and w_2', respectively. For an extended source of length w_s (see Fig. 8) generally first-order focussing is achieved. For convenience the following symbols are defined: w_1, w_2 = entrance slit widths, w_1', w_2' = exit slit widths, θ_L = emission angle (laboratory frame), $\Delta\theta_L$ = semiangular aperture, r_1 = inner cylinder radius, r_2 = outer cylinder radius, r_m = maximum radial distance, h_s = distance between symmetry axis and annular slit 1, h_i = distance between symmetry axis and annular slit 4, L_o = projection of the flight path onto the symmetry axis between source slit 1 and image slit 4, L' = path length in the electric field region, w_s = projection of slit 1 onto the symmetry axis (source length), w_i = projection of slit 4 onto the symmetry axis (detector length), U_A = deflection voltage on outer cylinder, r_c = distance of closest approach for off-axis electrons passing by the symmetry axis, and ρ = radius of the ion beam. According to Aksela et al. (Ak 70) the projection of the flight path onto the CMA axis (Z-axis) is given by

$$L_o = nr_1\cot\theta_L + 4r_1 k^{1/2}\cos\theta_L \exp(k\sin^2\theta_L) \times \int_0^{\sqrt{k}\sin^2\theta_L} \exp(-u^2)\,du \qquad \text{(III-1)}$$

where

$$k = E/U_A \ln(r_2/r_1) \quad \text{and} \quad n = (l_s + l_i)/r_1$$

It can be seen from Eq. (III-1) that L_o is a function of the variables n, k and Θ_L, where k depends on the energy E and the analyzer voltage U_A for fixed ratio of r_2/r_1. Thus the axial path length varies with n, U_A, E and Θ_L as $L_o = L(n, U_A, E, \Theta_L)$. Likewise the energy of electrons having path length L_o is $E_o = E(n, U_A, L, \Theta_L)$. From the Taylor series expansion for L_o one can show that for angular spread $\Theta_L \pm \Delta\Theta_L$ and energy variation $E \pm \Delta E$, the image is extended by ΔL such that

$$\Delta L = (\partial L/\partial E)\Delta E + (\partial L/\partial \Theta_L)\Delta\Theta_L + (\partial^2 L/\partial\Theta_L^2)\ \Delta\Theta_L^2 + \ldots \quad \text{(III-2)}$$

It is usual to define the energy dispersion D, which is related to the energy resolution as follows

$$D = E(\partial L/\partial E) \quad \text{(III-3)}$$

The base resolution R_b is defined as the ratio $\Delta E_b/E$, where ΔE_b is the maximum energy spread of the analyzer transmission function. The corresponding energy resolution R(FWHM) is given by R(FWHM) = $\Delta E/E$ where ΔE is the full width at half maximum (FWHM) intensity. Risley (Ris 72) has shown that the base resolution of the CMA can be expressed in the form

$$R_b \simeq (w_s + w_i)/D + \Delta L(\pm\Delta\Theta_L)/D + (r_c/r_1)^2 \quad \text{(III-4)}$$

(i) where the first term describes the degradation of resolution due to finite source- and detector length

(ii) the second term gives the degradation of resolution due to finite angular spread

(iii) and the third term takes into account the line broadening due to off-axis electrons having nonzero angular momenta.

For a well designed electron analyzer the apparatus function is approximately triangular (equal slit widths presumed). Then R(FWHM) is simply given by R(FWHM) $\simeq$ 1/2 R_b. Note that the focusing conditions of the CMA can be optimized by a proper choice of the parameters Θ_L, k and n. In particular it is

possible to minimize the first- and second order aberration terms. Using k = 1.3098, $\Theta_L \simeq 42.3^o$ and n≠2 first-order focusing (i.e. $\partial L/\partial\Theta_L \simeq 0$) is obtained, whereas second-order focusing (i.e. $\partial L/\partial\Theta_L = \partial L^2/\partial\Theta_L^2 \simeq 0$) requires k = 1.3098, $\Theta_L \simeq 42.3^o$ and n=2, respectively. We also note that second-order focussing (n=2) occurs as an asymptotic case of first-order focussing (n≠2). To determine the angular spread $\Delta\Theta_L$, the effective trace width l_{eff}, the source length w_s, the transmission T and the analyzer luminosity L, electron trajectories were studied. For this reason a cross-sectional view of the entrance aperture of the CMA is given in Fig. 9. In brief, the effective trace width l_{eff} viewed by the analyzer is

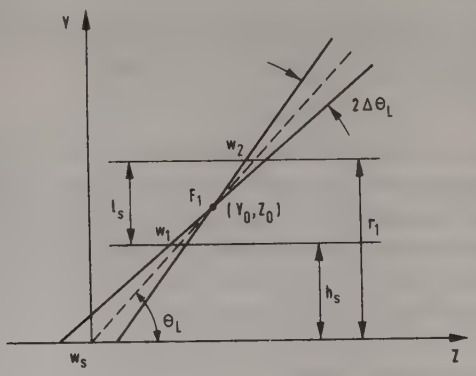

Fig. 9: Cross-sectional view of the entrance slit geometry

$$l_{eff} \simeq w_s + d\cot\Theta_L \qquad (d = 2\rho) \qquad \text{(III-5)}$$

where the source length w_s is expressed as

$$w_s = [(m \cdot l_s + h_s)/((1-m)\, l_s)]\, w_2 \qquad \text{(III-6)}$$

and $m=w_1/(w_1+w_2)$. For $w_1=w_2$ we obtain m=1/2. The semiangular divergence $\Delta\Theta_L$ then becomes

$$\Delta\Theta_L = \arctan\,(w_2 \sin^2\Theta_L/(2(1-m)l_s)) \qquad \text{(III-7)}$$

and the positions of the focal rings F_1 and F_2 are determined by

$$\begin{pmatrix} y_o \\ z_o \end{pmatrix} = (m \cdot l_s + h_s) \begin{pmatrix} 1 \\ \cot\theta_L \end{pmatrix} \qquad \text{(III-8)}$$

The étendue is given by the product of the entrance area F and the entrance solid angle $\Delta\Omega_L$, namely

$$\lambda = F\Delta\Omega_L \qquad \text{(III-9)}$$

in which the solid angle (cylindrical geometry) is $\Delta\Omega_L = (2\pi \sin\theta_L)2\Delta\theta_L$ and

$$T = \Delta\Omega_L/4\pi = \sin\theta_L\Delta\theta_L \qquad \text{(III-10)}$$

is called transmission. The transparency τ is defined as the ratio of the emergent electron flux to the electron flux entering the CMA. Finally the luminosity L is

$$L = F\Delta\Omega_L\tau = \lambda\tau \qquad \text{(III-11)}$$

For a cylindrical source region F is given by $2\pi\rho w_s$. In order to find the optimum operating conditions for the CMA, we estimated values of $\Delta\theta_L$, l_{eff}, R(FWHM), T, w_s and L as a function of the slit widths w_1 and w_2 (assuming $w_1=w_2$). The results are listed in Table 7. It is apparent from this table that R(FWHM) can be maximized by narrowing the slit-widths w_1 and w_2. This reduction of the angular divergence of the entrance apertures must be paid of course at the expense of luminosity. Consequently a compromise must be found between optimum energy resolution and minimum detectable intensity.

Table 7: Variation of significant spectrometer properties as a function of $w_1=w_2$ for fixed $\Theta_L=42.3^o$, k=1.3098, n=0.881, $2\rho\simeq1.5$ mm, $\tau=1$, and D=165.31 mm

w_1 mm	w_2 mm	$\Delta\Theta_L$ degrees	w_s mm	l_{eff} mm	R(WHM) w_s/D %	T %	$L/4\pi$ mm^2
1	1	2	3.54	5.19	2.14	2.1	0.350
0,5	0,5	1	1.77	3.42	1.07	1.1	0.092
0.2	0.2	0.5	0.71	2.36	0.43	0.4	0.013
0.1	0.1	0.2	0.35	2.00	0.21	0.2	0.003

2. Basic Construction

The cylindrical mirror analyzer used in this work has been described recently in the Diplom-Thesis of Paul (Pau 75). Therefore only a brief description of the most significant features will be given here. The analyzer was designed so that electrons emitted nominally under $\Theta_L=42.3^o$ with respect to the CMA axis were accepted. The general layout of the analyzer is depicted in Fig. 10 and the geometrical design parameters are found in Table 8. As can be seen from Table 7, the dimensions of the inner and outer cylinders r_1 and r_2 are 29.50 mm and 67.75 mm, respectively. The collimating slits, which defined a transmission T of 1.17 %, corresponding to an angular spread $2\Delta\Theta_L=2^o$, had an opening of 0.5 mm. In order to permit further reduction of the angular divergence, the entrance and exit slits are continously variable. An important consideration in the design of the CMA is the finite length of the capacitor, i.e. elimination of fringing fields. Hence fringe-field correction rings (Die 72) were placed along the top of the space between the inner and outer cylinders. The potential was distributed from one ring to another with a series of resistors connecting the rings and the analyzer cylinders. These rings also provided a more conducting surface

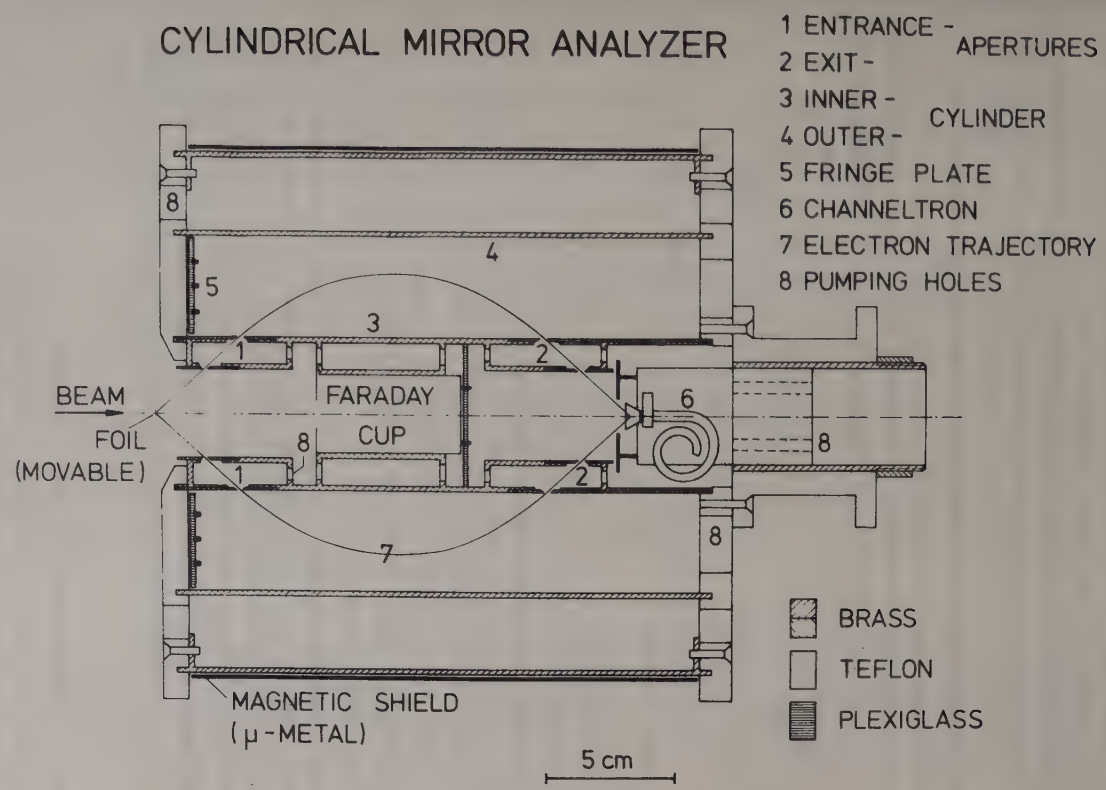

Fig. 10: Layout of the electrostatic electron spectrometer.

on the top face of the cylindrical condenser. In order to have high luminosity, k and n were selected to be k=1.3098 and n=0.881. For a disc-shaped source located on the analyzer axis only first-order focussing was obtained.

Table 8: Geometrical parameters for the cylindrical mirror analyzer

Quantity	Value
w_1, w_2 = entrance slits	0.5 mm
w_1', w_2' = exit slits	0.5 mm
Θ_L = emission angle	42.3°
$\Delta\Theta_L$ = semiangular aperture	1°
r_1 = inner cylinder	29.50 mm
r_2 = outer cylinder	67.75 mm
r_m = maximum radial range	53.4 mm
h_s = distance between CMA axis and slit 1 ($h_s=h_i$)	16.5 mm
L = focal length (w_s : w_i)	180.84 mm
L' = flight path in electric field region	116.00 mm
L_o = projection of the flight path onto the CMA axis between slit 1 and slit 4	144.57 mm
w_s = source length ($w_s=w_i$)	1.8 mm
r_c = distance of closest approach for off-axis electrons	<1.5 mm
$R(FWHM)_{theor}$ = theoretical resolution (extended source)	1.1 %

3. Magnetic and Electric Stray Field Reduction

Any magnetic and electric stray fields inside the apparatus alter the trajectories of low energy electrons. Therefore ferro-magnetic materials were eliminated in and around the target chamber. To provide a low risidual magnetic field environment the target- and spectrometer region was surrounded with annealed numetal. The residual magnetic field along the target chamber axis, as indicated in Fig. 11, was measured

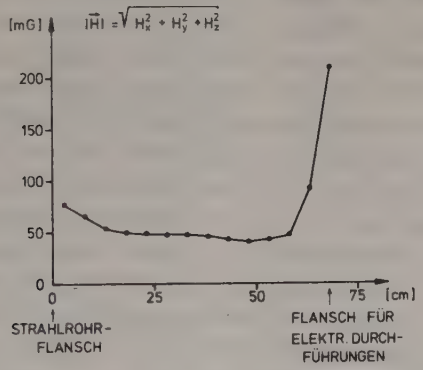

Fig. 11: Magnetic field along the target chamber axis.

with a precision magnetic field meter (Förster Mikrofeldsonde type FK-5-T9-5). To reduce the earth's magnetic field (∿200 mG) to less than 3 mG the analyzer was housed in an additional mumetal cylinder (see Fig. 10) Furthermore, it was found important to degauss the entire target chamber including the mumetal shield, using an alternating current, which was applied through a degaussing coil.

Electric fields due to contact potential differences, fringing fields and surface charges must also be avoided. In order to maintain surfaces with uniform conductivity and contact potential all surfaces in proximity to the electrons were co-

vered with a graphite layer. Other sources of disturbing electric fields are due to (i) biasing of the Faraday cup, (ii) positive charge of the ion beam and (iii) surface charging of the foil during ion bombardement. These effects are discussed later.

4. Electron Detection

Those electrons that passed the analyzer were detected by a channel electron multiplier (CEM), Valvo Type B 419 BL, used in the pulse counting mode. Basically a CEM or channeltron consists of a curved glass tube whose inside surface is coated with a semi-conducting material. This material serves as the secondary electron emitting dynode surface and also as the voltage divider which establishes the electrostatic field required for acceleration of the secondary electrons. These detectors must be operated in a vacuum environment of 10^{-4} torr or better. The channeltron connection for pulse counting mode is shown in Fig. 12a. Before impinging on the CEM cone, electrons were accelerated ($U_p \sim 100$ eV) to insure that all electrons with kinetic energies below eU_p have roughly the same detection efficiency. Since all the data were taken in relative units, we were not interested in any absolute value for the efficiency but only that this efficiency remained constant in time. Data runs were taken within 1 to 60 minutes so that possible changes in CEM efficiency were considered negligible. In Fig. 12b the signal pulse-rate versus operating voltage is shown for a constant test electron source of about 100 eV electrons. The gain of the CEM, about 1×10^8 corresponding to $\sim 10^{-11}$ Coulombs, was varied by adjusting the voltage $\Delta U = U_c - U_p$ across the channeltron. Above $U_c = 3$ keV spurious counts occured. Operation at relatively high pressure (1×10^{-4} torr) increased the probability of spurious signals. Furthermore, ripple voltages must be prevented from triggering the counting circuitry when the CEM is operated. The stray capacitance was minimized by connecting the preampli-

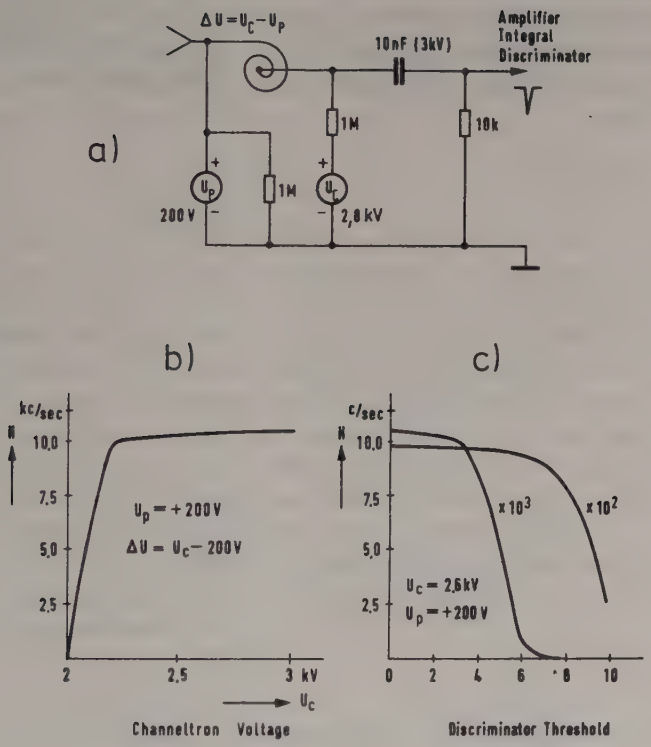

Fig. 12: a) Channeltron connection for pulse counting mode

b) Signal pulse-rate as a function of operating voltage using a constant test electron source of ∿100 eV electrons

c) Signal pulse-rate as a function of discriminator threshold

fier to the CEM output circuitry with the shortest length of shielded cable that is convenient. Finally in Fig. 12c the signal pulse-rate as a function of the discriminator threshold is shown. The background count rate ("dark" count rate) was 0.25 counts per second (cps). To ensure that nearly all pulses were counted, the discriminator level was adjusted so that the average signal amplitude was at least four times greater than the integral discriminator threshold. It was found that the gain of the CEM falls off quickly at count rates higher than 20 kcps. Normally no data were taken with count rates above 20 kcps.

IV. PERFORMANCE TEST OF THE ANALYZER

1. Calibration of the Analyzer

To test the electron spectrometer a point electron source with delta-function-like energy distribution is of considerable experimental value. Such an electron source (Ba 71) can serve to calibrate the absolute energy scale as well as to monitor the analyzer performance with respect to alignment, transmission and energy resolution. In order to assign absolute energy values to autoionization peaks, the analyzer constant C must be known. C is simply given by

$$C = (1/k)\ \ln r_2/r_1 = U_A/E \qquad \text{(IV-1)}$$

To determine C, a monochromatic point electron source (Pau 75) was used. This source is shown in Fig. 13. The main structure of the electron source consisted of a directly heated tungsten filament which was adjusted to the axis of the cylindrical mirror analyzer. Electrons leaving the negative filament were accelerated by the ground potential of a spherical copper mesh. Then they passed into the analyzer where they were deflected and focused onto the channeltron detector. If a voltage-U is applied to the filament the ejected electrons have energies $eU = E$ peaked around $E+\Phi$, where the energy shift Φ is due to (i) contact potential differences, (ii) voltage drop across the filament and (iii) thermal effects. In this case E and U_A satisfy the relation

$$(E + \phi)\ C = U_A \qquad \text{(IV -2)}$$

For large E and U_A, ϕ is negligible and C is merely the ratio U_A/E.

Electrons with energy E and constant flux were injected into the CMA and the spectrometer response was measured as a function of the sweep voltage U_A. The measured count-rate versus U_A is called the transmission function, analyzer resolution curve or spectrometer function. Resolution curves of the CMA

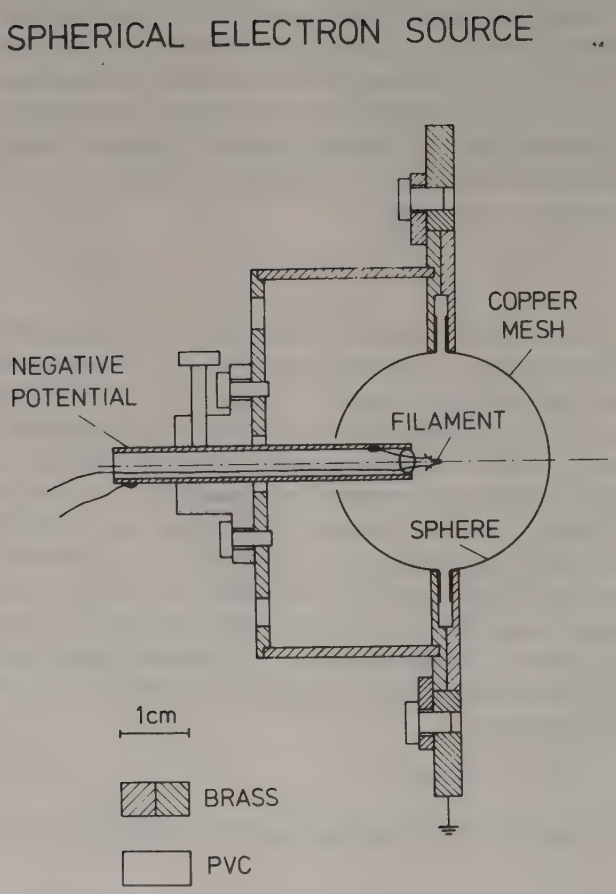

Fig. 13: Dimensional drawing of the monochromatic electron source.

for various settings of E ranging from 15 eV to 1 keV are plotted in Fig. 14. E and U_A were controlled with a digital

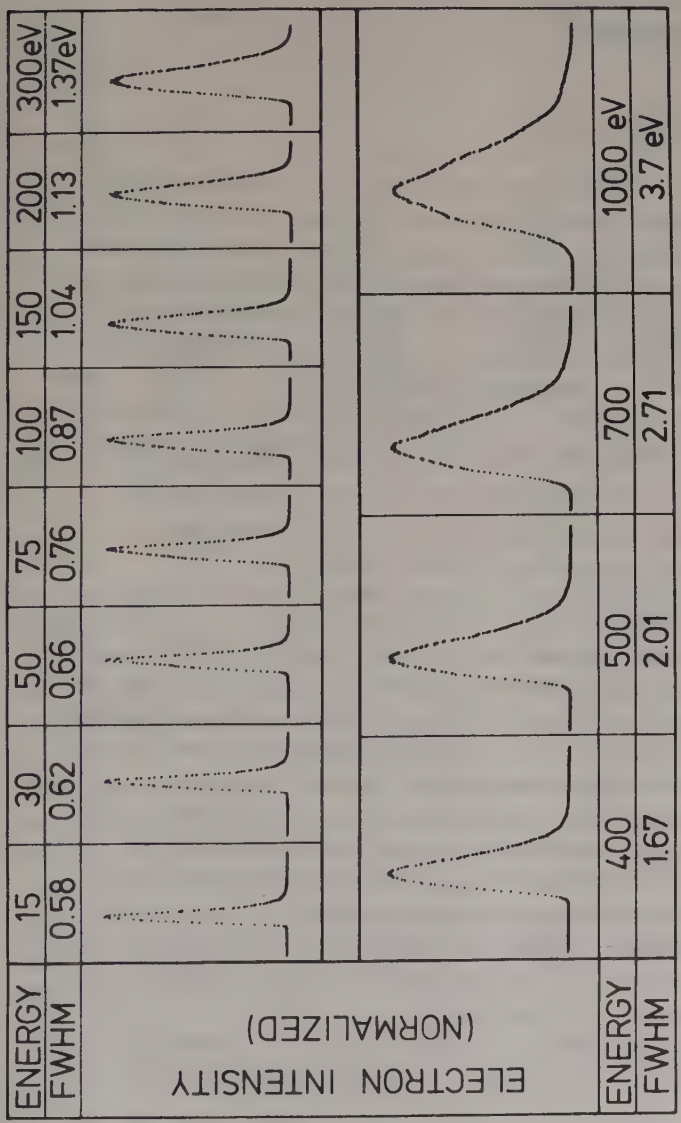

Fig. 14: Energy distributions for point source of electrons at different kinetic energies.

voltmeter (Dana model 4700) within 0.1 % accuracy. A fit of the experimental data yielded $(E+1.53)x0.629 \simeq U_A$ and $C_{exp} = 0.629 \pm 0.002$. It is noted that C_{exp} deviates by 0.9 % from the theoretical value $C_{theor} = (1/k)\ln(r_2/r_1) \simeq 0.6348$ as deduced from the dimensions of the CMA

2. Transmission Function

Now we consider the transmission function of the analyzer first for a point source and second for an extended source, whose axis coincides with the spectrometer axis. As shown by Sevier (Sev 72), the optimum design with respect to transmitted intensity and resolution is obtained for entrance and exit slits of equal width w. The fraction of electrons transmitted through the analyzer is proportional to the full width at half maximum (FWHM) of the resolution curve. For an electrostatic analyzer without aberration the FWHM is given by

$$\Delta E = Ew/D \qquad \text{(IV-3)}$$

Here D is the linear dispersion. ΔE also equals the total area under the transmission curve, namely

$$\int f(E, E')\, dE' = Ew/D \qquad \text{(IV-4)}$$

Kuyatt and Rudd (see Sev 72, Ru 74) have shown that Eq. (IV-4) holds for any electrostatic analyzer with linear dispersion D, independent of the size of the entrance slits and independent of whether aberration terms are present or not. In Fig. 15 observed analyzer transmission functions are indicated for constant electron flux and various kinetic energies E as obtained with the monochromatic point source. The electron current transmitted through the analyzer was approximately 1.6×10^{-15} A. Consequently space-charging effects in the spherical electron source were expected to be negligible. As can be seen from Fig. 15, the area under the transmission curves increases with increased kinetic energy E. Furthermore, the transmission functions seem to match the triangular line shape, however a tail occurs on the high energy side of the peaks.

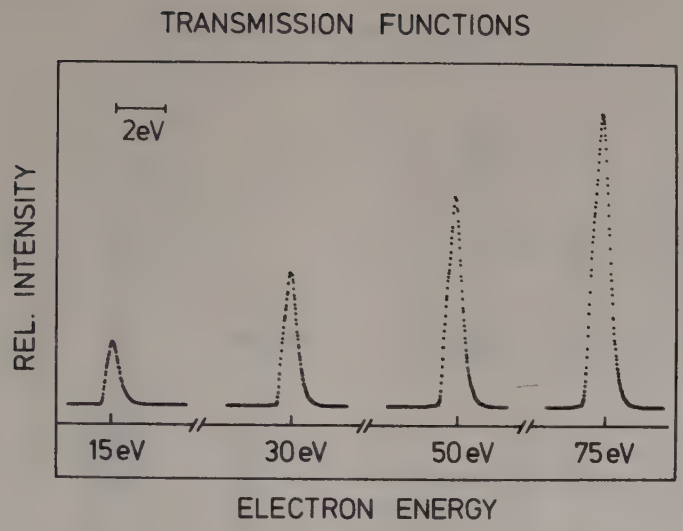

Fig. 15: Transmission functions of the analyzer for several fixed kinetic electron energies and constant electron flux.

We consider next the transmission function of the CMA for an extended source. In this connection it is important to know the geometric parameters of the source region. The transmission function depends on (i) the geometric source volume which is defined as the portion of the emerging ion beam seen through the defining apertures of the analyzer (Fig. 16) and (ii) the density distribution inside the ion beam and its angular divergence. In Fig. 17 a calculated resolution curve is shown. The ion beam diameter was 1.5 mm, the entrance slit widths were 0.5 mm and the nominal energy of the electrons 100 eV, respectively. The details of the calculation are given elsewhere (Pau 75). For this special case also the transparency was calculated yielding a value $\tau \simeq 25$ %.

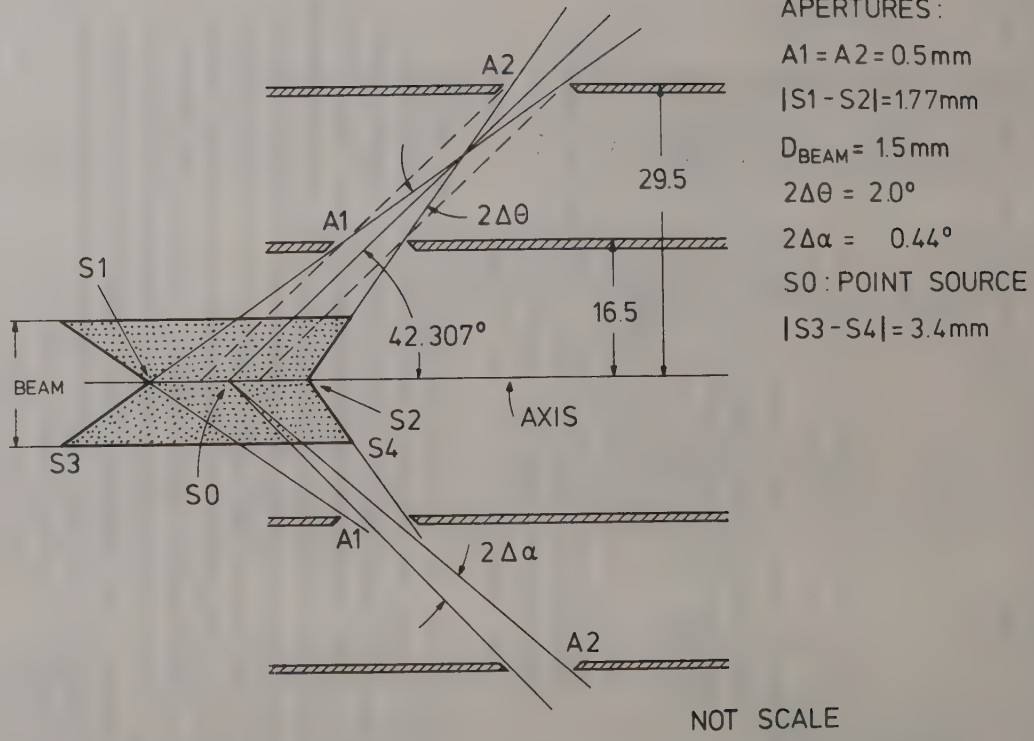

APERTURES :

A1 = A2 = 0.5 mm

|S1 - S2| = 1.77 mm

D_{BEAM} = 1.5 mm

2Δθ = 2.0°

2Δα = 0.44°

S0 : POINT SOURCE

|S3 - S4| = 3.4 mm

Fig. 16: Acceptance angular spread of the electron spectrometer

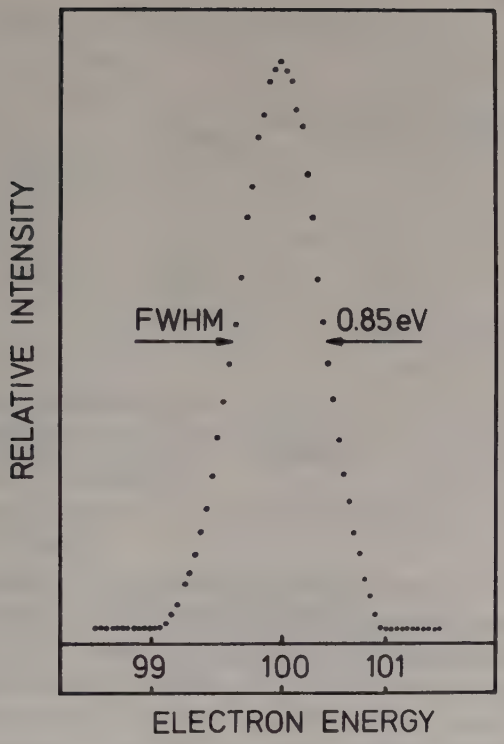

Fig. 17: Calculated shape of the transmission function for the electron analyzer with equal slit widths ($w_1 = w_2 = 0.5$ mm).

3. Line width and Energy Resolution

Figure 18 indicates the FWHM versus the electron energy. The straight line was determined from a linear least square fit to the experimental data points. We note that the deviation of the experimental points from the straight line towards zero energy might originate from the inherent energy spread of the ejected electrons and from contact potential differ-

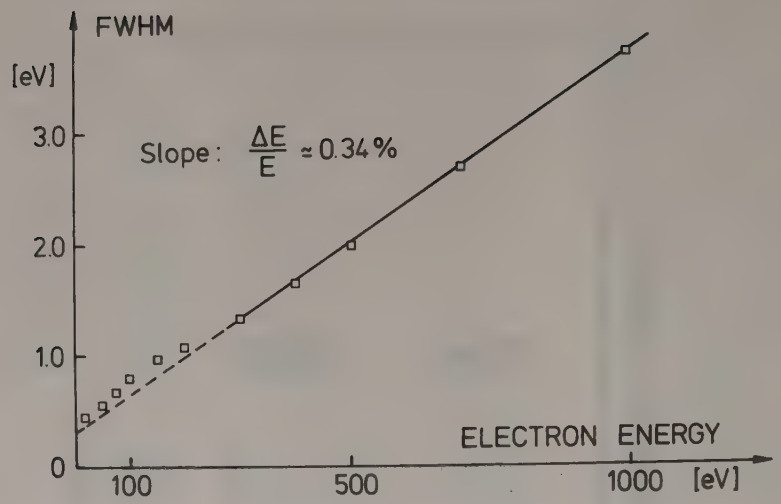

Fig. 18: FWHM as a function of electron energy for the CMA.

ences between the CMA and the electron source. The slope of this line gives the resolution R(FWHM) = $\Delta E/E \simeq 0.34$ % (point source) which agrees well with the theoretically predicted value R(FWHM) = $w_1/D = 0.30$ %. In addition the resolution for an extended source region was estimated (i) from the calculated transmission function (Fig. 17) and (ii) from the expression w_s/D, where w_s is the length of the source region (see Fig. 8). According to Fig. 17 we deduced R(FWHM) ≃ 0.85 %. Likewise the value R(FWHM) = $w_s/D \simeq 1.1$ % was estimated using w_s = 1.8 mm and D = 165.31 mm, respectively. In conclusion, the most important quantities of the CMA are summarized in Table 9.

Table 9: Summary of information about the CMA

Quantity	Value
slit widths $w_1 = w_2 = w_1' = w_2'$	0.5 mm
angular acceptance $\Theta_L \pm \Delta\Theta_L$	$42.3 \pm 1^{\circ}$
energy dispersion D	165.31 mm
aberration $\Delta L(+\Delta\Theta_L, -\Delta\Theta_L)/D$	<0.01 %
nonradial motion $(r_c/r_1)^2$	<0.3 %
transmission $\Delta\Omega_L/4\pi$	1.17 %
transparency τ	∿25 %
analyzer constant C	0.629±0.001
voltage energy conversion	$(E+1.53) \times 0.629 = U_A$
resolution R(FWHM)	
a) point source (second-order focusing)	0.34 %
b) finite source (first-order focusing)	0.85 %

V. EXPERIMENTAL APPARATUS

1. Ion Accelerator and Target Chamber

The experimental apparatus used in this work is displayed in Fig. 19. Ions from a Danfysik 350 keV ion accelerator were traversed through a foil and electrons emitted under $\Theta_L \simeq 42.3^o$ were energy dispersed with the cylindrical mirror analyzer. The ion beam was less than 1.5 mm in diameter when passing the target and was collected by a Faraday cup installed inside the CMA. For singly charged ions the energy of the incident beam particles ranged from about 50 keV to 350 keV. The general layout of the ion accelerator is exhibited in Fig. 19. Ions produced with a hot-filament hollow-cathode ion source were extracted and preaccelerated to 30 keV. The ion source was operated with gaseous and solid materials (Ax 73). After passing through a lens system the ion beam was magnetically analyzed to separate ions of different mass-to-charge ratio. The ion beam was admitted next into the acceleration column which determined the final beam energy. The beam particles then traversed a quadrupole triplet and were deflected by a bending magnet. Focusing and control of the beam was further accomplished through a second quadrupole triplet and a beam monitoring system. The beam line and the target chamber were pumped with a turbo-moleculor pump (Pfeiffer model THP 900 S). The total pressure in the target chamber was below 1×10^{-5} torr. An improvement of the pump-down time and base pressure was achieved with an additional cryopump.

The target chamber, including the electron spectrometer, foil wheel and foil drive mechanism was adjustable with respect to the ion beam axis. As depicted in Figs. 20 and 21 some of the beam collimating slits, the foil wheel, the foil translation- and rotation mechanism and the electron spectrometer were mounted on a table, which was itself adjusted with respect to the vacuum chamber and the beam line.

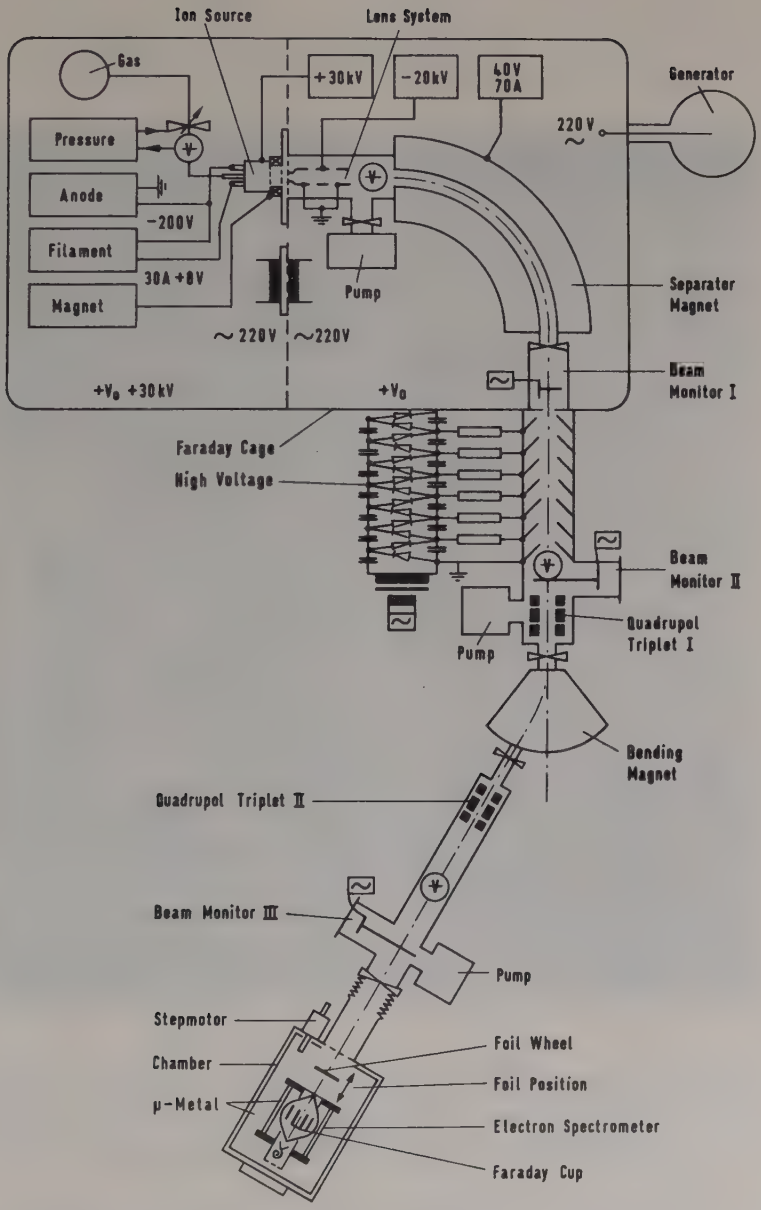

Fig. 19: Schematic drawing of experimental arrangement used for electron energy and time-of-flight measurements.

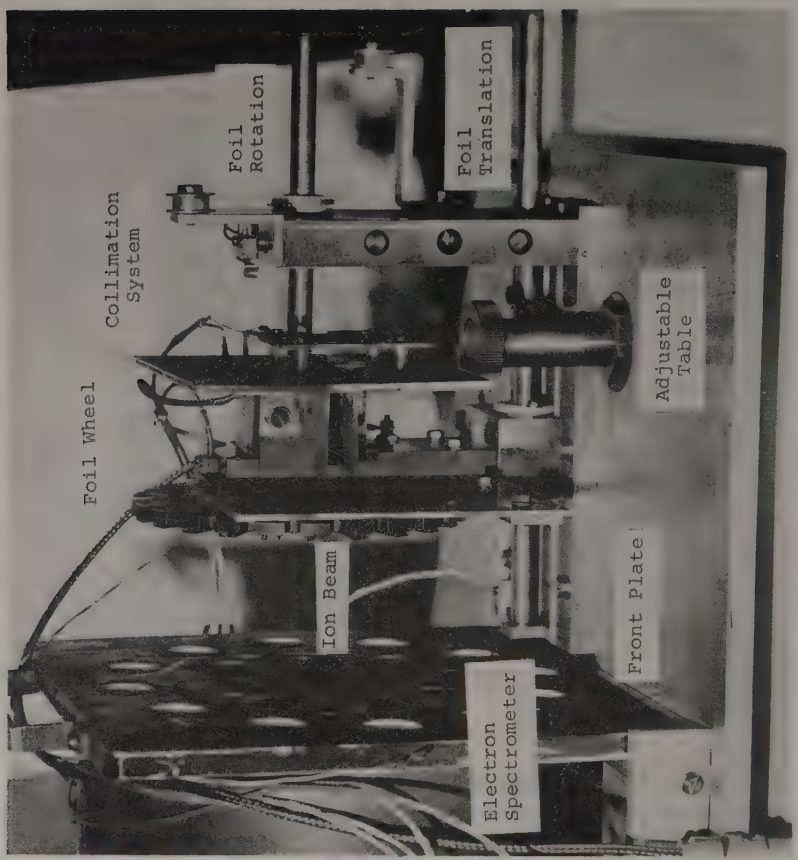

Fig. 20: Photo of the electron spectrometer, the foil wheel, the ion beam collimation system, the target rotation mechanism and the foil translation device.

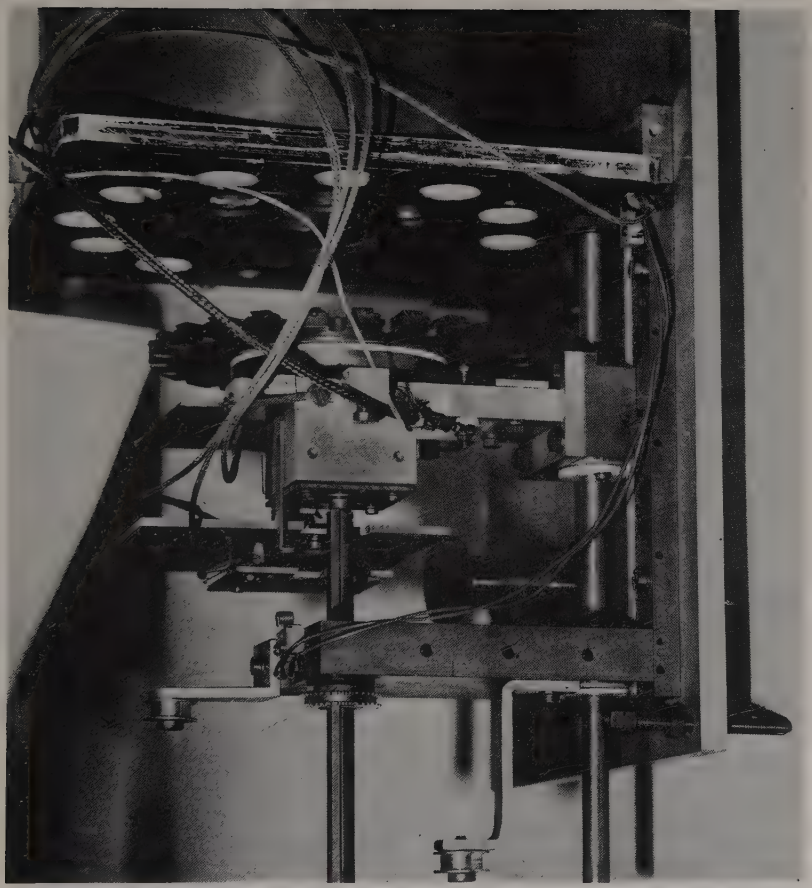

Fig. 21: The measuring system on its mounting

2. Ion Beam Collimation

Before passing through the foil, the ion beam was collimated. Fig. 22 illustrates the ion beam collimation system. To minimize sources of secondary electrons the beam was passed through three defining apertures with step-wise increasing diameter, so that the beam particles cannot strike the excit aperture. As is seen from Fig. 22, the ion beam moves left to right. To prevent electrons from entering the collimation system, a negative voltage was applied to the first defining aperture (diameter: 1 mm). Unwanted secondary electrons were surpressed by a condenser field between the second and third diaphragms. All apertures were painted with a graphite solution to further reduce the production cross section for secondary electrons. To monitor the beam position the defining apertures could be electrically connected with an ammeter. In general the ion accelerator was adjusted for maximum beam current at the Faraday cup.

3. The Target

Thin self-supporting carbon foils suited for these measurements, were produced by a method described in detail by several authors (Bra 54, Ka 59, De 60, Vou 63, Oon 67, Max 67, Ya 67). In brief, carbon foils were prepared by vaporizing graphite in a vacuum chamber on soap coated and polished microscope slides, utilized as substrates. The foil thickness (Sto 69) was controlled with a quartz crystal deposition monitor (Ki 71). Using this technique, carbon layers of (7±2) $\mu g/cm^2$ thickness were deposited. Then the carbon films were removed from the substrate by floating them off onto destilled water. We also produced aluminum-, copper-, silver-, and gold foils as well as carbon-silver and carbon-gold sandwich targets. These foils could be easily floated onto foil holders with holes of 3 mm diamter. 24 such foil holders could be mounted in the foil wheel (see Fig. 20, 21).

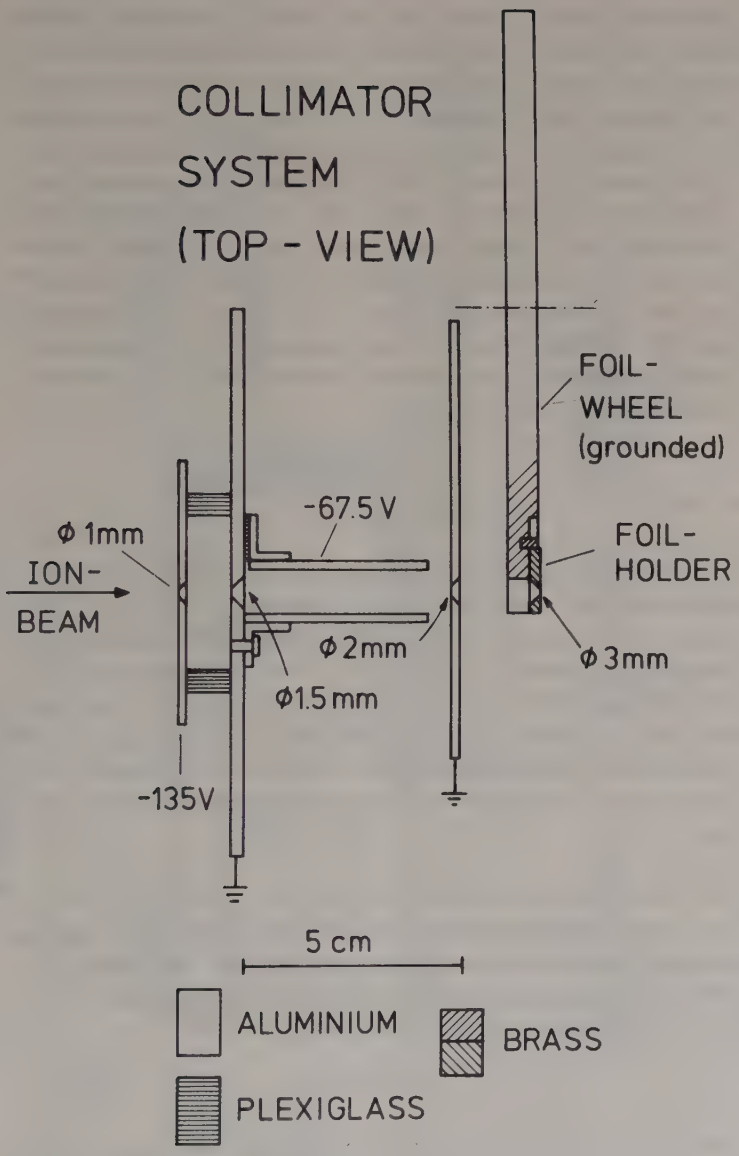

Fig. 22: Defining apertures of the ion beam.

The thinnest foils in practical use have a thickness of about 3 $\mu g/cm^2$. The lifetime of carbon foils increases (a) with increasing ion velocity and (b) for low beam currents (Do 74, Yn 76). However foil thickening processes due to hydrocarbon cracking can augment the thickness with time (see Chapter VI.1). In order to increase the lifetime of our carbon foils, the beam intensity was kept below 50 nA/mm^2. Foil brackage was indicated by a sudden enhancement of the current in the Faraday cup. The foil wheel was then rotated to place a new foil in the path of the ion beam. For light projectiles ($Z \leq 6$) penetrating through 7 $\mu g/cm^2$ thick carbon foils (intensity $\sim$30 nA/mm^2) electron spectra were accumulated up to several hours without foil breakage.

4. Faraday Cup and Beam Integration

After passing through the foil, the ion beam was collected in a Faraday cup. The Faraday cup assembly inside the CMA is shown in Fig. 23. To reduce the number of backscattered secondary electrons a negative biased diaphragm was placed inside the cup. Further, to ensure that electrons were prevented from escaping out of the cup the ion collector inside the cup was at a positive voltage. Generally, voltages of 67.5 volts were sufficient to keep all secondary electrons in the cup.

In order to average out fluctuations due to foil and beam current changes, the current measured in the Faraday cup was integrated. Thus electron energy spectra were recorded by counting the number of electrons at a given analyzer voltage U_A for a certain amount of charge $\bar{Q}$.

$$\bar{Q} = \int_{t}^{t+\Delta t} I(t)\, dt \qquad (V\text{-}1)$$

Because the observed charge $\bar{Q}$ equals a constant number of beam particles, normalization to the integrated beam current can correct for large current fluctuations. Before leaving

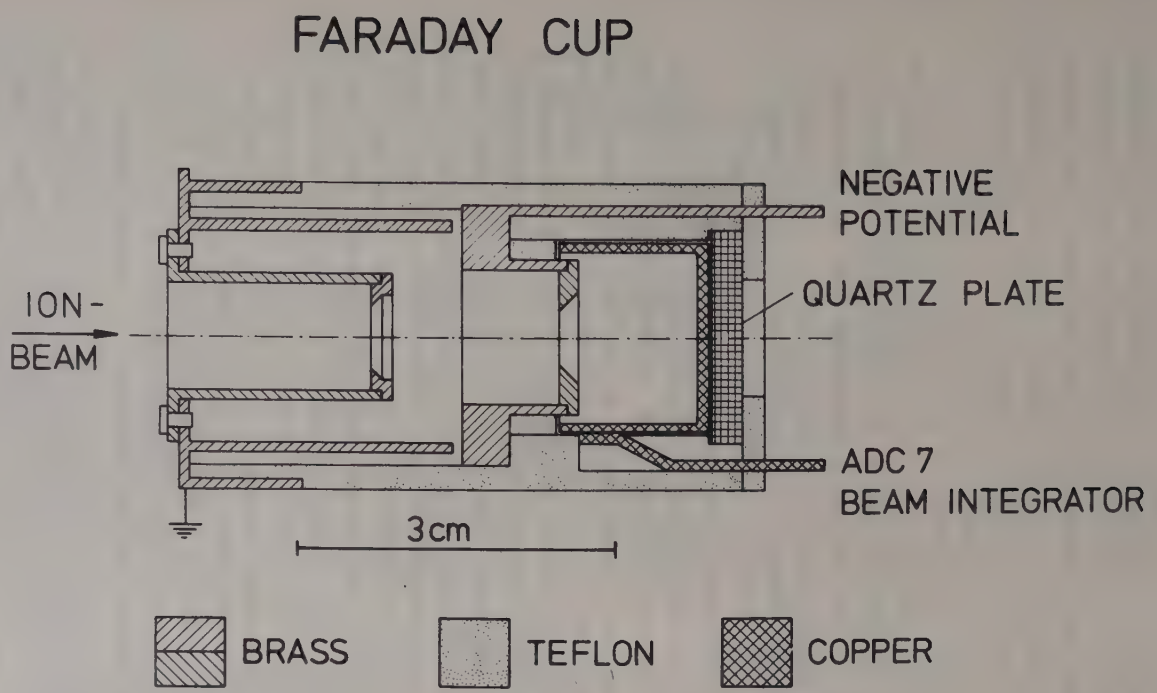

Fig. 23: Cross section of the Faraday cup

this section, we should note that the particle normalization is not adequate in the case of foil damage or foil breakage. Then the Faraday cup continues to receive charge but the number of accumulated electrons will be diminished. The details of data accumulation will be discussed in the next section.

5. Data Acquisition System

Fig. 24 is a schematic diagram illustrating the electronics for control of the electron spectrometer and the data acquisition system. Repeated scanning of electron energy spectra and decay curves was used for most of the results. Scans of electron energy spectra were made by altering the analyzer voltage U_A step-wise and accumulating simultaneously the count rate for each voltage increment ΔU_A. Thus in a typical experiment electrons ejected from the beam and/or foil under investigation were energy analyzed and then detected with a channel electron multiplier, whose output was connected with an amplifier and integral discriminator. The discriminator provided logic square wave pulses of +5 V and 0.5 μsec duration which were shaped and converted to produce signals compatible with the input of a Laben multichannel analyzer (Correlatron 1024) operated in the multiscaling mode. In a second circuit the current from the Faraday cup was converted to a frequency f using an analog-to-digital converter (HMI model ADC 7) whose output pulses were sent to a digital function generator (DFG). The DFG (i) counted the pulses from the ADC 7, (ii) normalized these counts to a preset amount of charge collected in the Faraday cup, (iii) programmed the analyzer voltage supply and (iv) controlled the multiscaler, i.e. when a preset number of counts corresponding to a certain amount of charge was reached the DFG triggered the channel advance of the multiscaler and at the same time addressed a digital-to-analog converter (DAC). To enhance the signal-to-noise ratio of the recorded data, repetitive scans were performed. After each scan a delayed pulse from the DFG caused the multiscaler

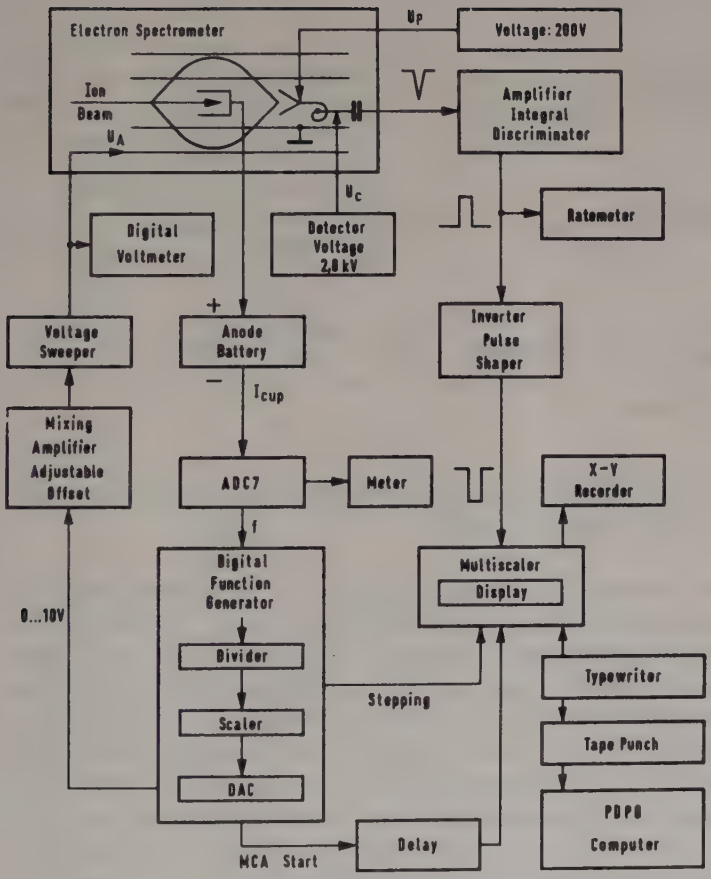

Fig. 24: Schematic drawing of the electronics for control of the electron spectrometer and the data acquisition system

to start again. To sweep a certain analyzer voltage span an offset adjustable amplifier was used. The readout of the multiscaler could be performed either with an x-y recorder or with a Teletype, which provided both printed and punched-tape output.

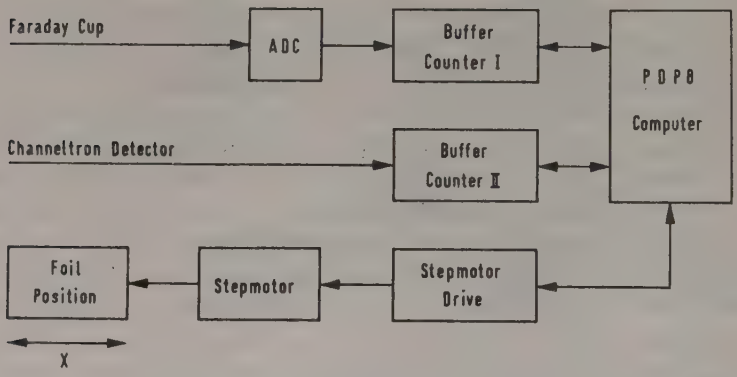

Fig. 25: Block diagram of the electronics for lifetime data measurement system

Next we consider the system used for lifetime measurements. The method is indicated schematically in Fig. 25. The target was moved up and down beam with a step motor which was controlled by a PDP8 computer. The advancement for a single motor step was 1.0417×10^{-2} mm (48 steps: 0.5 mm). The logic and circuitry of the interface used will be discussed in detail elsewhere (Wit 76). Therefore only a brief discription is given here. The interface primarily consisted of two scalers (buffer counter I and II). One of the scalers (see Fig. 25) counted pulses from a current digitizer (ADC) which was connected with the Faraday cup. While scaler I was counting scaler II was accumulating pulses from the channeltron detector. When a preset number of counts was reached in scaler I, corresponding to a specified amount of beam charge, the content of the data scaler was stored in the memory of the computer,

both scalers reset, and the step motor was commanded under program control to step to the next target position. Then the process was repeated. Normally data were taken with 48 target steps distance between each observation point.

VI. CHARACTERISTIC FEATURES OF BEAM-FOIL ELECTRON SPECTROSCOPY

1. Foil Interaction Processes

a) Charge Distribution

In BFAES it is important to know the charge state composition of the emerging beam. When fast moving ions are penetrating through a thin carbon foil an equilibrium charge state distribution is rapidly established by a dynamic balance of electron capture and electron loss processes. The target thickness required to attain equilibrium in the outermost shells is of the order 0.5 $\mu g/cm^2$. The resulting fraction of ions F_i^∞ (for down beam) in the charge state q_i can be determined by electrostatic or magnetic analysis where the mean charge $\bar{q}$ is given by

$$\bar{q} = \sum_i q_i F_i^\infty \qquad \text{(VI-1)}$$

The predicted equilibrium charge fractions for Li, Be, B, and C beams (Mar 68) versus beam velocity are plotted in Figs. 26-29. Qualitatively, we see that the most likely charge states for 300 keV ions penetrating through a foil stripper are Li^+, Be^+, B^+ and C^+, corresponding to a mean charge $\bar{q} \simeq 1$. Some additional points must be emphasized, however. It is known (B 72) that foils generally produce more highly excited and highly stripped ions than can be produced in gaseous targets (density effect). Two theories are presently being considered to explain these charge state differences in solid and gaseous targets. Thus Bohr and Lindhard (Bo 74) have proposed that the ion would become more highly stripped in the foil due to multiple collisions (high collision frequency). On the other hand Betz et al. (B 70, B 72, Gar 73, For 73) have assumed that the ion remains at the same charge it would have in the gas target but is highly excited (compound excitation). Such highly excited states can then decay via autoionization

(Auger transitions). Since autoionizing decays cause a drastic rearrangement of inner- and outer-shell states, Auger cascading contributes maintaining the excited level population and charge state distribution of the emerging beam. Recently Moak (Moa 76) has suggested that the effectiveness of electron capture processes in solids might be reduced without a corresponding reduction of electron loss processes. This effect would also move the average charge state to a higher level in solid targets.

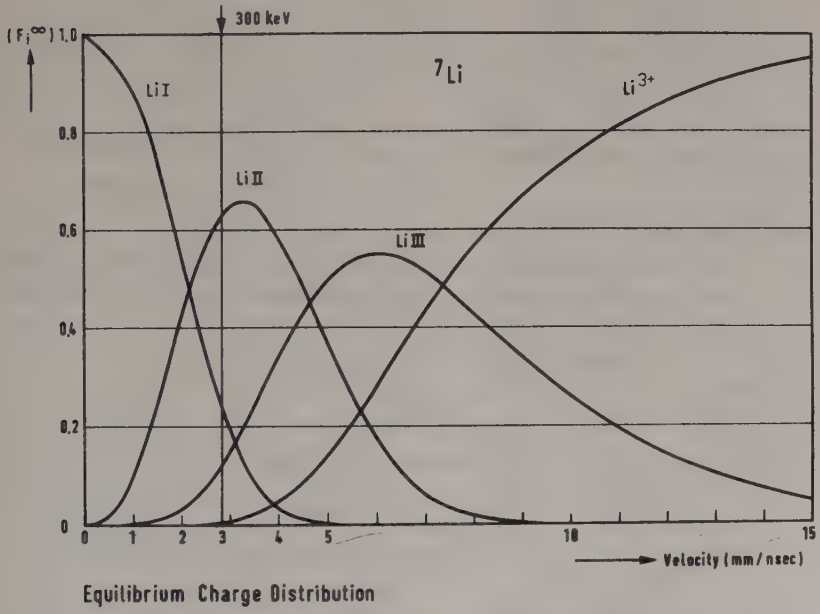

Fig. 26: Velocity dependence of the charge state distribution for lithium ions penetrating through carbon foils (Mar 68)

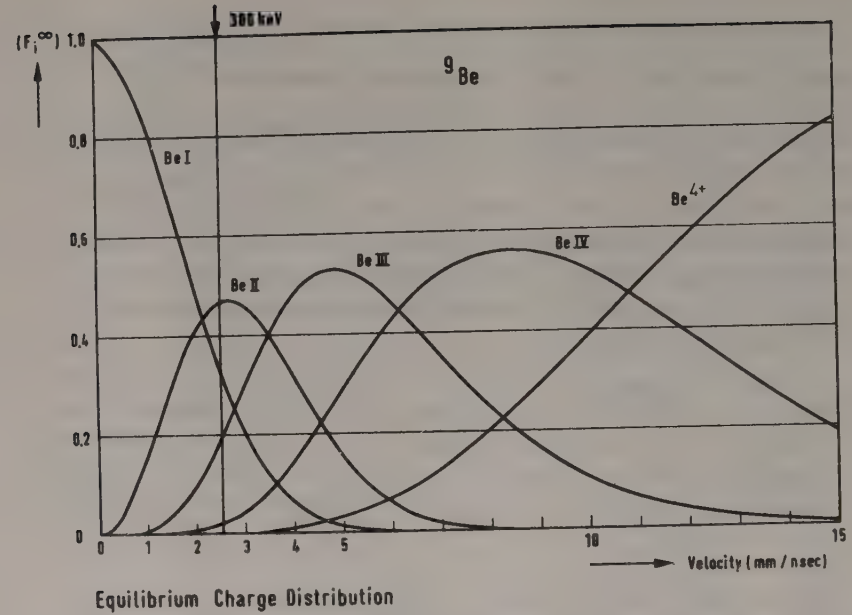

Fig. 27: Velocity dependence of the charge state distribution for beryllium ions penetrating through carbon foils (Mar 68)

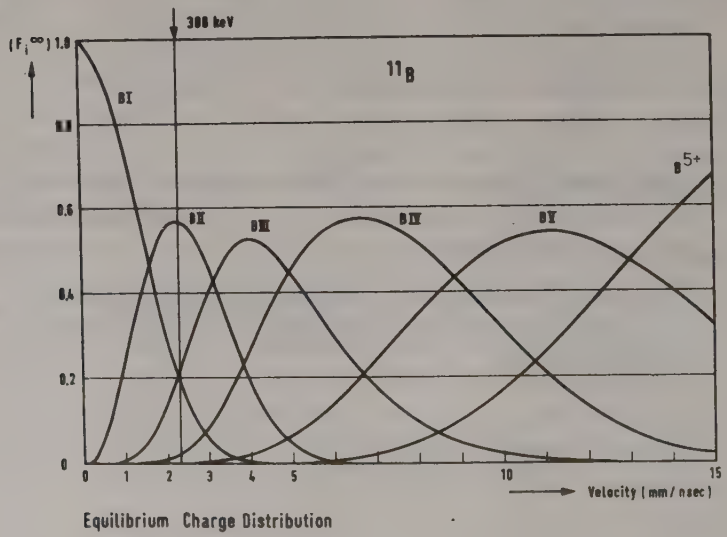

Fig. 28: Velocity dependence of the charge state distribution for boron ions penetrating through carbon foils (Mar 68)

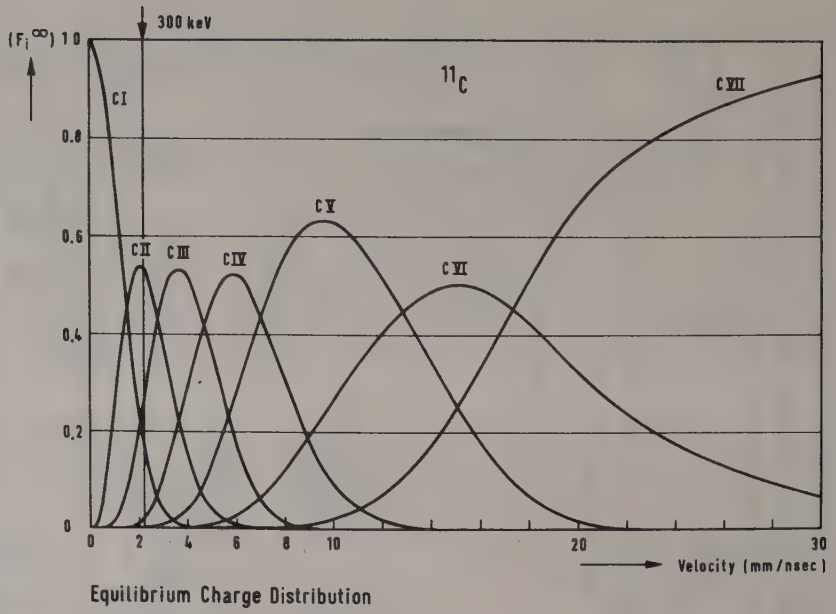

Fig. 29: Velocity dependence of the charge state distribution for carbon ions penetrating through carbon foils (Mar 68)

b) Energy Straggling and Angle Scattering

Information about energy straggling, mean energy loss and angular scattering of atoms transmitted through a foil are of primary importance in BFAES. As a result of many random soft collisions the beam particles experience energy loss and are deflected. The mean energy loss in the foil is given by

$$\Delta E = E_B^o - E_B \qquad \text{(VI-2)}$$

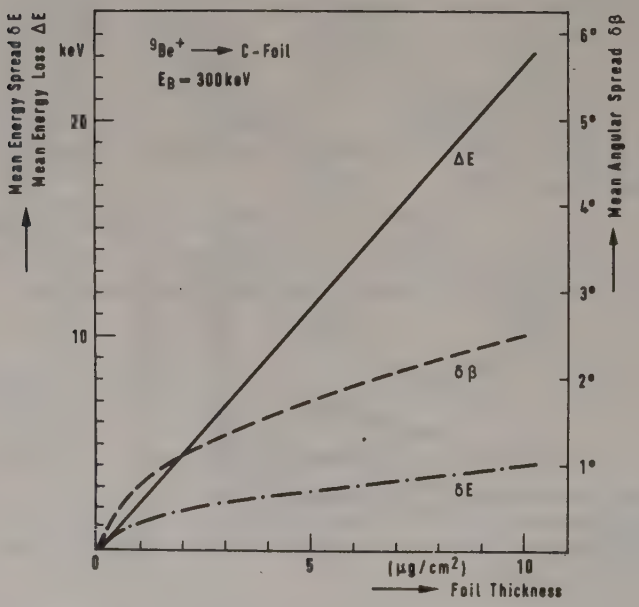

Fig. 30: Variation of mean energy loss, mean energy spread and mean angular spread versus foil thickness as deduced from the work of Biersack (Bier 75)

where E_B^o, E_B are the most probable beam energy before and after foil passage, respectively. Due to multiple collisions the beam particles are scattered into a cone with angular divergence $2\delta\beta$ ($\delta\beta$: rms scattering angle). The mean energy loss ΔE ,

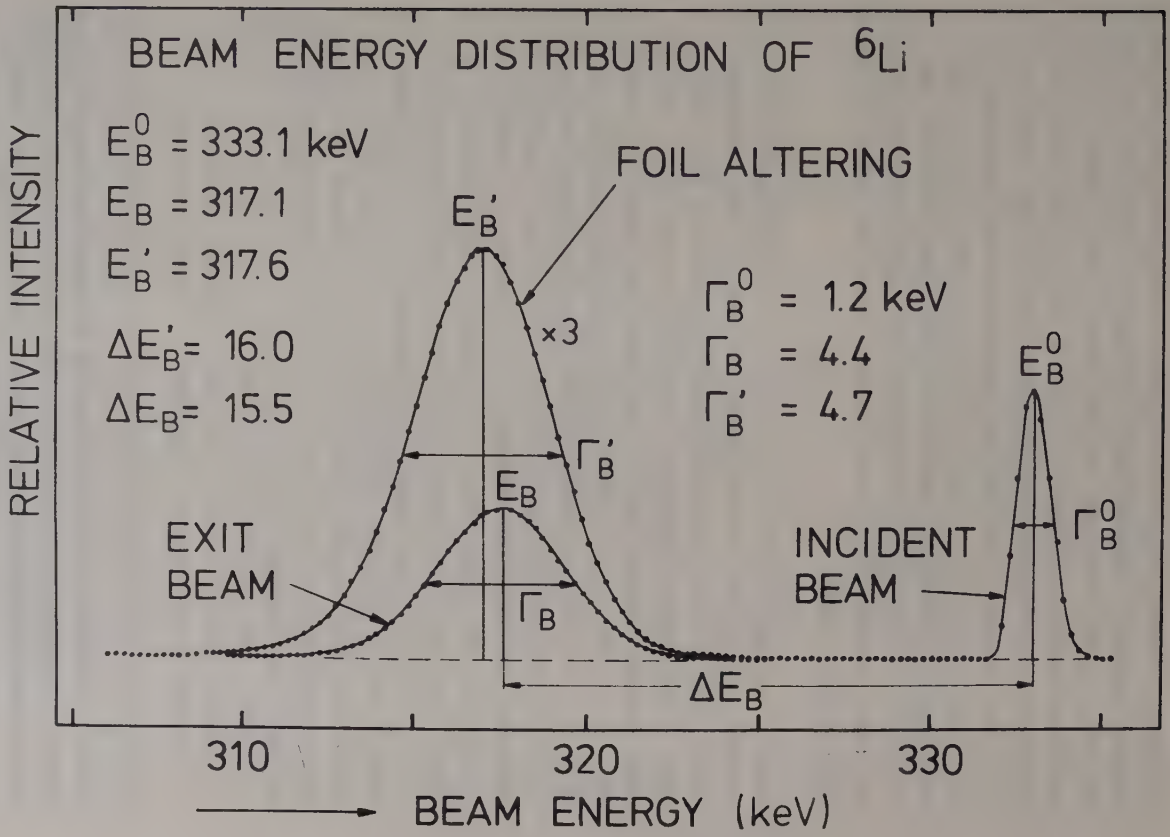

Fig. 31: Energy profiles of lithium ions transmitted through a carbon foil (Wit75)

the energy spread δE_B about the mean energy loss ΔE and the angular spread $\delta\beta$ versus foil thickness are shown in Fig. 30. Here δE_B is the half mean energy spread ($2\delta E_B$ = FWHM). It is apparent from Fig. 30 that δE_B and $\delta\beta$ are proportional to the square root of the foil thickness d ($\delta E_B \sim d^{1/2} E_B^{-1}$; $\delta\beta \sim d^{1/2} E_B^{-1}$). We note that the energy- and scattering distributions also depend upon the incident beam energy and the stopping power dE_B/dz (Bier 68, Bier 75) of the target material. We further note that energy straggling and multiple scattering are less pronounced for high incident particle velocities and low-Z target atoms.

Recently Wittmann (Wit 75) has used electrostatic analysis to measure energy-loss straggling of Li^+ ions in thin carbon foils. Fig. 31 shows typical energy profiles of a 333.1 keV lithium beam before and after leaving a carbon foil. The measured average energy loss in the target was found to be 15.5 keV. As can be seen the FWHM of the apparatus function was $\Gamma_B^o \simeq 1.2$ keV and the FWHM ($2\delta E_B$) of the transmitted beam was $\Gamma_B \simeq 4.4$ keV. The shape of the beam profile was approximately Gaussian. One important feature is the change in energy-loss straggling with time. After an irradiation dose of about 200 $\mu Q/mm^2$ the energy-loss straggling increased by as much as 6.4 % while the mean energy loss increased by 3.2 %. This pronounced variation in energy straggling of the beam corresponds to a substantial increase in foil thickness. According to Dobberstein and Henke (Do 74) this foil-thickening process is due to hydrocarbon cracking.

2. Kinematics of Electron Ejection

a) Relationship between Center-of-Mass and Laboratory Energies

Several kinematical effects will be of vital interest in projectile electron spectroscopy. In the following we assume that the incident beam particles are parallel to the axis of symmetry (Z-axis). The incident velocity is $\vec{v}_B$. First we consi-

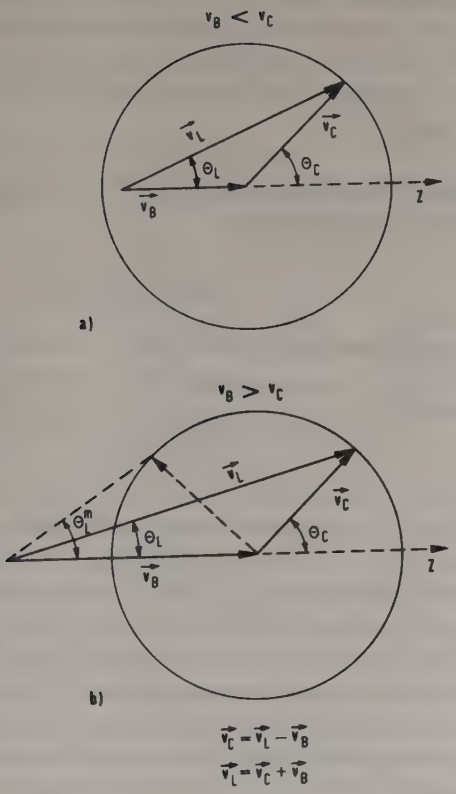

Fig. 32: Velocity vector diagrams illustrating the relation between laboratory and center-of-mass velocities and emission angles ($\beta = 0$).

der the case where the beam particles are scattered in forward direction. This assumption is generally justified at high beam energies. Fig. 32 illustrates the dynamics of electron ejection from a moving emitter. Here v_C, v_L are the velocities of the ejected electron in the center-of-mass frame and in the

laboratory frame, respectively. From the vector diagrams (Fig. 32) relations between the velocity and angle of emission in the particle rest frame and the corresponding velocity and angle of detection in the laboratory frame can be deduced. For convenience we introduce the following quantities, which are explained in Table 10.

Table 10: Physical quantities defined in the laboratory and center-of-mass frames

Quantity	Laboratory System	Center-of-Mass System
Electron Energy	E_{LAB} (E_L)	E_{CM} (E_C)
Electron Velocity	v_{LAB} (v_L)	v_{CM} (v_C)
Angle of Emission	Θ_{LAB} (Θ_L)	Θ_{CM} (Θ_C)
Solid Angle	$d\Omega_{LAB}$ ($d\Omega_L$)	$d\Omega_{CM}$($d\Omega_C$)

Due to the fast motion of the beam particles, autoionization lines arising from projectile emitters will be kinematically shifted. Under the condition $|\vec{v}_B| < |\vec{v}_C|$ (see Fig. 32 a) the vectors $\vec{v}_C$ and $\vec{v}_L$ can move on a circle of radius $|\vec{v}_C|$ centered at the origin of the ion rest frame. When $|\vec{v}_B| > |\vec{v}_C|$ (see Fig. 32 b), we find that Θ_L must be less than Θ_L^m. Furthermore let $E_L = m_e v_L^2/2$, $E_C = m_e v_C^2/2$, $E_B = M v_B^2/2$ and $\varepsilon = (m_e/M)E_B$ be, respectively, the electron energy in the LAB-system, the electron energy in the CM-system, the beam energy and the reduced beam energy, where m_e is the electron rest mass and M the projectile rest mass. A simple analysis based on $\vec{v}_C = \vec{v}_L - \vec{v}_B$ and $\vec{v}_L = \vec{v}_C + \vec{v}_B$ yields

$$E_C \cong E_L + \varepsilon - 2(\varepsilon E_L)^{1/2} \cos\Theta_L \qquad \text{(VI-3)}$$

$$E_L \cong E_C + \varepsilon + 2(\varepsilon E_C)^{1/2} \cos\Theta_C \qquad \text{(VI-4)}$$

where (Land 69)

$$\cos\Theta_C = \pm\cos\Theta_L[1-(\varepsilon/E_C)\sin^2\Theta_L]^{1/2} - (\varepsilon/E_C)^{1/2}\sin^2\Theta_L \qquad \text{(VI-5)}$$

In (VI-5) the +sign holds under the condition $v_B < v_C$. Moreover the condition for the square root $[1-(\varepsilon/E_C)\sin^2\theta_L]^{1/2}$ to be real is equivalent to the requirement

$$\sin\theta_L \leq v_C/v_B \quad \text{or} \quad \sin^2\theta_L \leq E_C/\varepsilon \qquad \text{(VI-6)}$$

If we consider the case $v_B<v_C$ expression (VI-6) is satisfied for all angles θ_L (see Fig. 32a). On the other hand, in the case $v_B>v_C$ (see Fig. 32b) the maximum angle of observation is defined by

$$\sin^2\theta_L^m = E_C/\varepsilon \qquad \text{(VI-7)}$$

We further note that for a given laboratory angle θ_L the "kinematical cut-off" is given by

$$E_C^m = \varepsilon\sin^2\theta_L \qquad \text{(VI-8)}$$

where E_C^m is the minimum center-of-mass energy which will be accepted by the electron spectrometer.

To study the kinematical Equations (VI-4) and (VI-5) we performed computer calculations for M = 9 amu and E_C = 97.78 eV. The results are plotted in Fig. 33. One striking phenomenon which can be seen from this figure is the change of E_L as a function of the observation angle θ_L. In particular, autoionization lines are kinematically shifted towards higher energies for small observation angles (forward direction). It is also apparent from Fig. 33 that the calculated "Doppler shift" sensitively depends upon the incident beam energy, e.g. for $\theta_L \simeq 42.3^\circ$ the kinematic shift increases with increasing projectile velocity. In the next graph, as depicted in Fig. 34, the laboratory energy E_L was varied as a function of θ_L for given $E_B \simeq 285$ keV and with E_C as a parameter. This plot clearly shows the kinematic cut-off for electrons ejected with low center-of-mass energies. A straight-forward application of Eq. (VI-8) yielded $E_C^m \simeq 7.8$ eV($\theta_L \simeq 42.3^\circ$; ε= 17.2 eV).

$$E_{LAB} = E_{CM} + \varepsilon(2\cos^2\theta_{LAB} - 1) + 2\cos\theta_{LAB} \times [\varepsilon E_{CM} + \varepsilon^2 E_{BEAM}(\cos^2\theta_{LAB} - 1)]^{1/2}$$

$$\varepsilon = \frac{m_e}{M_{Be}} \cdot E_{BEAM}$$

E_{BEAM} [keV]	a	b	c	d	e
E_{CM} = 97.78 [eV]	0	50	100	200	285

^{9}Be II (1s2s2p) $^4P_{5/2} \rightarrow (1s^2 + \varepsilon f)\ ^2F_{5/2}$

Fig. 33: Polar diagram indicating the LAB-frame energy E_{LAB} as a function of the emission angle θ_{LAB} for fixed rest-frame energy E_{CM} and variable beam energy E_{BEAM}

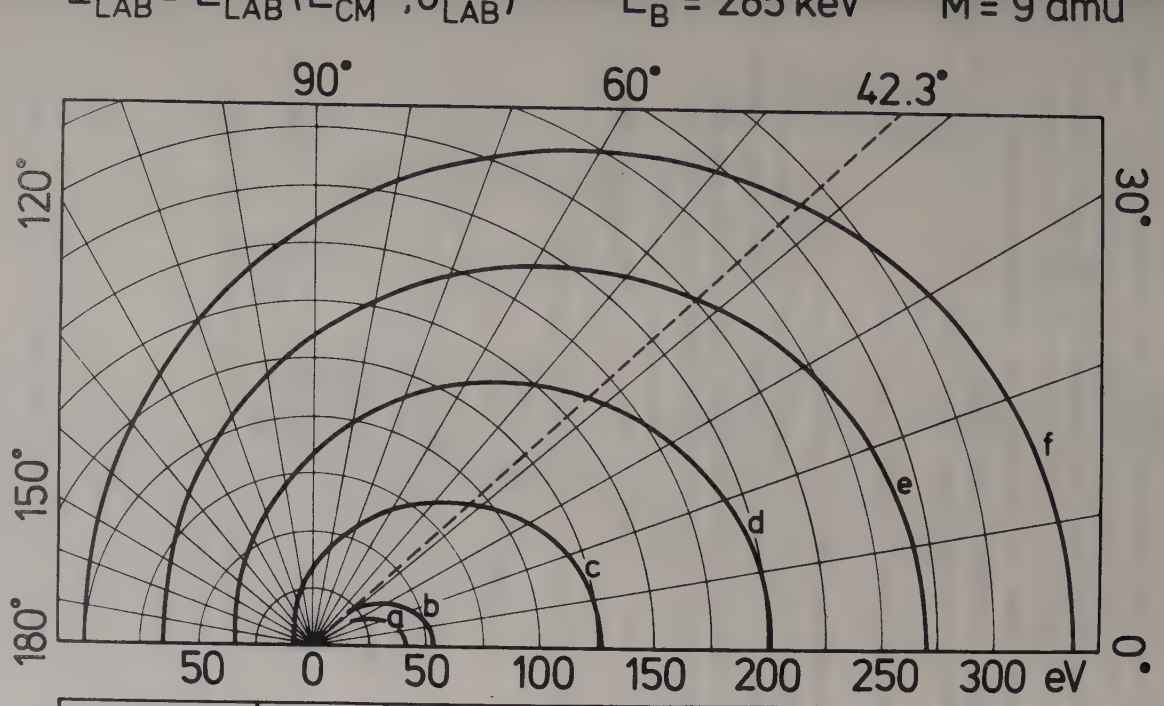

E_{CM} [eV]	a	b	c	d	e	f
	5	10	50	100	150	200

Fig. 34: Polar diagram indicating the LAB-frame energy E_{LAB} as a function of the emission angle θ_{LAB} for fixed beam energy E_{BEAM} and variable rest-frame energy E_{CM}

By far a more difficult problem is encountered when the emerging beam makes an angle β with the z-axis. We consider the case where the beam particles are scattered in a cone symmetric with respect to the beam axis. The kinematics of electron emission are exhibited schematically in Fig. 35. In what follows we refer to β as the cone angle. Let us take the observation angle for electrons emitted from the beam cone to be θ_L', the laboratory angle for electrons starting from the cone axis θ_L and the azimuthal angle Φ. Then θ_L and θ_L' are related by (Ru 74, Ris 74)

$$\cos \theta_L' = \cos\theta_L \cos\beta + \sin \theta_L \sin\beta \cos \Phi \qquad \text{(VI-9)}$$

We further assume that the correlation between θ_L, β and Φ is small (Ris 74) and that $\theta_C' \simeq \theta_C$. Due to the axial symmetry of the cylindrical mirror analyzer electrons ejected under different azimuthal angles Φ with respect to the ion beam axis will not be destinguished. If we take the average over Φ, so that

$$\langle \cos \theta_L' \rangle = (2\pi)^{-1} \int_0^{2\pi} \cos \theta_L' \, d\Phi = \cos \theta_L \cos\beta \qquad \text{(VI-10)}$$

and introducing (VI-10) into Eq. (VI-3) we obtain

$$\langle E_C \rangle \simeq E_L + \varepsilon - 2(\varepsilon E)^{1/2} \cos \theta_L \cos\beta \qquad \text{(VI-11)}$$

Combining Eq. (VI-10) with Eq. (VI-5) we can write

$$\langle \cos\theta_C' \rangle \simeq \pm\cos\theta_L \cos\beta[1-(\varepsilon/E_C)(1-\cos^2\theta_L \cos^2\beta)]^{1/2}$$
$$- (\varepsilon/E_C)^{1/2} (1-\cos^2\theta_L \cos^2\beta) \qquad \text{(VI-12)}$$

where the + sign holds for $v_B < v_C$. If we introduce expression (VI-12) into (VI-4) then

$$\langle E_L \rangle \simeq E_C + \varepsilon(2\cos^2\theta_L \cos^2\beta - 1)$$
$$+ 2\varepsilon\cos \theta_L \cos\beta[E_C/\varepsilon + \cos^2\theta_L \cos^2\beta - 1]^{1/2} \qquad \text{(VI-13a)}$$

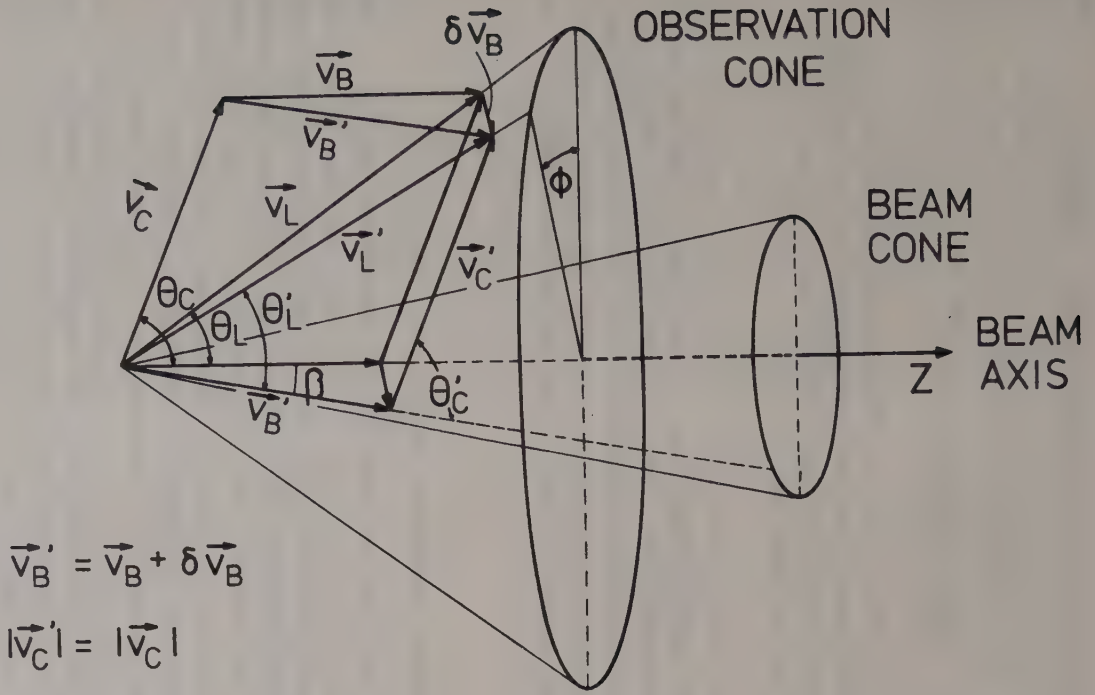

Fig. 35: Kinematics for observation of autoionization electrons from moving projectiles.

If $\beta \to 0$, we find that expression (VI-13a) reduces to

$$E_L \simeq E_C + \varepsilon(2\cos^2\theta_L - 1) + 2\cos\theta_L \times [\varepsilon E_C + \varepsilon^2(\cos^2\theta_L - 1)]^{1/2} \qquad \text{(VI-13b)}$$

We emphasize that expression (VI-13a) was derived for $v_B < v_C$, cylindrical symmetry and small cone angles β. The latter equations enable us to transform electron energies from the CM system to the LAB system and vice versa.

A serious problem in BFAES is line broadening caused by the kinematical transformation from the rest frame of the emitting ion to the laboratory frame. Thus the intrinsic resolution of the CMA will be degraded to some extent, mainly due to the finite acceptance of the electron spectrometer, the energy straggling of the projectiles in the foil and the angular scattering of the ion beam.

b) Kinematical Broadening Effects

In Secs. III.1 and IV.3 approximate expressions were given for the width $\Delta E_L \simeq E_L \cdot R$ of the spectrometer function. The finite energy resolution $R = \Delta E_L / E_L$ arises from the intrinsic nature of the focusing properties of the CMA, from the finite slit widths and from the extension of the source region. Several other effects contribute to the total instrumental linewidth. In order to determine the resulting line profile each instrumental distribution causing line broadening has to be convoluted with the apparatus function of the CMA. Under the oversymplified assumption that the kinematical line broadening effects are independent and additive we can expand Eq. (VI-13a) in powers of ΔE_C, $\Delta\theta_L$, ΔE_B and $\Delta\beta$. Thus

$$\Delta E_L = (\partial E_L/\partial E_C)\Delta E_C + (\partial E_L/\partial \theta_L)\Delta\theta_L + (\partial E_L/\partial E_B)\Delta E_B + (\partial E_L/\partial\beta)\Delta\beta + \text{h.t.} \qquad \text{(VI-14)}$$

where h.t. means higher order terms and ΔE_C, $\Delta\theta_L$, $\Delta E_B = 2\delta E_B$, $\Delta\beta = 2\delta\beta$ are the inherent width of the autoionizing state, the finite acceptance angular spread (FWHM) of the CMA, the FWHM of the energy distribution and the FWHM angular spread of the ion beam, respectively. The derivatives $\partial E_L/\partial E_C$, $\partial E_L/\partial\theta_L$, $\partial E_L/\partial E_B$, $\partial E_L/\partial\beta$,etc. are called line broadening factors. The first derivative coefficients are

$$\partial E_L/\partial E_C = 1 + \cos\theta_L \cos\beta/A^{1/2} \qquad \text{(VI-15a)}$$

$$\partial E_L/\partial\theta_L = -2\varepsilon\sin\theta_L \cos\beta[2\cos\theta_L \cos\beta + (A + \cos^2\theta_L \cos^2\beta)/A^{1/2}] \qquad \text{(VI-15b)}$$

$$\partial E_L/\partial E_B = (m_e/M)[2\cos^2\theta_L \cos^2\beta - 1 + \cos\theta_L \cos\beta \times (2A - E_C/\varepsilon)/A^{1/2}] \qquad \text{(VI-15c)}$$

$$\partial E_L/\partial\beta = -2\varepsilon\cos\theta_L \sin\beta\,[2\cos\theta_L \cos\beta + (A + \cos^2\theta_L \cos^2\beta)/A^{1/2}] \qquad \text{(VI-15d)}$$

where $A = (E_C/\varepsilon + \cos^2\theta_L \cos^2\beta - 1)^{1/2}$

For simplicity we choose $\beta = 0 \pm \delta\beta$. Then the derivative coefficient $[\partial E_L/\partial\beta]_{\beta=0}$ is zero. The first non-vanishing term with respect to $\beta=0$ is

$$[(1/2!)\ (\partial E_L^2/\partial\beta^2)]_{\beta=0} = -\varepsilon\cos\theta_L[2\cos\theta_L + (A + \cos^2\theta_L/A^{1/2})] \qquad \text{(VI-15e)}$$

Under the fairly realistic assumption of Gaussian shapes,

$$\Gamma(\Delta E_C) \simeq [\partial E_L/\partial E_C]\Delta E_C$$

$$\Gamma(\Delta\theta_L) \simeq [\partial E_L/\partial\theta_L]\Delta\theta_L$$

$$\Gamma(\Delta E_B) \simeq [\partial E_L/\partial E_B]\,\Delta E_B$$

$$\Gamma(\Delta\beta) \simeq [(1/2!)\partial^2 E_L/\partial\beta^2]\,\Delta\beta$$

$$\Gamma(\Delta E_L) \simeq E_L \cdot R$$

the partial width Γ_i may be added in quadrature. The equation for Γ_L now can be written as

$$\Gamma_L \simeq (\sum_i \Gamma_i^2)^{1/2} = \{\Gamma(\Delta E_C)^2 + \Gamma(\Delta\Theta_L)^2 + \Gamma(\Delta E_B)^2 + \Gamma(\Delta\beta)^2 + (E_L \cdot R)^2\}^{1/2} \qquad \text{(VI-16)}$$

Line broadening factors were calculated as a function of the beam energy for the (1s2s2p) $^4P^o_{5/2} \rightarrow (1s^2\varepsilon f)\ ^2F^o_{5/2}$ transition in BeII. As seen from Figs. 36 and 37 the effects of line broadening are especially pronounced in the important coefficients $\partial E_L/\partial\Theta_L$ and $\partial E_L/\partial E_B$. The variation of $\partial E_L/\partial E_C$ (Fig. 38) is less important, since the inherent widths for metastable autoionizing states such as (1s2s2p) $^4P^o_{5/2}$ are negligible small. We note that for laboratory angles close to 45°, $|\partial E_L/\partial\Theta_L|$ strongly increases with increasing beam energy, whereas $|\partial E_L/\partial E_B|$ decreases. Accordingly kinematical broadening effects should be less pronounced for detection angles close to 90°. Therefore line broadening might be reduced by selecting observation angles around 90°. However, for $\Theta_L \simeq 90^\circ$ the Doppler shift will be small and hence target and projectile lines are frequently overlapping.

We next turn to the evaluation of the total width Γ_L. As an example we consider the following problem: We assume that a 300 keV Be^+ beam is passed through a ∿7 μg/cm² thick carbon foil. In the energy region considered (see Fig. 30), the mean energy loss ΔE_L is of the order 15.8 keV, the energy straggling is expected to be $\Delta E_B = 2\delta E_B \simeq 8.2$ keV and the mean angular spread of the transmitted beam should be $\Delta\beta = 2\delta\beta \simeq 4.9^\circ$. Moreover, R, $\Delta\Theta_L$, Θ_L, E_C and E_L are 0.8 %, 1°, 42.3°, 97.78 eV and 158 eV,

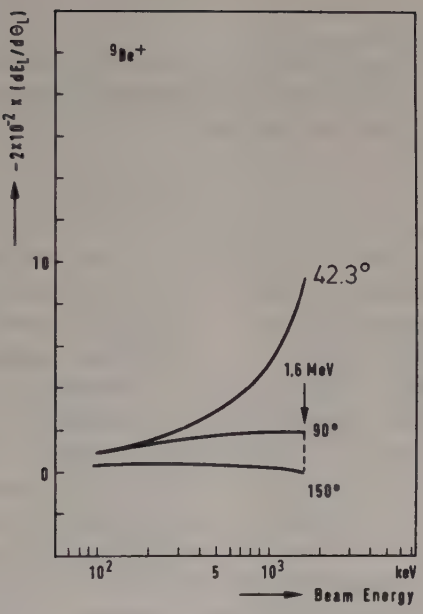

Fig. 36: Kinematic broadening factor as a function of beam energy. $E_B \simeq 1.6$ MeV corresponds to $v_B \simeq v_C$.

respectively. Inserting these values into Eqs. (VI-15a, b, c, d, e) and (VI-16) we obtained for the total FWHM $\Gamma_L \simeq 2.3$ eV (see Table 11) corresponding to an effective resolution $R_L \simeq 1.5$ %. It is obvious from Table 11 that the contribution $\Gamma(\Delta\Theta_L)$ plays the dominant role in the projectile energy region of interest.

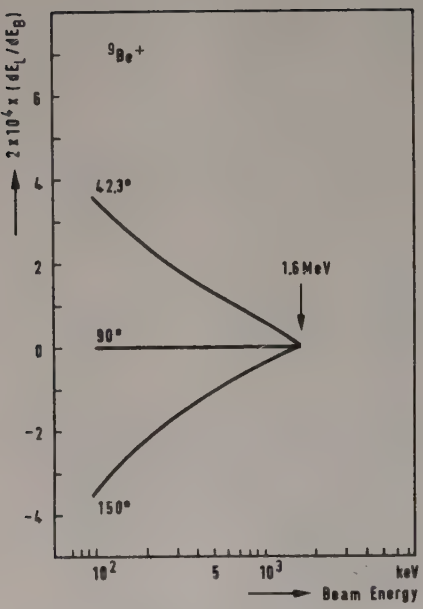

Fig. 37: Kinematic broadening factor as a function of beam energy (β = 0)

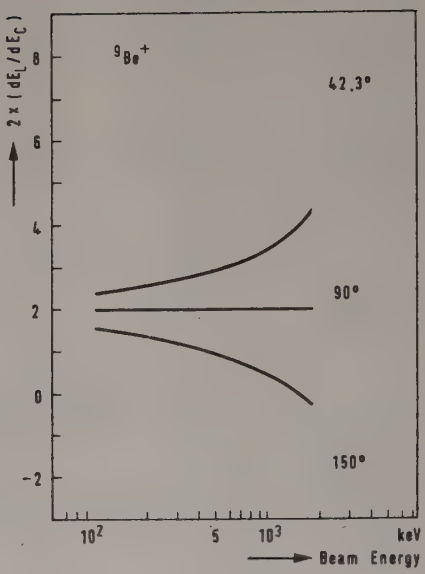

Fig. 38: Kinematic broadening factor as a function of beam energy (β= 0)

Table 11: Effective line width and energy resolution for the $(1s2s2p)\ ^4P_{5/2} \rightarrow (1s^2\varepsilon f)\ ^2F_{5/2}$ autoionization line

E_L/E_C	$\lvert\partial E_L/\partial E_C\rvert$	$\lvert\partial E_L/\partial\Theta_L\rvert$	$\lvert\partial E_L/\partial E_B\rvert$	$0.5 \times \lvert\partial^2 E_L/\partial\beta^2\rvert$
1.6	1.4	96.9	1×10^{-4}	53.2
$E_L \cdot R$	$\Gamma(\Delta E_C)$	$\Gamma(\Delta\Theta_L)$	$\Gamma(\Delta E_B)$	$\Gamma(\Delta\beta)$
1.3 eV	<0.1 eV	1.7 eV	0.8 eV	0.3 eV
FWHM $\simeq (\sum_i \Gamma_i^2)^{1/2} \simeq$ 2.3 eV; R_L = FWHM/$E_L \simeq$ 1.5 %				

c) Experimental Line Profiles

According to the last section the total width of autoionization lines will be strongly influenced by kinematical line broadening. Therefore this significant problem was also studied experimentally.

Prompt beryllium autoionization electron spectra typical of low-Z projectiles are shown in Fig. 39. The beryllium ions were passed through differing carbon exciter foils. The slit widths of the CMA were adjusted to be $w_1 = w_2 = w_1' = w_2' = 0.5$ mm. It is expected that the autoionization line widths should increase with increasing target thickness. This tendency can clearly be seen from Fig. 39. Consequently the effective resolution of projectile autoionization structures can be improved by reducing the foil thickness. Furthermore the energy straggling and angular scattering decreases proportional to E_B^{-1}. This is demonstrated in Fig. 40 where carbon electron energy spectra are presented for 300 keV $C^+ \rightarrow$ C-foil and 600 keV $C^{2+} \rightarrow$ C-foil collisions. In addition a variation of the beam energy (a) alters the charge state composition of the emerging beam and (b) gives rise to a displacement of the autoionization lines due to differing Doppler shifts. Hence the intensities of the main peaks are quite different in the two carbon spectra. As already mentioned the particle-foil interaction is increased for high-Z target and projectile atoms. This process was studied using carbon, aluminum, copper, silver and gold foils of approximately equal surface density. At this point we note that the narrowest peak widths were obtained for low-Z foils, i.e. for C-foils. In Fig. 41 a typical line profile is shown. This beryllium peak was recorded with an instrumental resolution $\Delta E_L/E_L \simeq 1.7$ %. Finally Table 12 lists observed instrumental widths and the corresponding energy resolution for the autoionizing decay of the $(1s2s2p)\ ^4P^o_{5/2}$ terms in LiI, BeII, BIII and CIV.

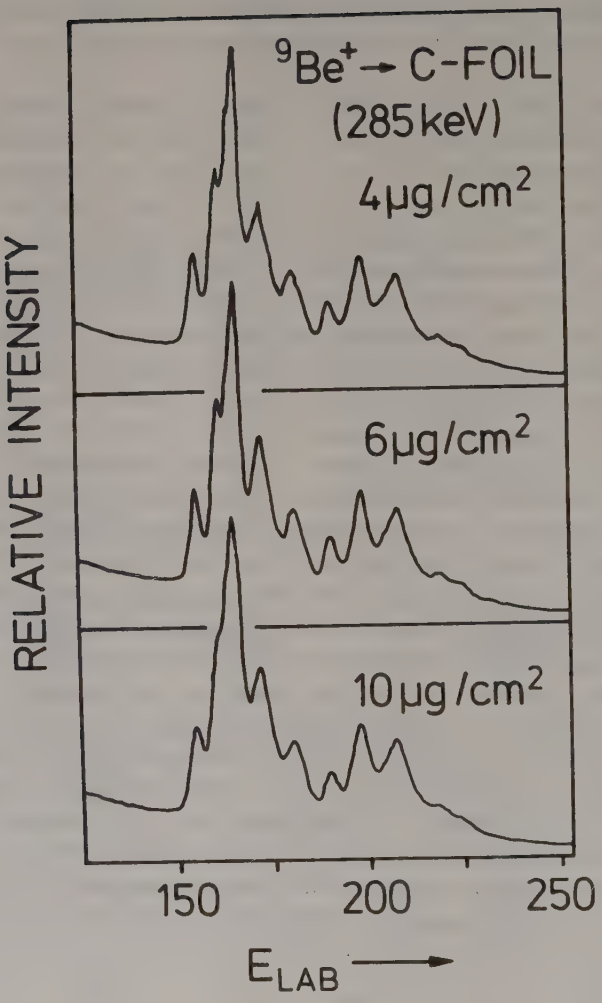

Fig. 39: The variations of peak width with foil thickness for Be^+ ions incident on three different carbon foils.

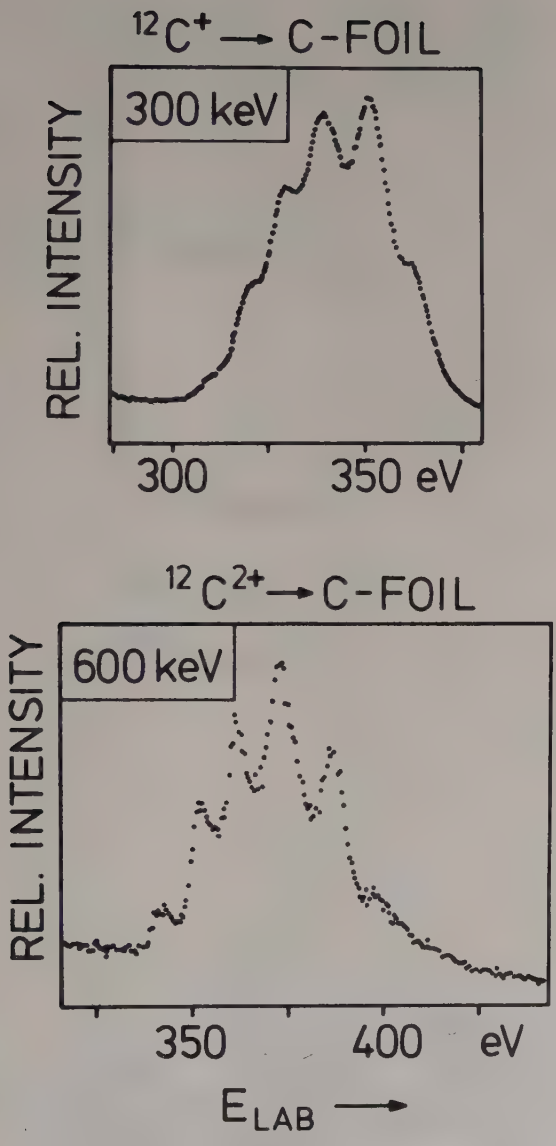

Fig. 40: Variations of peak position and peak intensity for 300 keV C^{+} and 600 keV C^{2+} ions incident on a 7 $\mu g/cm^2$ thick carbon foil.

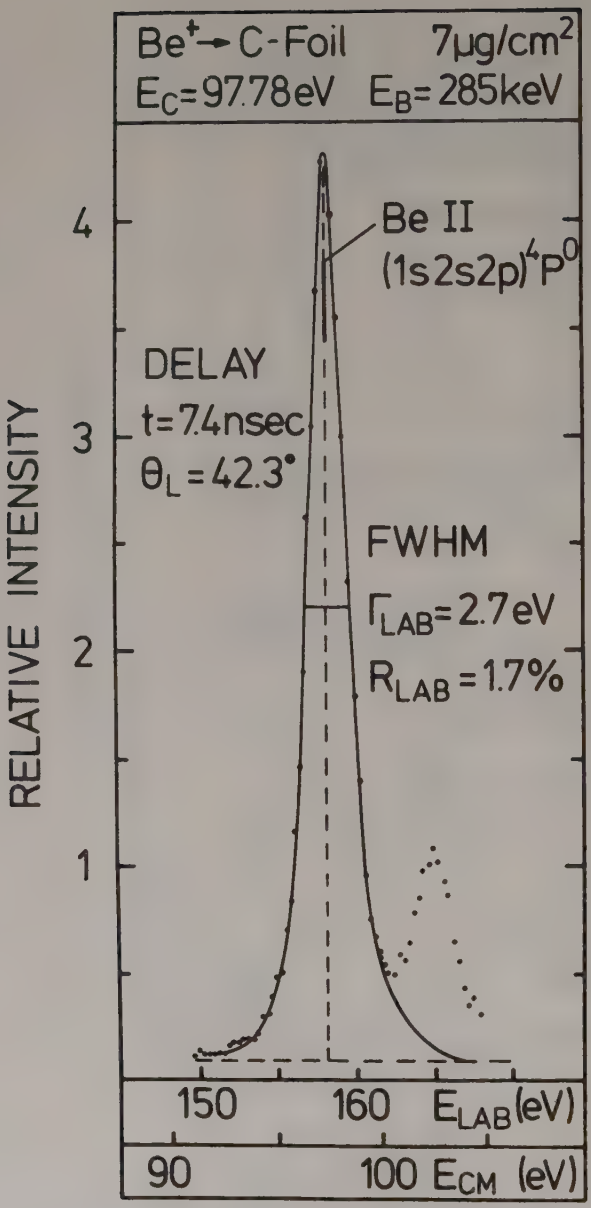

Fig. 41: The beryllium (1s2s2p) $^4P^o$ autoionization line obtained with slit widths $w_1 = w_2 = w_1' = w_2' = 0.5$ mm

Table 12: Measured width and energy resolution for the (1s2s2p) $^4P^o$ autoionizing decay of the lithium isoelectronic sequence up to Z = 6

Atomic System	Γ_L (FWHM)	R_L (FWHM)
LiI	2.2 eV	1.9 %
BeII	2.7 eV	1.7 %
BIII	4.1 eV	1.8 %
C IV	5.5 eV	1.8 %

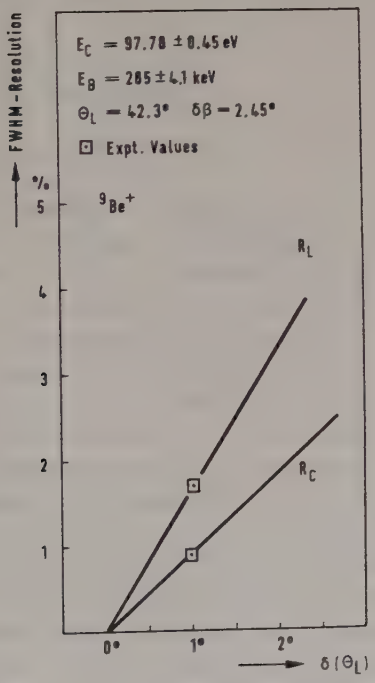

Fig. 42: Variation of the FWHM-resolution in the laboratory and center-of-mass frame as a function of the acceptance angular spread $\Delta\Theta_L$.

We can therefore conclude that the effective line width in BFAES mainly depends on (i) the acceptance of the electron spectrometer, (ii) the beam energy, (iii) the size and divergence of the ion beam and finally on the nuclear charge Z of the target and projectile atoms. As can be seen from Fig. 4.2, the acceptance angular spread $\Delta\Theta_L$ substantially determines the effective resolution of the cylindrical mirror analyzer. Consequently line broadening effects can partly be diminished by narrowing of the acceptance angular spread of the electron spectrometer (Pe 75).

VII. EXPERIMENTAL RESULTS

In these experiments H^+, He^+, Li^+, Be^+, B^+, C^+, Ne^+ and Ar^+ ion beams, typically of 300 keV beam energy, were passed through 7 $\mu g/cm^2$ thick carbon foils. The beam energy of about 300 keV was chosen to optimize the production of two- and three-electron ions in lithium, two-, three-, and four-electron ions in beryllium, three-, four-, and five-electron ions in boron and four-, five-, and six-electron ions in carbon. Electrons emerging from the ion beams at angles near 42.3^o with respect to the beam axis were collected and energy-analyzed using the CMA. The foil position was adjustable over a range of about 8 cm (tunable time delay: approximately 0-30 nsec).

1. Electron Energy Measurements

a) Effect of Continuum

Most of the data presented in this work are graphs of the collected electron count-rate as a function of energy at a particular delay time. In order to observe the "prompt" decays of short-lived Coulomb autoionizing states, the foil could be placed in view of the focus of the CMA. The total electron energy spectra show a continuum contribution plus an autoionization contribution. In the data runs with the foil in view the autoionization structures are superimposed on a slowly varying electron background. This background is due to direct collision processes. As an example Fig. 43 displays a prompt lithium spectrum resulting from 300 keV $Li^+ \rightarrow$ C-foil bombardment. This curve clearly shows a preponderance of low-energy electrons. Some characteristic features of the Li background spectrum are summarized as follows: (a) The maximum in the electron background occurs at about 51 eV, (b) the background spectrum represents a smooth curve which monotonically decreases with increasing energy, and (c) the high energy portion of the spectrum decreases approximately exponentially.

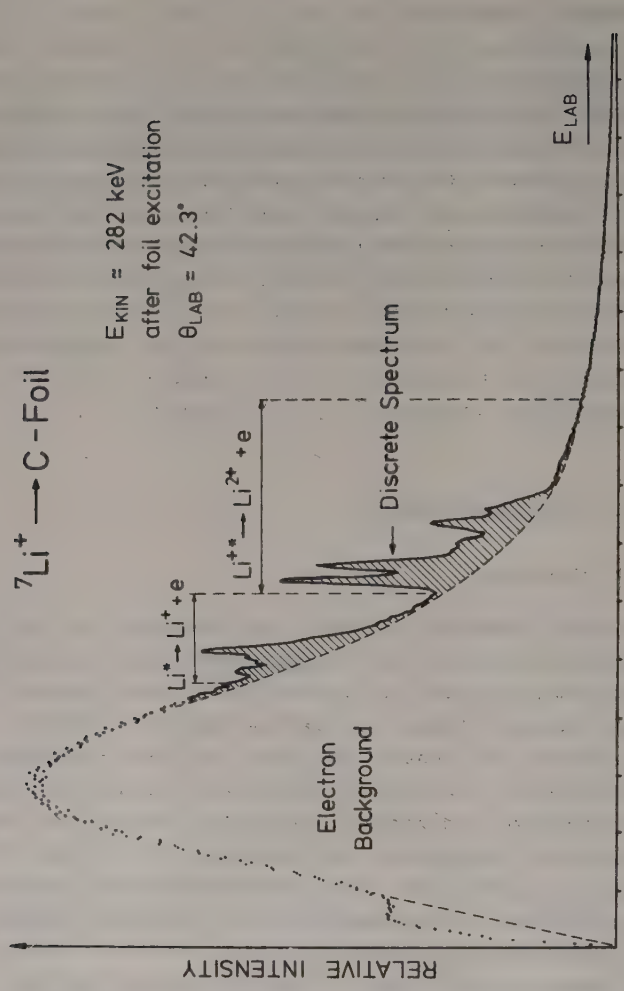

Fig. 43: Prompt electron energy spectrum produced by Li^+ + C-foil excitation. The discrete peaks are due to Coulomb autoionization of core-excited states in LiI and LiII. Energies are in eV.

The autoionization spectrum may be found by subtracting the continuum from the total spectrum. To eliminate the electron background, a special procedure for obtaining the autoionization spectra was established. The method consisted in scaling the continuous part of the prompt beryllium and lithium spectra so that both background curves became approximately equal.

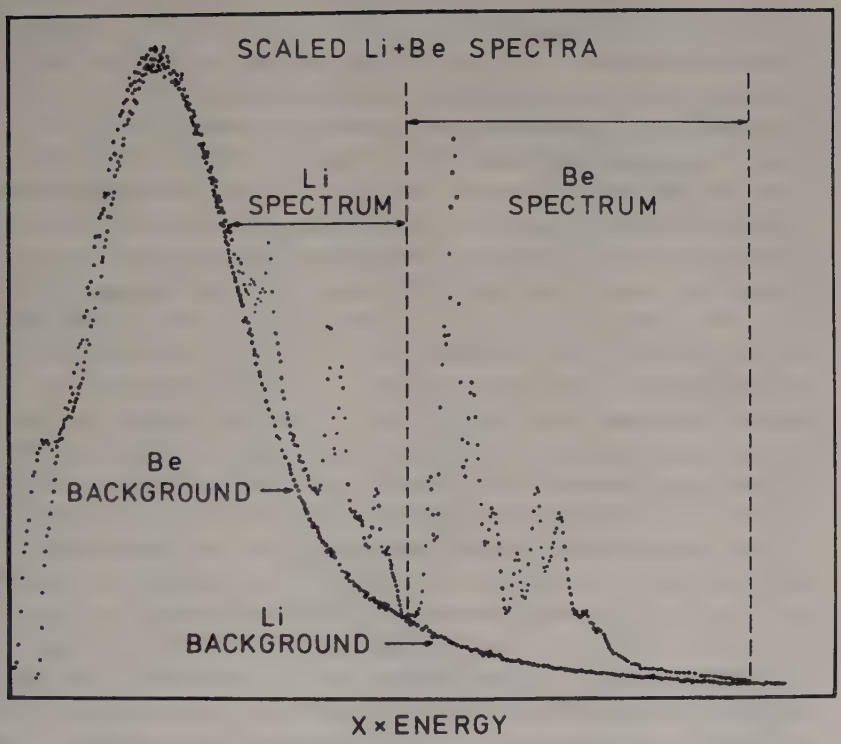

Fig. 44: Linear scaling procedure for a lithium and a beryllium spectrum.

Then the background count-rate of the Be spectrum was subtracted from the Li spectrum and vice versa. This linear scaling procedure is illustrated in Fig. 44. Finally we note that in the case of the prompt B and C spectra exponential background curves were subtracted.

b) Energy Calibration

Although the CMA was calibrated by use of a monochromatic electron source (see Chapter IV), the absolute transition ener-

gies of autoionization lines are subject to systematic errors, which must be adequately taken into account. The most important uncertainties are: (i) Electron energies may be shifted due to contact potential differences. (ii) Charging of the foil surface during ion bombardment may produce an axial field gradient; this positive charge distribution would tend to slow down and deflect the prompt electrons but not the delayed ones. (iii) The positive charge of the ion beam may produce an additional electric field which decelerates the electrons created inside the beam region ($\Delta E \sim I/\sqrt{E_B}$; with I = beam current and E_B = beam energy; for I = 100 nA and E_B = 300 keV the maximum energy loss ΔE is of the order $\sim 10^{-3}$ eV). (iv) Misalignment of the CMA symmetry axis with respect to the ion beam axis can cause kinematic energy shifts (Pe 73). (v) The Doppler shifts of the autoionization lines crucially depend on the energy of the emerging beam and on the angle of electron ejection. The major contributions to these errors stem from the uncertainty in the determination of the beam energy. In this connection we note that the energy of the incident beam must be corrected for the change in beam energy as a result of energy loss processes in the foil. If the surface density of the foil were accurately known, the mean energy loss of the transmitted beam could be determined from the stopping cross sections given by Biersack (see Chapter VI). In this study the uncertainty in the foil thickness is expected to be ~20 %. In addition we recall that the foil thickness can increase during the course of an experiment (Chapter VI). Hence the uncertainty in the foil thickness introduces considerable uncertainty in the mean energy loss of the ion beam. To avoid the difficulty of velocity determination of the beam after passage through the foil, the Li, Be, B and C spectra were calibrated using the (1s2s2p) $^4P^o$ decays (Hol 67, Be 73, Zie 75, Br 75) as calibration lines. Since the prompt and delayed spectra could be obtained successively with the same foil, the electron energy scale was established to an accuracy of at least ±0.2 eV. In particular, to establish the absolute energy scale in the lithium spectra an energy value of 51.99±0.01 eV (Zie 75) was adopted for the LiI (1s2s2p)

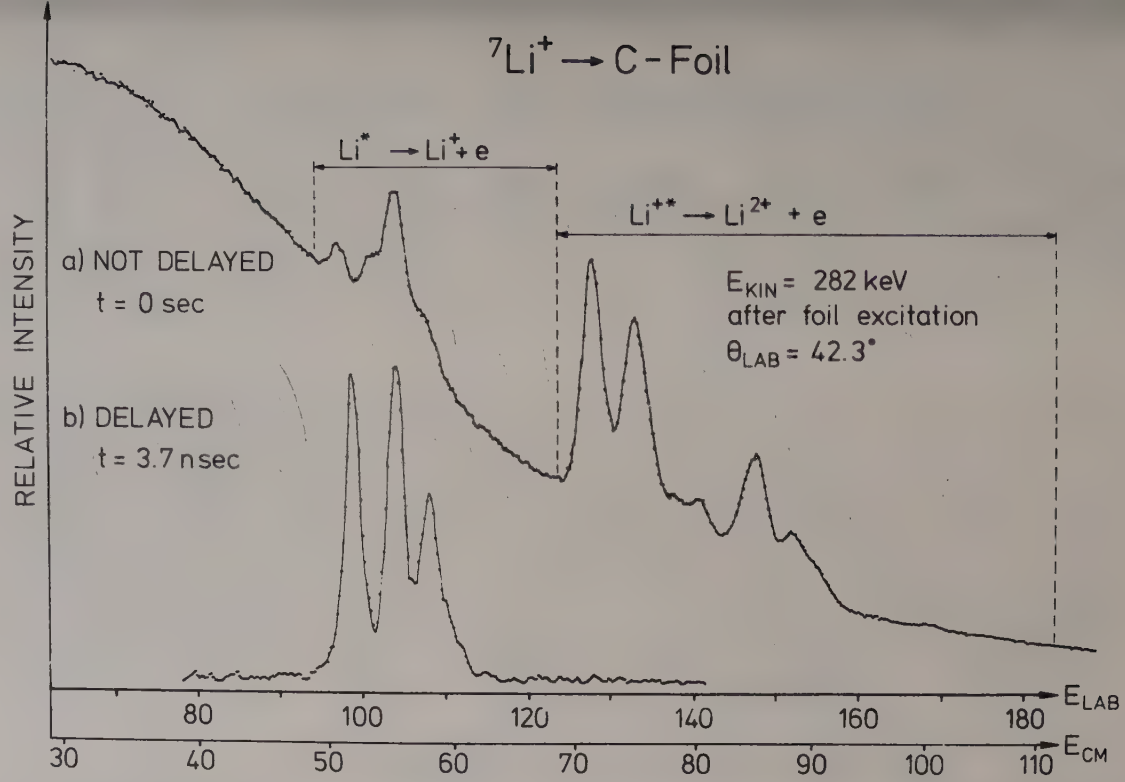

Fig. 45: Prompt and 3.7 nsec delayed lithium electron energy spectrum scaled both in the laboratory frame (E_{LAB}) and in the rest frame of the emitting projectiles (E_{CM}). Energies are in eV.

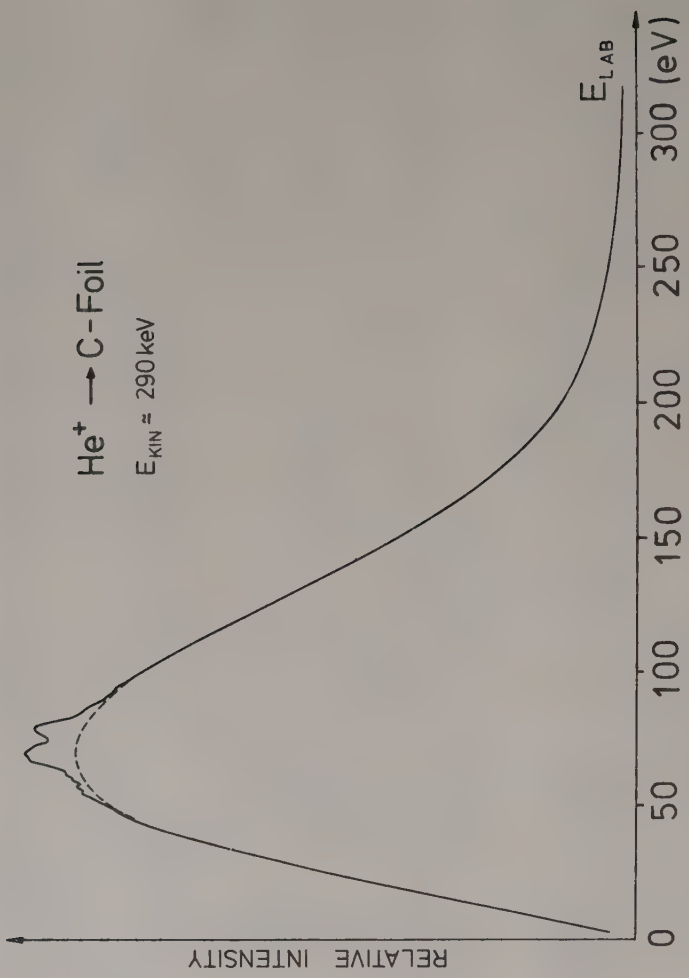

Fig. 46: Electron energy spectrum for He^+ + C-foil collisions.

$^4P^o$ decay. As a typical result we show in Fig. 45 a prompt and a delayed lithium spectrum, which were absolutely calibrated using the (1s2s2p) $^4P^o$ autoionization line in LiI.

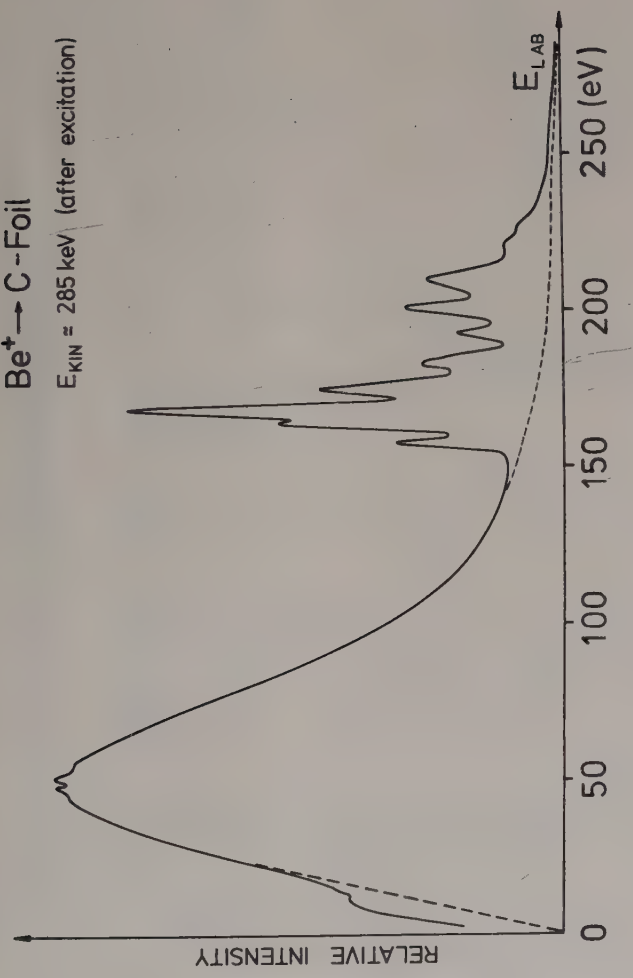

Fig. 47: Beryllium electron energy spectrum with the foil in view of the CMA. Data shown are plotted in the LAB-frame.

c) Prompt Spectra

Some representative electron energy spectra with the target directly in view are shown in Figs. 45-49 and 52-54. All data presented in this section were taken in a relative sense and

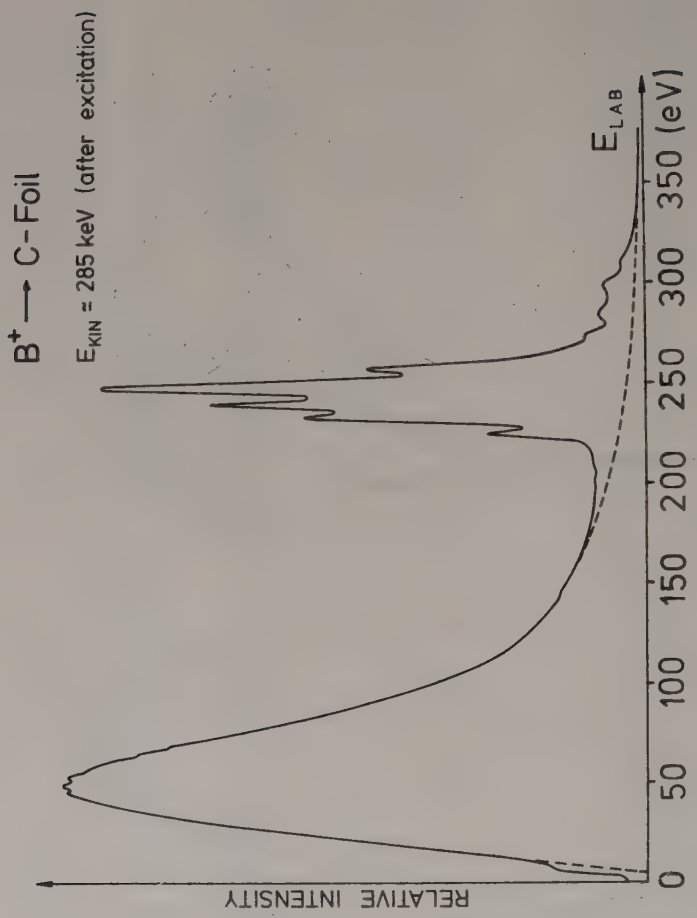

Fig. 48: Prompt boron electron energy spectrum.

were not corrected for the dispersion of the CMA.

One of the objects of primary interest in this work is the spectroscopic assignment of the prompt Li-, Be-, and B-autoionization structures (Figs. 45, 47 and 48) which will be discussed in detail in Chapter IX. We also studied autoionization spectra of helium, carbon, neon and argon (Figs. 46, 49 and 52-54).

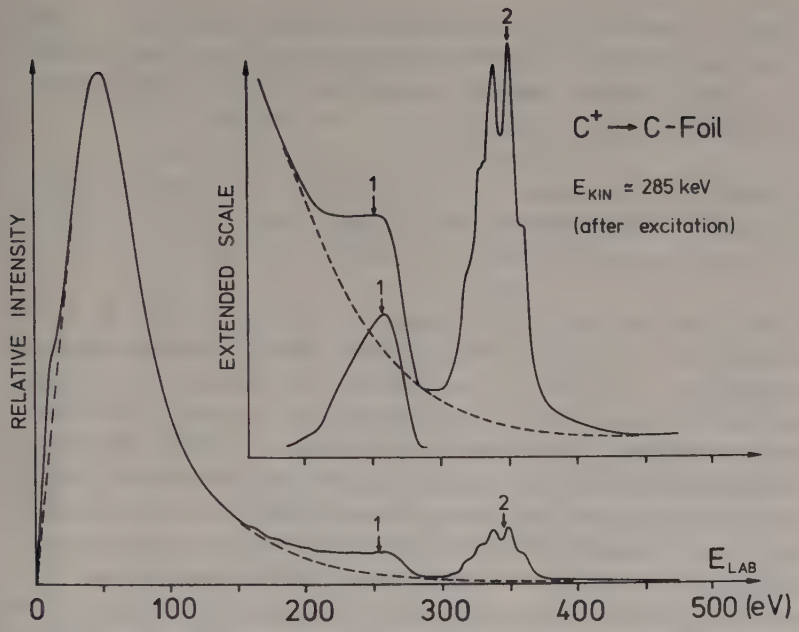

Fig. 49: Prompt carbon electron spectrum (LAB-frame). The spectrum is composed of lines corresponding to the Auger emission of the target atoms (1) as well as the Doppler-shifted counterpart (2) arising from Auger transitions of the carbon projectiles.

These structures display lines so closely spaced that our resolution is inadequate to reveal much more then the gross features of the spectra. A qualitative description of the He, C, Ne and Ar spectra is given in the following.

In Fig. 46 the electron energy spectrum of helium is shown. It can be seen that the background is quite significant for the helium spectrum (Fig. 46) and less pronounced for the lithium, beryllium, boron and carbon autoionization structures (Figs. 45, 47, 48, and 49). We note that helium is the simplest two-electron system which can autoionize. The origin of the auto-

ionization pattern in Fig. 46 is attributed to decays of doubly excited $(2lnl')\ ^{3,1}L$ $(n \geq 2)$ terms in HeI. The strong population of HeI^{**} doubly excited states is also confirmed from optical beam-foil measurements (Be 73, Mar 74, Be 75).

A typical beryllium spectrum produced by 300 keV Be^+ → C-foil collisions is displayed in Fig. 47 and the results for 300 keV B^+ → C-foil excitation are indicated in Fig. 48.

We next turn to the autoionization spectra of carbon. As a representative result we present in Fig. 49 an electron spectrum obtained for a 300 keV C^+ beam passing through a 7 $\mu g/cm^2$ carbon foil. As can be seen from Fig. 49 two separated autoionization structures occur, which are labeled 1 and 2. The C K-shell vacancy production may be understood in terms of the molecular-orbital (MO) model. Within the frame work of this model, K-shell vacancy production can occur due to level crossings at small internuclear distances (Fa 65, Lich 67, Bar 72, Kess 74). At intermediate energies the concept of diabatic orbitals can be used to qualitatively explain the data. To use this concept the average electron velocity v_e must be greater than the incident projectile velocity v_i (Gar 73), or

$$V = v_i / v_e < 1 \qquad \text{(VII-1)}$$

For 300 keV C^+ → C-foil collisions considered here $V_L < 1$ and $V_K < 1$ (Fig. 50), i.e. the MO model can be applied.

As illustrated in the C+C correlation diagram (Fig. 51) separated atom (C) states are connected with united atom (Mg) states having the same angular momentum projection m_l ($m_l = 0:\sigma$; $m_l = 1 : \pi$) and the same number of radial nodes, i.e. equal n-l-1. Since there are initial vacancies in the C 2p-levels of both collision partners, these vacancies may be transferred to the 1s shell in close collisions due to $2p\pi$-$2p\sigma$ rotational coupling. In the case of symmetric collisions such as C+C, where the $1s\sigma$ and $2p\sigma$ orbitals can match, the K-shell vacancies are

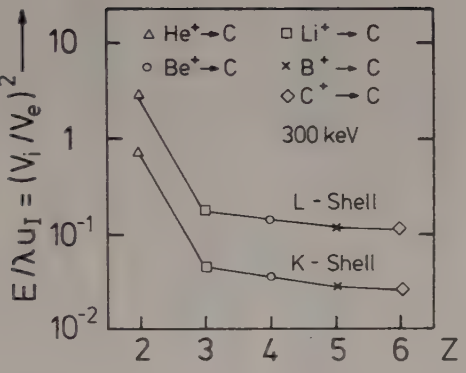

Fig. 50: Variation of $(v_i/v_e)^2$ as a function of the projectile nuclear charge ($Z_1 \leq 6$). $E = \mu v^2/2$ and $\lambda = \mu/m_e$. Here μ is the reduced mass, m_e is the electron mass and u_I is the binding energy of the K-shell and L-shell electron of the larger atom.

distributed among the target and projectile atom. In fact, examination of the experimental C spectrum reveals that the two differing autoionization features correspond to K Auger electrons from the target (1) and K Auger electrons from the projectile (2). It is seen from the inset of Fig. 49 that the C-K Auger lines of the target are greatly broadened to about $2\,\Delta E_L \simeq 36$ eV, where ΔE_L is the width of the L-band in graphite. The maximum of the target Auger peak occurs approximately at 262 eV. Moreover,the Auger spectrum from the foil displays a low energy tail which might result from inelastically scattered C-K Auger electrons emitted within the escape depth of the foil. Finally,the small humps appearing on this low energy tail might be due to plasma loss peaks.

The Ne-K Auger emission subsequent to beam-foil excitation at bombarding energies between 1.4 and 20 MeV has been investigated by Groeneveld et al. (Groe 75, Groe 76). It has been found that the Ne electron spectra are dominated by lines resulting from initial Li-like and Be-like neon ions. Very recently

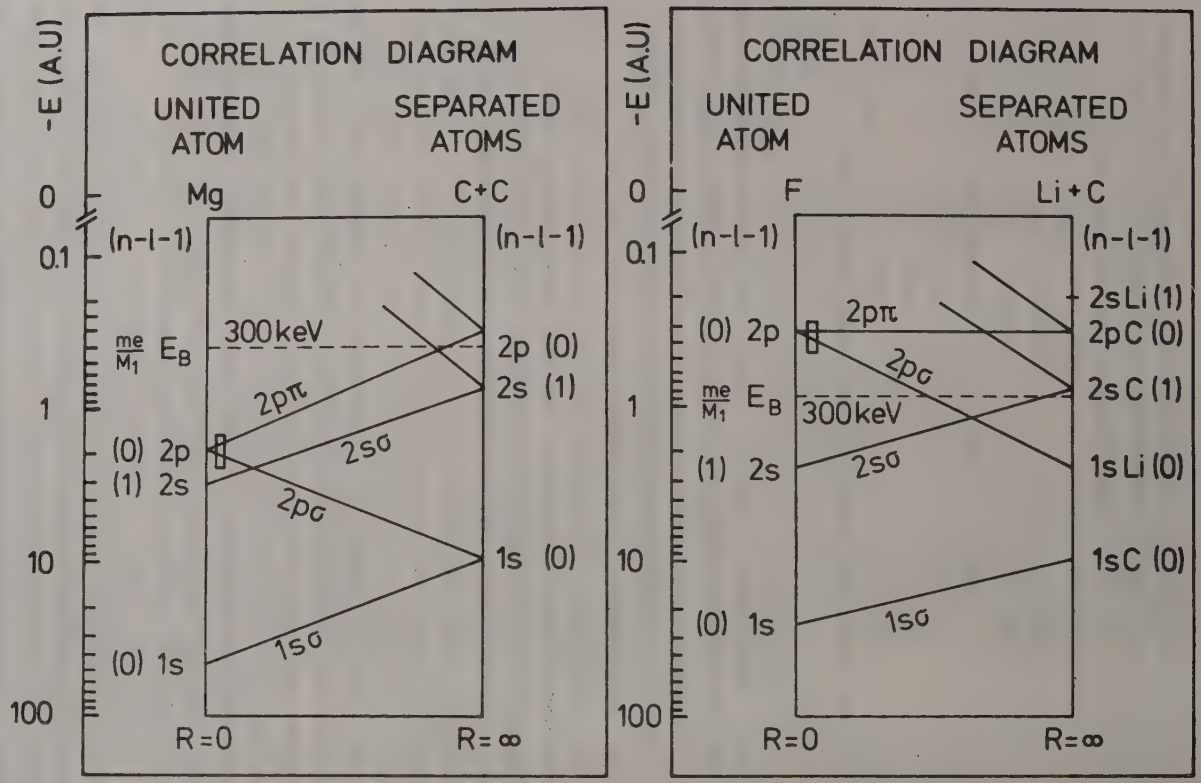

Fig. 51: Correlation diagrams for the C+C and Li+C systems. $(m_e/M)E_B$ is the reduced beam energy. Above the dashed line discrete projectile states are not defined.

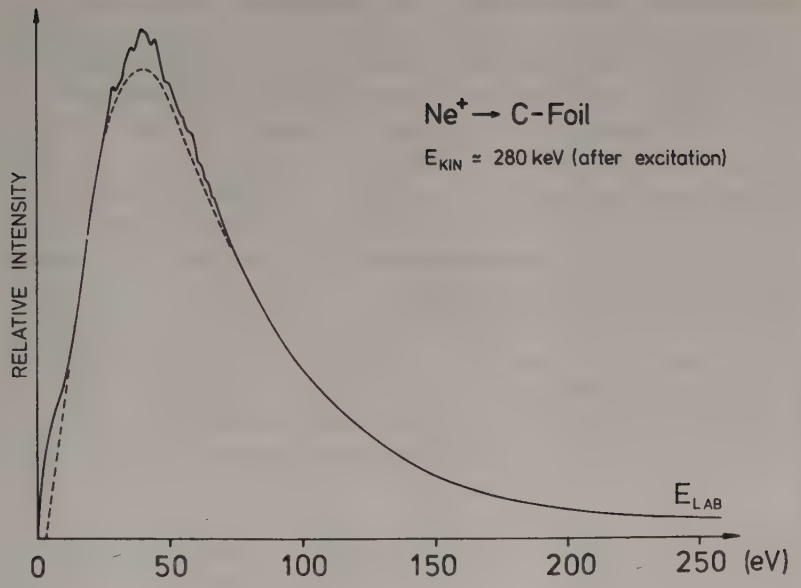

Fig. 52: Prompt neon electron spectrum in the range 0-250 eV.

Schneider et al. (Schnei 76) have studied Li and Be-like Ne-K Auger spectra by 45 MeV Cl^{12+} ion impact on a neon gas target.

In this work Ne-L autoionization-electron spectra were recorded. A typical electron energy spectrum of Ne produced by 300 keV Ne^{+} impact on carbon is plotted in Fig. 52. In the considered energy range Ne-L vacancies should be populated preferentially and the most probable charge state emerging from the carbon foil should be $\sim$+1. Hence, the neon projectiles emerging from the foil may be primarily Ne^{+} with significant numbers of Ne and Ne^{2+} present also. Indeed the autoionization lines superimposed on the electron background near E_{LAB} = 50 eV (see Fig. 52) are due to Ne L-shell vacancies. Furthermore it is expected that the observed Ne structures might be dominated by autoionizing transitions arising from the following ionic state configurations:

(1) $1s^2 2s2p^6 nl$, $1s^2 2s2p^5 nln'l'$ and $1s^2 2p^6 nln'l'$ states in NeI;

(2) $1s^2 2s2p^5 nl$, $1s^2 2s2p^4 nln'l'$ and $1s^2 2p^5 nln'l'$ states in NeII;

(3) $1s^2 2s2p^4 nl$, $1s^2 2s2p^3 nln'l'$ and $1s^2 2p^4 nln'l'$ states in NeIII.

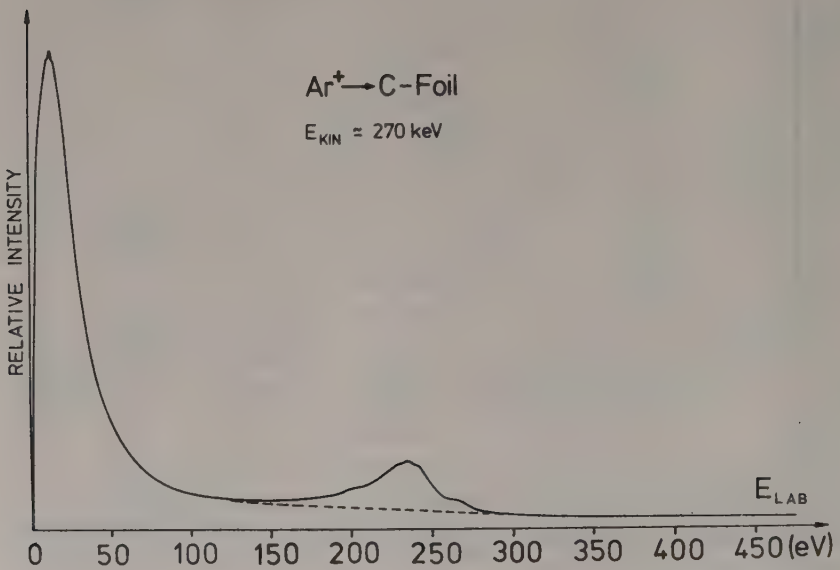

Fig. 53: Ar electron spectrum between 0 and 450 eV observed with 300 keV Ar^+ on carbon.

In Fig. 53 an electron energy spectrum in the range 0-450 eV is presented for 300 keV Ar^+ ions on carbon. Although this spectrum is essentially unresolved, the most intense components between 125 and 300 eV suggest considerable Ar-L shell and C-K shell excitation. In Ar^+ → C-foil collisions L-shell vacancies may be produced by level crossing of the rapidly rising $3d\sigma$ level in the quasi-molecule formed during the collisions. Such strong promotion effects are often known to occur when energy levels of projectile and target happen to coincide (level

matching). As Garcia et al. (Gar 73) and Kessel et al. (Kess 74) have shown, the binding energy of the carbon 1s electron is approximately equal to the binding energy of the 2p electron in argon; but the C 1s electron is somewhat more tightly bound than the argon 2p electron. Thus, we would expect to find vacancies in the Ar L-shell, whereas the C K-shell electrons should not be promoted, consistent with the gas-target data of Fortner et al. (For 74). On the other hand ionization in the outer shells modifies the screening of the Ar 2p-electrons by the outer-shell electrons. This process can cause "swapping" in the relative position of the C 1s-level and the Ar 2p-level so that C-K vacancies are produced instead. The C-K vacancy production as a result of the $Ar^+ \rightarrow$ C-foil interaction should be a charge state dependent effect. Hence, it is expected that the C-K vacancy production might increase with increasing beam energy.

For comparison, Fig. 54 shows the electron energy spectrum for 600 keV $Ar^{2+} \rightarrow$ C-foil collisions. The most noticeable feature of this spectrum is that the Ar-L Auger structures are kinematically shifted towards higher energies, i.e. the Ar-L and C-K Auger spectra completely overlap. As a consequence, we are unable to assign the individual peaks of the spectrum. Finally it might be instructive to compare the area under the Auger structures at 300 keV and 600 keV. Figs. 53 and 54 clearly show that the total Ar-L and C-K Auger yield increases with incident beam energy.

In summary we conclude that the inner-shell vacancy production in $C^+ \rightarrow$ C and $Ar^+ \rightarrow$ C-foil collisions can be qualitatively described in terms of the MO model. We further note that the electron promotion mechanism is not effective in 300 keV $H^+ \rightarrow$ C and $He^+ \rightarrow$ C-foil collisions where a Born-type description might be more appropriate. Complications may arise in a molecular description for $Li^+ \rightarrow$ C-foil collisions. The correlation diagram of this process is illustrated in Fig. 51. Within the foil the carbon 2p states are spread out and the lithium valence elec-

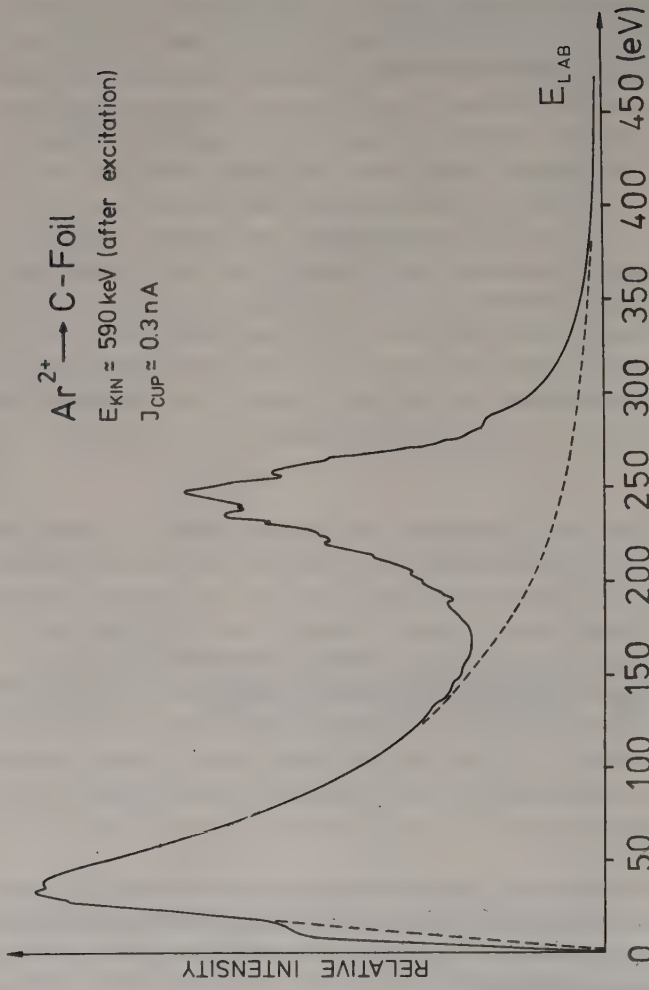

Fig. 54: Ar electron spectrum between 0 and 450 eV observed with 600 keV Ar^{2+} on carbon.

trons are shared with the foil atoms due to the collective ion-foil interaction process. That is for the outer lithium states an effective continuum may exist making the applicability of the MO model questionable.

d) Delayed Spectra

We consider next the delayed electron energy spectra. Due to specific selection rules (see Table 3) the downstream spectra are less complicated than those with the foil in view of the spectrometer. As a typical result we show in Fig. 55 various beryllium spectra taken with the foil in view and slightly downstream so that time delays in the range 0-1.4 nsec resulted. These spectra contain several interesting features which will be discussed in Chapter IX. Figure 56 represents a delayed boron and a delayed carbon spectrum. The A and B peaks (see Fig. 56) will be of great importance in our later consideration of metastable autoionizing quintet, sextet and septet states (Chapter IX). Furthermore various carbon electron spectra as measured at particular points downstream from the foil between 0-21.4 nsec are displayed in Figs. 57 a-d. It should be noted that these spectra are normalized to the height of the dominating peak in the spectrum. For a detailed discussion of the delayed lithium, beryllium, boron and carbon spectra the reader is referred to Chapter IX.

2. Intensity Measurements

a) Relative cross sections and yields

Figure 58 is a schematic drawing of a cross section experiment in which the projectiles are directed toward target atoms which are essentially at rest in the laboratory frame. For a given beam velocity v_i the cross section, differential in angle θ_C and the electron energy E_C, can be calculated from the following equation

$$\sigma(E_C, \theta_C) = \frac{d^2\sigma}{dE_C d\Omega_C} \simeq \frac{(N_e - N_o)\exp(Z/v_i\tau)}{(Q/q)(\Delta Z/v_i\tau)(d\Omega_C/d\Omega_L)\Delta\Omega_L\,(dE_C/dE_L)\Delta E_L N_C d\tau_A \eta} \qquad \text{(VII-3)}$$

where N_e is the number of ejected electrons at a distance Z from the foil in a solid angle $\Delta\Omega_L$; N_o is the number of background counts; $\Delta Z = w_s$ is the length of the beam viewed by the

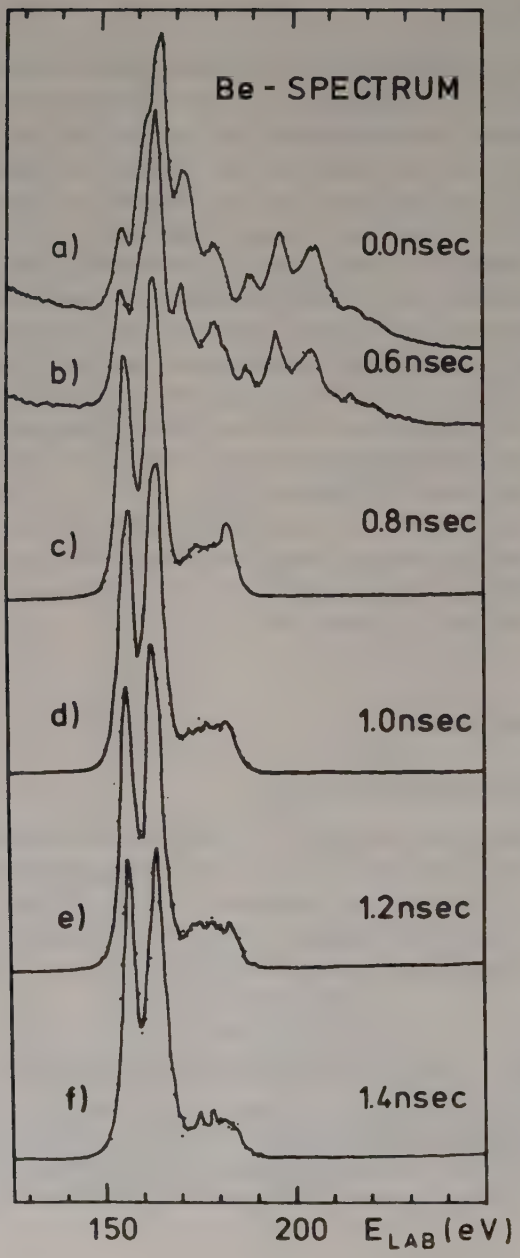

Fig. 55: Electron spectra above 130 eV recorded at various positions slightly downstream from the foil. The spectra are normalized to the height of the second strong peak in the spectrum.

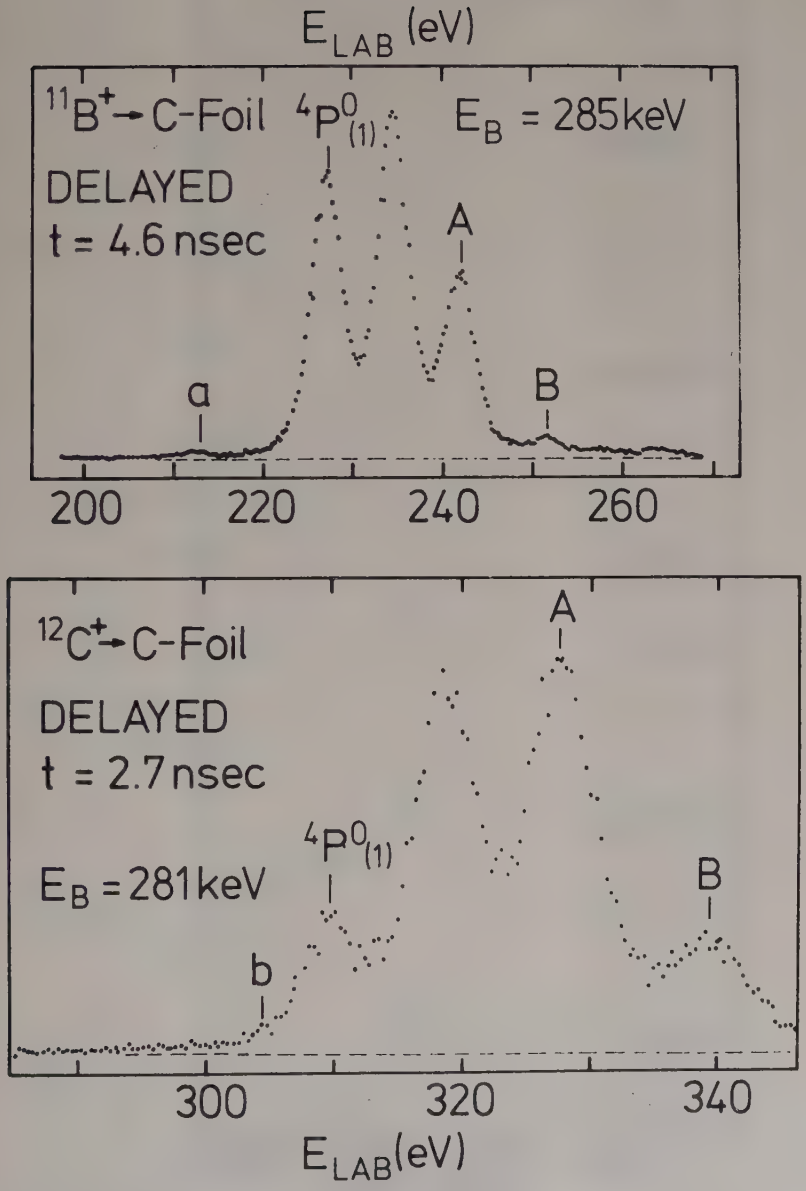

Fig. 56: Delayed spectra of electrons emitted by 285 keV boron and 281 keV carbon beams

Fig. 57 a:

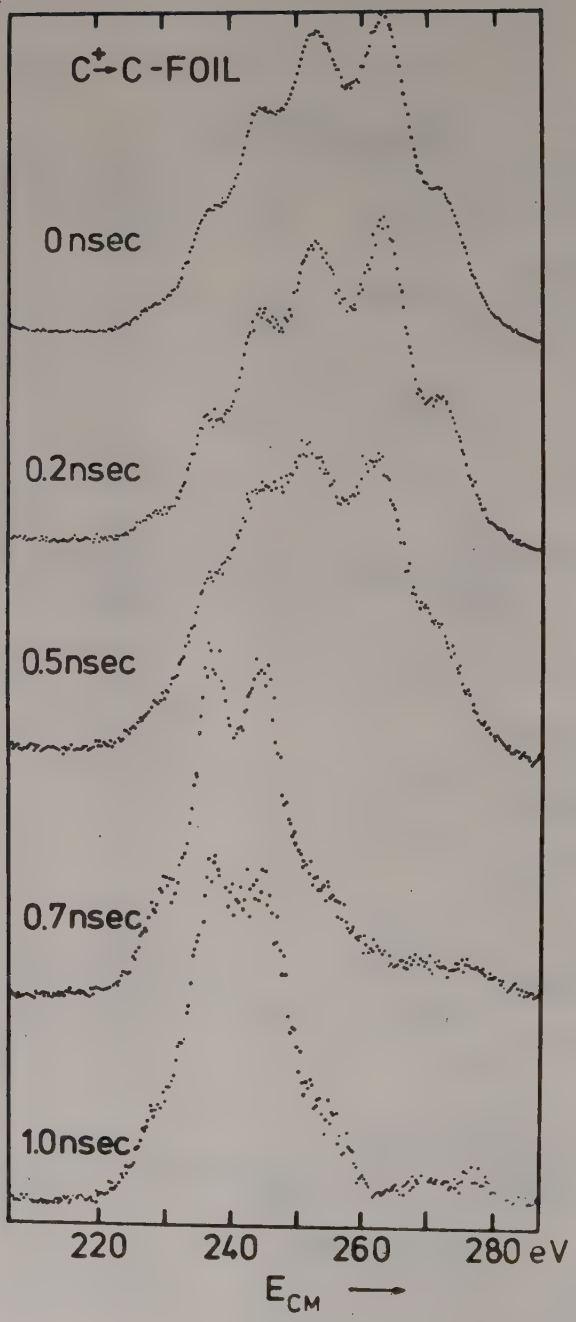
C+→C-FOIL
0 nsec
0.2nsec
0.5nsec
0.7nsec
1.0nsec
220
240
260
280 eV
E_CM

Fig. 57 b:

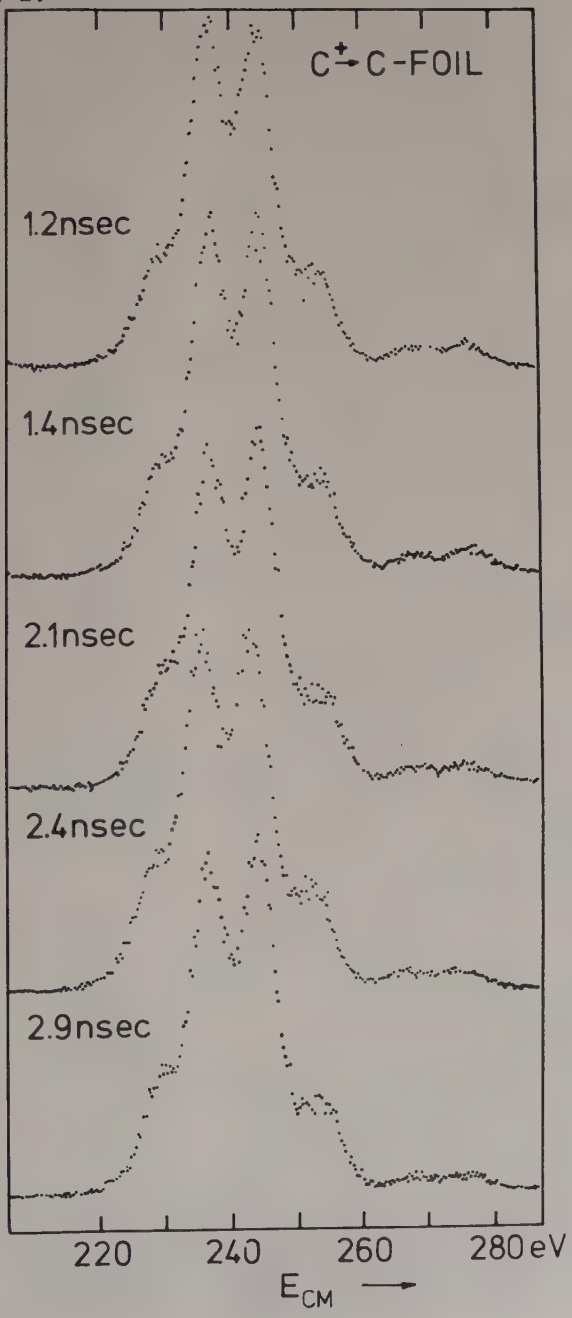
C+→C-FOIL
1.2nsec
1.4nsec
2.1nsec
2.4nsec
2.9nsec
220
240
260
280 eV
E_CM

Fig. 57 c:

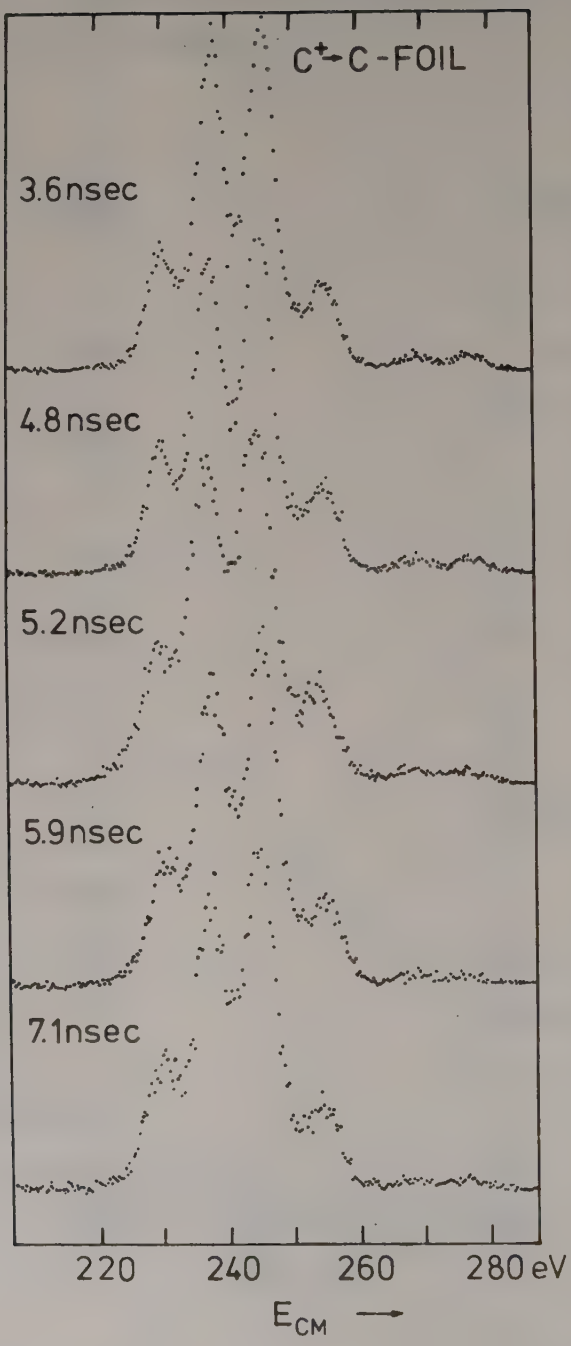
C+→C-FOIL
3.6nsec
4.8nsec
5.2nsec
5.9nsec
7.1nsec
220
240
260
280 eV
E_CM →

Fig. 57 d:

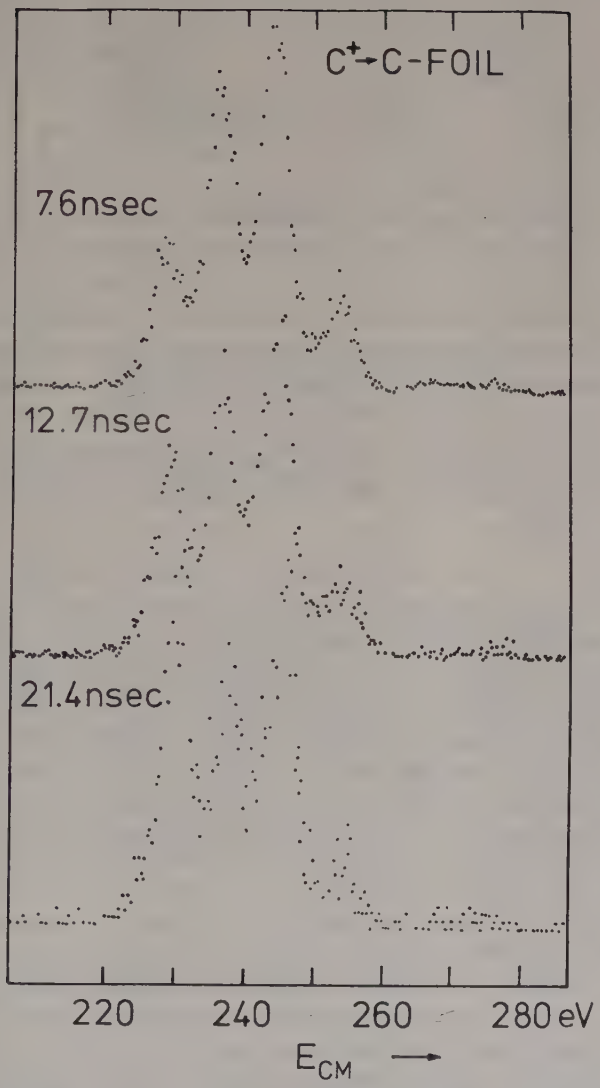

Fig. 57: Carbon electron spectra with the viewing area centered directly at the foil and at several downstream positions. The spectra are normalized to the height of the strongest peak in the spectrum.

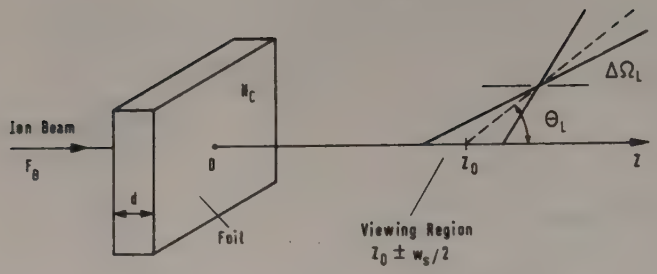

Fig. 58: Schematic drawing of a cross section experiment. F_B is the particle flux per sec cm^2; d is the foil thickness, N_C is the number of foil atoms per cm^3 ($N_C \simeq 11.3 \times 10^{22}$ atoms/cm^3); $\Delta\Omega_L$ is the solid angle in the LAB-frame. Θ_L is the electron emission angle in the LAB-frame. w_s is the length of the source region.

spectrometer; τ is the mean life of the decaying state; Q is the total charge collected in electron charge units; $\bar{q}$ is the mean charge of the emerging beam; $d\Omega_C/d\Omega_L$ is the solid-angle transformation factor; $\Delta\Omega_L$ is the solid angle of the electron spectrometer; dE_C/dE_L is the energy transformation factor; ΔE_L is the energy range accepted by the spectrometer; N_C is the number of target atoms per cm^3; d is the foil thickness; τ_A is the transparency of the CMA and η is the efficiency of the electron detector. The axial symmetry of the beam further insures that $d\Phi_C = d\Phi_L$, therefore

$$d\Omega_C/d\Omega_L = d(\cos\Theta_C)/d(\cos\Theta_L) \qquad \text{(VII-4)}$$

Setting β equal to zero and using Eq. (VI-12), we find

$$d\Omega_C/d\Omega_L = 2k^{1/2}\cos\Theta_L + (1-k\sin^2\Theta_L)^{1/2} + k\cos^2\Theta_L(1-k\sin^2\Theta_L)^{-1/2} \quad (v_B < v_C) \qquad \text{(VII-5)}$$

where $k = \varepsilon/E_C$ and ε is the reduced beam energy. Then the electron yield per ion incident on the target is obtained from

$$\int_{E_C-\Delta E_C/2}^{E_C+\Delta E_C/2} \int_0^{2\pi} \int_0^{\pi} \sigma(E_C, \theta_C)\sin\theta_C \, d\theta_C d\Phi dE_C = \sigma(E_C) = Y(E_C)/n \qquad \text{(VII-6)}$$

$\sigma(E_C)$ being the single differential cross section, $Y(E_C)$ the yield per ion emerging from the foil and $n=N_C \cdot d$ the number density of the target per cm^2, respectively. Thus, the yield (Sm 73) is given by

$$Y(E_C) = \frac{N_e(E_C)\exp(Z/v_i\tau)}{(Q/\bar{q})(\Delta Z/v_i\tau)(d\Omega_C/d\Omega_L)(\Delta\Omega_L/4\pi)\ \tau_A\eta} \qquad \text{(VII-7)}$$

where $N_e(E_C)$ is the integrated number of autoionization electrons (area under a peak) observed in a line or spectral feature of centroid energy E_C. Yields may be extracted from the observed spectra by using Eq. (VII-7).

To extract an absolute total yield of delayed (1s2s2p) $^4P^o$ electron emitters in BeII one must be able to determine the fraction of the spatially distributed delayed decays which take place within view of the analyzer. In order to make an estimate of this number we assumed $\tau \sim 1.3 \times 10^{-8}$ sec decay for all BeII (1s2s2p) $^4P^o$ emitters. Using this mean life, we estimated the absolute yield per incident ion at 300 keV to be of the order $\sim 1 \times 10^{-3}$. This yield is listed in Table 13 along with yields obtained by other groups (Dmi 72, Sm 73). We also mention here that Wittmann has studied yields for helium-like states in LiII (Wit 76) by means of optical beam-foil spectroscopy. Thus, Wittmann has measured a peak absolute yield per incident beam particle of ~ 1 % for the single (1s2p) $^3P^o$ state in LiII ($E_B \simeq 300$ keV). Due to the strong excitation of the LiII (1s2p) $^3P^o$ states at 300 keV beam energy, lithium-like quartet states such as (1s2s2p) $^4P^o$ might be dominantly populated by electron capture from the corresponding (1s2s) ^3S

and (1s2p) ^3P helium-like ions. This mechanism has also been discussed by Dmitriev et al. (Dmi 72) and Smith and coworkers (Sm 73) as one of the most likely to dominate. In summary, we note that some percent of the emerging beam should be in metastable autoionizing states at 300 keV beam energy. In particular Smith et al. (Sm 73) have shown that individual (1s2s2p) $^4P^o_{5/2}$ states of oxygen and fluorine may have populations as much as 1 % of the total beam.

Table 13: Comparison of (1s2s2p) $^4P^o$ yield measurements for beryllium, boron, carbon, nitrogen and oxygen.

Z	Ion	Velocity 10^8 cm/sec	Yield % J = 5/2	J = 3/2,1/2	Average
4	$^9Be^+$	2.5			∿0.1[a]
		3.4	7.5±1.5[b]	3.0 ± 0.7[b]	
5	$^{11}B^{2+}$	3.4			4.5±1[b]
6	$^{12}C^{3+}$	3.4	2.0±0.3[b]		
7	$^{14}N^{4+}$	4.8	1.3±0.2[b]		
8	$^{16}O^{5+}$	5.0	0.5±0.2[b]		
			0.14±0.07[c]		
		8.3	0.73±0.04[c]		

Table footnote: a = this work; b = Dmitriev et al. (Dmi 72); c = Smith et al. (Sm 73)

We also studied relative cross sections of the continuous electron distribution. We recall that the double differential cross section is inversely proportional to $\Delta E_L \simeq R \cdot E_L$ where R is resolution of the analyzer and E_L the electron energy.

Figure 59 represents the measured electron energy distribution from the backsurface of a carbon foil for 310 keV H^+ → C-foil bombardment. It is evident from this figure that a small Auger peak is superimposed on the continuum distribution. This structure results from C-KLL Auger transitions (C-KLL

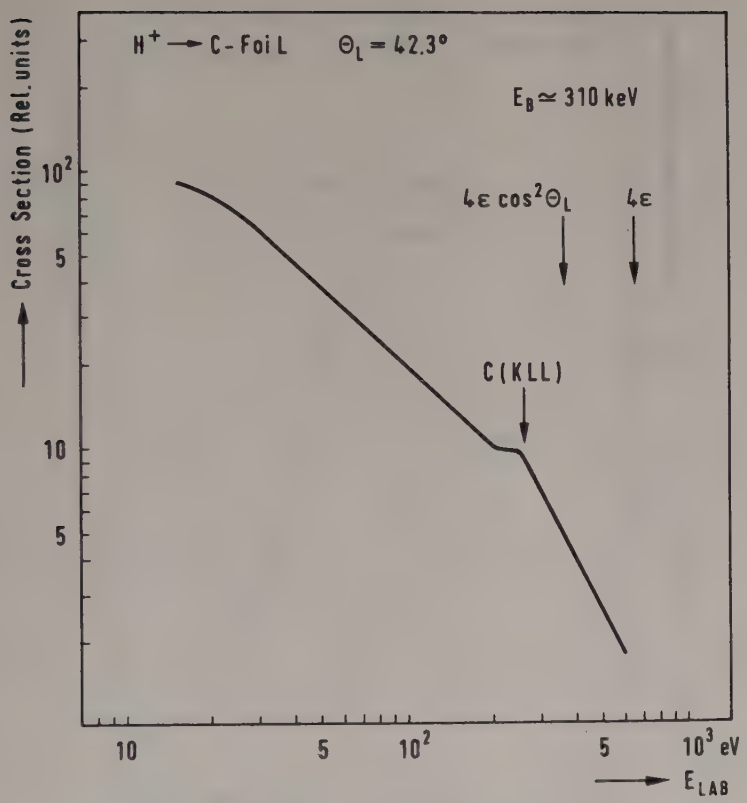

Fig. 59: Energy distribution of electrons ejected from a 7 µg/cm^2 carbon foil by 310 keV H^+ → C-foil bombardment.

electrons with energies of 243-267 eV). This result also indicates that the resolving power used here is not adequate to reveal structure in the KLL peak. But from the theoretical data of Beck and Nicolaides (Beck 75) it is clear that the onset of the C-KLL spectrum should occur at about 243.6 eV, corresponding to the KL_1L_1 transition energy. We further note that the C-KLL Auger group from the last monolayer of the foil has also been observed by Folkmann and coworkers (Fol 75).

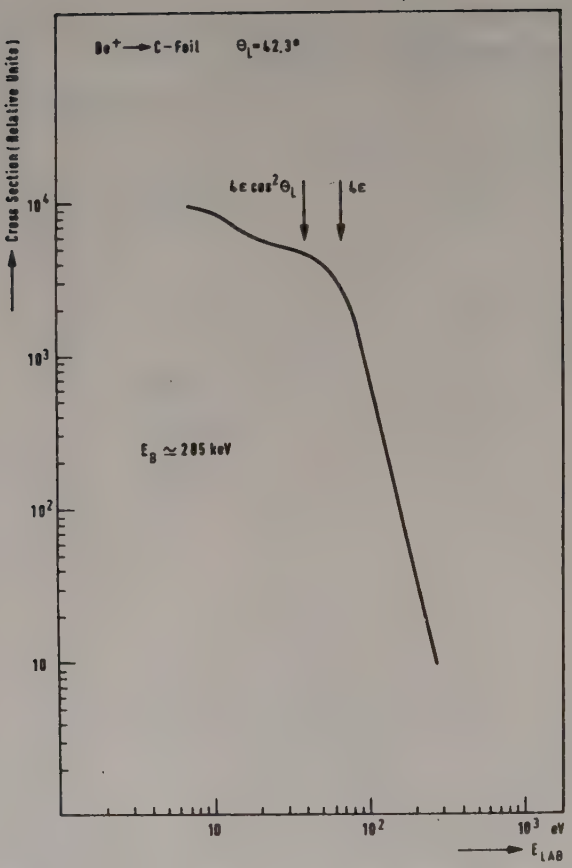

Fig. 60: Energy distribution of electrons ejected from a 7 $\mu g/cm^2$ carbon foil by 285 keV Be^+ → C-foil bombardment.

In Figs. 60-62 the electron energy distributions for Be^+ → C-foil, B^+ → C-foil and C^+ → C-foil collisions are graphically shown as a function of ejected electron energy. The contribution arising from high energy Auger electrons was subtracted. As can be seen all curves (Figs. 59-62) indicate a preponder-

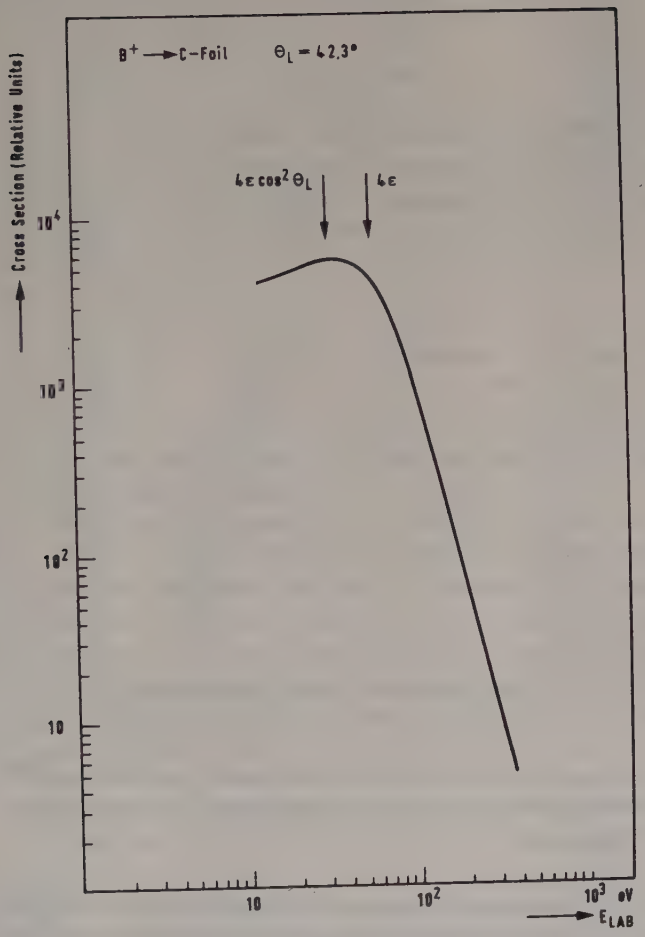

Fig. 61: Energy distribution of electrons ejected from a 7 μg/cm^2 carbon foil by 285 keV B^+ → C-foil bombardment.

ance of low-energy electrons and decrease monotonically with increasing electron energy. Above $E_L = 4\varepsilon$ the curves show very nearly exponential dependence, i.e. the high energy portions of

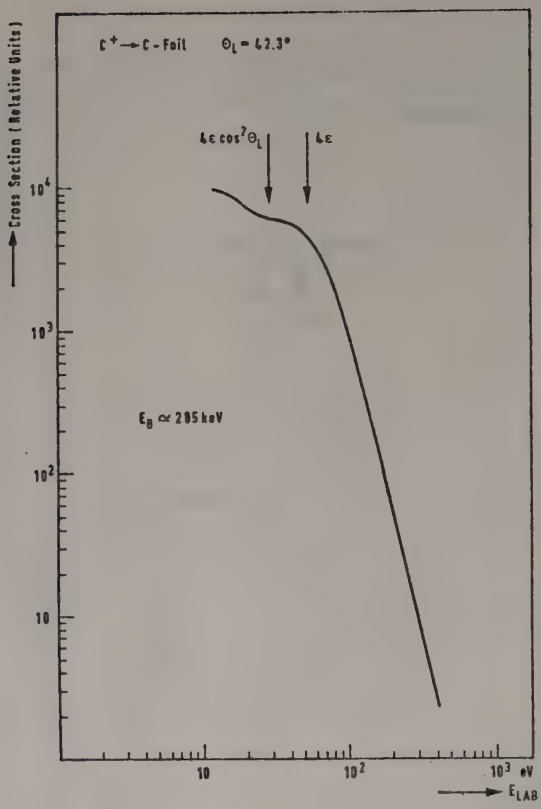

Fig. 62: Energy distribution of electrons ejected from a 7 μg/cm^2 carbon foil by 285 keV C^+ → C-foil bombardment.

the continuous spectra represent straight lines on a semi-logarithmic scale. Furthermore, a broad maximum appears in the distribution of the continuum electrons corresponding to those electrons, emitted with energies characteristic of direct projectile-electron binary encounters. As Blauth has shown, (Blau 57) the maximum energy which can be transferred in a classical projectile-electron encounter is given by

$$E_{max} = 2\varepsilon\cos^2\theta_L - 2\cos\Psi(u_I\varepsilon)^{1/2} + 2(\varepsilon\cos^2\theta_L)^{1/2}$$

$$\times\ [\varepsilon\cos^2\theta_L + u_I - 2\cos\Psi(u_I\varepsilon)^{1/2}]^{1/2} \qquad \text{(VII-8)}$$

where u_I is the binding energy of the electron, Ψ is the angle between the incident projectile and the electron, θ_L is the emission angle of the electron with respect to the beam axis and ε is the reduced beam energy. For $\Psi = 0$ and $u_I = 0$ (free target electron at rest) Eq. (VII-8) simplifies to the well-known formula (Groe 75a)

$$E_{max} = 4\varepsilon\cos^2\theta_L = 4(m_e/M)E_B\cos^2\theta_L \qquad \text{(VII-9)}$$

For free electrons at rest this so-called binary encounter peak would be a delta-function distribution. The finite width of the observed binary encounter peak (see Figs. 60-62) is due to the effect of the momentum distribution (Zie 74) of the electrons. It should be further pointed out that the exact shape of the continuum emission cross section is uncertain for electron energies below ∿30 eV due to contributions of low energy auto-ionization electrons. It should be also noted that the binary encounter peak moves towards lower electron energy for increasing projectile mass and constant beam energy. Finally Table 14 gives E_{max} for differing values of projectile mass M.

Table 14: Position of the binary encounter peak as a function of the projectile mass for θ_L=42.3° and E_B=300 keV.

Projectile	M(amu)	E_{max} (eV)
$^4He^+$	4.002	90.0
$^7Li^+$	7.016	51.3
$^9Be^+$	9.012	40.0
$^{11}B^+$	11.009	32.7
$^{12}C^+$	12.000	30.1

b) Effect of Finite Time Window

The number of electrons per incoming projectile transmitted through the electron analyzer depends on the initial population N_i of the autoionizing level, the effective length of the beam observed, the particle velocity v_B after the foil and upon the autoionization probability W^a_{ik} from level i to the final ionic level k. Thus, the number of electrons detected is given by

$$N(i \to k) \sim N_i (l_{eff}/v_B) W^a_{ik} = N_i \Delta t W^a_{ik} = N_i \gamma \qquad \text{(VII-10)}$$

where $(l_{eff}/v_B) = \Delta t$ is called time window and $\gamma = \Delta t W^a_{ik} = (l_{eff}/v_B) W^a_{ik}$ is the time-window factor. γ is a measure of the probability of decay within the viewing region defined by the entrance slit system of the CMA (see Fig. 16). Expression (VII-10) is valid only if cascades can be neglected. In Fig. 63 the time-window factor is plotted as a function of the beam energy for constant beam segment $l_{eff} \simeq 3.4$ mm. It is apparent from this figure that the electron analyzer is more sensitive to observation of fast decaying states. In addition, as indicated in Fig. 64, the sensitivity of the CMA to longer-lived states can be increased by increasing the length of beam observed. However this is only possible at the expense of energy resolution.

3. Decay Curves

By selecting a specific autoionization line and measuring its intensity as a function of distance from the foil, decay curves can be obtained (see also Chapter V). If the velocity of the emergent beam is known, the decrease of intensity is directly related to the mean lifetime of the excited states. In the simplest case the observed decay profiles can be fitted to a function of the type

$$N(Z) = N_1 \exp(-Z/v_B \tau_1) + N_2 \qquad \text{(VII-11)}$$

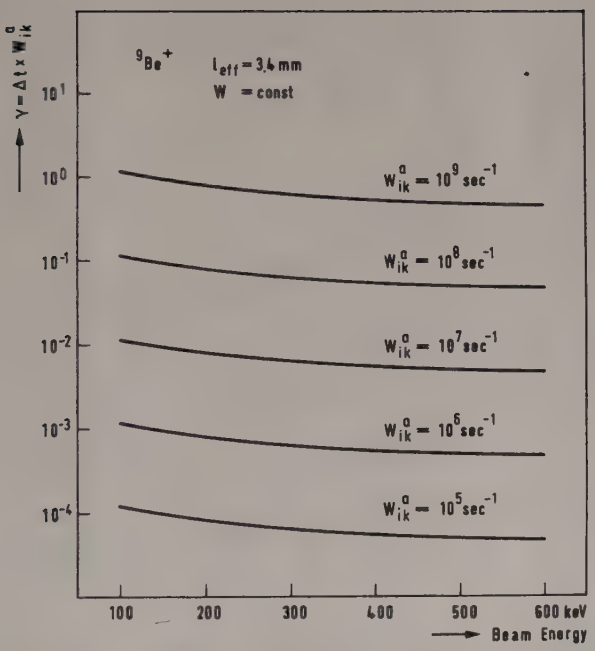

Fig. 63: Time-window factor versus beam energy for various autoionization rates.

where N_1 and N_2 are constants, Z is the distance from the target, v_B is the beam velocity after the foil and τ_1 the lifetime of the excited level under study. It should be noted that lifetime measurements using the beam-foil technique are limited for several reasons. The most important are: (a) Due to the finite extension of the viewing region of the CMA, lifetimes shorter than 10^{-9} sec are generally inaccessible by means of BFAES. (b) On the other hand lifetime measurements of very long-lived states are limited by the finite length of the foil drive mechanism. (c) Moreover, owing to angular scattering of the beam particles the detection efficiency may change as a function of the foil-to-spectrometer distance, in

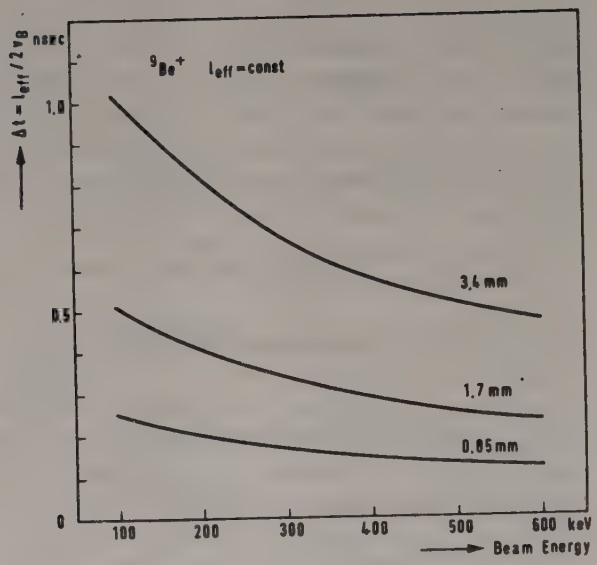

Fig. 64: Time window of the analyzer versus beam energy for various beam segments.

particular at larger distances. (d) Additional errors may be caused by the uncertainties in the determination of the ion velocity. (e) The major errors frequently arise due to cascading from higher levels into the excited level being measured or due to background contributions. Therefore corrections for cascading and background must be made (Cur 70). (f) We further note that the decay of an unresolved neighboring autoionization line (blending) can also produce significant departures from single-exponential decay profiles.

As examples we present here decay curves from autoionizing states in beryllium. The decay characteristics of the mean features of the beryllium spectrum (Fig. 65) are shown in Figs. 66-77. Thus, a decay profile taken at an energy adjacent to peak 1 (see Fig. 65), is indicated in Fig. 66. In Fig. 67,

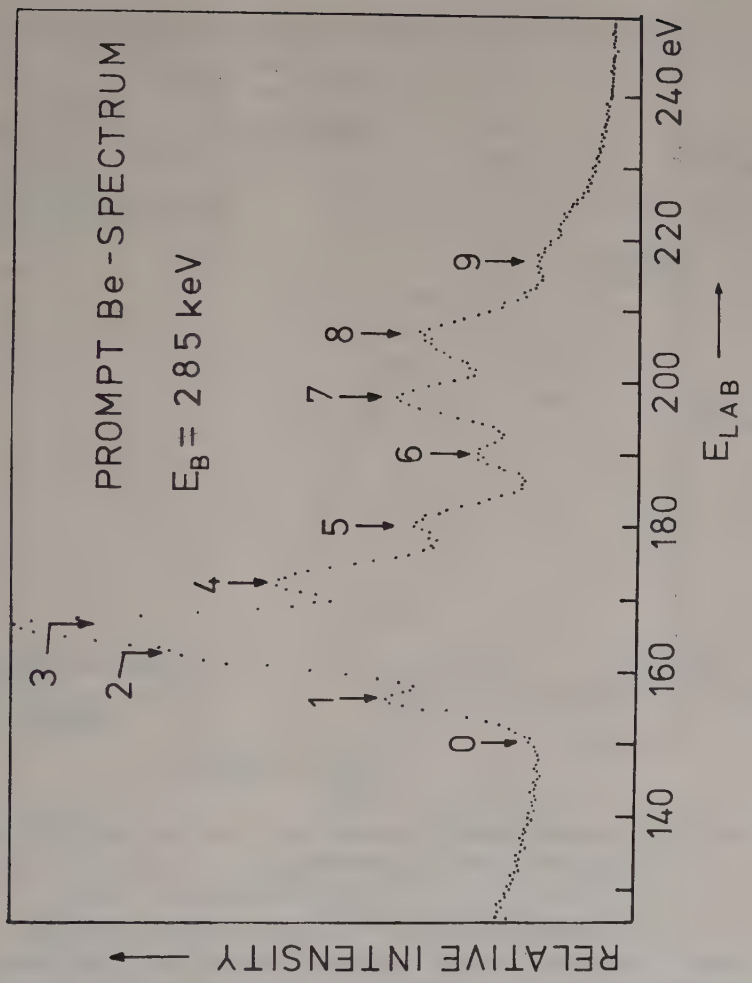

Fig. 65: Prompt electron energy spectrum produced by 285 keV beryllium ions. The arrows indicate the energy positions where decay profiles were recorded.

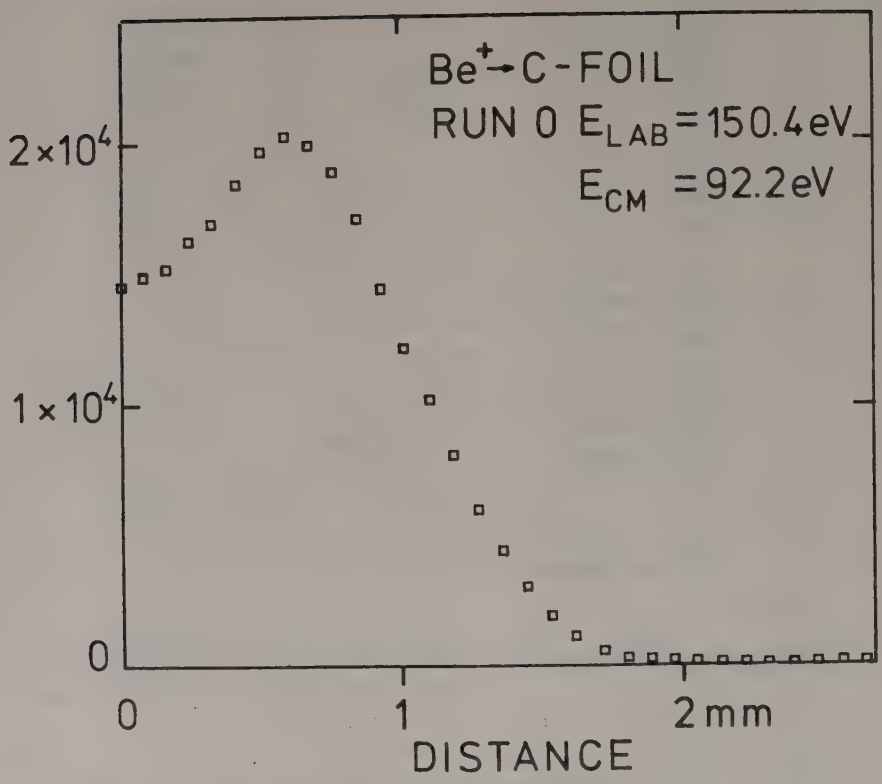

Fig. 66: Intensity profile versus distance from the foil for $E_{CM} \simeq 92.2$ eV (linear plot).

we present a decay profile of electrons emitted from the $(1s2s^2)\ ^2S$ states in BeII (peak 1). As the BeII $(1s2s^2)\ ^2S$ states are expected to be very short-lived, Fig. 67 represents also an example of the measured spatial window function of the analyzer. From the observed window curve a spread ΔZ(FWHM) of about 1 mm was deduced corresponding to a time uncertainty Δt(FWHM) $\simeq$ 0.4 nsec at 300 keV beam energy. The effect of cascading is illustrated in the next graph. It is seen from Fig. 68 that the $(1s2s2p)\ ^4P^o$ states in BeII are strongly populated

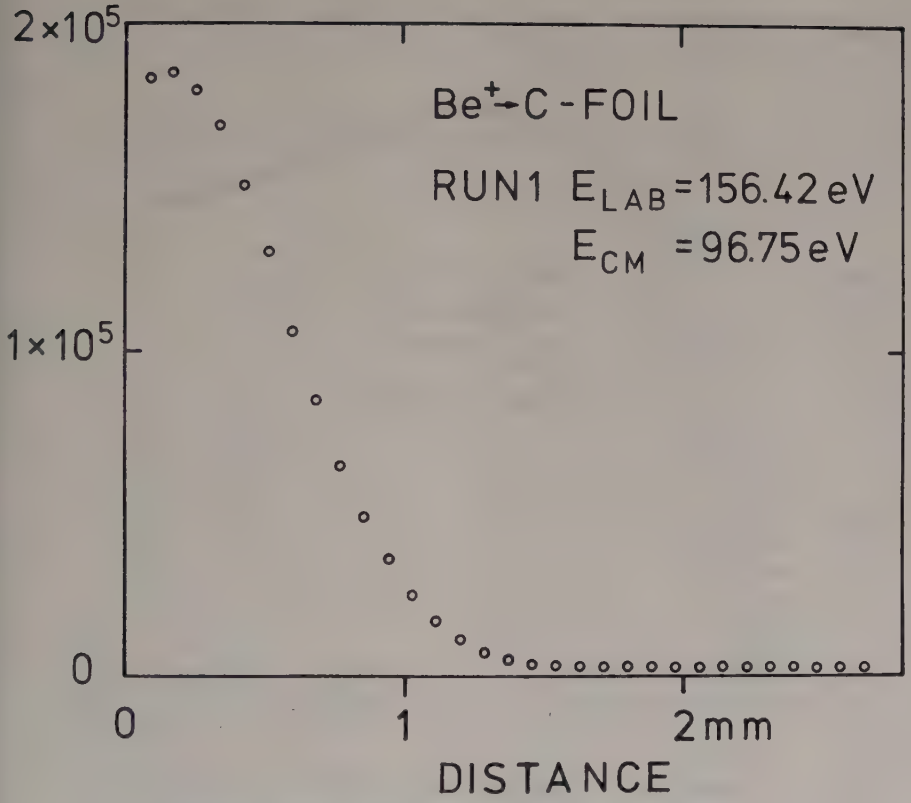

Fig. 67: Intensity profile versus distance from the foil for peak 1 centered at $E_{CM} \simeq 96.75$ eV (linear plot).

by cascades. This "cascade-feeding" might be explained by optical dipole transitions from higher-lying quartet states. In such a case the intensity of the observed decay profiles varies in a quite complicated way which, moreover, should depend on the particle energy. A detailed discussion of the decay modes of quartet states is given in Chapter IX.

Decay profiles were taken also for shoulder 2 on the low-ener-

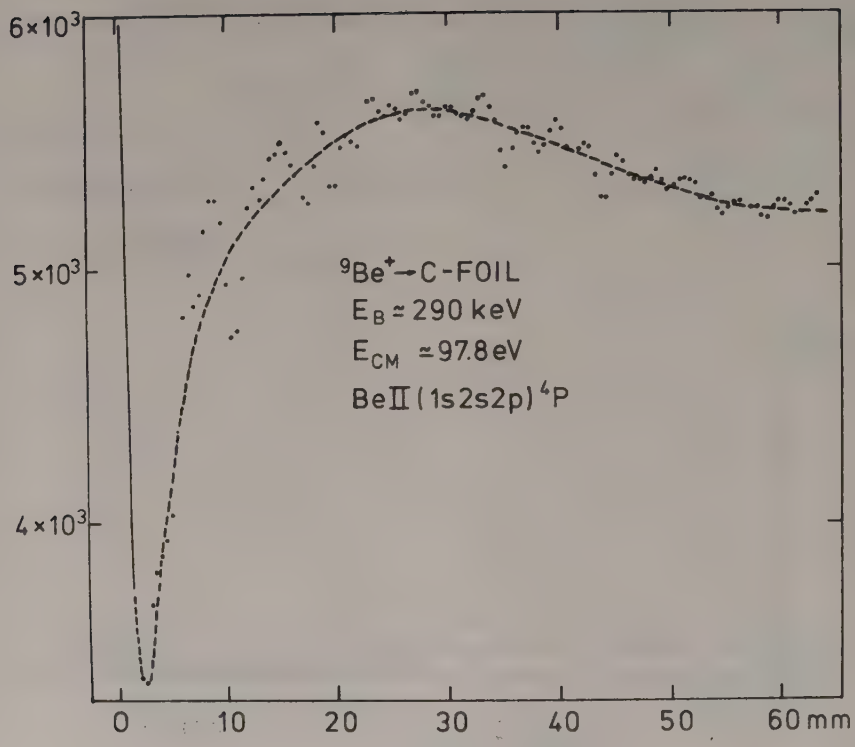

Fig. 68: Decay profile for the (1s2s2p) $^4P^o$ state in BeII (linear scale). The dashed curve drawn through the data is to guide the eye.

gy side of peak 3 (see Fig. 65), of which examples are shown in Figs. 69-71. According to Fig. 70 one might expect a shorter-lived component to appear (∿5 nsec) in the decay profile as well as a longer-lived one (∿132 nsec). In order to confirm the exponential character of the faster decay we subtracted constant fractions of background, as indicated in Fig. 71. In fact, the decay profile becomes nearly single exponential, if one subtracts an appropriate number of counts.

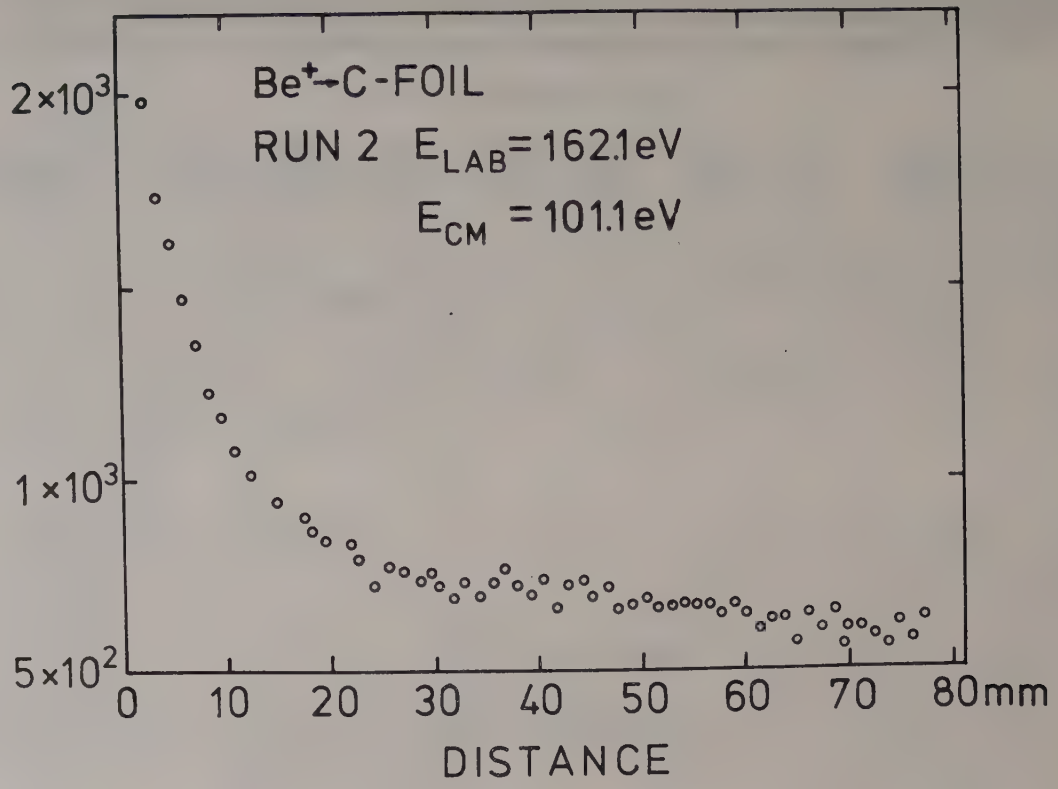

Fig. 69: Intensity profile versus distance from the foil for shoulder 2 centered at $E_{CM} \simeq$ 101.1 eV (linear scale).

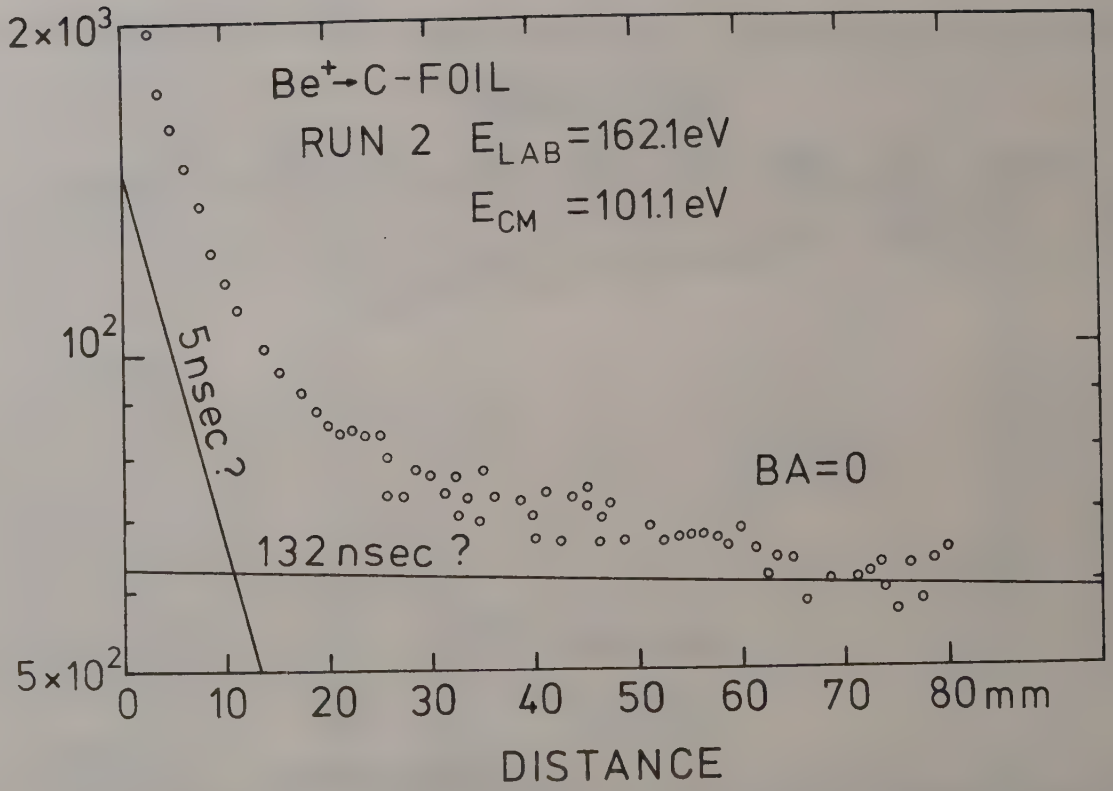

Fig. 70: Semilog plot of the intensity versus distance from the foil (shoulder 2). The straight lines represent a graphical decomposition of the data assuming zero fraction background.

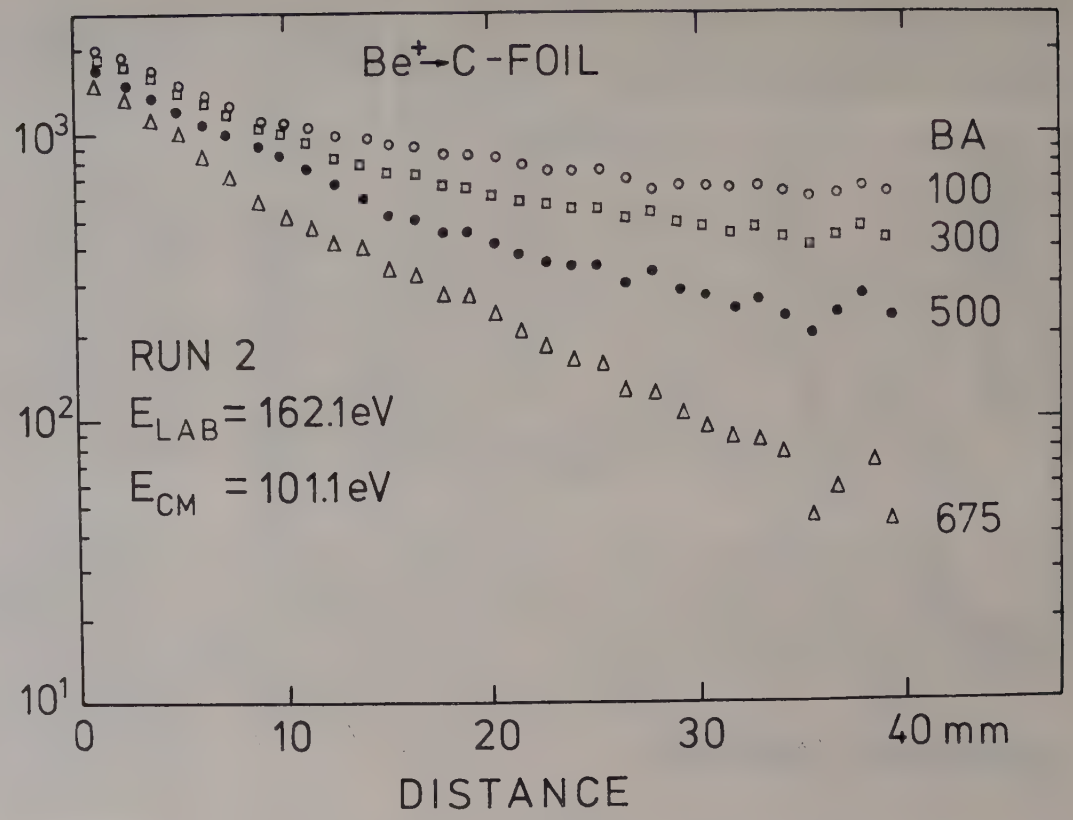

Fig. 71: Semilog plot of the intensity versus foil position for shoulder 2 at $E_{CM} \approx 101.1$ eV. Data are corrected for different amount of background.

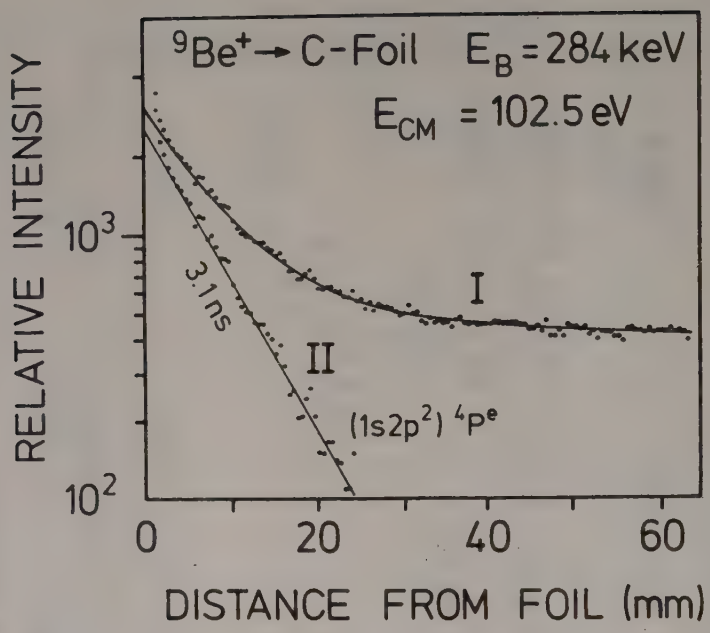

Fig. 72: Intensity as a function of foil-to-spectrometer distance. Curve I represents the measured data points. The smooth curve drawn through the data is the function $N_1\exp(-t/\tau_1) + N_2\exp(-t/\tau_2) + N_3$. Curve II shows the remaining decay curve for the $(1s2p^2)\ ^4P$ state in BeII where the straight line represents the least-squares fit to the data points (semilogarithmic scale).

The results for E_{CM} = 102.5 eV are shown in Figs. 72 and 73. Fig. 72 is a semilogarithmic plot. The most striking characteristic to be noted is that the decay curve is not single exponential, thus suggesting the presence of more than one excited system. Therefore the measured profile was fitted to a function of the form

$$N(Z) = N_1\exp(-Z/v_B\tau_1) + N_2\exp(-Z/v_B\tau_2) + N_3 \qquad \text{(VII-11)}$$

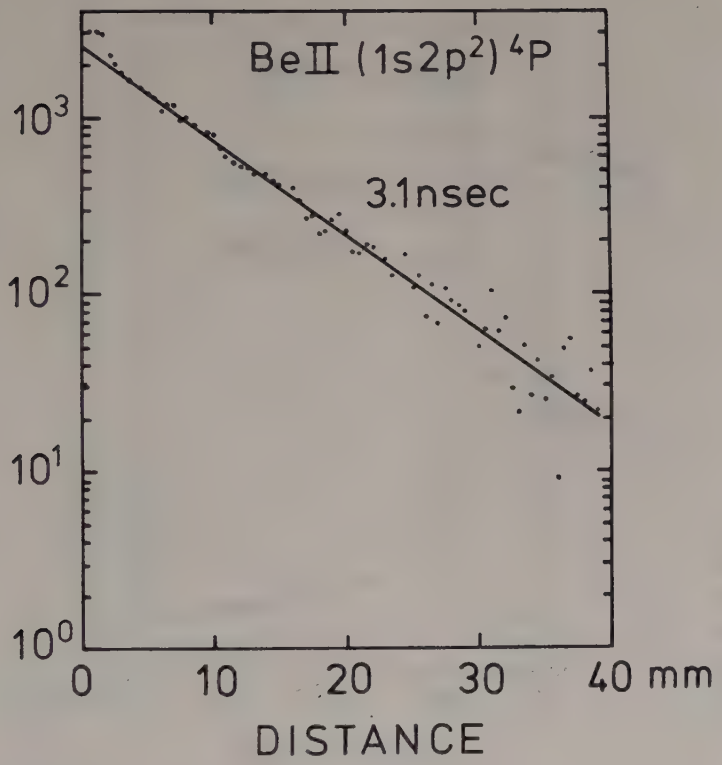

Fig. 73: Decay in flight of the BeII($1s2p^2$) ^4P state, obtained at a beam energy of about 284 keV.

where N_1, N_2 and N_3 are constants and τ_1 and τ_2 are the lifetimes of the differing autoionizing levels 1 and 2, respectively. The amount of counts corresponding to the background and the contribution from the long-lived component was then subtracted. This analysis enabled us to examine the decay of the ($1s2p^2$) $^4P^o$ states in BeII. It is evident from Fig. 73 that the remaining decay curve II is approximately single exponential. The final results of this analysis are presented in Chapter IX.

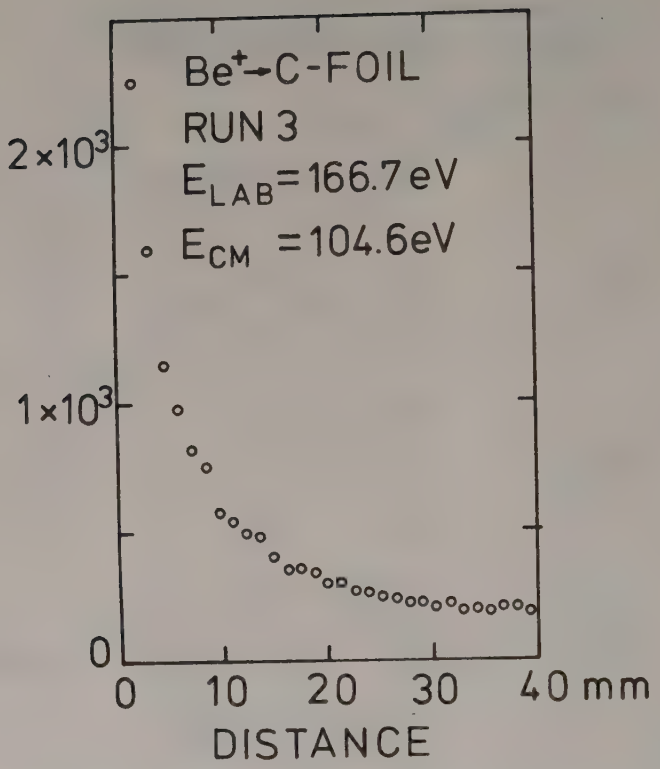

Fig. 74: Counts versus foil position for peak 3 centered at $E_{CM} \simeq 104.6$ eV (linear plot).

Departures from a single-exponential decay profile can be seen also in Figs. 74-76. Furthermore Fig. 77 represents a semilog plot for peak 4 centered at about $E_{CM} \simeq 109.6$ eV. This curve was graphically fitted to a single exponential function giving a mean life of the order 5.2 nsec. We also studied autoionizing decays of carbon projectiles. However, these results will be discussed elsewhere (Br 76).

In summary, we conclude that there is evidence to suggest the

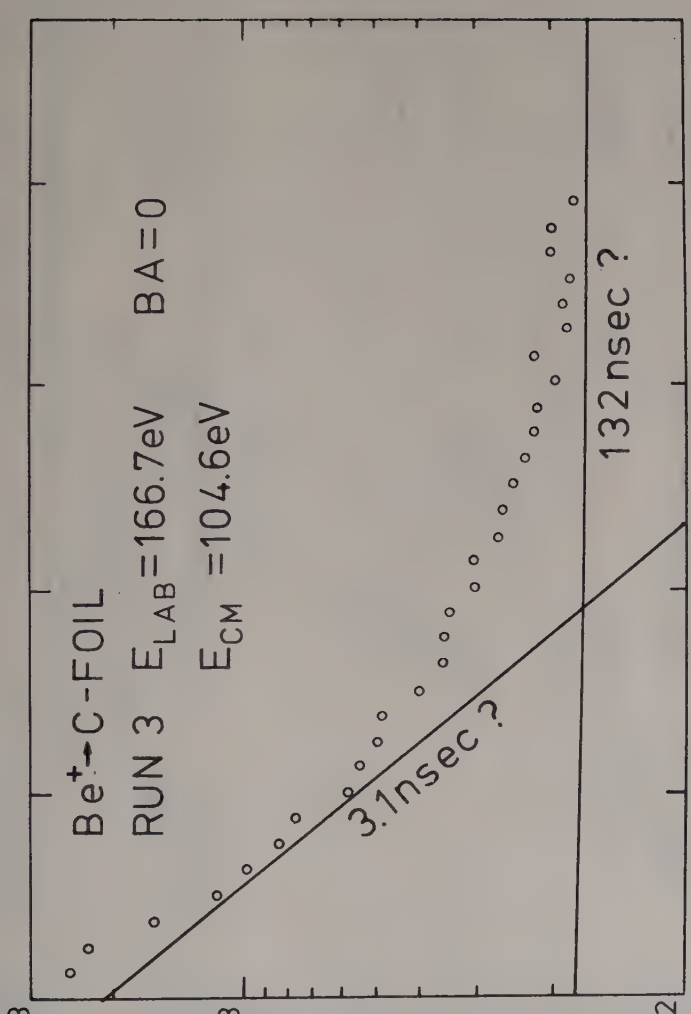

Fig. 75: Semilog plot of counts versus foil position for peak 3 at $E_{CM} \approx 104.6$ eV.

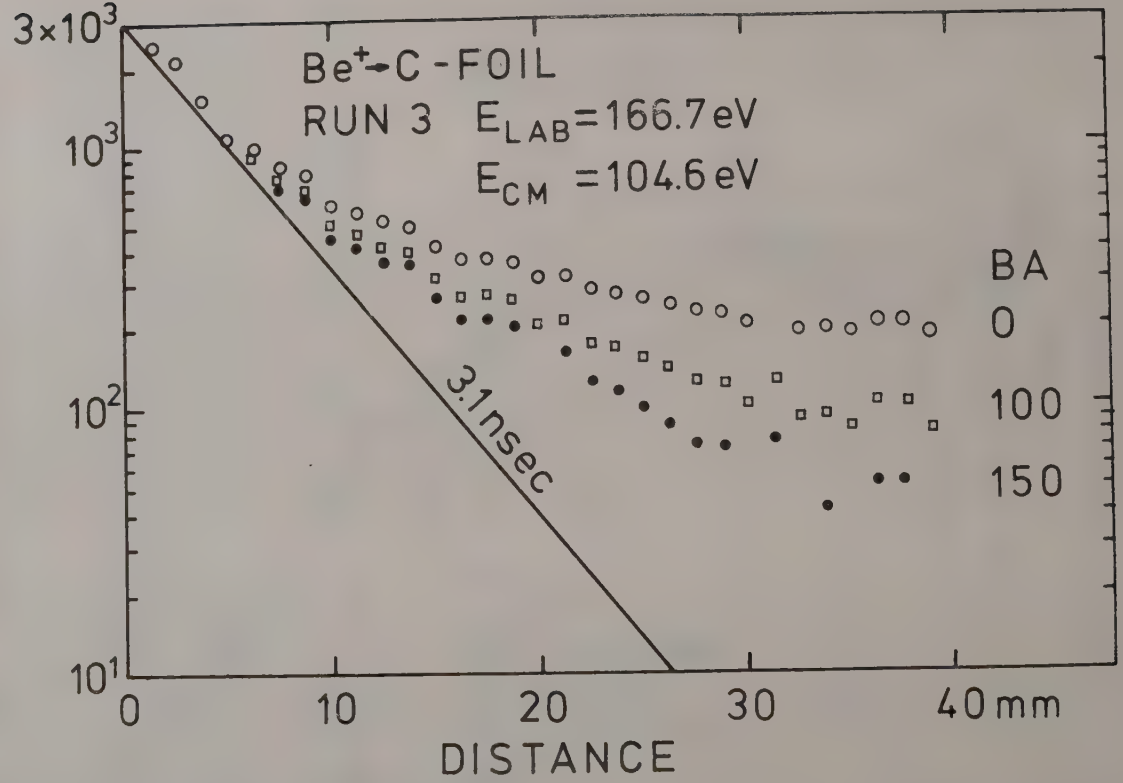

Fig. 76: Semilog plot of counts for peak 3 at $E_{CM} \approx 104.6$ eV. Data are corrected for different number of background counts.

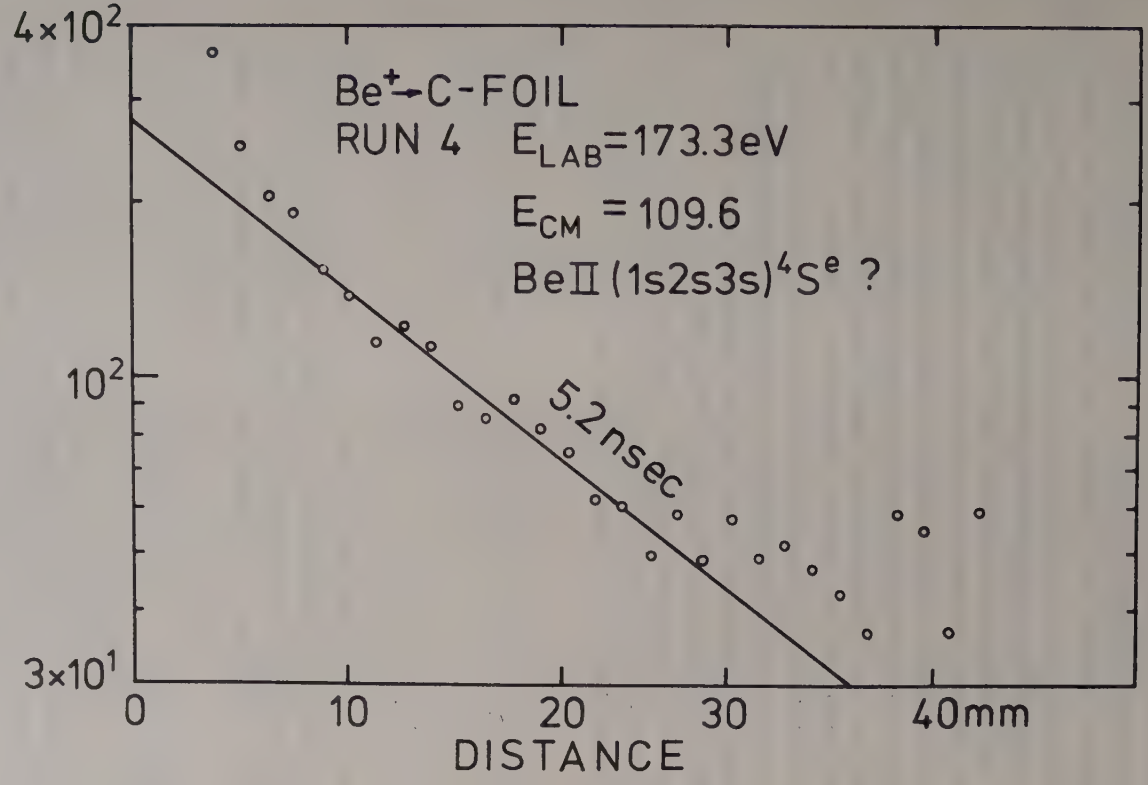

Fig. 77: Semilog plot of counts versus foil position for peak 4 centered at about 109.6 eV.

presence of autoionizing states having lifetimes in the nanosecond region as well as rather long-lived states with mean lifetimes greater than 100 nsec. We further note that metastable autoionizing states with nonzero orbital angular momentum and $J > 1/2$ may be created with M_L alignment. Spin-orbit coupling might transfer some alignment to the adjacent continuum and to the nearby Coulomb autoionizing states having equal parity and J quantum numbers. Such an angular momentum alignment might cause the decay profiles to depart from the single exponential form. In particular zero-field "electron-beats" could arise with modulation frequencies characteristic of the fine-structure and hyperfine-structure separations of the autoionizing state under study. This effect could eventually explain the modulation seen in the decay profile of the $(1s2s2p)\ ^4P^o$ states in BeII (see Fig. 68).

VIII. THEORETICAL CONSIDERATIONS

1. Autoionization Energies

The object of this chapter is threefold: (i) To estimate autoionization energies of core-excited states for $Z \leq 6$ using the quantum defect method (QDM) and the screening method (SM), (ii) to study the effect of electron correlation (CORR) on autoionization energies, and (iii) to present "guiding rules" which may help to select the most probable decay channels for observing highly excited "atomic complexes".

a) Quantum Defect and Screening Method

To account for the observed autoionization structures, theoretical calculations and energy estimates were made. Thus, excitation energies of core-excited states may be extrapolated by the application of the quantum defect and the screening methods.

It is well known that the term energies of hydrogen-like atoms are given by the simple Bohr formula

$$E = E_\infty - R_A Z^2/n^2 \qquad \text{(VIII-1a)}$$

where $R_A = R_\infty/(1+m_e/M)$ is the Rydberg constant ($R_\infty \simeq 13.605$ eV), Z is the nuclear charge and n the principal quantum number. If Z is replaced by the effective nuclear charge Z^* and n by the effective quantum number n^*, one obtains the general formula for Rydberg series of many electron atoms, namely

$$E = E_\infty - R_A (Z^*)^2/(n^*)^2 \qquad \text{(VIII-1b)}$$

Here the integral valued principal quantum number n is retained by writing $n^* = n - \Delta n$, where Δn is the so-called quantum defect and E_∞ can be determined from optically measured energy levels.

More specifically, when the eigenvalues of highly excited states are expressed by Eq. (VIII-1b) then, in most cases, the identities of different series become apparent, since the fractional parts of the n*'s should differ only slightly from one member of a series to another member of the same series.

In Table 15 we present data concerning effective quantum numbers (EQN's) for the (2, nA) ^1S and (2, nA) $^1P^o$ states in BeIII (Lip 75). As discussed in Appendix XV, the (2, nA) ^1S resonances involve strong mixing of the configurations 2sns and 2pnp, corresponding to (2sns + 2pnp) wave functions. It also follows from Appendix XV that the (2, nA) $^1P^o$ states involve strong mixing of the 2snp and the ns2p states, leading to (2snp + ns2p) wave functions. In spite of this complexity the fractional part of the EQN's (see Table 15) is a rather slowly varying function in the BeIII** (2, nA) ^1S and the BeIII** (2, nA) $^1P^o$ levels. That is, once the quantum defect for one member of a series is approximately known, the energy levels of the whole series may be extrapolated using Eq. (VIII-1b).

Observations of the (1s2snd) ^4D and (1s2pnd) $^4D^o$ terms in LiI (Be 72, Be 73) from radiative decays have shown that these states have quantum defects close to zero. Therefore, excitation energies of levels such as (1s2s ^{3}Snd) ^4D with $n \geq 3$ may be estimated assuming zero-order quantum defect. As an example let us compute the BeII (1s2s ^3S 4d) ^4D energy above the BeII ground state. According to Eq. (VIII-1b) the procedure is to calculate

$$E(1s2s4d\ ^4D) \simeq E(1s2s\ ^3S) - 13.605 \times 2^2 / 4^2 \text{ eV}$$

where $E(1s2s\ ^3S) \simeq 136.797$ eV (Sto 75), yielding the result $E(1s2s4d\ ^4D) \simeq 133.40$ eV. We note that this energy value deviates only by 40 meV from 133.36 eV, as deduced from the optical beam-foil measurements of Hontzeas et al. (Hon 73).

Using Eq. (VIII-1b) and assuming zero quantum defects, electron

Table 15: Effective quantum numbers for some resonances in BeIII** (Lip 75)

Classification odd: $\pi = 1$ even: $\pi = 0$ (N, nα) 2S+1,L,π	Effective quantum number n^*	Quantum Defect Δn	Energy below total Ionization E(a.u.)
(2, 2A) 1 0 0	1.71555	0.28445	- 3.52900
(2, 3A) 1 0 0	2.74632	0.25368	- 2.59664
(2, 4A) 1 0 0	3.74409	0.25591	- 2.32101
(2, 5A) 1 0 0	4.74927	0.25073	- 2.19951
(2, 6A) 1 0 0	5.75693	0.24307	- 2.13578
(2, 7A) 1 0 0	6.76452	0.23548	- 2.09834
(2, 8A) 1 0 0	7.76927	0.23073	- 2.07455
(2, 2A) 1 1 1	1.85689	0.14311	- 3.30509
(2, 3A) 1 1 1	2.97365	0.02635	- 2.50890
(2, 4A) 1 1 1	3.98875	0.01125	- 2.28284
(2, 5A) 1 1 1	4.99965	0.00035	- 2.18003
(2, 6A) 1 1 1	6.00756	-0.00756	- 2.12469
(2, 7A) 1 1 1	7.01212	-0.01212	- 2.09152
(2, 8A) 1 1 1	8.01316	-0.01316	- 2.07008

Table footnote: $E\ (a.u.) = -(4)^2/2N^2 - (3)^2/2(n^*)^2$ with N = 2; 1 a.u. ≃ 27.21 eV.

energies (in a.u.; 1 a.u. ≃ 27.21 eV) were estimated for a variety of Li-like, Be-like, B-like and C-like states. The results are tabulated in Appendix VII.

Excitation energies of autoionizing states may be deduced also from known energy levels of core analogous atoms, which exhibit nearly the same energy differences. This approach is called here screening method (SM). A straight forward application of this method is discussed in the following.

In order to compute the LiI (1s3l3l') excitation energies, we

may employ simple screening considerations based upon the assumptions that:

(a) The 1s core electron forms a spherically symmetric potential which partially screens the Li nuclear charge.

(b) The field outside a sphere of radius $0.5292 \times (3^2/3) \times 10^{-8}$ cm = $3a_o$ encloses most of the charge distribution of the 1s electron and is identical to an effective field with residual charge $Z - \sigma \simeq 2$(He-like). Thus, the procedure is to take the eigenvalues of the $3s^2$, 3s3p, $3p^2$, 3s3d, 3p3d, etc. states of HeI** (Lip 75) relative to the LiIII ground state, i.e.

$$E(\text{LiI}\,1s3131') \simeq E(\text{LiIII}\ 1s) - E(\text{HeI}\ 3131')$$

where E(LiIII 1s) ≃ 81.03 eV. In this way good agreement was found between our estimated LiI $1s(3s3p\ ^3P^o)\ ^2P^o$ energy and a UV-absorption line observed by Ederer et al. (Ed 70) (see Table 16). We suggest that the tentative identification of this UV-resonance appearing at 71.16 ± 0.02 eV is right, since the lowest LiI (1s3131') level, namely $1s(3s^2\ ^1S)\ ^2S$ cannot be excited by E1 transitions from the LiI ground state. Furthermore, we assume that the screening constant σ is nearly equal for the differing 1s3131' levels. Hence, we may scale our calculated 1s3131' energy positions to the experimentally deduced resonance. The results of this scaling procedure are given in the last column of Table 16.

Some of the features of the 1s3131' states merit further discussion. Due to strong mutual interaction of the excited 31 and 31' electrons and much weaker perturbation of the 1s and 31 and the 1s and 31' orbitals, the $1s(3131'\ ^{3,1}L)\ ^{4,2}L^{\pi}$ coupling prescription might be appropriate, where the (3131') parent states can be constructed from helium-like eigenstates. In addition, we propose a classification of the 1s3131' states as follows:

$$[1s(3, n\alpha)\ ^{3,1}L]\ ^{4,2}L^{\pi}$$

Table 16: Excitation energies of some LiI (1s3l3l') states above the LiI ($1s^2 2s$) ground state.

Spectroscopic Assignment	Lipsky's Notation	Excitation Energies eV		
		SM [a]	Exp. [b]	Scaled [a]
$1s(3s^2\ ^1S)\ ^2S$	$[1s(3,3A)\ ^1S]^2S$	71.40		71.09
$1s(3s3p\ ^3P^o)\ ^2P^o$	$[1s(3,3A)\ ^3P^o]^2P^o$	71.47	71.16±0.02	71.16
$1s(3p^2\ ^1D)\ ^2D$	$[1s(3,3A)\ ^1D]^2D$	71.67		71.36
$1s(3p^2\ ^3P)\ ^2P$	$[1s(3,3A)\ ^3P]^2P$	71.87		71.56
$1s(3s3p\ ^1P^o)\ ^2P^o$	$[1s(3,3A)\ ^1P^o]^2P^o$	71.91		71.60
$1s(3p3d\ ^1D^o)\ ^2D^o$	$[1s(3,3A)\ ^1D^o]^2D^o$	72.08		71.77
$1s(3s3d\ ^3D)\ ^2D$	$[1s(3,3A)\ ^3D]^2D$	72.16		71.85
$1s(3p3d\ ^3D^o)\ ^2D^o$	$[1s(3,3A)\ ^3D^o]^2D^o$	72.45		72.14

Table footnote: a = this work; b = Ederer et al. (Ed 70).

where the $(3, n\alpha)\ ^{3,1}L$ notation (see Appendix XV) was adopted for the He-like parent states. To summarize, we have calculated LiI 1s3l3l' excitation energies by means of simple screening considerations. The comparison of our $[1s(3, 3A)\ ^3P^o]^2P^o$ energy value with a UV-resonance clearly demonstrates that the extrapolated energy values are reasonable.

b) The Effect of Electron Correlation on Autoionization Energies

From the theoretical point of view the difficulties associated with autoionizing states stem from the fact that they are not true eigenstates of the Hamiltonian (Lip 66, Nic 73). The most common approaches currently used to calculate excitation energies of autoionizing states are variational methods (Lip 66, Hol 67, Junk 73, Lar 75) or perturbational methods (Saf 69, Cha 70, Gol 74, Ke 75).

In order to assign the observed autoionization structures, Fricke (Fri 75, Br 75a) has carried out Hartree-Fock (HF) calculations for two and three electron atoms. Appendix VIII shows results for some energy values as computed with the HF method. However, the HF states do not include any correlation effects, i.e. the HF approximation (central field approximation) represents the interaction of the electrons in an average fashion, neglecting the detailed way in which their motions are correlated (Co 63). According to Sinanoglu electron correlation is defined as the rest of the energy and of the wave function beyond the HF approximation (Sin 68, Sin 70, Beck 74). Therefore, the exact energy may be written as the sum of two parts

$$E = E_{HF} - E_{CORR} \qquad \text{(VII-2)}$$

where E_{HF} corresponds to the HF energy and E_{CORR} is the correlation error.

For Li most of the spectral features have been identified (Be 73, Br 74, Pe 75, Br 75b, Be 75) and corresponding state energies have been given with high accuracy (Zie 75). Therefore, lithium autoionization data may serve to study electron correlation. Theoretical results on LiI (1s2121') energies are listed in Table 17 along with experimental data (Zie 75). We focus first on the LiI ($1s2s^2$) ^2S state, because this state constitutes a good example for strong correlation effects. A comparison of the LiI ($1s2s^2$) HF energy with the corresponding experimental value reveals that the correlation error is $E_{CORR} \simeq -1.7$ eV. To reduce this error Fricke (Fr 75) has extended the HF calculation to a multiconfigurational Hartree-Fock (MCHF) calculation taking into account the mixing of the $1s2s^2$ and $1s2p^2$ configurations. The perturbed ^2S state has the following structure in terms of the $1s2s^2$ and $1s2p^2$ configurations, namely

$$|^2S\rangle \simeq \alpha_1 |1s2s^2\ ^2S\rangle + \alpha_2 |1s2p^2\ ^2S\rangle$$

Table 17: Computed excitation energies above the LiI ($1s^2 2s$) ground state of some prominent lithium states in comparison with experimental data

LiI*	RHF[a] eV	MCRHF[b] eV	MCHF[c] eV	ZEM[d] eV	RZEM[e] eV	RRVM[f] eV	EXP[g] eV
E ($1s2s^2\ ^2S$)	58.05	56.51		56.56	56.54		56.352±0.010
E_{RES} ($1s2s^2\ ^2S$)	- 1.70	- 0.16		- 0.21	- 0.19		0
E ($1s2s2p\ ^4P^o$)	59.14	57.66	57.44	57.84	57.84	57.47	57.385±0.010
E_{RES} ($1s2s2p\ ^4P^o$)	- 1.76	- 0.28	-0.055	- 0.46	- 0.46	-0.085	0
E ($1s2s2p\ ^2_2P^o$)	59.14	59.08*	58.96	58.74	58.73		58.912±0.006
E_{RES} ($1s2s2p\ ^2_2P^o$)	- 0.23	- 0.17	-0.048	+ 0.17	+ 0.18		0
E ($1s2s2p\ ^2_1P^o$)	59.14	61.12*	60.60	60.55	60.54		60.398±0.006
E_{RES} ($1s2s2p\ ^2_1P^o$)	+ 1.26	- 0.72	-0.20	- 0.15	- 0.14		0

Table footnote:
RHF = Relativistic Hartree-Fock; MCRHF = Multiconfigurational Relativistic Hartree-Fock; MCHF = Multiconfigurational Hartree-Fock; ZEM = Z-Expansion Method; RZEM = Relativistic Z-Expansion Method; RRVM = Rayleigh-Ritz Variational Method; EXP = Experimental; a = Fricke (Fri 75); b = Fricke (Fr 75, Br 75 a, Groe 75 a); c = Weiss (Wei 70, Wei 71); d = Safronova et al. (Saf 69); e = Goldsmith (Gol 74); f = Holøien and Geltman (Hol 67, Zie 75); g = Ziem et al. (Zie 75); E_{RES} ≈ Residual Energy.

This procedure leads to a correlation error of about -0.16 eV (see Table 17). The next correction one can make is to add the $(1s2s3s)\ ^2S$ and $(1s2p3p)\ ^2S$ states, so that

$$|^2S\rangle \simeq \alpha_1|1s2s^2\ ^2S\rangle + \alpha_2|1s2p^2\ ^2S\rangle$$

$$+ \alpha_3|1s2s3s\ ^2S\rangle + \alpha_4|1s2p3p\ ^2S\rangle$$

However, it should be emphasized that an infinite number of $(1s^2ns)\ ^2S$ states of identical symmetry but lower energy exist which may destroy the validity of the variational foundation of the HF approximation ("variational collapse"). We further comment that it is not necessary to actually carry out the calculation of autoionization energies in this way. As we will see, several of the excited state calculations that have been done for $Z \leq 6$ will not start with the HF approximation. Hence, it might be convenient to define the risidual energy E_{RES}, which is the difference between any calculated energy E_{CAL} and the exact value of that quantity. Thus, we can write

$$E = E_{CAL} + E_{RES} \qquad \text{(VIII-3)}$$

When considering correlation effects in atoms with inner-shell vacancies an often used method is the configuration interaction (CI) procedure (Wei 61). Weiss has demonstrated that extended CI calculations are capable of yielding rather accurate results fore core-excited states in LiI (Wei 70, Wei 71). However, the complexity of such calculations is often unnecessary, since much simpler CI or Z-expansion methods (Saf 69, Gol 74) are capable of yielding accurate enough results to assign most of the observed autoionization features. For example Safronova et al. (Saf 69) have used a non-relativistic Z-expansion theory combined with second-order non-relativistic expansion of the electron electrostatic interaction. The energy values of three-to-five electron systems ($Z \leq 6$) thus calculated are presented in Appendix IX. A slightly different approach is found in the work of Goldsmith (Gol 74). Goldsmith has computed energy ma-

trix elements for Li-like $1s2s^2$, $1s2p^2$ and 1s2s2p states by means of a relativistic Z-expansion combined with second order calculations of the interelectron electrostatic interaction. LiI, BeII and BIII matrix elements, as deduced from the theory of Goldsmith are given in Appendix X. As can be seen from Table 17 the relativistic and non-relativistic Z-expansion theories give nearly identical correlation errors, i.e. in the case of the LiI $(1s2s^2)\ ^2S$ state, the residual energy is of the order -0.2 eV.

Furthermore Holøien and Geltman (Hol 67) have calculated Li-like quartet states using the Rayleigh-Ritz variational method. In this connection we note that diagonalization of the Hamiltonian with respect to a basis set is equivalent to optimizing the expansion coefficients of the trial function. In addition the Hylleras-Undheim theorem (Hy 30, MacD 33) states that if a trial function is made up of a linear combination of N orthogonal functions, the variational technique will yield N energy levels which are upper bounds to the first N levels of the Hamiltonian. The results of Holøien et al. on LiI, BeII, BIII and CIV are collected in Appendix XI. Moreover, by inspecting the (1s2s2p) $^4P^o$ energies in LiI we find that the values of Holøien et al. and Weiss are in very good agreement with experiment, whereas the Z-expansion methods give an error of 0.46 eV. We also note that the correlation error for the (1s2s2p) HF-energy is -1.76 eV.

In summary the predicted energy positions of the eight lowest LiI (1s2lnl') states are plotted in Fig. 78 along with experimental results (Zie 75). The left side of Fig. 78 indicates the MCRHF energies of Fricke. We note that some of these J levels are reversed from correct order.

Finally, we comment on the LiII (2s2p) $^{3,1}P^o$ resonances. Table 17 shows theoretical results for these states in comparison with experimental data. The details of electron correlation for doubly excited states are discussed in Appendix XV.

Li I (1s2l2l') Energy Values Below Total Ionization

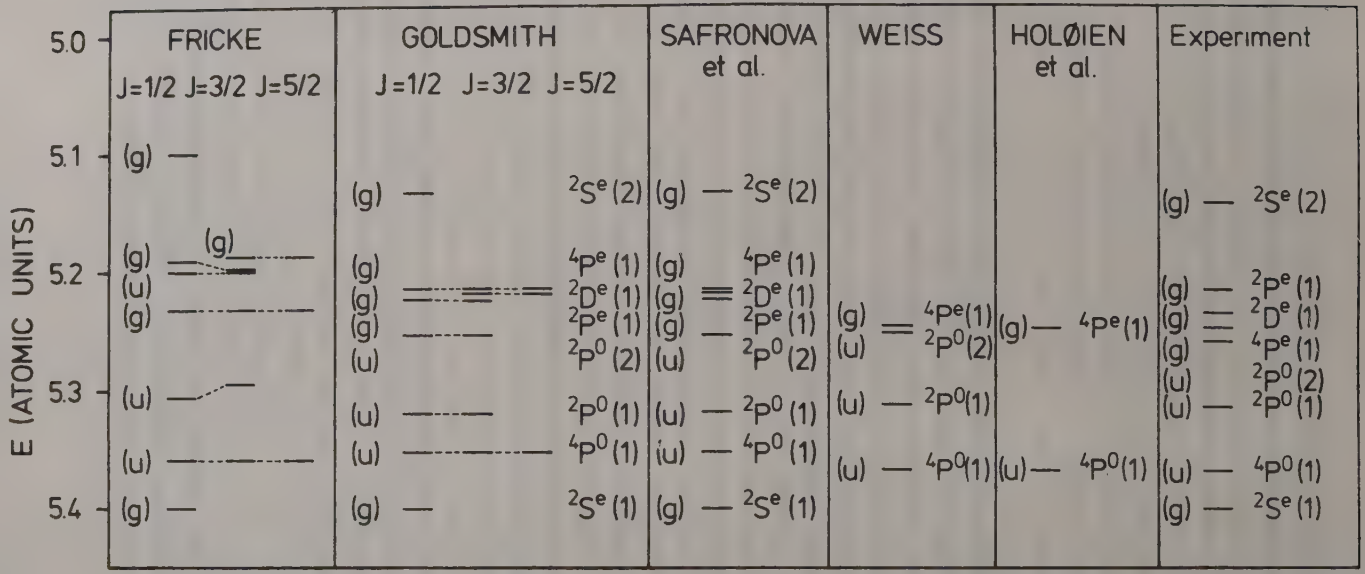

$^2S^e(1) = (1s2s^2)\,^2S^e$ $^4P^e(1) = (1s2p^2)\,^4P^e$ g = gerade (even)

$^4P^0(1) = (1s2s2p)\,^4P^0$ $^2P^e(1) = (1s2p^2)\,^2P^e$ u = ungerade (odd)

$^2P^0(1) = 1s(2s2p^3P)\,^2P^0$ $^2D^e(1) = (1s2p^2)\,^2D^e$ 1 A.U. = 27.21 eV

$^2P^0(2) = 1s(2s2p\,^1P)\,^2P^0$ $^2S^e(2) = (1s2p^2)\,^2S^e$

Fig. 78: Theoretical and experimental term energies in lithium. The energies labeled "Experiment" are deduced from Ziem, Bruch and Stolterfoht (Zie 75). These are compared to the corresponding MCRHF energies (Fri 75, Br 75 a, Groe 75 a) on the left and to the theoretical results of Goldsmith (Gol 74), Safronova et al. (Saf 69), Weiss (Wei 70, Wei 71) and Holøien and Geltman (Hol 67). The levels labeled $^2S^e(1)$ and $^2S^e(2)$, etc. are the first and second eigenvalues, respectively. The eigenvalues are given below total ionization. The purpose here is merely to show the level orderings as obtained in the calculations of these states.

Table 18: Computed LiII (2s2p) $^{3,1}P^o$ excitation energies above the LiII ($1s^2$) ground state in comparison with experimental data

LiII**	RHF[a] eV	DGM[b] eV	CI[c] eV	TDM[d] eV	EXP[e] eV
$E(2s2p\ ^3P^o)$	148.29		146.97	147.08	147.02
$E_{RES}(2s2p\ ^3P^o)$	- 1.27		- 0.05	- 0.06	0
$E(2s2p\ ^1P^o)$	148.29	150.59	150.33	150.54	150.31
$E_{RES}(2s2p\ ^1P^o)$	2.02	- 0.28	- 0.02	- 0.23	0

Table footnote: RHF = Relativistic Hartree-Fock; DGM = Diagonalization Method (Feshbach Method); CI = Configuration Interaction; TDM = Truncated Diagonalization Method; EXP = Experimental; a = Fricke (Fr 75); b = Balashov et al. (Bal 70); c = Chan et al. (Chan 67); d = Lipsky et al. (Br 75b).

In brief, energy positions for doubly and triply excited states may be obtained using the truncated diagonalization method (TDM). Lipsky and coworkers have shown that the Hamiltonian can be separated, e.g.

$$H = H^o + H'$$

where the eigenvalues of H^o correspond to the autoionizing levels, while H' is a perturbation which induces the transitions to the adjacent continuum. This decomposition is accomplished by the application of Feshbach operators P and Q, which are defined as follows

$$Q = \sum_{n=1}^{N} |\Psi_n><\Psi_n| \quad \text{and} \quad P = 1-Q$$

Here the states n>N include continuum eigenstates of H_{NI} as well as the discrete states not included in Q. H^o and H' are given by (Lip 66)

$$H^o = H_{NI} + QH_C\,Q + PH_C\,P$$

$$H' = PH_C\,Q + QH_C\,P$$

where $H_{NI} = \sum_i (p_i^2/2m - Ze^2/r_i)$ and H_C is the Coulomb operator. Thus energies of the autoionizing levels are obtained by diagonalization of H^o in the subspace formed by N antisymmetrized basis functions, which may be constructed from products of Slater-type orbitals. The problem then reduces to that of finding trial functions which do not contain terms corresponding to the allowed channels, i.e. for doubly excited He-like states below the n=2 threshold (see Appendix XV), no hydrogenic 1s states. Eigenvalues of doubly excited states in LiII and triply excited states in LiI are listed in Appendix XV. As can be seen from Table 18, the TDM yields eigenvalues with residual errors close to zero.

2. Autoionization Decay Channels

In this section we present additional rules which are much less restrictive than the selection rules discussed in Chapter II. These rules may be stated as follows:

(1) The autoionization channel requiring the least energy transfer is most likely (Fa 65).

As an example let us consider the autoionizing decay of the [1s(3, 3A) $^3P^o$] $^2P^o$ state (traditional assignment: 1s(3s3p $^3P^o$) $^2P^o$) in LiI, as illustrated in Fig. 79. The overlap of the [1s(3, 3A) $^3P^o$] $^2P^o$ wave function with the (1s2s $^{3,1}S$) εp and the (1s2p $^{3,1}P$) εs continua is presumedly stronger than with the $1s^2$εp continuum, so that the decay channels leading to the LiII (1s2s) $^{3,1}S$ and the LiII (1s2p) $^{3,1}P^o$ final ionic states might be favoured.

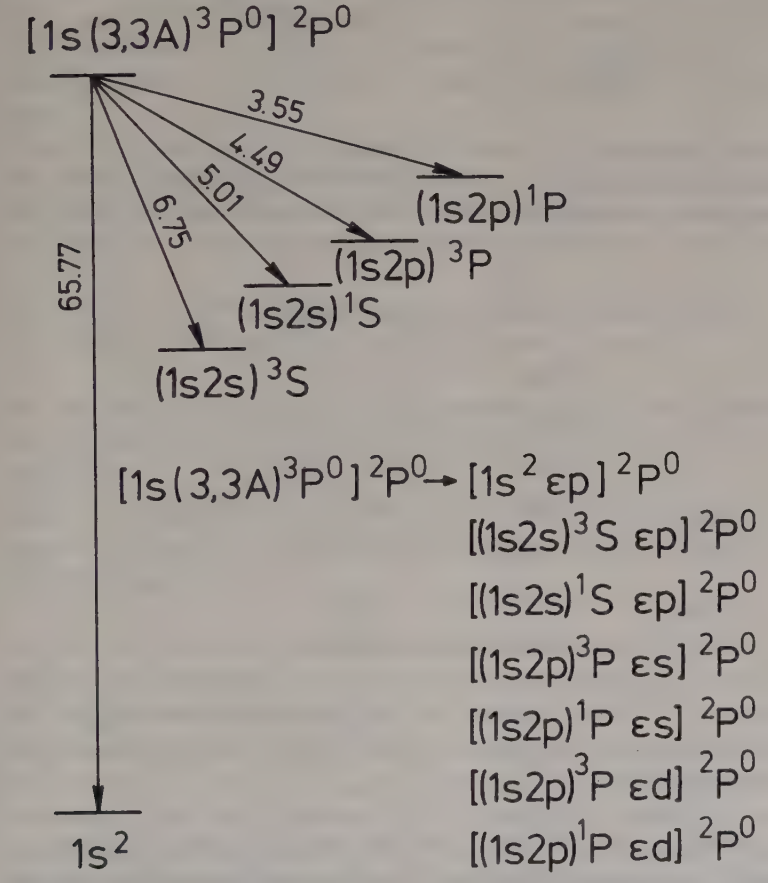

Fig. 79: Competing decay channels of the LiI [1s(3,3A) $^3P^o$] $^2P^o$ term.

For the continuous spectrum the radial wave function R_{El} is characterized by a positive value E of the total energy and by the orbital quantum number l. The asymptotic form of R_{El} is

$$R_{El}(r) \sim (kr)^{-1} \sin(kr - \pi l/2 + \delta_l)$$

where $k = \sqrt{2E}$ and δ_l is the phase-shift for the partial wave l (Beth 57). From this expression it is clear that the density R^2_{El} of the continuum is inversely proportional to E, i.e.

$$R^2_{El} \sim k^{-2} \sim 1/E$$

We can interpret this result as follows: The strength of coupling with the continuum is strongest near threshold ($E \sim 0$). In other words, the branching ratio of the $[1s(3,3A)\ ^3P^o]\ ^2P^o$ state might be roughly proportional to (Mac 74)

$$(V_1^2 + V_2^2 + V_3^2 + V_4^2)/V_5^2 \sim E_{1s^2} / E_{1s2l}$$

where $V_1 = \langle 1s3s3p\ ^2P^o | H | (1s2s\ ^3S)\ \varepsilon p\ ^2P^o \rangle$

$V_2 = \langle 1s3s3p\ ^2P^o | H | (1s2s\ ^1S)\ \varepsilon p\ ^2P^o \rangle$

$V_3 = \langle 1s3s3p\ ^2P^o | H | (1s2p\ ^3P)\ \varepsilon s\ ^2P^o \rangle$

$V_4 = \langle 1s3s3p\ ^2P^o | H | (1s2p\ ^1P)\ \varepsilon s\ ^2P^o \rangle$

$V_5 = \langle 1s3s3p\ ^2P^o | H | (1s^2 \varepsilon p\ ^2P^o \rangle$

and $E_{1s^2} = E(1s3s3p\ ^2P^o) - E(1s^2)$

$E_{1s2l} = E(1s3s3p\ ^2P^o) - E(1s2l)$

From Fig. 79 it is apparent that $E_{1s^2} \simeq 65.8$ eV and $E_{1s2l} \sim 5$ eV. Consequently, the above branching ratio should have a value of magnitude ~13:1.

(2) States for which configurations add (plus states) have shorter lifetimes than those for which configurations subtract (minus states).

As Fano has pointed out, autoionization occurs with substantial probability only in a region where the electrons are close to one another and close to the nucleus (Fa 61, Fa 65). Especially in LiI, the probability of finding both L-shell electrons close to the nucleus is larger for the (1s2snp + 1s2pns) $^{4,2}P^{o}$ states than for the (1s2snp - 1s2pns) $^{4,2}P^{o}$ states (Hol 67). This would then account for the difference in widths of the two series (see Appendix XV).

(3) The states lying lowest in energy for a given spin and angular momentum always belong to the series with the largest width.

(4) Within a Rydberg series states with lower principal quantum number decay faster than those with higher principal number ($1/n^3$-law).

(5) States of high spin and angular momentum quantum numbers are longer-lived than those with low S and L numbers.

(6) Autoionization involving minimum transfer of orbital momentum between electrons is more likely than otherwise (see Appendix XII).

This rule explains why the $1s2s2p^2 \rightarrow 1s^2 2p\varepsilon p$ decay channel may be more probable than the $1s2s2p^2 \rightarrow 1s^2 2s\varepsilon s$ and the $1s2s2p^2 \rightarrow 1s^2 2s\varepsilon d$ channels.

(7) The most probable modes of Auger deexcitation are those transitions in which two electrons are rearranged simultaneously (two-electron transitions).

The probability for three-electron autoionization transitions is much smaller ($\sim 10^{-3}$) than for two-electron autoionization processes. Such many-electron transitions become possible due to many-body effects (Cha 71, Ke 75). Thus, for example, the autoionizing decay from the Be-like $1s2p^3$ configuration to the $1s^2 2p\varepsilon s$ or the $1s^2 2p\varepsilon d$ continua should be more likely than the

competing $1s2p^3 \rightarrow 1s^2 2s\varepsilon p$ or $1s2p^3 \rightarrow 1s^2 2s\varepsilon f$ transitions, where in the latter three p electrons are involved in the rearrangement of the L-shell, namely $2p \rightarrow 1s$, $2p \rightarrow 2s$ and $2p \rightarrow \varepsilon p$ ($2p \rightarrow \varepsilon f$).

(8) States which have no adjacent continuum of equal [L, S, J, π] will be very narrow and must either photodecay or decay via one of the possible L, S, or parity-violating perturbations.

(9) Metastable autoionizing ^4L, ^5L, ^6L and ^7L states other than the lowest lying one of a given term system also decay radiatively to other states of the same multiplicity. The lifetimes of such states will then be determined by the decay rates for both E1 transitions and autoionization.

For instance, let us consider the level diagram for core-excited quartet states in LiI (Fig. 80). It is seen that apart from the (1s2s2p) $^4P^o = {}^4P^o(1)$ state, the higher levels are preferentially depopulated by E1 transitions. Finally, it should be noted that these rules are not independent, but may be interrelated in one way or another. The results of this and previous chapters are now applied to make assignments of Be, B and C autoionization structures. The discussion of the results is given in the following.

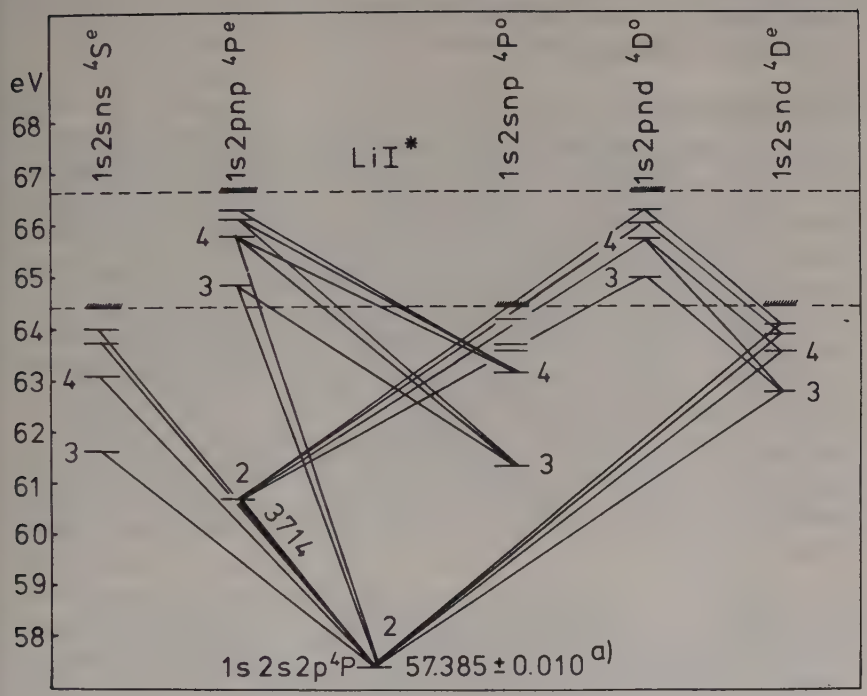

Fig. 80: Term scheme for the LiI quartet system. Some possible optically allowed transitions are indicated. The excitation energy of the lowest quartet-level (1s2s2p) ^4P is taken from reference Ziem et al. (Zie 75).

IX. DISCUSSION OF EXPERIMENTAL RESULTS

1. Lithium Autoionization Lines

a) Prompt Spectra

A specific feature of the prompt lithium spectrum in Fig. 45 is the concentration of peaks into two basic groups. It is assumed that the lower lying group can be attributed to initially core-excited three electron systems in LiI and the higher lying group of peaks to LiII $2lnl'(n \geq 2)$ and LiI $2l2l'nl''$ $(n \geq 2)$ configurations with double K-shell vacancies. A weaker structure at about 100 eV (E_{CM}) is due to doubly excited $3lnl'$ $(n \geq 3)$ states in LiII. We note that triply excited LiI $2l2l'nl''$ $(n \geq 2)$ and doubly excited LiII $3lnl'$ $(n \geq 3)$ states are generally not observed by other physical methods such as UV-absorption (Ed 70), beam-gas excitation (Pe 75) electron impact (Breu 76) and H^+ or He^+ impact on lithium vapour targets (Zie 75, Stol 76).

The prompt lithium spectrum in the energy region from 40 to 70 eV (E_{CM}) is illustrated in Fig. 81. The details of the prompt lithium spectrum have been discussed previously (Br 75b, Appendix XV). The autoionization features in Fig. 81 are due to 1s2snl and 1s2pnl states. The lowest lying peak centered at $E_{CM} \simeq 50.8$ eV is identified as $(1s2s^2)\ ^2S = {}^2S(1)$ (Br 74, Zie 74, Br 75a, Pe 75, Br 75b, Zie 75). This interpretation is consistent with the $^2S(1)$ term energy predicted by Bhatia and Temkin (Bha 76). The peaks around 55 eV may be accounted for by $1s(2s2p\ ^3P^o)\ ^2P^o$, $1s(2s2p\ ^1P^o)\ ^2P^o$, $(1s2s\ ^3S)3p\ ^2P^o$, $(1s2p^2)\ ^2D$ and $(1s2p^2)\ ^2S$ terms. As can be seen the photo-absorption data are in good agreement with the experimental peak energies. The line energies associated with the $(1s2p^2)\ ^2D$ and ^2S states (see Fig. 81) are based on term energies obtained from the $H^+ \rightarrow Li$ and $He^+ \rightarrow Li$ measurements of Ziem et al. (Zie 75). An energy level diagram of the LiI doublet term scheme is exhibited in Fig. 82. We see that the odd and even parity doublet

states lying below the (1s2s) ^3S threshold can only autoionize to the adjacent ($1s^2\varepsilon l$) ^2l continuum.

The high energy portion of the prompt lithium spectrum is displayed in Fig. 83. The main peaks are numbered 1 through 7 in order of increasing energies. At 300 keV beam energy the lithium projectiles emerging from the foil are primarily Li^+ (He-like) with significant numbers of neutral Li atoms present as well. In the energy group between 70 and 90 eV (E_{CM}) two-electron systems arise from LiII 2lnl' ($n \geq 2$) and three-electron systems from LiI 2l2l'nl" ($n \geq 2$) configurations. A comparison to theoretically predicted term energies indicates an overlap of doubly excited states in LiII and triply excited states in LiI. The dominating peaks 1 and 2 (see Fig. 83) are identified as decays of LiII (2, 2A) ^1S, $^3P^o$ and LiII (2, 2A) ^1D, $^1P^o$ states. The energy resolution at 300 keV beam energy was insufficient to resolve the (2, 2A) ^1S - (2, 2A) $^3P^o$ splitting of about 0.75 eV and the (2, 2A) ^1D - (2, 2A) $^1P^o$ separation of about 0.37 eV. A striking result of the spectral analysis is that peak 3 cannot be interpreted in terms of doubly excited states in LiII. Therefore an assignment due to Coulomb autoionization of triply excited states is made. Lowest terms of the possible relevant configurations of LiI*** are

LiI ($2s^2$ 2p) $^2P^o$
LiI ($2s2p^2$) ^4P , ^2D, ^2S, ^2P, and
LiI ($2p^3$) $^4S^o$, $^2D^o$, $^2P^o$.

The energies of some of the known LiI*** terms are tabulated in Table 19. They are based on calculations of Nicolaides (Nic 73, Nic 76) and Ahmed and Lipsky (Ahm 75, Br 75b). A schematic diagram of various $^2P^o$ and ^2S energy levels from triply excited states in LiI (Br 75b, Appendix XV) is indicated in Fig. 84. As can be seen, the lowest term of the 2l2l'nl" configuration with n = 2, ($2s^2$ 2p) $^2P^o$, lies below the (2, 2A) $^1S[(2s^2)\ ^1S]$ threshold. Consequently, the ($2s^2$2p) $^2P^o$ resonance may be associated with the LiII (2, 2A) ^1S series limit. In addition the decay channels of some prominent triply excited

Table 19: Energy values of some triply excited states in LiI

Classification	Energy (eV) above LiI ground state	Energy (eV) above $(1s2s)\ ^3S$
$(2s^22p)\ ^2P^o$	141.7[a] 142.55[b]	77.3[a] 78.14[b]
$(2s2p^2)\ ^2D$	144.9 [a]	80.5 [a]
$(2s2p^2)\ ^2S$	147.39[b]	82.98[b]
$(2p^3)\ ^2P^o$	148.5 [a] 149.21[b]	84.1 [a] 84.79[b]

Table footnote: a = Nicolaides et al. (Nic 73, Nic. 76); b = Lipsky et al. (Ahm 75, Br 75b).

state configurations are collected in Appendix IV, which also lists possible three electron autoionization transitions. We further note that the Li-like $(2p^3)\ ^4S^o$ states are metastable with respect to Coulomb autoionization and should therefore decay mainly radiatively. However, the allowed $(2p^3)\ ^4S^o \rightarrow (1s2p^2)\ ^4P$ transition has never been observed.

A segment of the prompt lithium spectrum around E_{CM} = 80 eV is displayed in Fig. 85 together with the following theoretically predicted peak positions: (i) The helium-like (2, 2A) ^1D, (2, 2A) $^1P^o$, (2, 2B) ^1S and (2, 2A) ^3S levels in LiII (Br 75b, Appendix XV) decaying to the LiIII 1s final ionic state. (ii) The lithium-like $(2s^22p)\ ^2P^o$ and $(2s2p^2)\ ^2D$ levels in LiI (Nic 73, Nic 76) which can leave the residual LiII ion in either the $(1s2s)\ ^{3,1}S$ or $(1s2p)\ ^{3,1}P^o$ states. (iii) The lithium-like $(2s^22p)\ ^2P^o$, $(2s2p^2)\ ^2S$ and $(2p^3)\ ^2P^o$ transition energies, as deduced from the work of Ahmed and Lipsky (Ahm 75, Br 75b, Appendix XV).

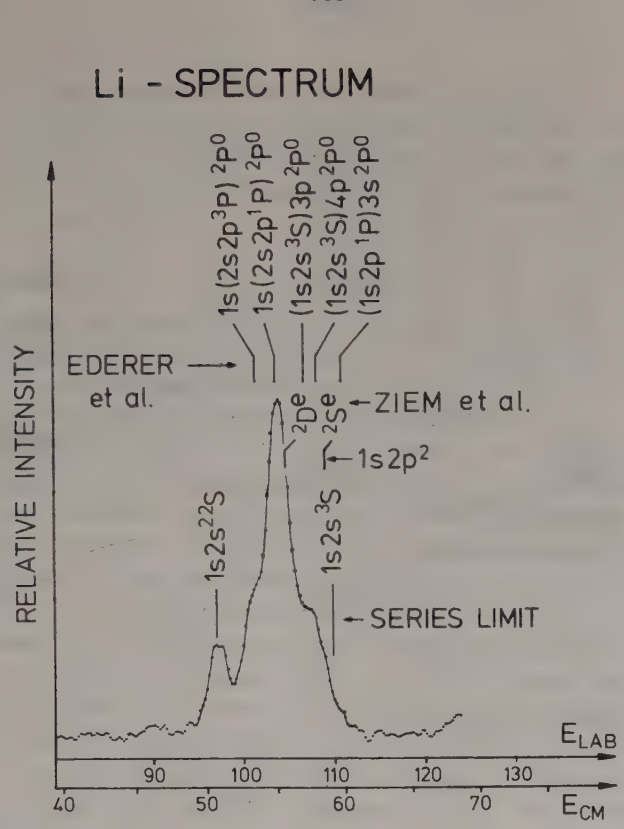

Fig. 81: LiI autoionization spectrum between 40 and 60 eV (background subtracted). The main group of lines which occurs at about 55 eV coincides with $^2P^o$ resonances observed by Ederer et al. (Ed 70). The energy positions of the $(1s2p^2)$ ^2D and ^2S states were deduced from the work of Ziem et al. (Zie 75).

The predicted transition energies as indicated in Fig. 85 are upper limits. Evidently, the structure near 80 eV is best assigned to decays of initial $2s2p^2$ double 1s-hole states. Furthermore, it is assumed that the $(2s^22p)$ $^2P^o$ line energies overlap with transition energies originating from the (2, 2A) ^1D,

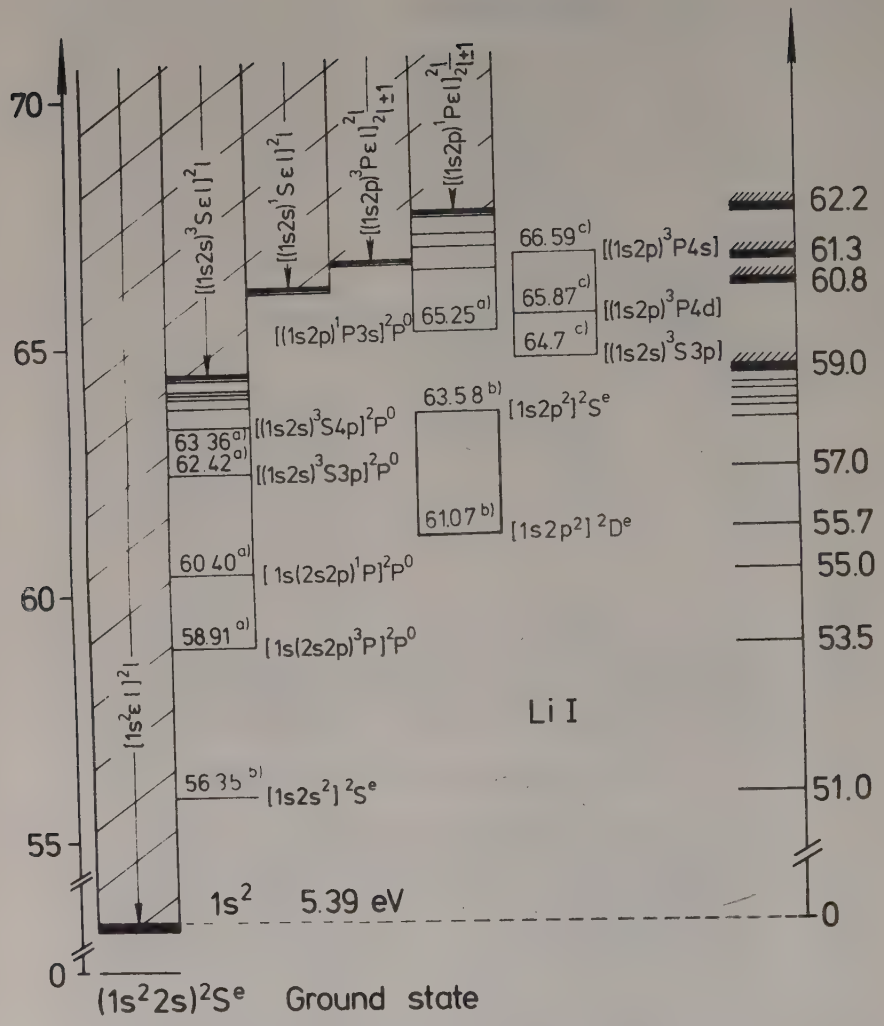

Fig. 82: Energy level diagram for the LiI doublet system. The excitation energies are derived from: (a) Photoabsorption data of Ederer et al. (Ed 70); (b) $H^+ \rightarrow Li$ and $He^+ \rightarrow Li$ data of Ziem et al. (Zie 75); (c) Predicted

excitation energies of Cooper et al. (Co 70). On the right-hand side of the figure we indicate the predicted transition energies of LiI doublet states decaying to the adjacent $(1s^2\varepsilon l)\ ^2l$ continuum. Energies are in eV.

(2, 2A) $^1P^o$ and (2, 2B) ^1S resonances.

The higher lying spectral features (see Fig. 83), namely peaks 4 to 6, coincide with theoretical energy values for LiII 2lnl' states with the nl' electron being excited into the n = 3 shell or higher. Above the n = 2 series limit autoionization lines resulting from the decay of doubly excited two-electron systems are less probable. Nevertheless a small structure (peak labeled 7; see also Fig. 86) occurs in the high energy portion of the prompt lithium spectrum which can be attributed to LiII 3lnl' ($n \geq 3$) initial states decaying to the $1s\varepsilon l$ continuum. According to rule 1 (Chapter VII.2) autoionization of 3lnl' ($n \geq 3$) levels leads principally to the $2l\varepsilon l'$ continua. However, as indicated in Appendix XV a small fraction of these LiII** states can decay also to the 1s final ionic state in LiIII. Such two-electron excitation states converging to the n = 3 series limit have been observed in helium by Madden and Codling (Mad 65) and Dhez and Ederer (Dh 73). An equivalent structure has been seen also in the H^- electron energy spectrum of Risley and coworkers. Due to a large number of closely spaced LiII** levels above the n = 2 threshold the observed features between 100 and 115 eV (see Fig. 86) are assumed to be composite.

To summarize, these measurements give the first experimental observation of LiII 3lnl' states. This observation demonstrates that the collective foil excitation populates such highly excited states with considerable cross section.

In LiI, doubly excited 1snln'l' (n, n' ≥ 3) states containing two electrons in the n = 3 shell or higher may be also formed,

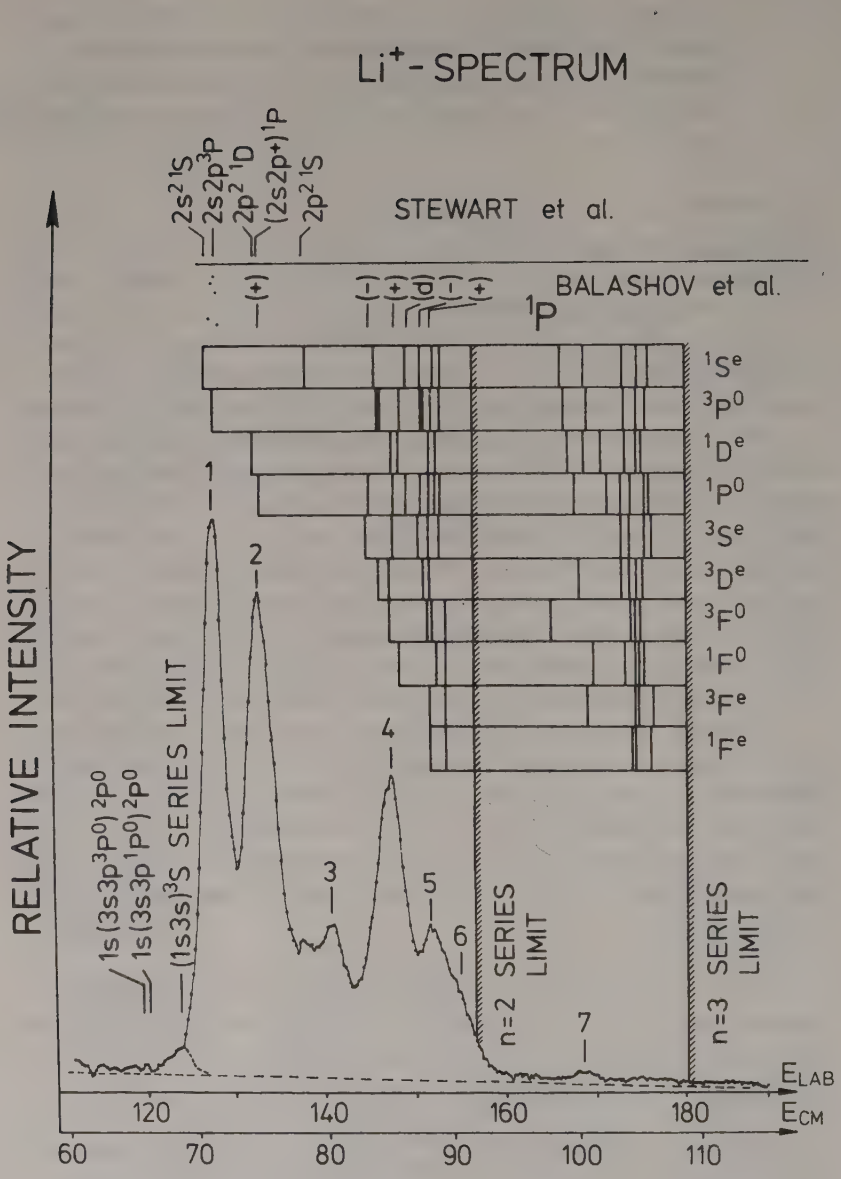
Li+ - SPECTRUM
STEWART et al.
BALASHOV et al.
2s2 1S
2s2p3P
2p2 1D
(2s2p+)1P
2p2 1S
1P
(+)
(-)
(+)
(d)
(-)
(+)
1Se
3P0
1De
1P0
3Se
3De
3F0
1F0
3Fe
1Fe
RELATIVE INTENSITY
1s(3s3p3P0)2P0
1s(3s3p1P0)2P0
(1s3s)3S SERIES LIMIT
1
2
3
4
5
6
7
n=2 SERIES LIMIT
n=3 SERIES LIMIT
ELAB
ECM
120
140
160
180
60
70
80
90
100
110

Fig. 83: Lithium autoionization structures between 60 and 110 eV (background subtracted) in comparison with: (a) The six lowest transition energies of LiII $^1P^o$ resonances deduced from Balashov's calculation (Ba 70), (b) Stewart and coworker's (Chan 67, Per 68) energy values of the configurations $(2s^2)\ ^1S$, $(2s2p)\ ^{1,3}P^o$, and $(2p^2)\ ^1S$, ^1D (traditional classification), (c) the main LiII $^{1,3}S$, $^{1,3}P^o$, $^{1,3}D$, $^{1,3}F^o$ and $^{1,3}F^e$ energy values above the LiIII ground state (Appendix XV).

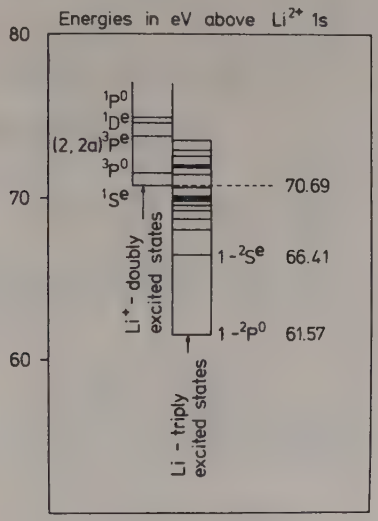

Fig. 84: Schematic diagram of computed energy levels from triply excited states in LiI and doubly excited states in LiII. (1-^2P^o) denotes the $(2s^2 2p)\ ^2P^o$ term and (1-^2S^e) the $(2s2p^2)\ ^2S$ term.

but none have so far been observed in beam-foil spectroscopy. Referring back to Fig. 83, a small structure converging towards the series limit $1s3s\infty l \rightarrow 1s^2\varepsilon l$ at $E_{CM} \simeq 68.8$ eV might presumedly be attributed to autoionizing transitions of LiI $1s3lnl'$ $(n \geq 3)$ configurations decaying to the final ionic

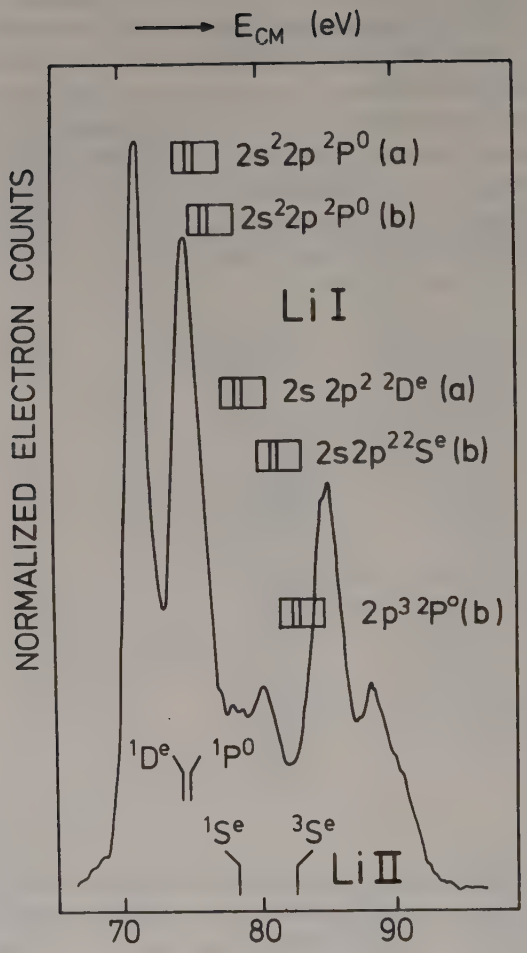

Fig. 85: Segment of the prompt lithium spectrum in comparison with predicted transition energies of (i) the (2, 2A) ^1D, (2, 2A) $^1P^o$, (2, 2B) ^1S and (2, 2A) ^3S states in LiII and (ii) the ($2s^2 2p$) $^2P^o$, ($2s2p^2$) ^2D, ($2s2p^2$) ^2S and ($2p^3$) $^2P^o$ states in LiI. a = Nicolaides et al. (Nic 73, Nic 76); b = Lipsky et al. (Ahm 75, Br 75b).

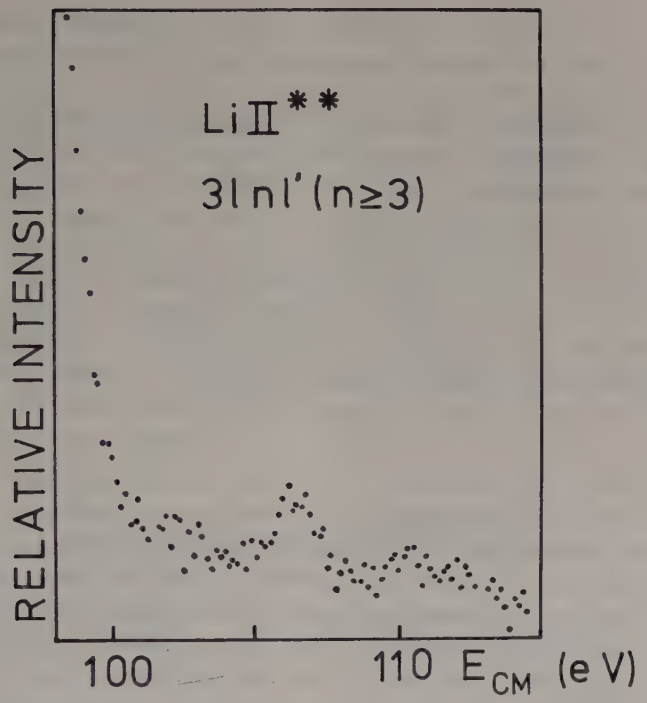

Fig. 86: Segment of the prompt lithium spectrum (peak 7). The spectral features originate from 3lnl' → 1sεl" autoionizing decays in LiII.

state LiII $1s^2$. As already noted in Section VIII.2, doubly excited states such as 1s3lnl' are expected to decay predominantly to the (1s2s) $^{3,1}S\varepsilon l$ and the (1s2p) $^{3,1}P\varepsilon l$ continua, giving rise to low energy autoionization electrons.

We also studied relative cross sections. For this purpose the data were corrected for the dispersion of the analyzer and each characteristic autoionization structure was separately integrated with respect to energy in order to obtain relative cross sections for electron production. Competing radiative

Table 20: Relative cross sections and cross section ratios for $Li^+ \rightarrow$ C-foil excitation ($E_B \simeq 300$ keV; $\theta_L \simeq 42.3^o$)

Atomic System	Number of K-Shell Vacancies	Initial Configurations	Relative Cross Section $\sigma_i / \sum_j^n \sigma_j$	Relative Cross Section const x σ_i
LiI	1	1s2lnl'($n \geq 2$)	25.4 %	1
LiI	1	1s3lnl'($n \geq 3$)	∿8.2 %	∿0.32
LiI	2	2l2l'nl"($n \geq 2$)	∿14.5 %	∿0.57
LiII	2	2l2l'	31.7 %	1.25
LiII	2	2lnl'($n \geq 3$)	∿15.7 %	∿0.62
LiII	2	3lnl'($n \geq 3$)	∿4.5 %	∿0.18

transitions were neglected. The relative cross sections and cross section ratios estimated in this manner are given in Table 20. Since the exact branching ratios associated with the 1s3lnl' ($n \geq 3$) and 3lnl' ($n \geq 3$) initial configurations are not known, the relative cross sections deduced for these states should be regarded only as rough estimates. The decomposition of the higher energy portion into initial 2l2l'nl" ($n \geq 2$), 2l2l' and 2lnl' ($n \geq 3$) components is approximate due to partial overlap of transitions for Li and Li^+ projectiles.

From Table 20 it can be seen that about 66.4 % of the autoionizing systems (e.g. 2l2l'nl" ($n \geq 2$), 2l2l', 2lnl' ($n \geq 3$) and 3lnl' ($n \geq 3$)) are produced with double K-shell vacancies and the rest (33.6 %; 1s2lnl' ($n \geq 2$) and 1s3lnl' ($n \geq 3$)) with single K-shell vacancies. This clearly demonstrates that double K-shell removal appears to be dominant when compared to single K-shell excitation for 300 keV Li^+ impact on thin carbon foils. Another surprising observation is the strong population of triply excited 2l2l'nl" ($n \geq 2$) states in the $Li^+ \rightarrow$ C-foil interaction process. It should be noted that the creation of states like 2l2l'nl" in LiI probably involves two-electron excitation in conjunction with electron pick-up processes. A detailed discussion of foil-excitation mechanism is

given in Chapter X.

It should be noted that ions going through the foil eject many electrons from the foil-surface (see Chapter VII). These "continuous" electrons constitute serious background problems. Recently the electron energy distribution subsequent to ion-foil bombardment has been studied by Pferdekämper et al. (Pfe 75). Our approach here was to integrate the continuous electron energy distribution and the autoionization structures separately with respect to energy. The relative cross sections and cross section ratios for Li^+ → C-foil collisions are compared in Table 21. As can be seen, for one emitted autoionization electron about 58 electrons are produced by direct collision processes.

Table 21: Comparison of the electron-background and autoionization-electron-production cross sections for Li^+ → C-foil collisions ($E_B \simeq 300$ keV; $\Theta_L \simeq 42.3^o$)

Contributing process	Relative Cross Section	
	$\sigma_i / \sum_{j=1}^{2} \sigma_j$	const x σ_i
Electron Background	98.3 %	57.83
Autoionization Spectrum	1.7 %	1

b) Delayed Spectra

Time-delayed beam-foil Auger electron emission spectra have been reported for oxygen and fluorine by Donally et al. (Don 71) and Sellin et al. (Sel 71), for chlorine and argon by Sellin et al. (Sel 72) and Pegg et al. (Pe 72), for aluminum and silicon by Haselton et al. (Ha 75), and for lithium-like N, O and Ne ions by Groeneveld et al. (Groe 75). The electron decay-in-flight of highly excited projectile ions has been measured as a function of distance downstream from an exciter foil and lifetimes of Li-like (1s2s2p) $^4P^o_{5/2}$ states have been

determined. In the course of the work presented here also attempts have been made to measure autoionizing decays of quartet states in LiI. The lowest lying quartet states are:

LiI (1s2sns)	^4S	$n \geq 3$
LiI (1s2snp)	$^4P^o$	$n \geq 2$
LiI (1s2snd)	^4D	$n \geq 3$
LiI (1s2snf)	$^4F^o$	$n \geq 4$
LiI (1s2sng)	^4G	$n \geq 5$
LiI (1s2pnp)	^4P	$n \geq 2$
LiI (1s2pnd)	$^4D^o$	$n \geq 3$
LiI (1s2pnf)	^4F	$n \geq 4$
LiI (1s2png)	^4G	$n \geq 5$

In Fig. 87 we show a level diagram of the most prominent odd and even-parity quartet states in LiI converging to the (1s2s) ^3S and (1s2p) $^3P^o$ series limits. The excitation energies indicated in the level scheme are based on theoretical estimates (Hol 67, Appendix VII) and on optical line identifications (Buch 69, Mar 70, Be 73). To set the energy level diagram for the LiI quartet system on an absolute scale we used the (1s2s2p) $^4P^o = {}^4P^o(1)$ excitation energy as obtained from the work of Ziem, Bruch and Stolterfoht (Zie 75). From Table 22 we see that the fine structure splittings within the LiI (1s2s2p) $^4P^o$ term are of the order $\sim 10^{-4}$ eV while the doublet quartet splitting due to the electrostatic interaction is of the order of ~ 1 eV (see Table 16), so that the LS coupling scheme can be applied. However, for the (1s2s2p) ^4P terms in LiI the hyperfine splittings are of comparable order as the fine structure separations (see Table 22). In this case different J states are strongly mixed (breakdown of IJ coupling) producing different lifetimes for the different hyperfine components F (see Appendix XIII and XIV). The nuclear spins, the magnetic dipole and electric quadrupole moments for atoms with $Z \leq 6$ are listed in Table 23. It is seen that

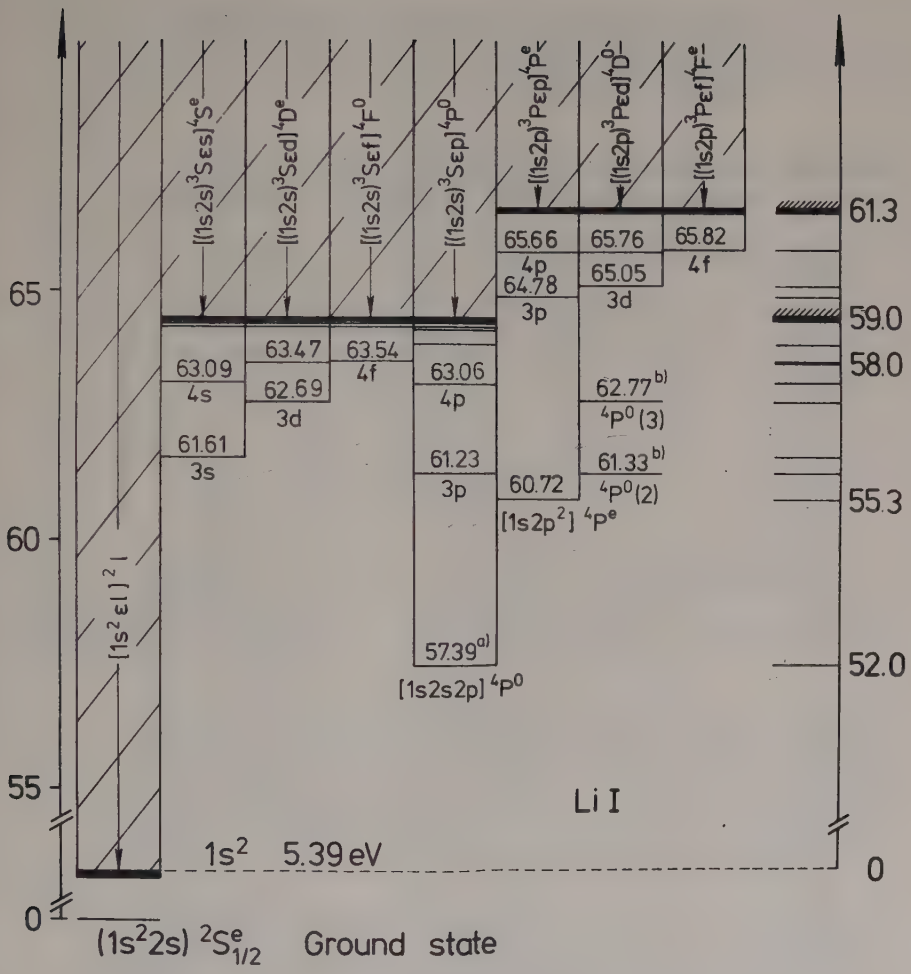

Fig. 87: Energy level diagram for the LiI quartet system. The excitation energies are derived from: (a) $He^+ \rightarrow Li$ data of Ziem et al. (Zie 75); (b) Calculations of Holøien and Geltman (Hol 67). The energies of the unlabeled levels have been estimated using the quantum defect method. On the right-hand side of the figure we in-

dicate the predicted transition energies of LiI quartet states decaying to the adjacent $(1s^2\varepsilon l)^2 l$ continuum. Energies are in eV.

Table 22: Fine structure splitting and fine and hyperfine constants for $(1s2s2p)\ ^4P^o$ state of lithium (in mK)

Quantity	Experiment mK	Theory mK
$E_{5/2} - E_{1/2}$	-1724.70[a]	-2610[b]
$E_{5/2} - E_{3/2}$	+ 997.34[a]	+ 575[b]
C_{SO}	- 154.47[a]	- 325[b]
C_{SS}	+ 184.47[a]	- 185[b]
$a_C(^7Li)$	+ 172.09[a]	+ 172[b]
$a_C(^6Li)$	+ 65.16[a]	+ 65[b]

Table footnote: a = Levitt et al. (Lev 71); b = Manson (Ma 71); 1 mK ≃ 1.23985×10^{-7} eV.

apart from ^{12}C projectiles, which have nuclear spin I = 0, hyperfine mixing should influence the autoionizing decay of long-lived metastable states; but, no such hyperfine effects have been observed so far in the decays of Li-like $(1s2s2p)\ ^4P^o$ ions (Fel 68, Dmi 72, Pe 73, Sel 73).

Fig. 87 shows a delayed spectrum taken at a time delay of about 3.7 nsec. The prominent peaks in the delayed Li spectrum can be identified as transitions from metastable autoionizing quartet states where the spins of all three electrons are aligned. The lowest energy peak in Fig. 87 is attributed to the initial $^4P^o(1)$ state in LiI. This quartet state is metastable against both Coulomb autoionization and electric dipole transitions, whereas the energetically higher lying quartet states are depleted mainly by allowed radiative decays to lower lying quartet states. Due to the differential metastability

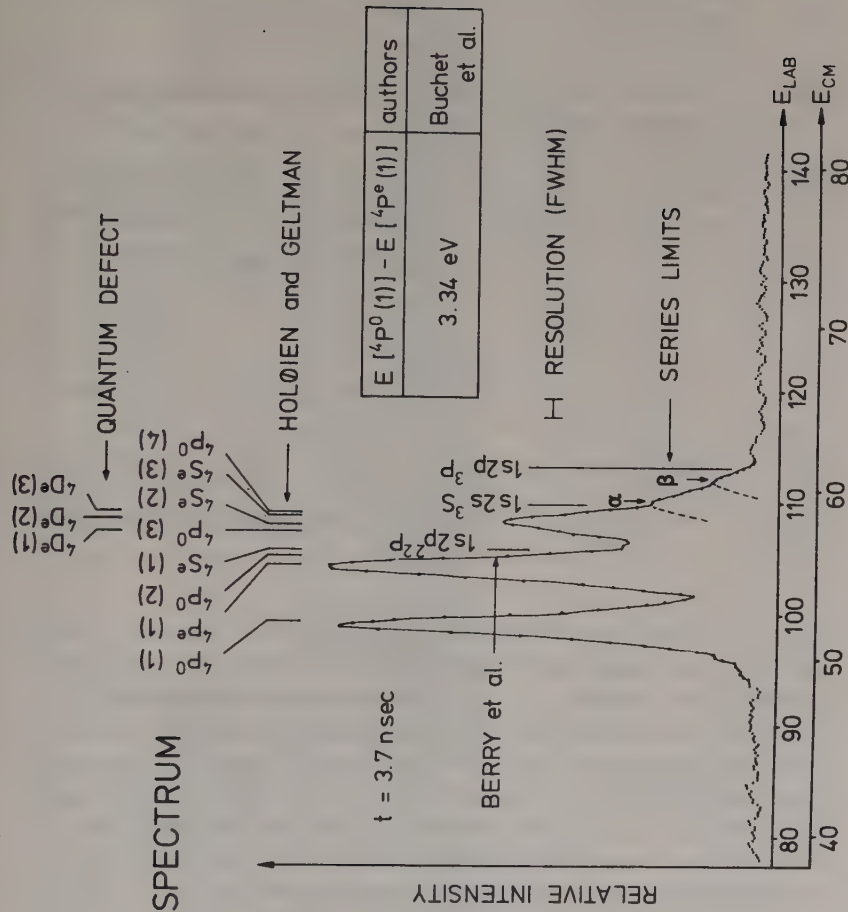
Li - SPECTRUM
QUANTUM DEFECT
HOLØIEN and GELTMAN
H RESOLUTION (FWHM)
SERIES LIMITS
BERRY et al.
t = 3.7 n sec
RELATIVE INTENSITY
E [4P0 (1)] - E [4Pe (1)]
3.34 eV
authors
Buchet et al.
1s2p 3P
1s2s 3S
1s2p2 2P
α
β
ELAB
ECM

Fig. 88: Electron decay-in-flight spectrum from metastable autoionizing quartet states in ^{7}LiI. The spectrum refers to a time delay of about 3.7 nsec. Energies are in eV.

Table 23: Nuclear spins, magnetic dipole and quadrupole moments for $Z \leq 6$ (Mat 68)

Nuclear Charge Z	Atom	Nuclear Spin I	Dipole Moment (nuclear magnetons)	Quadrupole Moment (barns)
3	^{6}Li	1	+0.82201	-0.008
3	^{7}Li	3/2	+3.25629	-0.03 -0.045
4	^{9}Be	3/2	-1.17744	+0.049
5	^{10}B	3	+1.8oo68	+0.0745
5	^{11}B	3/2	+2.68864	+0.0372
5	^{12}B	1	+1.oo3	
6	^{12}C	o	o	

within the ^{7}LiI hyperfine structure levels (see Appendix XIII and XIV) the lowest lying peak in the delayed spectrum is expected to be composed of many components having different lifetimes. It is assumed that the second strong line in Fig. 88 can be attributed mainly to the initial $(1s2p^2)\ ^4P$ state. This interpretation is justified by the agreement of the energy separation of the two strongest peaks in this experiment (3.33 eV) as compared to the optical $^4P(1) - {}^4P^o(1)$ transition energy of 3.34 eV (Buch 69, Mar 70, Be 73).

The third strong peak at about 1 eV below the (1s2s) ^3S series limit is an admixture of several autoionization lines. Above the (1s2s) ^3S threshold, two unresolved peaks appear (indicated by label α and β), which might originate from $[(1s2p)\ {}^3P^o\ np]\ {}^4P$ $(n \geq 3)$, $[(1s2p)\ {}^3P^o\ nd]\ {}^4D^o$ $(n \geq 3)$ and $[(1s2p)\ {}^3P^o\ nf]\ {}^4F$ $(n \geq 4)$ levels.

Li II**
(eV)
170
160
n=2
(2,nA)1S^e BROAD
(2,nB)1S^e NARROW
(2,nA)1P^o BROAD
(2,nB)1P^o NARROW
(2,nC)1P^o VERY NARROW
(2,nA)1P^e METASTABLE
(2,nA)1D^o METASTABLE
(2,nA)1D^e NARROW ?
(2,nB)1D^e BROAD ?
(2,nC)1D^e VERY NARROW
(2,nA)1F^o
(2,nB)1F^o
(2,nC)1F^o
(2,nA)1F^e METASTABLE
(2,nA)3F^e METASTABLE
(2,nC)3F^o
(2,nB)3F^o
(2,nA)3F^o
(2,nC)3D^e METASTABLE
(2,nB)3D^e BROAD
(2,nA)3D^e NARROW ?
(2,nA)3D^o METASTABLE
(2,nA)3P^e METASTABLE
(2,nC)3P^o VERY NARROW
(2,nB)3P^o NARROW
(2,nA)3P^o BROAD
(2,nB)3S^e VERY NARROW
(2,nA)3S^e NARROW ?

Fig. 89: Energy level diagram for doubly excited states in LiII below the n = 2 ionization threshold. Excitation energies are measured from the LiI ($1s^2 2s$) ground state. Series labeled "broad" are strongly autoionizing. Series labeled "metastable" should decay preferentially via E1 transitions.

Another metastable autoionizing state would be ($1s2p^2$) ^2P which decays mainly by photon emission to the low-lying ($1s^2 2p$) $^2P^o$ level in about 0.015 nsec (Be 73). Finally, no autoionization lines which could be attributed to metastable LiII** states were found at 300 keV beam energy. An energy level diagram for doubly excited states in LiII below the n = 2 ionization limit is displayed in Fig. 89. The series labeled "metastable" (see Appendix XV) should decay preferentially via E1 transitions. These allowed optical transitions are much too fast for the emitting projectile states to live for several nanoseconds flight time.

2. Beryllium Autoionization Lines

a) Prompt Spectra

Recently we have reported the first measurements of Auger electron ejection from energetic beryllium ions excited by thin carbon foils (Br 74, Br 75a, Br 76a; see also Fig. 90). Complete spectroscopic line-identification was not possible because of insufficient term energy calculations of three-to-five electron systems. However with the help of theoretical estimates of transition energies we are now able to interpret many of the observed structures.

The prompt Be spectrum as plotted in the center-of-mass frame is displayed in Fig. 91. Here several features can be noted; first the strong excitation of core-excited states in BeII, secondly the structures corresponding to autoionization of

four-electron systems in BeI, and lastly the occurence of autoionization lines originating from doubly excited states in BeIII and triply excited states in BeII.

The lowest lying (energetically) and most intense lines in Fig. 91 can be assigned mainly to initial three-electron beryllium ions. Comparison with theoretically predicted transition energies shows that the peak group between 90 and 110 eV (E_{CM}) is dominated by 1s2l2l' configurations in BeII such as $1s2s^2$, 1s2s2p and $1s2p^2$. The first peak in the Be spectrum (at 96 eV) corresponds to the $(1s2s^2)\ ^2S \rightarrow (1s^2\varepsilon s)\ ^2S$ Auger transition in BeII (Br 75a). The next higher peaks can be identified as due to the initial $(1s2s2p)\ ^2_2P^o$ and $(1s2s2p)\ ^2_1P^o$. The strongest line in the spectrum is due to the $(1s2p^2)\ ^2D \rightarrow (1s^2\varepsilon d)\ ^2D$ Auger decay.

Beryllium is of particular interest since it is the simplest atomic system where highly excited four-electron states are possible. It is to be expected that four-electron states such as $(1s2s^22p)\ ^{3,1}P^o$ will be present in the region of the dominating 1s2l2l' line structure. The peaks labeled 1 and 2 may be attributed to initial three-, and four-electron systems. Thus peak 1 is assumed to be composed of the decays

$$(1s2p^2)\ ^2S \rightarrow (1s^2\varepsilon s)\ ^2S$$

$$(1s2s\ ^3S3l) \rightarrow (1s^2\varepsilon l)$$

$$(1s2s2p^2) \rightarrow (1s^22s\varepsilon s(\varepsilon d))$$

$$(1s2s2p^2) \rightarrow (1s^22p\varepsilon p) \quad \text{and}$$

$$(1s2p^3) \rightarrow (1s^22p\varepsilon s(\varepsilon d)).$$

The BeII $(1s2p^2)\ ^2S$ Auger decay might be responsible for the shoulder on the low energy side of peak 1. We further note that autoionizing levels may often decay to different final ionic states, giving rise to several lines of different intensities. For example, the BeI $(1s2s2p^2)$ states can decay to the $1s^22p$ and $1s^22s$ final states in BeII, leading to a double peak structure with an energy spacing of 3.96 eV; and state

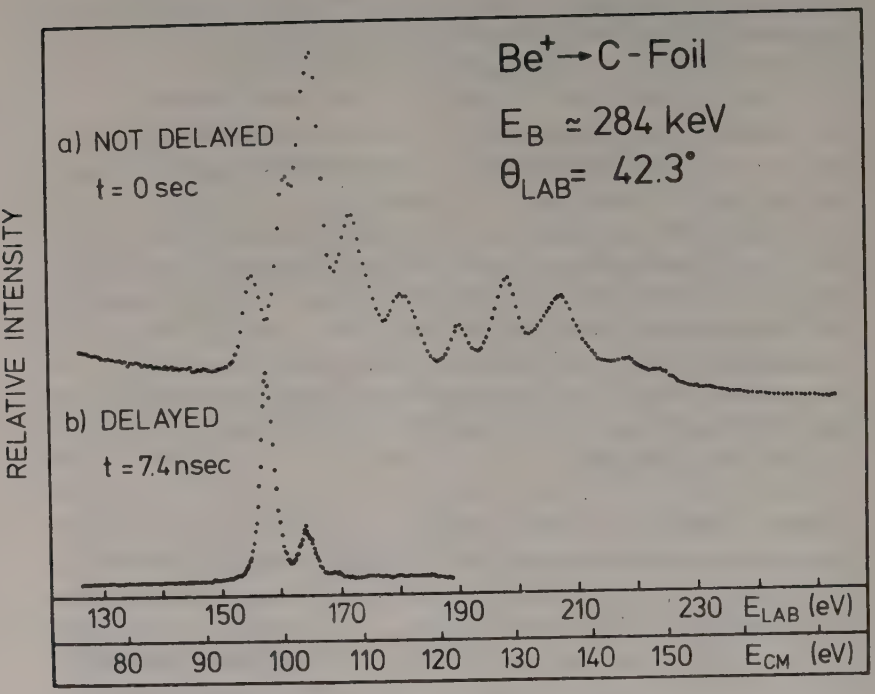

Fig. 90: Electron decay-in-flight spectra from autoionizing states of 284 keV beryllium ions plotted in the laboratory and in the rest frame of the emitting projectiles. The upper spectrum refers to "foil-zero" position and the lower spectrum to a time delay of about 7.4 nsec, respectively.

configurations like $1s2p^3$ are expected to decay dominantly to the $1s^2 2p\varepsilon s$ or $1s^2 2p\varepsilon d$ continua (see Section VIII.2: rule 7).

At $E_{CM} \simeq 118.6$ eV (corresponding to the BeII (1s2s) $^3S\infty l \rightarrow 1s^2\varepsilon l$ series limit) the drop of intensity indicates that many of the Li-like states observed do converge to this limit. Above 118.6 eV, lines resulting from core-excited three-electron

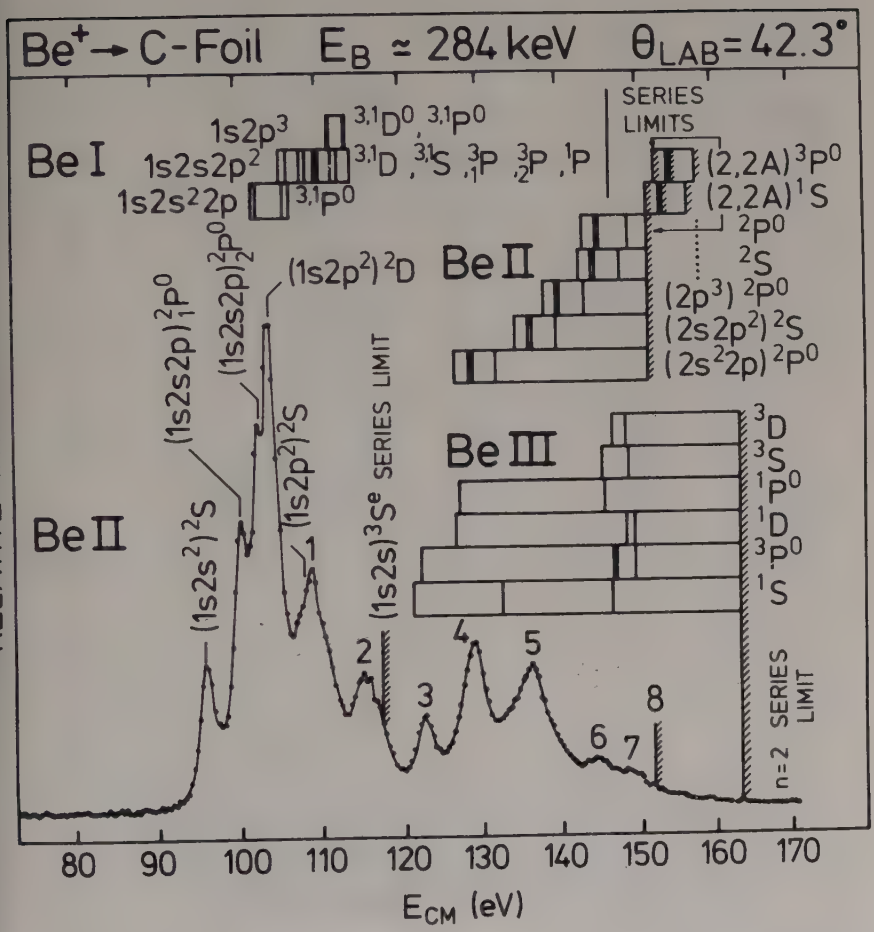

Fig. 91: Prompt beryllium spectrum between 80 and 170 eV (E_{CM}) for 300 keV Be^+ + C-foil collisions.

systems are less likely. Hence, the higher lying autoionization features may arise principally from state configurations of the type BeIII 2lnl' ($n \geq 2$) and BeII 2l2l'nl" ($n \geq 2$) having

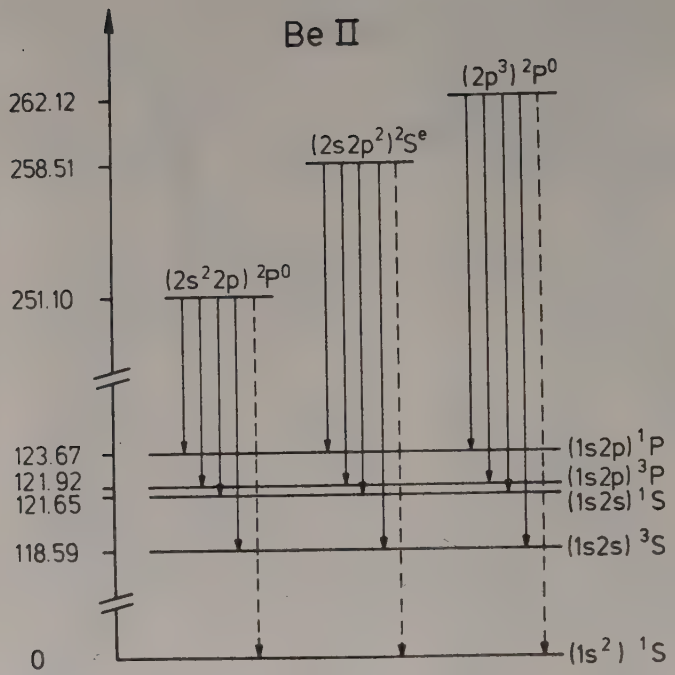

Fig. 92: Decay scheme for some triply excited states in BeII. The allowed decays are designated by the solid lines. The three electron autoionization transitions are designated by the dashed lines. The energies are from the work of Ahmed and Lipsky (Ahm 75).

two K-shell vacancies. The prompt Be spectrum above 118.6 eV is compared with; (a) predicted transition energies associated with the lowest doubly excited states in BeIII (Lip 75), and (b) theoretical line energies for some triply excited states in BeII as deduced from Ahmed and Lipsky's calculation (Ahm 75). For further clarity, the decay of three-electron systems with double K-shell vacancies was studied more closely. Pre-

viously, Bruch et al. (Br 75b, Appendix XV) have shown that the $(2s^2 2p)\ ^2P^o$ and $(2s2p^2)\ ^2S$ terms have allowed Auger decay channels leading to the (1s2s) $^{3,1}S\varepsilon l$ and (1s2p) $^{3,1}P^o\varepsilon l'$ continua. The decay scheme for the $(2s^2 2p)\ ^2P^o$, $(2s2p^2)\ ^2S$ and $(2p^3)\ ^2P^o$ three-electron systems of beryllium is illustrated in Fig. 92. The energy levels are those given by the TDM calculation of Ahmed and Lipsky (Ahm 75). The decay of the most probable transitions are indicated by the solid lines. The decay of $(2s^2 2p)\ ^2P^o$, $(2s2p^2)\ ^2S$ and $(2p^3)\ ^2P^o$ states to the $1s^2$ final ionic state are indicated by dashed lines. Such three electron autoionization transitions may occur, when two L-electrons fill simultaneously the two K-shell vacancies and the energy is transferred to a third L-shell electron. The intensities of three electron autoionization lines should represent only a small fraction ($\sim 10^{-3}$) of the "normal" lines (Af 75, Ke 76).

We identify peak 3 in Fig. 91 as due to decay from (2, 2A) ^1S and (2, 2A) $^3P^o$ helium-like states in BeIII. The most outstanding result of the spectrum is the strong population of triply excited states in the $Be^+ \rightarrow$ C-foil excitation process. These are the prominent peaks (indicated by label 4 and 5) in the high energy portion of the prompt spectrum, which are attributed mainly to $2s^2 2p$, $2s2p^2$ and $2p^3$ configurations in BeII. In the energy region near 129 eV (peak 4) decays from helium-like states overlap with autoionization transitions from lithium-like states. The shoulder on the low energy side of peak 4 is expected to occur from decays of (2, 2A) ^1D and (2, 2A) $^1P^o$ levels. The proximity of the maximum of peak 4 to the predicted $(2s^2 2p)\ ^2P^o$ line energies, suggests that this structure is dominated by initial $(2s^2 2p)\ ^2P^o$ states in BeII. At about 136.5 eV another broad structure can be seen (peak 5). We identify this peak as due to decay from $(2s2p^2)$ configurations in BeII. This interpretation is consistent with the predicted $(2s2p^2)\ ^2S$ transition energies. Finally, the high energy shoulder of peak 5 may be identified with Li-like $(2p^3)$ beryllium ions.

The highest energy group of lines in the prompt beryllium

spectrum (peak 6 and 7) supposedly arise from 2lnl' and 2121'nl" configurations with a double ionized K-shell and with one electron being excited into the n = 3 shell or higher. The lowest series limit for triply excited systems is indicated by the label 8. In Fig. 91 we also show the BeIII $2l\infty l' \rightarrow 1s\varepsilon l''$ (n = 2) series limit at which energy there appears a drop-off in intensity. Between the n = 2 limit and the limit labeled 8 additional series limits may arise from three-electron systems in BeII (see upper part of Fig. 91).

The prominent spectral lines in the prompt Be spectrum are in agreement with theory. Line broadening due to the finite acceptance of the angular spread of the analyzer, energy straggling and angle scattering make a total identification of the foil-excited Be spectrum impossible. It is expected that many more lines corresponding to a great number of possible transitions remain unresolved.

Table 24: Relative excitation cross sections for $Be^+ \rightarrow$ C-foil bombardment ($E_B \simeq 300$ keV; $\Theta_L \simeq 42.3^o$)

Atomic System	Number of K-shell Vacancies	Initial Configurations (n, n', n" ≥ 2)	Relative Cross Section $\sigma_i / \sum_{j=1}^{n} \sigma$	const x σ_i
BeI BeII	1 1	1snln'l'n"l" 1snln'l'	69.0 %	1
BeIII	2	2121'	10.2 %	0.15
BeIII	2	2lnl' (n ≥ 3)	6 %	0.09
BeIII	2	2lnl' (n ≥ 2)	16.2 %	0.23
BeI BeII	2 2	2lnl'n'l"n"l"' 2ln'l"n"l"'	14.8 %	0.21

We studied also relative intensities of the Be autoionization lines. Intensity ratios and relative cross sections are given in Table 24. From the prompt Be spectrum it is shown that the

amount of initially core-excited states with single K-shell vacancies is about 69 % and with double K-shell vacancies about 31 %. More specifically, for the helium-like BeIII lines which lie partially under the lithium-like BeII lines we estimated a fraction of about 16.2 % (e.g. 10.2 % BeIII 2l2l' plus 6 % BeIII 2lnl' levels with $n \geq 3$). From Table 24 we see that the prompt Be spectrum contains about 14.5 % autoionization lines arising from triply excited $2s^2 2p$, $2s2p^2$ and $2p^3$ states. Furthermore, it is expected that initial BeI 2lnl'n'l"n"l"' ($n, n', n" \geq 2$) states with double K-shell vacancies cascade through the Li-like states by Auger emission. Thus four-electron systems such as $2s^2 2p^2$, $2s2p^3$ and $2p^4$ in BeI can make significant contributions to core-excited states in BeII. The reorganization of 2lnl'n'l"n"l"' states may occur in two stages, as follows: (1) Auger transitions populating an intermediate state, for example the BeI ($2s^2 2p^2$) state may decay in a first step to the $1s2s^2$ state in BeII, namely BeI ($2s^2 2p^2$) → BeII ($1s2s^2$) + εs(εd). (2) The intermediate excited state subsequently decays by Auger effect. As an example the "cascade-fed" ($1s2s^2$) state in BeII decays via Auger transition to the $1s^2$ final ionic state in BeIII, i.e. BeII ($1s2s^2$) → BeIII ($1s^2$) + εs. Allowed Auger decays of four-electron Be atoms following the creation of double K-vacancies are listed in Table 25.

Table 25: Cascade scheme for decay of double K-vacancies in beryllium

BeI		BeII		BeIII
$2s^2 2p^2$	→	$1s2s^2$	→	$1s^2$
$2s^2 2p^2$	→	1s2s2p	→	$1s^2$
$2s^2 2p^2$	→	$1s2p^2$	→	$1s^2$
$2s2p^3$	→	1s2s2p	→	$1s^2$
$2s2p^3$	→	$1s2p^2$	→	$1s^2$
$2p^4$	→	$1s2p^2$	→	$1s^2$

An alternative decay mode of four-electron systems containing a double ionized core would be a three electron autoionization transition such as

$$\text{BeI } (2s^2 2p^2) \rightarrow \text{BeII } (1s^2 2p) + \varepsilon p$$

where the final BeII $(1s^2 2p)$ state in turn decays ratiatively to the BeII $(1s^2 2s)$ ground state. A cascade scheme for the de-excitation of the $2s^2 2p^2$, $2s2p^3$ and $2p^4$ states via three electron transitions and subsequent optical decays is given in Table 26.

Table 26: Cascade scheme for three electron autoionization transitions in BeI

BeI		BeII		BeII
$2s^2 2p^2$	→	$1s^2 2s$		
$2s^2 2p^2$	→	$1s^2 2p^*$	→	$1s^2 2s$
$2s2p^3$	→	$1s^2 2s$		
$2s2p^3$	→	$1s^2 2p^*$	→	$1s^2 2s$
$2p^4$	→	$1s^2 2p^*$	→	$1s^2 2s$

All transitions listed in this table are three electron Auger processes except those accompanied by an asterisk (*) which decay by dipole radiation. It should be mentioned that three electron autoionization processes are expected to occur with low probability.

In conclusion, we note that the observed population of 1s2lnl' ($n \geq 2$) states in BeII is presumedly increased due to Auger cascades as originating from 2lnl'n'l"n"l"' (n, n', n" ≥ 2) levels in BeI. The Auger decay of four-electron systems having two K-shell vacancies, could be confirmed by coincidence experiments.

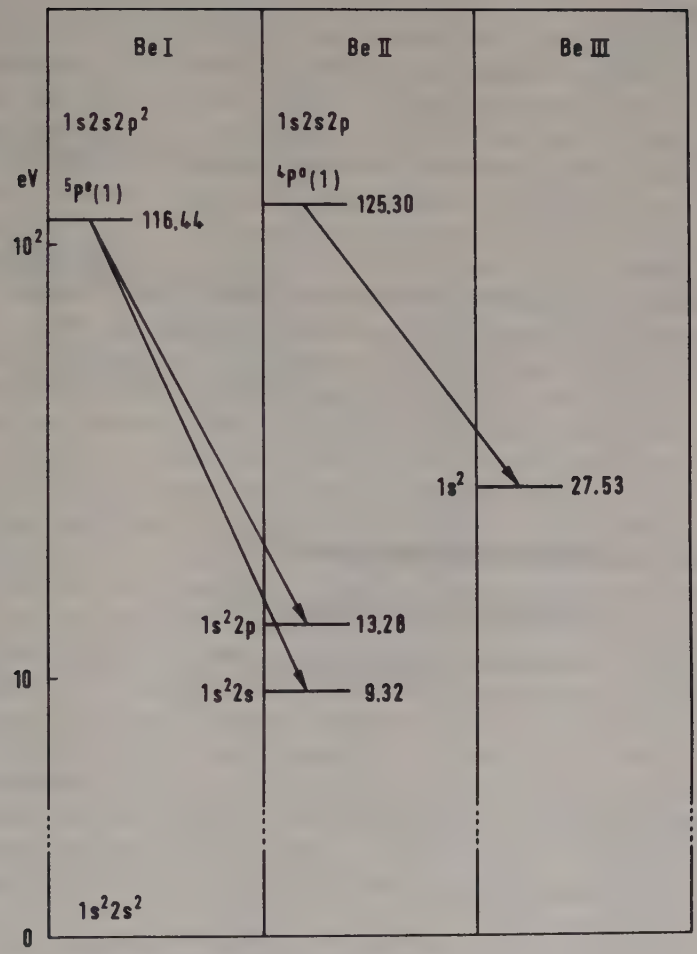

Fig. 93: Partial energy level diagram illustrating the autoionizing decay of the $(1s2s2p^2)\ ^5P$ term in BeI and the $(1s2s2p)\ ^4P^o$ term in BeII. Autoionization transitions are indicated by arrows. The excitation energies (Saf 69) are given above the $1s^22s^2$ ground state in BeI.

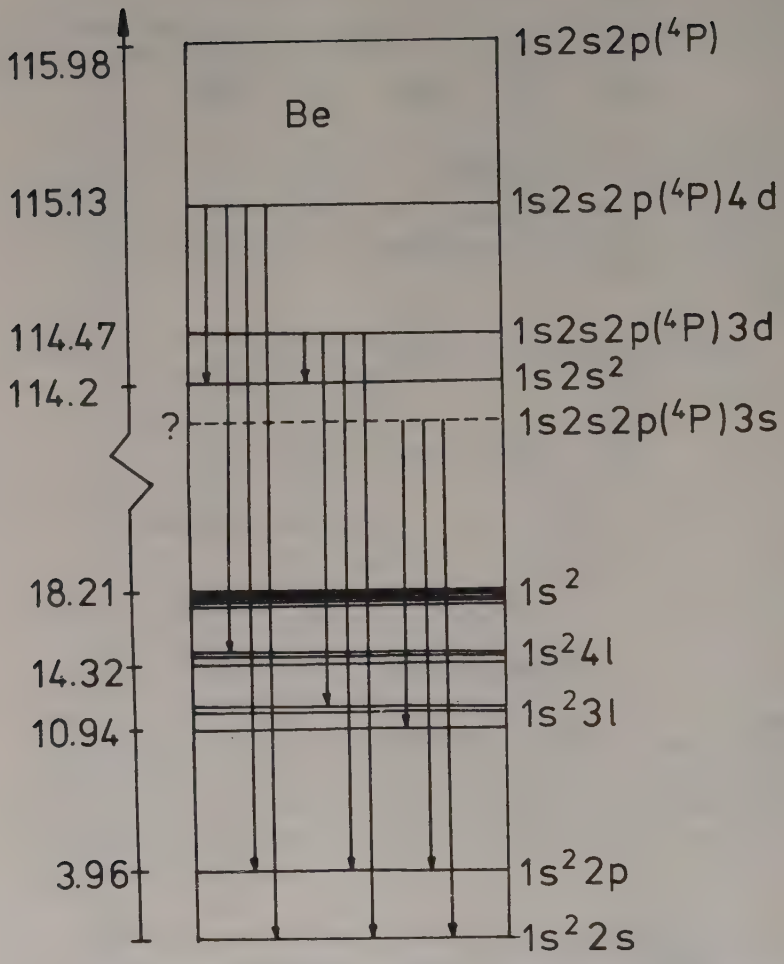

Fig. 94: Partial energy level diagram showing competing autoionization transitions for some 1s2s2p ($^4P^o$)nl configurations in BeI.

b) Delayed Spectra

Identification of lines in the delayed Be spectra is based on theoretical predictions of transition energies in three-electron and four-electron systems. Reliable calculations of term energies with ±0.1 eV accuracy were done for some of the lowest lithium-like quartet states in BeII (Hol 67). An energy level diagram of beryllium showing the Auger decay of the BeII $(1s2s2p)\ ^4P^o = {}^4P^o(1)$ and the BeI $(1s2s2p^2)\ ^5P = {}^5P(1)$ terms is represented in Fig. 93. The term energy of the lowest quintet state is based on the theoretical calculation of Safronova et al. (Saf 69, Appendix IX). Beryllium is of considerable interest since it is the simplest atomic system where quintet terms may occur. Such core-excited states in BeI with all four electrons aligned (2S+1 = 5) are of particular importance, since as yet unidentified lines in the optical beam-foil spectra can be classified as transitions among quintet states. We further note that the lowest lying quintet state, namely $(1s2s2p^2)\ ^5P$, is both metastable with respect to Coulomb autoionization and photon decay, whereas the higher lying quintet states may decay to other quintet states by radiative transitions. Similarly, three-electron quartet terms, apart from $(1s2s2p)\ ^4P^o$, are depleted mainly by E1 transitions. Such photon decays among quartet levels in BeII, using the beam-foil light source, were studied by Hontzeas et al. (Hon 73). Furthermore, Dmitriev et al. (Dmi 72) have investigated the increase of charge due to autoionization of beryllium projectiles within the time of travel through a charge exchange chamber after beam-foil excitation. They have obtained $\tau_{5/2} = (55\pm20) \times 10^{-8}$ sec for the $^4P^o(1)_{5/2}$ and $\tau_{3/2,1/2} = (8\pm3) \times 10^{-8}$ sec for the $^4P^o(1)_{3/2,1/2}$ states in BeII. The existence of metastable four-electron systems was reported by Cocke et al. (Cock 72) and Pegg et al. (Pe 73). However, no experimental work was performed for metastable autoionizing quintet states for $Z \leq 6$.

For the first time decay-in-flight spectra of long-lived meta-

stable states in beryllium were reported by Bruch et al. (Br 74, Br 75c, Br 76a). In the delayed Be spectra characteristic peaks were observed which were interpreted to be related to the Auger decay of the BeI ($1s2s2p^2$) ^5P state. Here we present additional data concerning long-lived metastable states in BeII and BeI.

The lowest metastable autoionizing beryllium-like states can be characterized as: ($1s2s2p^2$) ^5P; ($1s2s2p3s$) $^5P^o$, ($1s2s2p3p$) ^5S, ^5P, ^5D; ($1s2s2p3d$) $^5P^o$, $^5D^o$, $^5F^o$; ($1s2p^3$) $^5S^o$, $^3S^o$; ($1s2p^2$ 3s) ^5P, ($1s2p^2 3p$) $^5S^o$, $^5P^o$, $^5D^o$; ($1s2p^2 3d$) ^5P, ^5D, ^5F. Competing decay mechanisms for some 1s2s2p ($^4P^o$)nl levels in BeI are illustrated in Fig. 94. As an example, the 1s2s2p3d level in Fig. 94, can decay to the $1s2s^2$, $1s^2 2s$, $1s^2 2p$ and $1s^2 3d$ final ionic states.

Samples of electron energy spectra taken with the foil being moved to different upstream positions are indicated in Figs. 95a-d. The observed autoionization structures are compared to the following theoretical line energies:

(i) The lowest transition energies of lithium-like $^4P^o(1)$, $^4P(1)$, $^4P^o(2)$, $^4S(1)$, $^4D(1)$, $^4P^o(3)$, $^4S(2)$, $^4P(2)$, $^4D(2)$ and $^4D^o(2)$ terms in BeII (Appendix VII, XI, Fig. 93) decaying to the BeIII $1s^2$ final ionic state.

(ii) The four-electron $^5P(1)$ term in BeI (Appendix IX, Fig. 93) which can leave the residual BeII ion in either the ($1s^2 2s$) ^2S or ($1s^2 2p$) $^2P^o$ state, which have energy spacing of 3.96 eV (see Fig. 93).

(iii) The four-electron ($1s2p^3$) $^5S^o$ = $^5S^o(1)$ term which may be deexcited both via E1 radiation and magnetic autoionization (the most probable Auger decay channel should lead to the ($1s^2 2p$) $^2P^o$ final ionic state in BeII).

(iv) Possible line energies associated with the [$1s2s2p(^4P^o)$ 3d] $^5L^o$ levels, decaying to the BeII $1s^2 2s$, $1s^2 2p$ and $1s^2 3d$ final states.

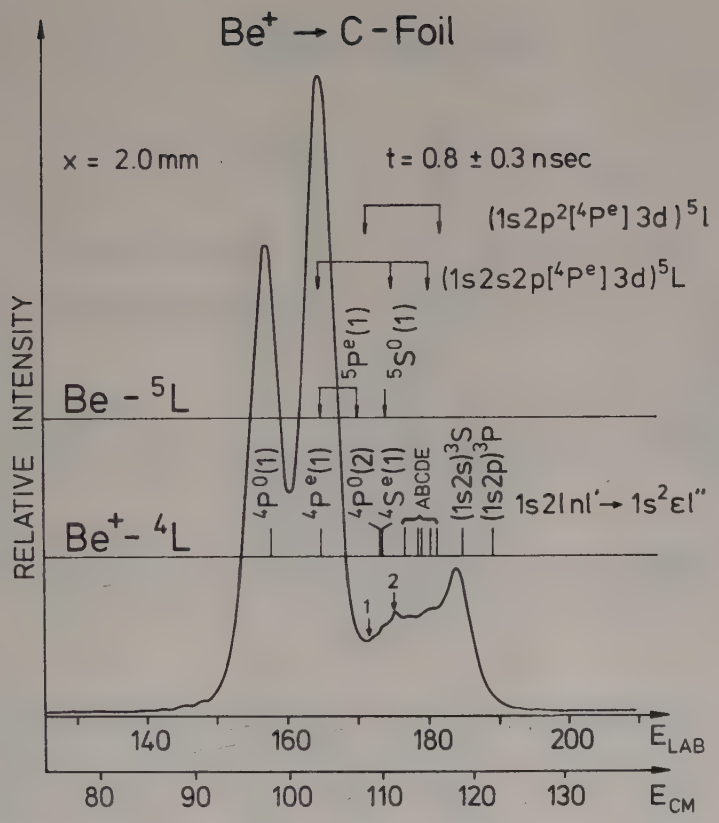

Fig. 95a: Electron energy spectrum from a 284 keV beryllium beam viewed 2 mm downstream from the exciting foil. A: (1s2s3d) $^4D = {}^4D(1)$; B: (1s2p3s) $^4P^o = {}^4P^o(3)$; C: (1s2s4s) $^4S = {}^4S(2)$; D: (1s2p3p) $^4P = {}^4P(2)$ and (1s2s4d) $^4D = {}^4D(2)$; E: (1s2p3d) $^4D^o = {}^4D^o(2)$.

(v) Possible energy positions of the $[1s2p^2\ (^4P)\ 3d]\ ^5L$ levels, decaying to the $1s^22p$ and $1s^23d$ residual ionic state.

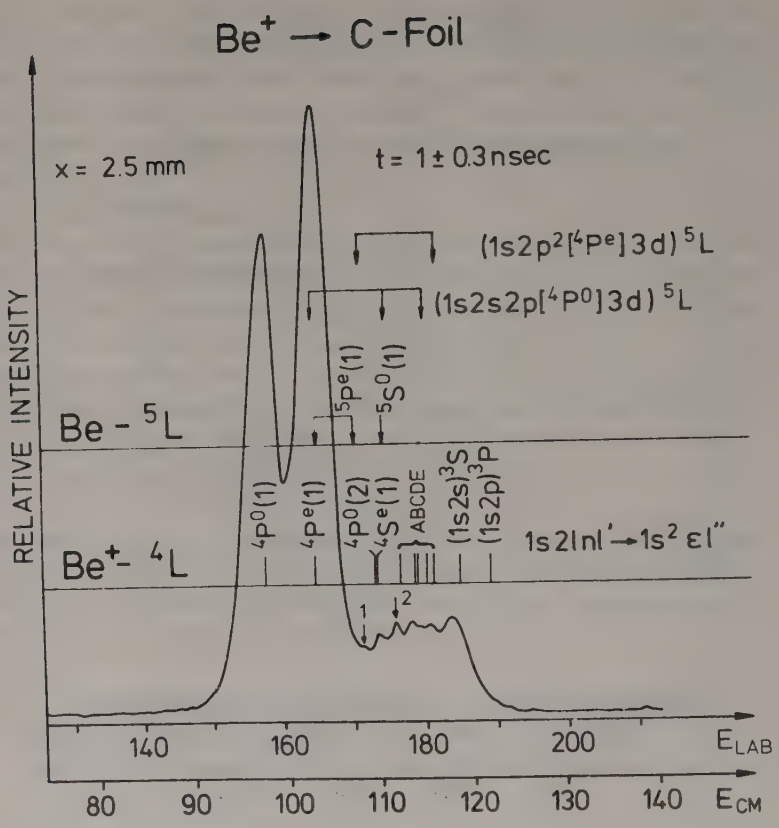

Fig. 95b: Electron energy spectrum from a 284 keV beryllium beam viewed 2.5 mm downstream from the exciting foil.

We identify the first strong line in Fig. 95a-d as due to the $^4P^o(1)$ term the energy of which was taken to be 97.77 eV (Hol 67) and was used to calibrate the energy scale in the center-of-mass frame. The second strong peak should contain contribution for both $^4P(1)$ and $^5P(1)$ decays. This is supported by agreement between the experimental line energy and calculated transition energies. The small hump (indicated by

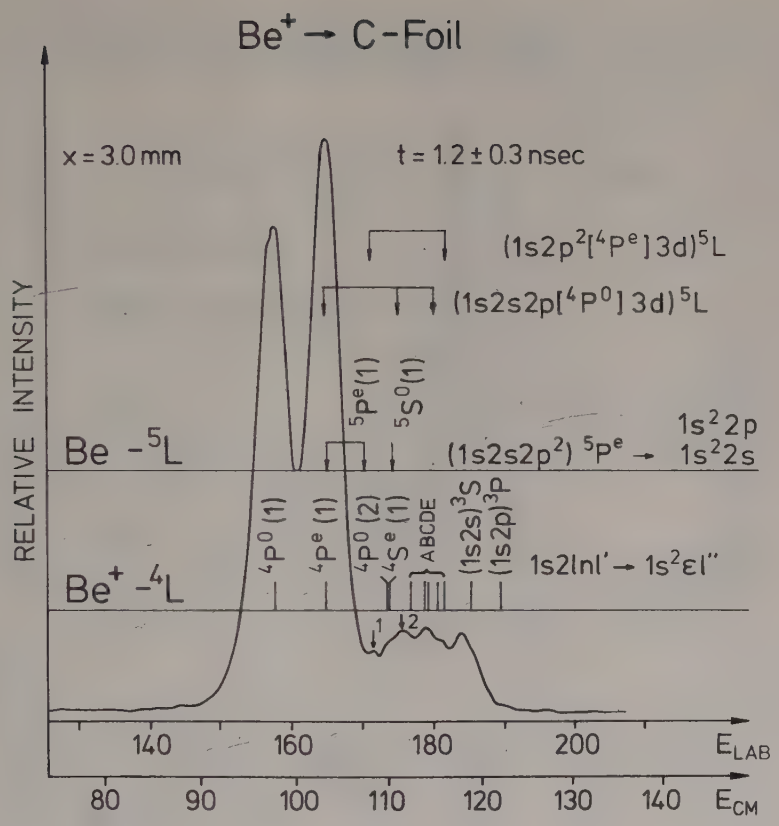

Fig. 95c: Electron energy spectrum from a 284 keV beryllium beam viewed 3 mm downstream from the exciting foil.

label 1) on the high energy side of the second strong peak is probably due to the initial $^5P(1)$ state in BeI. The small peak labeled 2 is tentatively identified as originating from the BeI $(1s2p^3)$ $^5S^o$ level. We note that four-electron $(1s2p^3)$ $^5S^o$ states decay primarily via E1 transitions and hence contribute little to the far downstream spectra. Some of the

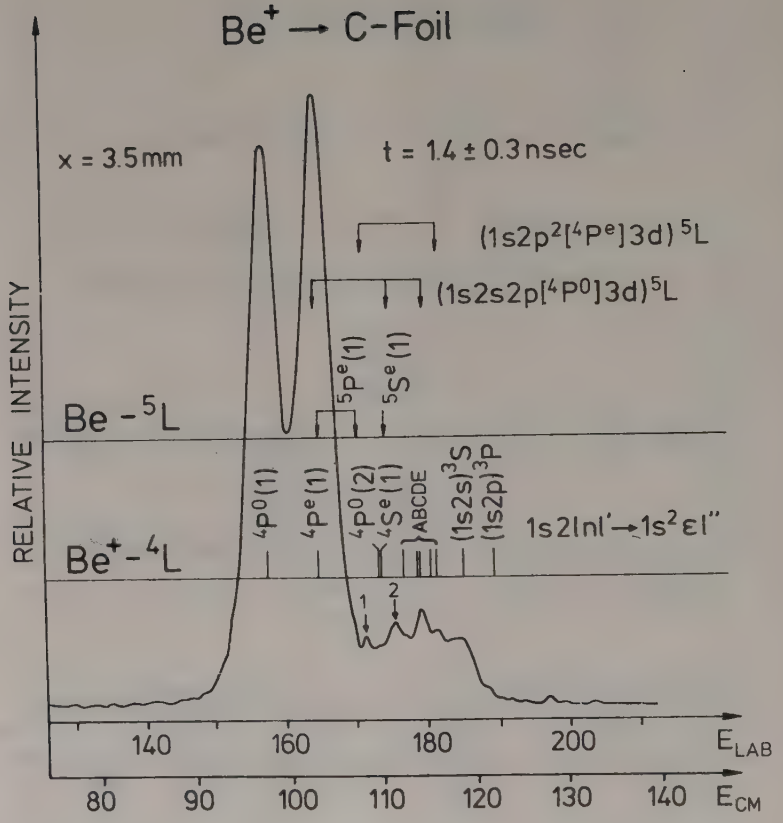

Fig. 95d: Electron energy spectrum from a 284 keV beryllium beam viewed 3.5 mm downstream from the exciting foil.

features between 110 and 120 eV (E_{CM}) might be also attributed to spectator states with a weakly bound (3l, 4l) electron attached to a three electron core (Br 76a). It is assumed that the main components above $E_{CM} \simeq 108$ eV arise from initial lithium-like quartet states. In the case of the three-electron systems, the $^4P(1)$, $^4P^o(2)$, $^4S(1)$, $^4D(1)$ = A, $^4P^o(3)$ = B,

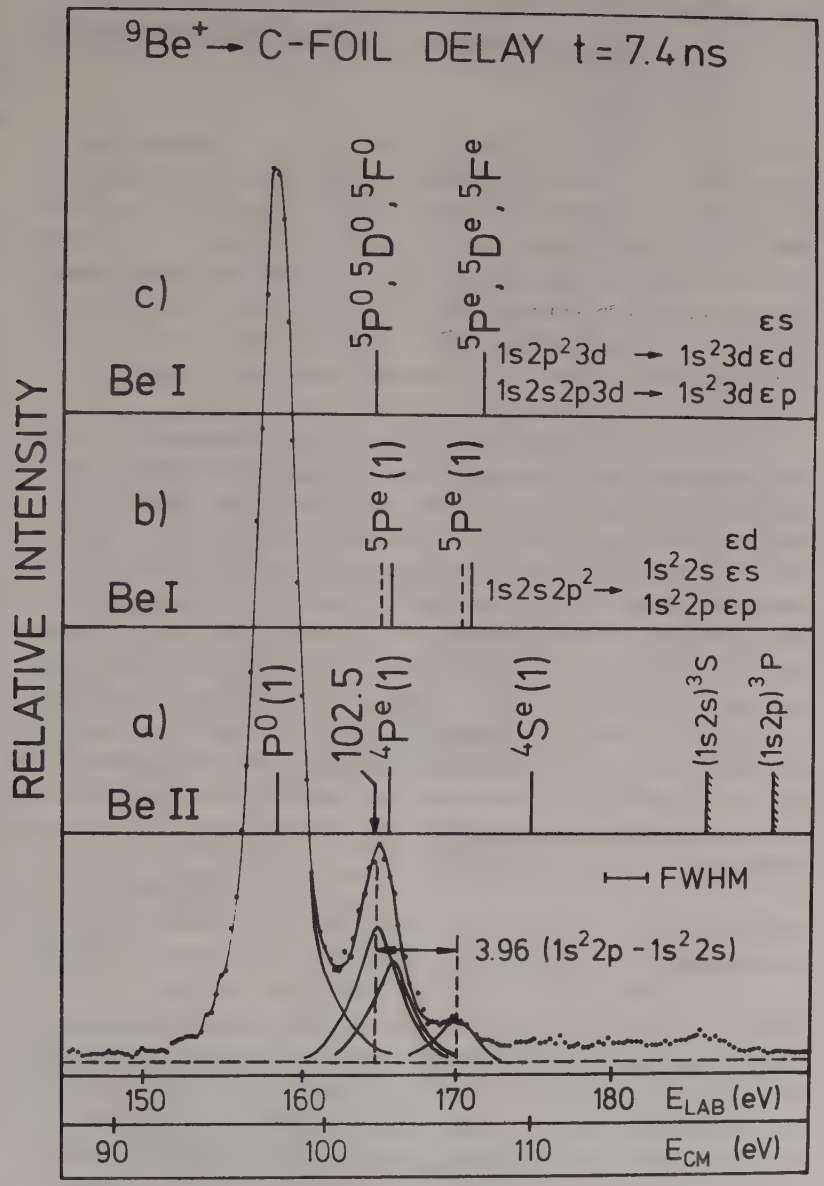
$^9Be^+$ → C-FOIL DELAY t = 7.4 ns
RELATIVE INTENSITY
c)
Be I
$5p^0\ 5D^0, 5F^0$
$5p^e, 5D^e, 5F^e$
$1s2p^2 3d \rightarrow 1s^2 3d\,\varepsilon d$
$1s2s2p3d \rightarrow 1s^2 3d\,\varepsilon p$
εs
b)
Be I
$5P^e(1)$
$5P^e(1)$
$1s2s2p^2 \rightarrow$
$1s^2 2s\,\varepsilon s$
$1s^2 2p\,\varepsilon p$
εd
a)
Be II
$P^0(1)$
102.5
$4P^e(1)$
$4S^e(1)$
$(1s2s)^3S$
$(1s2p)^3P$
FWHM
3.96 $(1s^2 2p - 1s^2 2s)$
150
160
170
180
E_{LAB} (eV)
90
100
110
E_{CM} (eV)

Fig. 96: Spectrum of autoionization electrons from the decay in flight of metastable beryllium ions. The delay time is 7.4 nsec.

$^4S(2)$ = C, $^4P(2)$ = D, $^4D(2)$ = D and $^4D^o(2)$ = E states (see Figs. 95a-d) all have allowed E1 decay channels, while the (1s2s2p) $^4P^o \rightarrow (1s^2ns)\ ^2S$ transitions are optically forbidden. The $^4P^o(1)$ Auger decay should make the major contribution to the far downstream spectra. For lithium-like states in BeII series limits are established at $E_{CM} \simeq 118.6$ [(1s2s) ^3S] and at $E_{CM} \simeq 121.9$ eV [(1s2p) $^3P^o$]. As can be seen from Figs. 95 a-d no dominant lines were observed above the (1s2p) ^3P limit.

A 7.4 nsec delayed spectrum of beryllium is presented in Fig. 96. This spectrum is simpler than the spectra obtained some millimeters beyond the exciting foil (see Figs. 95a-d). In Fig. 96 three main lines from initial (1s2s2p) $^4P^o$, $(1s2p^2)\ ^4P$ and $(1s2s2p^2)\ ^5P$ states were observed at about 97.8, 102.4 and 106.4 eV, respectively. We believe that the discrepancy between the calculated position for $(1s2p^2)\ ^4P = {}^4P(1)$ predicted at $E_{CM} \simeq 103.1$ eV and the center of the experimental peak at $E_{CM} \simeq 102.5$ eV is significant, in view of the reproducibility $\Delta E_{CM} = \pm 0.2$ eV of the measurement. The theoretical estimate for the $^4P(1) - {}^4P^o(1)$ energy separation (Hol 67, Appendix XI) should be good to at least the same accuracy, and in fact fits data for quartet levels in BeII (Hon 73) within experimental uncertainty.

The spectral feature at about 102.5 eV is a blend of lines associated with the decay of $^4P(1)$ and $^5P(1)$ states. A decay curve obtained at $E_{CM} \simeq 102.5$ eV (see also Section VII.3) is shown in Fig. 97. These data were fitted to three exponentials plus background. Correction was made for energy loss in the foil. The dotted curve in Fig. 97 shows the computer generated three exponential fit and the crosses indicate the experimental data points. The 0.4 nsec time constant might be a time window effect and should not be assigned to a specific auto-

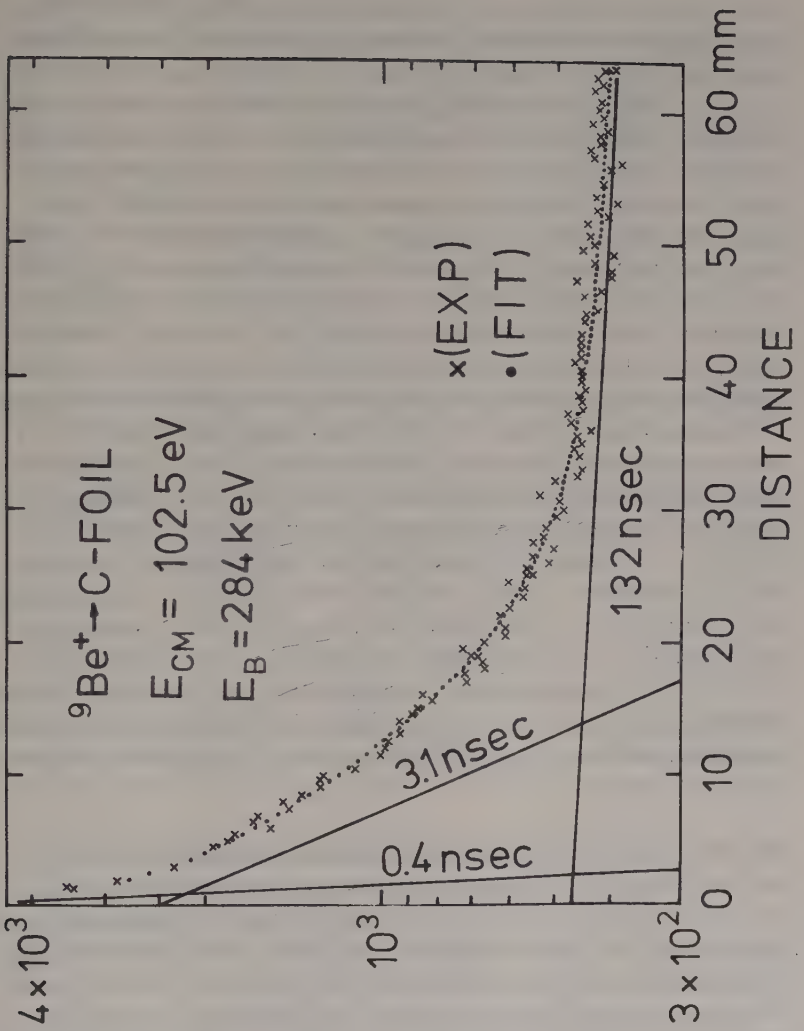

Fig. 97: Decay curve for blend of BeI and BeII autoionization lines at E_{CM} = 105.5 eV. The crosses indicate the experimental data points and the dotted curve shows a computer generated three exponential fit.

ionizing level. We attribute the 3.1 nsec decay component to the lithium-like $(1s2p^2)\ ^4P$ level in BeII. This result is in agreement with the mean life obtained by Hontzeas et al. (Hon 73). The results for the E_{CM} = 102.5 eV decay profile further indicate that there is a decay component with a lifetime of the order of 132 nsec. We interpret this as confirmation of the existence of metastable autoionizing four-electron systems. In principle, two distinct types of Auger transitions should be responsible for this long-lived component: (i) $1s2s2p3l) \rightarrow (1s^2 3l\varepsilon p)$, or (ii) $(1s2s2p^2) \rightarrow (1s^2 2p\varepsilon p)$. Although BeI quintet terms arising from the (1s2s2p3l) configurations are metastable with respect to Coulomb autoionization, electric dipole transitions to lower lying quintet states seem to be possible (Br 75c). On the other hand, the $(1s2s2p^2)\ ^5P$ term is metastable towards Coulomb autoionization and electric-dipole transitions as well. Hence, the long-lived component might be interpreted as a cumulative effect of $(1s2s2p^2)\ ^5P$ (J = 3, 2, 1) decays originating from relativistic interactions (spin-orbit, spin-other-orbit and spin-spin coupling) and from admixtures of Coulomb autoionizing levels. Furthermore, the $(1s2s2p^2)\ ^5P$ states will mix with their $(1s2s2p^2)\ ^{1,3}S$, $^{1,3}P$ and $^{1,3}D$ counterparts via hyperfine coupling. From these considerations it might be expected that the decay curve corresponding to the $(1s2s2p^2)\ ^5P$ term is a composite of various different decays.

The remaining peak in Fig. 96 near 106.4 eV is attributed to the BeI $(1s2s2p^2)\ ^5P$ level decaying to the BeII $(1s^2 2s)\ ^2S$ final ionic state. This line identification is consistent with Safronova's and Kharitonova's calculation which predicts the $^5P(1)$ transition energy to be 0.7 eV higher. We further note that the centroid energy of 106.4±0.5 eV agrees well with a recent unpublished calculation of Schwarz and Chang (Schwa 76, Br 76b). By scaling up the $(1s^2 2p)\ ^2P^o$ - $(1s^2 2s)\ ^2S$ relative spacing, which is 3.96 eV, we determined the line center of the $1s2s2p^2 \rightarrow 1s^2 2p\varepsilon p$ transition to appear at 102.4±0.5 eV. The line-identification of the peak around 102.4 eV is also

supported by a graphical peak deconvolution of the spectrum (see Fig. 91) where the relative intensities of the $^4P(1)$ and the $^5P(1)$ components were estimated from the decay profile in Fig. 97. The transition energies associated with the BeI $(1s2s2p^2)$ ^5P state are given in Table 27 together with theoretical data as deduced from the calculations of Safronova et al. (Saf. 69) and Schwarz et al. (Schwa 76, Br 76c). From Table 25 the absolute term energy of the $(1s2s2p^2)$ ^5P state in BeI was estimated to be 115.7±0.5 eV (excitation energy as measured from the BeI ground state).

Table 27: Transition energies (eV ion rest frame) for metastable autoionizing transitions involving initial core-excited $(1s2s2p^2)$ ^5P states in beryllium

Suggested Transition	Transition Energy (eV) Experiment	Theory
$(1s2s2p^2) \rightarrow (1s^22p\varepsilon p)$	102.4±0.5[a]	102.32[b]
		103.17[c]
$(1s2s2p^2) \rightarrow (1s^22s\varepsilon s)$	106.4±0.5[a]	106.28[b]
$(1s^22s\varepsilon d)$		107.13[c]

a = this work; b = Schwarz and Chang (Schwa 76, Br 76b); c = Safronova et al. (Saf 69).

Table 28: Comparison of lifetimes obtained in this work with other experimental values

Initial State	Auger Electron Detection nsec	Photon Detection nsec
BeII $(1s2s2p)$ $^4P^o$	∿164[a]	
BeII $(1s2p^2)$ ^4P	3.1±0.4[a]	3.1 0.2[b]
BeI $(1s2s2p^2)$ ^5P	132 ±50[a]	
BeII $(1s2s3s)$ ^4S (?)	5.2±1[a]	

a = this work; b = Hontzeas et al. (Hon 73)

We also studied the Auger decay of the (1s2s2p) $^4P^o$ state in BeII as a function of time of flight. As can be seen from Fig. 98, the decay curve shows considerable curvature which is ascribed to optical cascades from higher lying quartet states. The slope of the straight line fitted to the data for the (1s2s2p) $^4P^o$ Auger decay in beryllium yields an average mean life of ∿164 nsec. Owing to our restricted time delay of a maximum of 35 nsec, we were not able to extract detailed information on the differing decay rates involved in the (1s2s2p) $^4P^o$ Auger decay. Finally, the measured lifetimes obtained in this work are tabulated in Table 28. The uncertainties in the lifetimes are mainly due to errors introduced by cascading, blending and background corrections and by errors associated with the determination of the velocity of the emerging beam.

In summary, we have measured the mean life of the ($1s2p^2$) ^4P level by detecting the Auger electron emission. In addition we have made assignments of observed features as due to initial four-electron quintet states.

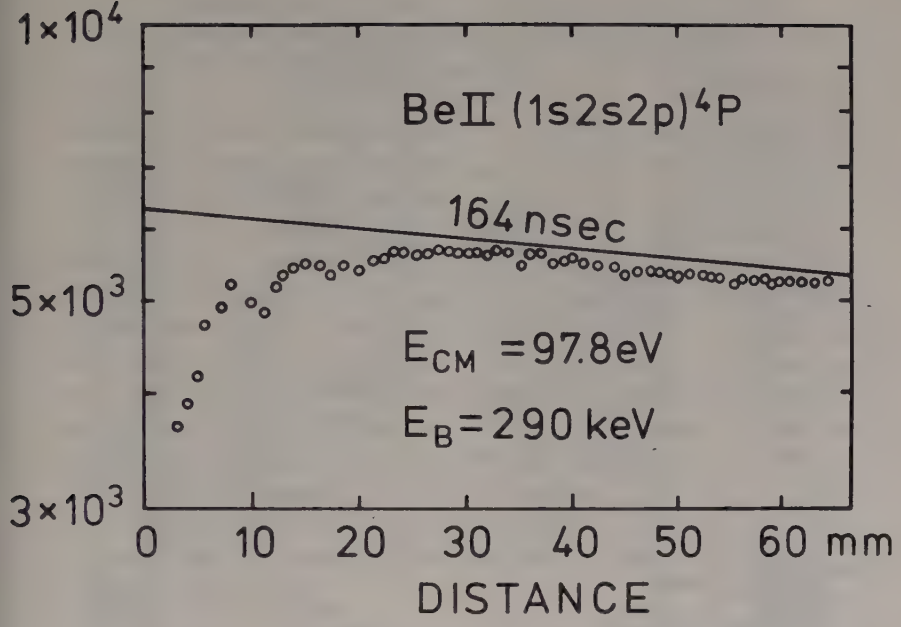

Fig. 98: Decay curve of the (1s2s2p) $^4P^o_{1/2,\ 3/2,\ 5/2}$ states in BeII. The open circles represent the data points and the straight line represents a single exponential fit giving a mean life of approximately 164 nsec.

3. Boron- and Carbon Autoionization Lines

a) Prompt Spectra

The prompt boron spectrum obtained for 300 keV B^+ → C-foil collisions is shown in Fig. 99. It is suggested that the main spectral features between 140 and 230 eV (E_{CM}) originate from the decay of three-to-five electron boron ions. Due to a large number of possible inner-hole state combinations in three-to-five electron systems the prompt boron spectrum should be a

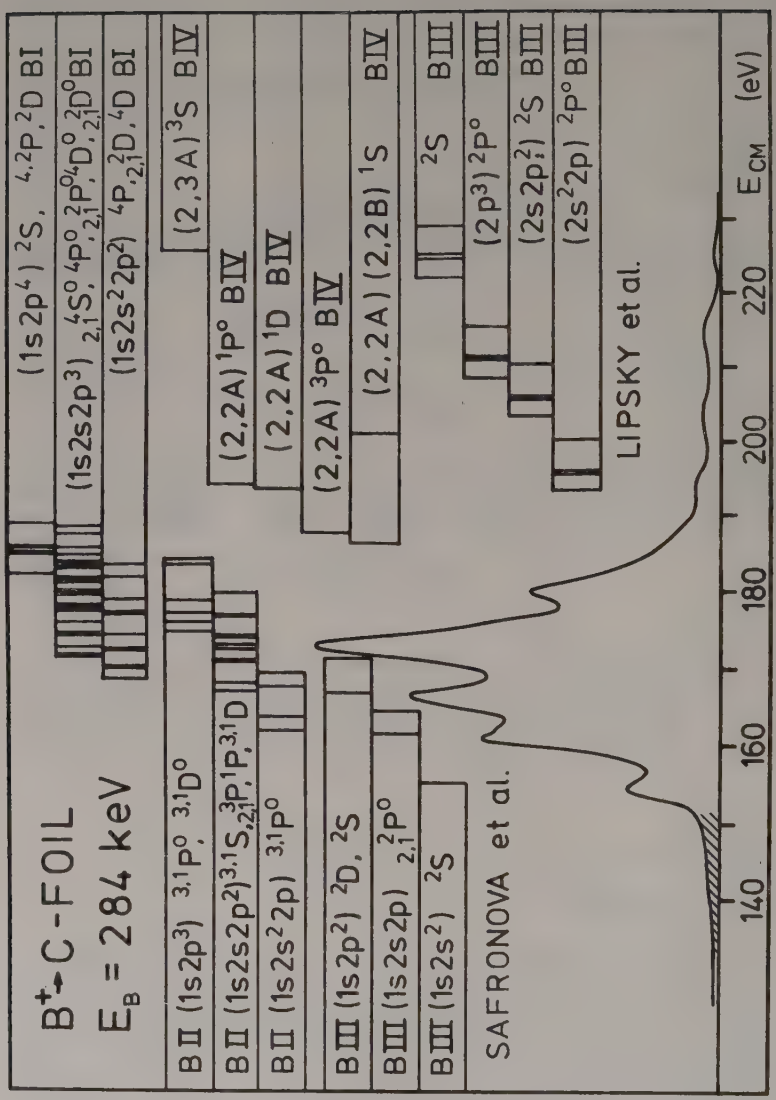
B+-C-FOIL
E_B = 284 keV
(1s 2p^4) 2S, 4,2P, 2D BI
(1s2s2p^3) 4,1S°, 4P°, 2,1P°, 4D°, 2,1D° BI
(1s2s^2 2p^2) 4P, 2,1D, 4D BI
(2,3 A) 3S BIV
(2,2A) 1P° BIV
(2,2A) 1D BIV
(2,2A) 3P° BIV
(2,2A) (2,2B) 1S BIV
B II (1s2p^3) 3,1P°, 3,1D°
B II (1s2s2p^2) 3,1S, 3,2,1P, 3,1D
B II (1s2s^2 2p) 3,1P°
B III (1s2p^2) 2D, 2S
B III (1s2s2p) 2,1P°
B III (1s2s^2) 2S
2S BIII
(2p^3) 2P° BIII
(2s2p^2) 2S BIII
(2s^2 2p) 2P° BIII
SAFRONOVA et al.
LIPSKY et al.
140
160
180
200
220
E_CM (eV)
RELATIVE INTENSITY

Fig. 99: High energy portion of the prompt boron spectrum produced by 300 keV B^+ → C-foil excitation. The shaded area presumedly represents contribution due to three-electron processes.

composite of many autoionization lines. The complexity of the observed B spectrum is further increased due to the overlap of the Doppler-shifted lines from the boron projectiles with C K-Auger peaks from the target. A qualitative description of carbon K-shell vacancy production in 300 keV B^+ → C-foil collisions may be achieved in terms of the molecular orbital (MO) model (Mey 73). For carbon atoms excited by boron ions the MO model predicts: (a) promotion of 1s (boron) electrons via $2p\sigma$ - $2p\pi$ rotational coupling at small internuclear distances and (b) transfer of vacancies from the $2p\sigma$ (boron) to the $1s\sigma$ (carbon) states via radial coupling as the particles separate. According to Meyerhof (Mey 73) the sharing ratio $\sigma_K(C)/\sigma_K(B)$ should be of the order 8×10^{-2}, where $\sigma_K(C)$ and $\sigma_K(B)$ are the carbon K and the boron K shell vacancy production cross sections, respectively.

For a specific line-identification theoretical autoionization energies associated with two-to-five electron boron systems were incorporated into Fig. 99. It is to be seen that the first peak at about 155 eV can be attributed to the formation of core-excited $(1s2s^2)\ ^2S$ states in BIII. The structure between 160 and 180 eV (E_{CM}) may be accounted for by components of three-to-five electron systems characterized by single K-shell vacancies. An energy level diagram of such core-excited states in BIII, BII and BI is indicated in Fig. 100. The most important terms are:

(i) $(1s2s2p)\ ^{2,1}P^o$ and $(1s2p^2)\ ^2D,\ ^2S$ of three-electron BIII.

(ii) $(1s2s^22p)\ ^{3,1}P^o$, $(1s2s2p^2)\ ^{3,1}S, {}^{3}P,\ ^1P,\ ^{3,1}D$ and $(1s2p^3)\ ^{3,1}P^o,\ ^{3,1}D^o$ of four-electron BII.

(iii) $(1s2s^22p^2)\ ^4P,\ ^{2,1}D,\ ^4D$, $(1s2s2p^3)\ ^{4}S^o,\ ^4P^o,\ ^{2,1}P^o,\ ^4D^o,\ ^{2,1}D^o$ and $(1s2p^4)\ ^2S,\ ^{4,2}P,\ ^2D$ of five-electron BI.

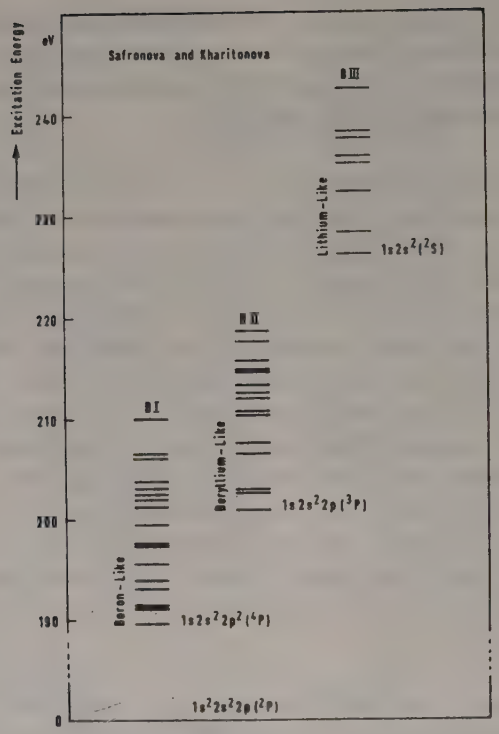

Fig. 100: Energy level diagram of the lowest core-excited states in BI, BII and BIII as measured from the BI ($1s^2 2s^2 2p$) ground state. The energy positions were deduced from the computation of Safronova et al. (Saf 69).

In this connection we note that two possible final states exist for the Auger decay of the beryllium-like ($1s2s^2 2p$) and ($1s2s2p^2$) configurations (i.e. $1s^2 2s$ and $1s^2 2p$) leading to double peaks separated by about 6 eV. As can be seen from Fig. 99 the difference in energy between the second and third strong line is nearly equal to the $1s^2 2s$-$1s^2 2p$ spacing in BIII. Therefore, these features may result predominantly from the ($1s2s^2 2p$)

$^{3,1}P^{o} \rightarrow (1s^2 2p\varepsilon s)\ ^{3,1}P^{o}$ and $(1s2s^2 2p)\ ^{3,1}P^{o} \rightarrow (1s^2 2s\varepsilon p)\ ^{3,1}P^{o}$ Auger transitions. The weaker structures above 185 eV apparently do not result from core-excited states having single K-vacancies, but from a readjustment of double K-hole states such as BIV 2lnl' ($n \geq 2$), BIII 2lnl'n'l" ($n, n' \geq 2$), BII 2lnl'n'l" n"l"' ($n, n', n" \geq 2$) and BI 2lnl'n'l"n"l"' n"' l^{iv} ($n, n', n", n"' \geq 2$). The principal contribution of the structure above 185 eV could be due to initial 2lnl'n"l" ($n, n' \geq 2$) triply excited states in BIII. Thus far, no detailed calculations on four-electron and five-electron states characterized by an empty, doubly ionized core, have been attempted. Quite possibly four-electron states such as BII 2lnl'n'l"n"l"' with n, n' and $n" \geq 2$ and five-electron BI 2lnl'n'l"n"l"' n"' l^{iv} with n, n', n" and $n"' \geq 2$ can decay in a sequence of Auger transitions. For example the readjustment of the BI $2s^2 2p^3$ state may lead in a first step to the intermediate $1s2p^3$ state in BII, namely

$$(1) \quad 2s^2 2p^3 \rightarrow 1s2p^3 \varepsilon s$$

where the BII $1s2p^3$ state in turn can decay to the adjacent $1s^2 2p\varepsilon s(\varepsilon d)$ continuum:

$$(2) \quad 1s2p^3 \rightarrow 1s^2 2p\varepsilon s(\varepsilon d)$$

Finally, in a third step, the BIII $1s^2 2p$ state is deexcited via E1 radiation as follows

$$(3) \quad 1s^2 2p \rightarrow 1s^2 2s + \hbar\omega$$

Such decay mechanism suggest that core-excited beryllium-like states are likely to be excited by Auger cascades from boron-like states with double K-shell vacancies.

A semilog plot of the electron energy spectrum in boron is displayed in Fig. 101. The high energy peaks, labeled G, H, I, J, K and L are attributed to multiply excited states involving double K-vacancies. This identification is supported by agreement between experimental and calculated transition energies. A segment of the boron spectrum between 190 and 230 eV is pre-

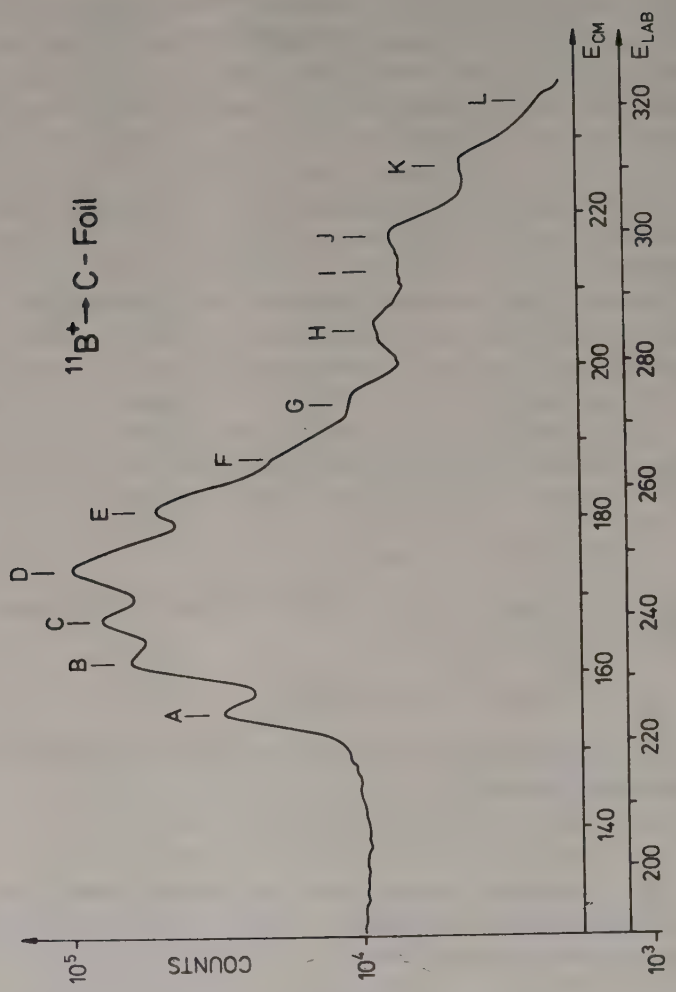

Fig. 101: Electron spectrum from boron beam, as observed with the foil in view of the spectrometer (intensity scale logarithmic). The observed peaks are labeled A to L.

sented in Fig. 102 along with predicted transition energies associated with the decay of triply excited states in BIII. We

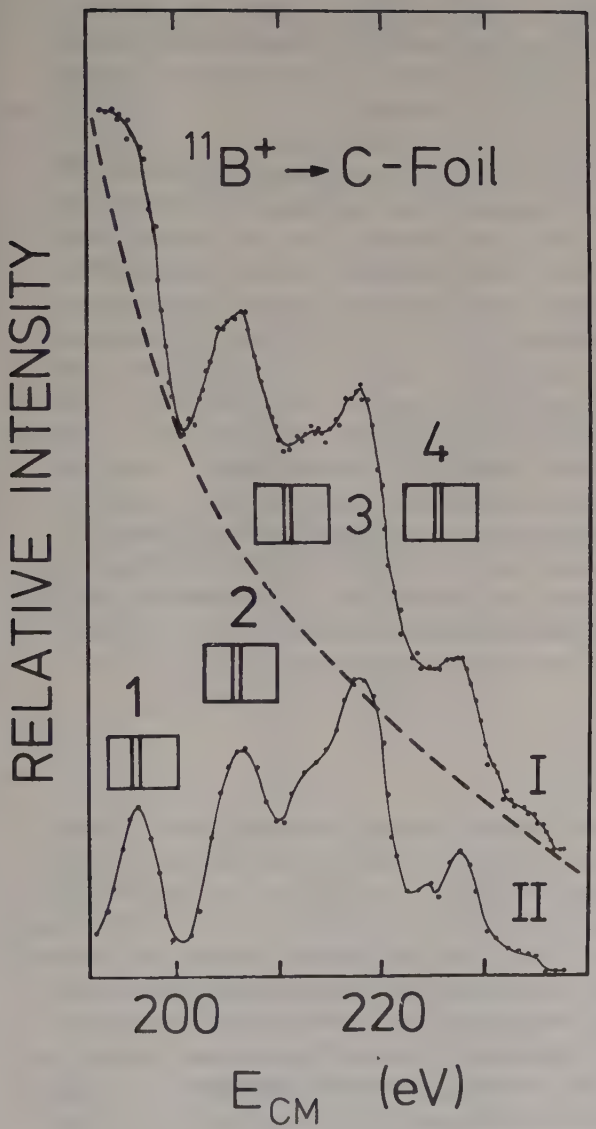

Fig. 102: Segment of boron electron energy spectrum (linear scale) plotted in the projectile rest frame. Curve I represents the original data points. Curve II is corrected for electron background. Labels 1, 2, 3 and 4 correspond to the Auger decay of the $(2s^2 2p)\ ^2P^o$, $(2s2p^2)\ ^2S$, $(2p^3)\ ^2P^o$ and the next higher ^2S term in BIII, respectively.

suggest that the peak at about 196 eV originates from the Auger decay of the lithium-like $(2s^2 2p)\ ^2P^o$ term. The peak at about 206 eV is probably due to the $(2s2p^2)\ ^2S$ term in BIII. Similarly the peak at about 208 eV may contain contributions from decays arising from $(2p^3)$ configurations.

Another interesting feature of the boron spectrum (see Fig. 99) is the occurence of structure in the low-energy region between 140 and 150 eV (E_{CM}). For this structure two explanations can be considered. The first is the decay of core-excited states in BII due to three-elctron Auger processes; where for example in in the decay of the 1s2snl'n'l" (n, n' $\geq$ 2) level, the 2s electron may fill the K-shell vacancy (i.e. 2s $\rightarrow$ 1s) while the nl' electron is emitted (i.e. nl' $\rightarrow$ εl') and the n'l" electron is simultaneously excited or ejected (i.e. n'l" $\rightarrow$ n"l" or n'l" $\rightarrow$ εl"), thus lowering the kinetic energy of the emerging εl' electron (see Fig. 2). The second explanation would be inelastically scattered Auger electrons emitted within the escape depth of the foil. In this connection it should be noted that Auger electrons may excite plasma oscillations in the carbon foil. The excitation of plasmons have probably been observed by Richard et al. (Rich 73) for 30 MeV O on Si and Al targets.

b) Delayed Spectra

Boron: Metastable autoionizing quartet states of the LiI isoelectronic sequence were studied by measuring both photon and electron emission (Mar 70, Sel 73, Mar 74, Br 76, To 76). By detecting the secondary electron ejection of foil-excited oxygen and fluorine beams as a function of distance downstream from a carbon foil the Oak Ridge group (Sel 71) observed two characteristic structures (originally labeled A and B), which could not be attributed to decays of lithium-like states. Pegg et al. (Pe 73) and Junker and Bardsley (Junk 73) suggested that these features might originate from autoionizing transitions of four- and five-electron systems.

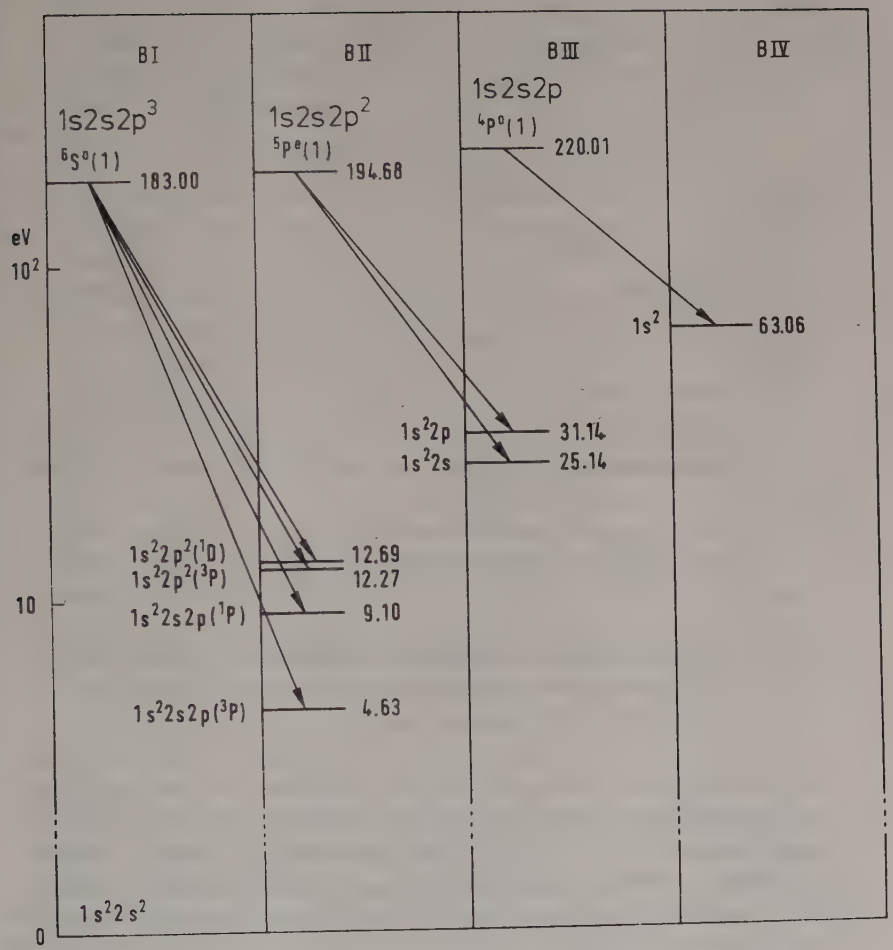

Fig. 103: Partial energy level diagram representing autoionizing decays of the $^4P^o(1)$, $^5P(1)$ and $^6S^o(1)$ terms in boron. Autoionization transitions are indicated by arrows. The excitation energies (Saf 69) are given above the $1s^22s^2$ ground state in BII.

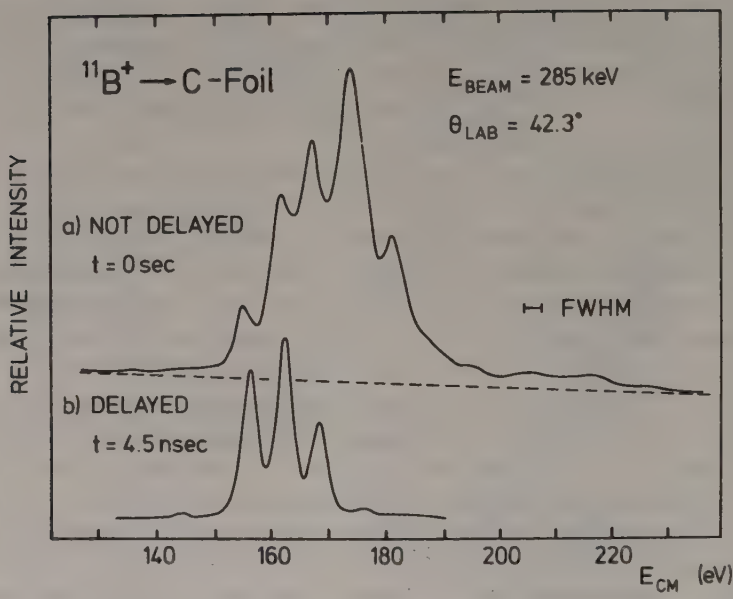

Fig. 104: High energy portion of the prompt and delayed spectra of autoionization electrons emitted in flight by 285 keV boron ions.

A boron energy level diagram based on theoretical calculations of Holøien and Geltman (Hol 67) and Safronova et al. (Saf 69) is indicated in Fig. 103. The most metastable quartet, quintet and sextet states are $(1s2s2p)\ ^4P^o$, $(1s2s2p^2)\ ^5P$ and $(1s2s2p^3)\ ^6S^o$, respectively. These lowest lying terms are both metastable with respect to Coulomb autoionization and radiative transitions, whereas the higher lying ^4L, ^5L and ^6L terms are expected to decay primarily via (E1) transitions.

The most metastable core-excited boron states are: (i) BIII $(1s2s2p)\ ^4P^o = {}^4P^o(1)$ decaying to the $1s^2\varepsilon l$ continuum, (ii) BII $(1s2s2p^2)\ ^5P = {}^5P(1)$ decaying dominantly to the $1s^22s\varepsilon l$ and the $1s^22p\varepsilon l$ continuum states and (iii) BI $(1s2s2p^3)\ ^6S^o = {}^6S^o(1)$

which is adjacent to six different continua $1s^2 2s2p(^{1,3}P^o)\varepsilon l$, $1s^2 2p^2(^1D, ^1S, ^3P)\varepsilon l$ and $1s^2 2s^2(^1S)\varepsilon l$, respectively. The $^6S^o(1)$ term should decay primarily to the $(1s^2 2s2p)\ ^3P^o$ and $(1s^2 2p^2)\ ^3P$ final ionic states. Therefore, we expect five prominent lines grouped in the following way:

(a) A single peak due to the BIII $^4P^o(1)$ deexcitation.

(b) A double peak structure with an energy separation of 6 eV ($1s^2 2s\ ^2S$ - $1s^2 2p\ ^2P^o$) associated with the BII $^5P(1)$ Auger decay.

(c) A double peak structure characterized by a peak separation of 7.64 eV ($1s^2 2s2p\ ^3P^o$ - $1s^2 2p^2\ ^3P$) arising from the Auger decay of the lowest $^6S^o$ term in BI.

A prompt and a 4.5 nsec delayed electron energy spectrum of boron is shown in Fig. 104. At 285 keV beam energy the charge state composition of the boron beam is restricted mainly to the charge states 0, 1 and 2. Hence, the most prominent peaks displayed in Fig. 104b should arise from core-excited BI, BII and BIII levels. In Fig. 105 a 4.5 nsec delayed spectrum of boron in the energy range 135 to 190 eV (E_{CM}) is depicted. The observed spectral features are indicated in comparison with the three-electron $^4P^o(1)$, $^4P(1)$, $^4S(1)$ and $^4P^o(2)$ energy positions as deduced from the work of Holøien et al. (Hol 67) together with the four-electron $^5P(1)$, $^5S^o(1)$ and $^3S^o(1)$ and the five-electron $^6S^o(1)$ energies as estimated from the computation of Safronova et al. (Saf 69). According to the predicted energy positions we can ascribe the four prominent peaks of the spectrum to Auger transitions associated with the $^4P^o(1)$, $^5P(1)$ and $^6S^o(1)$ terms. In the following this interpretation is discussed.

We identify the first strong line as due to autoionization of the BIII $^4P^o(1)$ level in accordance with Holøien and Geltman (Hol 67). The energy scale was established by assigning a value of 156.95 eV to the $^4P^o(1)$ peak. The origin of the second strong peak at 163.0 eV is expected to occur mainly from the

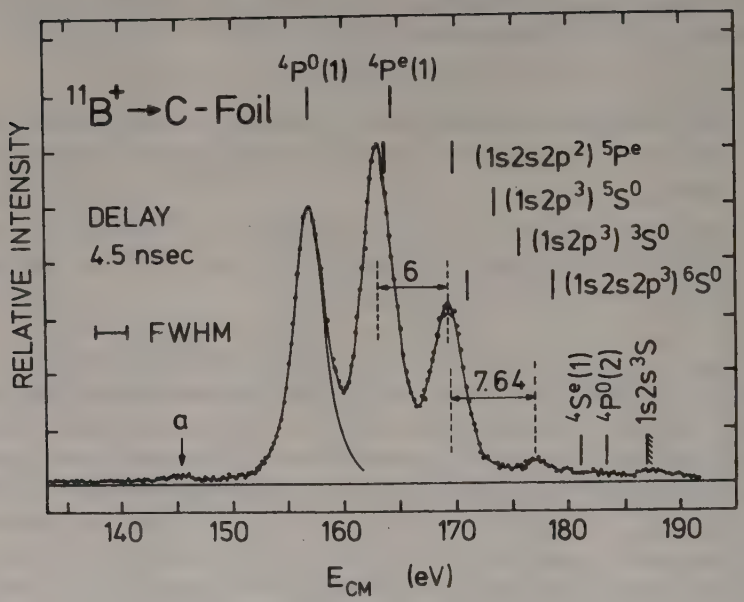

Fig. 105: 4.5 nsec delayed electron energy spectrum due to decays of metastable autoionizing states in BI, BII and BIII.

$(1s2s2p^2)\ ^5P$ decay in BII. In the energy range around 163 eV additional weaker lines may arise from autoionization of the $(1s2p^2)\ ^4P = {}^4P(1)$ and the $(1s2p^2)\ ^2P$ terms in BIII. The center of the $^4P(1)$ autoionization line is predicted at 164.23 eV. Due to competing optical decay channels the $(1s2p^2)\ ^4P$ and $(1s2p^2)\ ^2P$ terms are deexcited dominantly via E1 transitions. Thus the mean lives of the $(1s2p^2)\ ^4P$ and $(1s2p^2)\ ^2P$ states in BIII are 2.1 nsec (Mar 70) and 3.9 psec (Kny 76), respectively. It is suggested that the $(1s2p^2)\ ^4P$ and ^2P levels are almost entirely depleted after a time of flight of 4.5 nsec. We therefore exclude the $(1s2p^2)\ ^4P$ and ^2P Auger decays as dominant contribu-

tions to the second intense peak at $E_{CM} \approx 163$ eV. This is supported by the observed energy separation of 6.1 eV between the first and second peak. This spacing is about 1.2 eV lower than the BIII $^4P(1) - {}^4P^o(1)$ term difference of 7.289 eV, which is known with high accuracy from the optical beam-foil spectrum. Consequently, the peak at 163 eV is assigned mainly due to initial $(1s2s2p^2)\ ^5P$ terms in BII decaying to the $1s^22p$ final ionic state. This line-identification is also supported by the $(1s2s2p^2)\ ^5P \rightarrow 1s^22p\varepsilon p$ transition energy deduced from the work of Safronova et al. (Saf 69) who predict the line center at 163.6 eV, i.e. 0.6 eV higher. The third strong line at 169 eV is identified mainly as the $(1s2s2p^2)\ ^5P \rightarrow 1s^22s\varepsilon s(\varepsilon d)$ transition. This assignment is confirmed by the energy spacing of the second and third peak which is close to the $1s^22p - 1s^22s$ energy separation of 6.0 eV. The spectroscopic assignment of the peaks at 163 and 169 eV is also supported by the measured intensity ratio of about 2:1. According to rule 6 (Section VIII. 2) the $1s2s2p^2 \rightarrow 1s^22p\varepsilon p$ decay channel is probably more likely than the $1s2s2p^2 \rightarrow 1s^22s\varepsilon s(\varepsilon d)$ channel. Furthermore, the $^5P(1)$ term (see Table 5) is coupled via eight distinct channels to the $1s^22p\varepsilon p$ continuum, whereas for the mixing with the $1s^22s\varepsilon s$ and $1s^22s\varepsilon d$ continua only five decay channels are allowed. Therefore, the observed branching ratio of $\sim$2:1 associated with the $^5P(1)$ term seems reasonable.

The additional weaker line at 176.7 eV may be assigned due to the $(1s2s2p^3)\ ^6S^o \rightarrow (1s^22s2p)\ ^3P^o\varepsilon s(\varepsilon d)$ transition. This interpretation is consistent with the predicted transition energy of Schwarz et al. (Schwa 76). It should be noted that the $(1s2s2p^3)\ ^6S^o$ term energy of Safronova et al. (Saf 69) is about 2 eV higher than the experimentally deduced value. By scaling up we determined the $(1s2s2p^3)\ ^6S^o \rightarrow (1s^22p^2)\ ^3P\varepsilon p$ line center which has to appear at 7.64 eV lower energy (see Fig. 103 and 105). This value of 169.1 eV nearly coincides in energy with the $(1s2s2p^2)\ ^5P \rightarrow 1s^22s\varepsilon s(\varepsilon d)$ transition. From the above considerations it follows that the peak at 169 eV is a blend of auto-

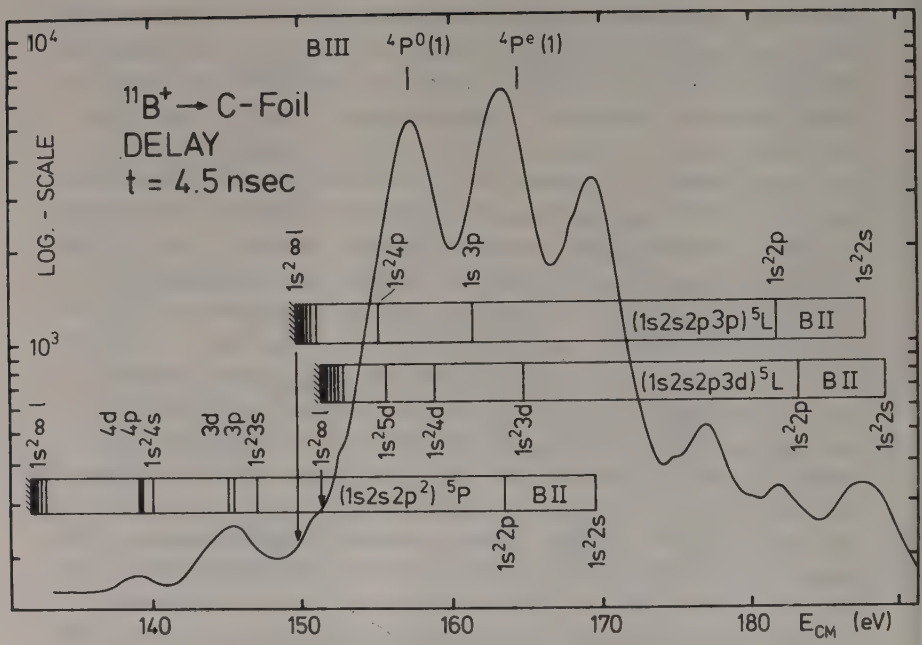

Fig. 106: Semilog plot of the 4.5 nsec delayed boron spectrum.

ionization lines arising from quintet and sextet states. Additional weaker lines in the considered energy range could arise from the $(1s2p^3)\ ^5S^o \rightarrow 1s^2 2p\varepsilon s(\varepsilon d)$ and the $(1s2p^3)\ ^3S^o \rightarrow 1s^2 2p\varepsilon s(\varepsilon d)$ Auger transitions. However, it is assumed that the $(1s2p^3)\ ^5S^o = {}^5S^o(1)$ and the $(1s2p^3)\ ^3S^o = {}^3S^o(1)$ levels decay mainly via the most probable (E1) transitions $^5S^o(1) \rightarrow {}^5P(1)$ (λ = 1324.5 Å; τ = 0.75±0.08 nsec) and $^3S^o(1) \rightarrow (1s^2 2p^2)\ ^3P$ ($\lambda \simeq$ 63.8 Å), respectively. From all these considerations on magnetic autoionizing BIII ^{4}L, BII ^{5}L and BI ^{6}L terms we conclude that the interpretation of the four prominent features is well justified.

Finally, a less intense structure labeled a (see Fig. 105) was observed. This structure becomes more pronounced in a logarith-

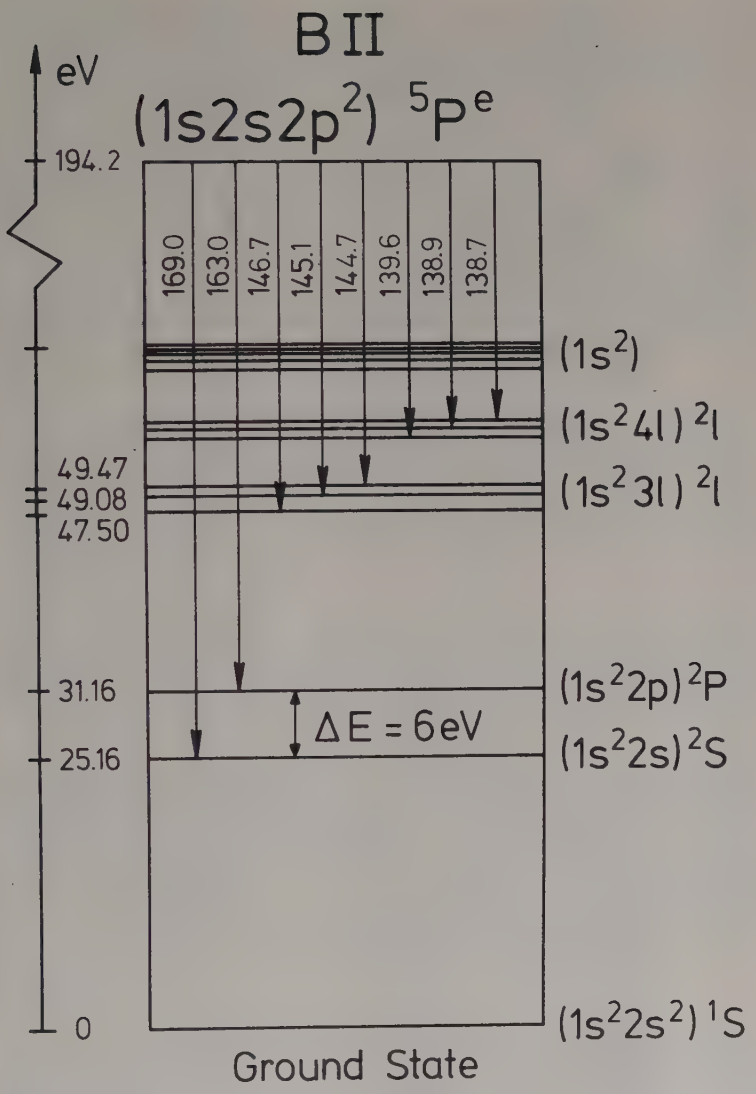

Fig. 107: Energy level diagram for boron showing autoionizing transitions from the $(1s2s2p^2)\ ^5P$ state in BII. Transitions leading to the $(1s^2nl)\ ^2L$ $(n^2 3)$ final ionic states are higher order processes.

mic plot as indicated in Fig. 106. It is apparent from this figure that two peaks occur on the low-energy tail of the (1s2s2p) $^4P^o$ peak. These low-energy lines appearing at $E_{CM} \simeq$ 139 eV ($E_{LAB} \simeq$ 211.4 eV) and $E_{CM} \simeq$ 146 eV ($E_{LAB} \simeq$ 219.8 eV) might be explained as three electron autoionization transitions characterized by simultaneous filling of a K-shell hole and excitation of a valence-shell electron with emission of a single electron. The interpretation of these low-energy peaks as three electron Auger processes requires that all other possibilities be ruled out. Alternative possibilities include the following: (a) Short-lived Coulomb autoionizing states such as $1s2s^2$ and $1s2s^22p$ may be cascade fed through long-lived systems at higher excitation. (b) Sputtered carbon atoms and molecular clusters may be excited by 285 keV boron impact. These possibilities can be ruled out by energetic considerations. It should be noted that the BIII ($1s2s^2$) $^2S \rightarrow (1s^2\varepsilon s)$ ^2S and the BII ($1s2s^22p$) $^3P^o \rightarrow (1s^22p\varepsilon s)$ $^3P^o$ Auger transitions occur at $E_{CM} \simeq$ 155 eV and $E_{CM} \simeq$ 161.6 eV, respectively. Furthermore, the Auger deexcitation of carbon atoms and molecular clusters emerging from the target should not lead to line groups around $E_{LAB} \simeq$ 211.4 eV and $E_{LAB} \simeq$ 219.8 eV. A further possibility which can also be ruled out is the excitation of restgas atoms and molecules.

We are left, then, with metastable autoionizing quintet states of the type 1s2lnl'n'l" ($n, n' \geq 2$) to explain the observed satellite structures. More specifically, the following three electron transitions are most probable (see Fig. 107):

$(1s2s2p^2)$ $^5P \rightarrow 1s^23s\varepsilon s(\varepsilon d)$

$(1s2s2p^2)$ $^5P \rightarrow 1s^23p\varepsilon p$

$(1s2s2p^2)$ $^5P \rightarrow 1s^23d\varepsilon s$

$(1s2s2p^2)$ $^5P \rightarrow 1s^24s\varepsilon s(\varepsilon d)$

$(1s2s2p^2)$ $^5P \rightarrow 1s^24p\varepsilon p$

$(1s2s2p^2)$ $^5P \rightarrow 1s^24d\varepsilon s.$

As can be seen from Figs. 106 and 107 the $1s2s2p^2 \rightarrow 1s^2 n l \varepsilon l'$ ($n \geq 3$) three electron transitions are converging to the $1s2s2p^2 \rightarrow 1s^2 \infty l \varepsilon l'$ low-energy series limit at 131.13 eV. Underlying the validity of the central field approximation only $\Delta l = 0$, i.e. monopole transitions (shake-up) would be allowed, leading to the $1s^2np$ ($n \geq 3$) and $1s^2ns$ ($n \geq 3$) final ionic states. It should be noted that for highly excited states such as $1s2s2p^2$ strong deviations from the central field may occur, so that $\Delta l \neq 0$ electron promotion should be allowed as well. It is apparent from Fig. 106 that the satellite structures decrease with increasing Δn, which supports our interpretation if the $1/\Delta n^3$-rule is accepted for the three electron process.

So far not mentioned small features appear on the high and low energy side of the spectrum (see Fig. 106). They could arise due to autoionization of BII $1s2s2pnl\ ^5L$ terms with $n \geq 3$ decaying alternatively to the $1s^22s$, $1s^22p$ and $1s^2nl$ ($n \geq 3$) final ionic states.

The experimental results exhibit four prominent features which we believe can be attributed to ^4L, ^5L and ^6L Auger transitions. The three strongest lines are interpreted due to autoionization of quartet and quintet terms. We assigned the fourth line due to autoionization of BI five-electron sextet terms. However, further experimental evidence has to be found for five-electron sextet systems. Furthermore, we have observed satellite lines which were assigned due to autoionization of quintet states in BII. As a consequence of the strong population of quintet terms radiative transitions among higher members of the quintet series are expected to occur, but have not been reported yet in the literature.

Carbon: The decay modes of the lowest lying metastable autoionizing levels in carbon are represented in Fig. 108. It is seen that the most metastable carbon terms are (in order of increasing multiplicity): $(1s2s2p)\ ^4P^o = {}^4P^o(1)$, $(1s2s2p^2)\ ^5P = {}^5P(1)$, $(1s2s2p^3)\ ^6S^o = {}^6S^o(1)$ and $(1s2s2p^3 3s)\ ^7S^o = {}^7S^o(1)$. Fig. 109

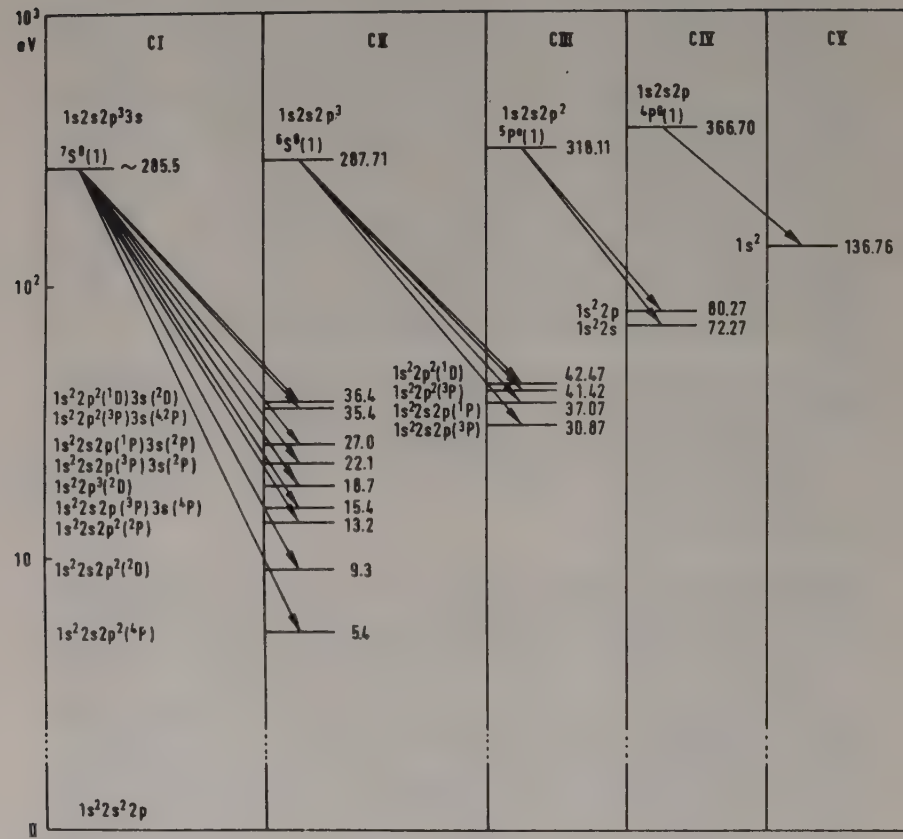

Fig. 108: Partial energy level diagram representing autoionizing decays of the $^4P^o(1)$, $^5P(1)$, $^6S^o(1)$ and $^7S^o(1)$ terms in carbon. Autoionization transitions are indicated by arrows. The excitation energies (Saf 69) are given above the $1s^22s^22p$ ground state in CII.

shows a 2.6 nsec delayed spectrum in the energy range from 0 to 450 eV (E_{LAB}). The high-energy spectral features are associated with the decay of lithium-like $^4P^o(1)$, beryllium-like $^5P(1)$,

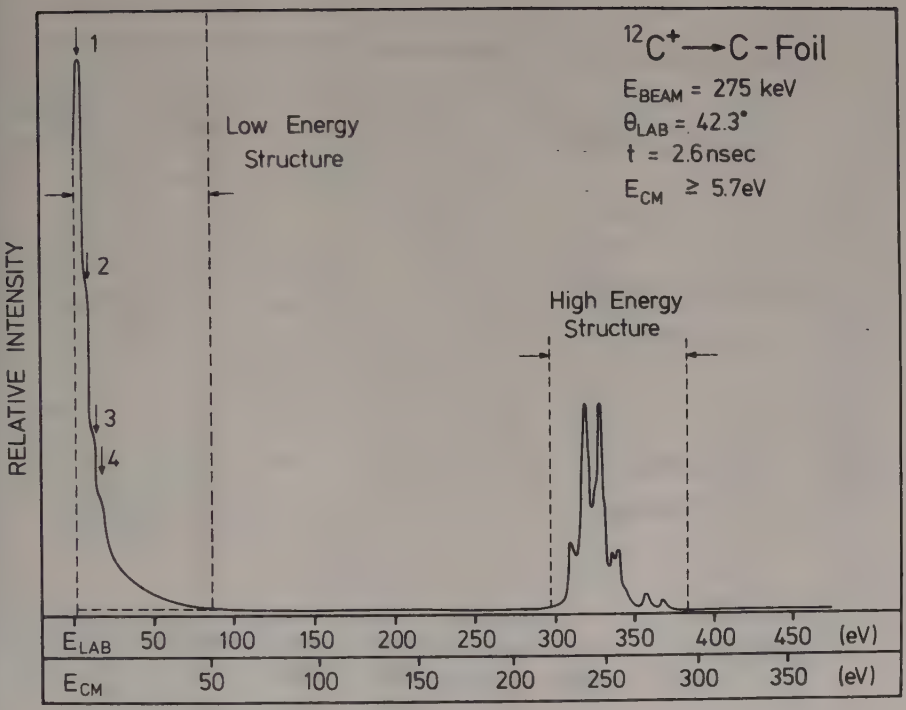

Fig. 109: Spectrum of electrons from highly excited carbon projectiles undergoing decay in flight.

boron-like $^{6}S^{o}$ and carbon-like $^{7}S^{o}$ terms. At 300 keV beam energy core-excited levels belonging to the charge state 0, 1 and 2 are populated preferentially. Hence, the strongest peaks in the high-energy structure around $E_{CM} \simeq 240$ eV (see Fig. 109) is dominated by transitions from four-electron quintet, five-electron sextet and six-electron septet terms. The low-energy structure below E_{CM} = 50 eV may be accounted for as ion-restgas spectra and due to decay of projectile states formed from configurations of the type CIII $1s^{2}nln'l'$, CII $1s^{2}nln'l'n"l"$ and CI $1s^{2}nln'l'n"l"n"'l"'$.

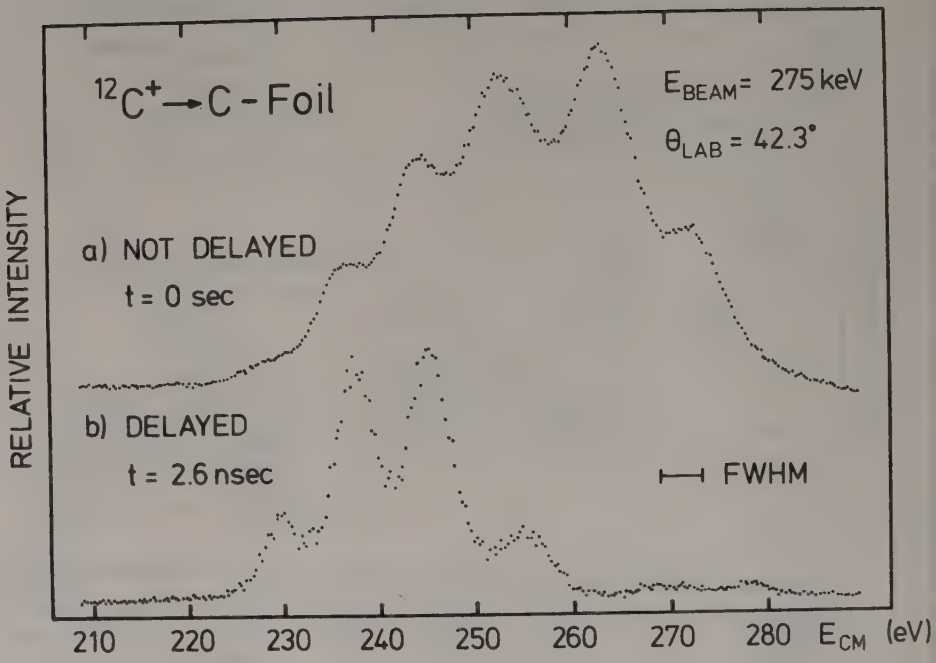

Fig. 110: Prompt and 2.6 nsec delayed electron spectrum of beam-foil excited carbon ions, plotted in the rest frame of the emitting ion.

The high energy portion of the prompt and 2.6 nsec delayed spectrum of autoionization electrons emitted in flight by a 275 keV C beam following passage through a carbon foil is indicated in Fig. 110. Due to specific selection rules the time-delayed carbon spectrum displayed in the lower part of Fig. 110 is less complicated than the upper spectrum with the foil in view of the electron spectrometer. The delayed autoionization electron spectrum is compared to theoretical predicted line energies (Saf 69) as indicated in Fig. 111. It is seen that four prominent peaks appear at 229.9, 237.5, 245.5, 255.5 eV (E_{CM}). The lowest energy peak is attributed to the

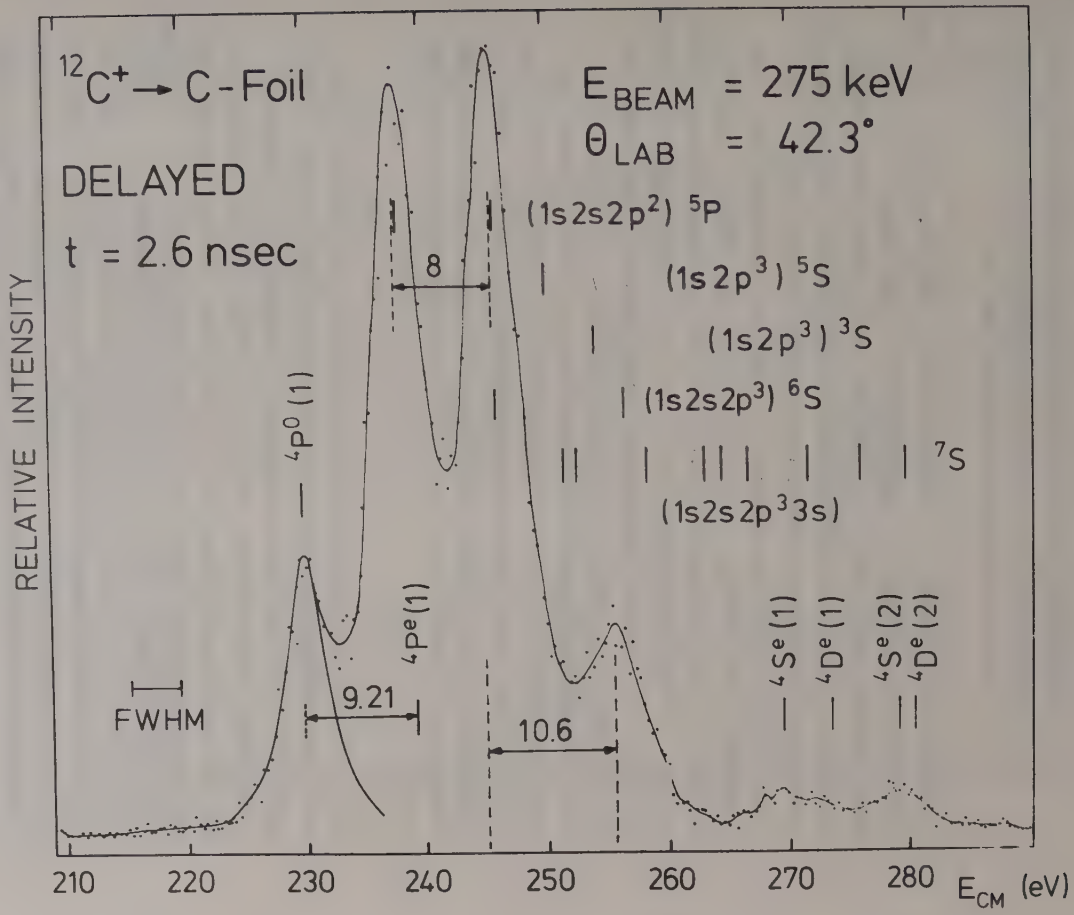
$^{12}C^{+}$ → C-Foil
DELAYED
t = 2.6 nsec
E_{BEAM} = 275 keV
θ_{LAB} = 42.3°
$(1s2s2p^2)\ ^5P$
$(1s2p^3)\ ^5S$
$(1s2p^3)\ ^3S$
$(1s2s2p^3)\ ^6S$
^7S
$(1s2s2p^3 3s)$
RELATIVE INTENSITY
$^4P^o(1)$
$^4P^e(1)$
$^4S^e(1)$
$^4D^e(1)$
$^4S^e(2)$
$^4D^e(2)$
8
9.21
10.6
FWHM
210
220
230
240
250
260
270
280
E_{CM} (eV)

Fig. 111: Spectrum of electrons emitted by 275 keV carbon ions undergoing decay in flight. The spectrum was recorded for a time delay of 2.6 nsec after excitation. The predicted line energies were deduced from the calculations of Safronova et al. (Saf 69).

lithium-like ($1s2s2p$) $^4P^o$ state in CIV. The energy scale in the center-of-mass frame was established by assigning a value of 229.9 eV to the $^4P^o(1)$ peak (Hol 67). We further note that the peak at 237.5 eV on the high-energy side of the $^4P^o(1)$ line is associated mainly with the Auger decay of the ($1s2s2p^2$) ^5P term in CIII. This line-identification is consistent with the ($1s2s2p^2$) $^5P \rightarrow 1s^2 2p\varepsilon p$ transition energy of Schwarz et al. (Schwa 76) and Schneider et al. (Br 76c). A typical decay curve at $E_{CM} \simeq 238.5$ eV is shown in Fig. 112. We would expect a short-lived ($\tau \simeq 1.1$ nsec) component to appear due to autoionization of the CIV $^4P(1)$ level. A striking result of Fig. 112 is a major decay component with an average mean life of about 3.7 nsec. We have not identified the source of this 3.7 nsec decay. In addition three long-lived components originating from autoionization of the ($1s2s2p^2$) $^5P_{3,2,1}$ states in CIII (hyperfine coupling is zero) should contribute to the observed decay profile.

We next turn to the interpretation of the peak at 245.5 eV, which is a blend of lines due to autoionization of the $^5P(1)$ and $^6S^o(1)$ states. This assumption is supported by recently calculated term energies of carbon 1s-hole states (Schwa 76, Br 76c) and experimental data of Schneider et al. (Schnei 76a). Thus Schneider and coworkers predict the ($1s2s2p^2$) $^5P \rightarrow 1s^2 2s\varepsilon s$ (εd) and ($1s2s2p^3$) $^6S^o \rightarrow (1s^2 2p^2)\ ^3P\varepsilon p$ transitions to appear at 245.5 and 245 eV, respectively. The remaining intense peak at 255.5 eV should result mainly from the ($1s2s2p^3$) $^6S^o \rightarrow (1s^2 2s2p)\ ^3P^o \varepsilon s(\varepsilon d)$ Auger decay. It is also to be expected that autoionization lines originating from ($1s2s2p^3 3s$) $^7S^o$ states will be present in the delayed carbon spectra. In fact the peaks above

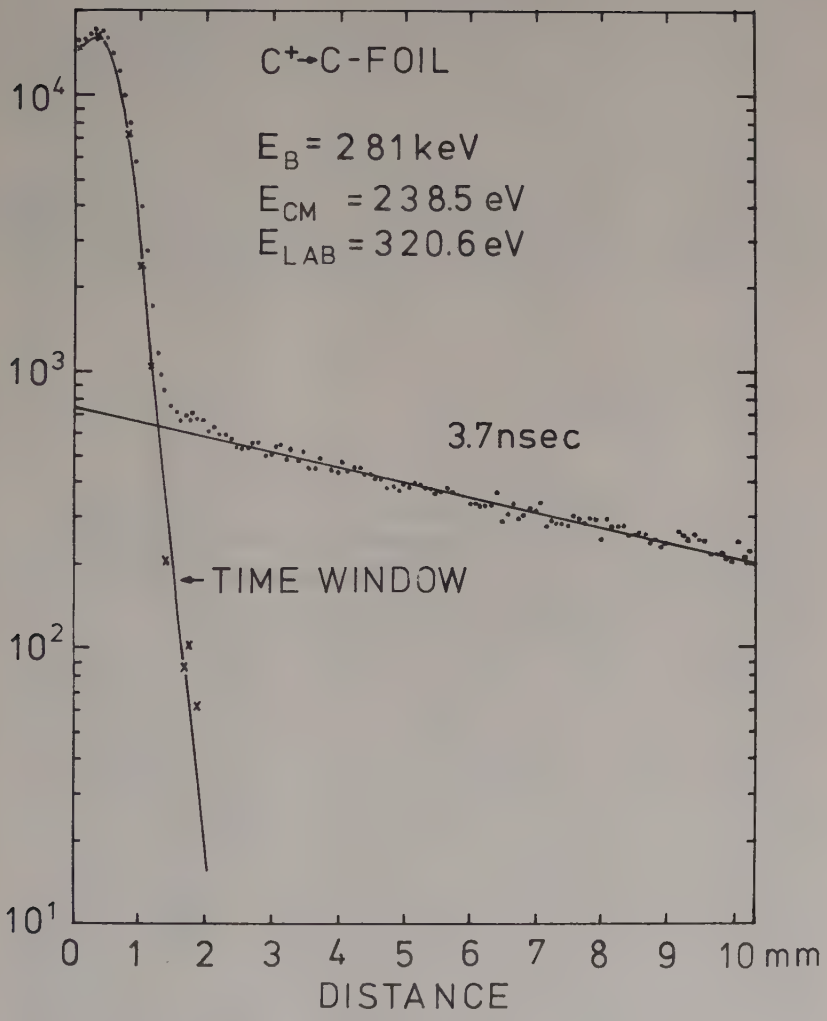
C+→C-FOIL
E_B = 281 keV
E_CM = 238.5 eV
E_LAB = 320.6 eV
3.7nsec
TIME WINDOW
10^4
10^3
10^2
10^1
0 1 2 3 4 5 6 7 8 9 10 mm
DISTANCE

Fig. 112: Decay curve at $E_{CM} \simeq 238.5$ eV for a carbon beam of about 281 keV. The full line represents the best single exponential fit to the experimental data yielding an average mean life of 3.7±1 nsec. The difference between this line and the experimental data points are denoted by crosses.

160 eV may be a composite of lines arising from lithium-like quartet states and carbon-like septet states. Finally, we would like to mention that branching ratio studies associated with the $(1s2s2p^2)\ ^5P$ and $(1s2s2p^3)\ ^6S^o$ decays were also done (Br 76c).

4. Concluding Remarks

a) Triply Excited Terms

In conclusion, autoionization lines of 2-, 3-, 4-, 5- and 6-electron systems for $Z \leq 6$ were observed. The most prominent spectral features in the prompt electron emission spectra were identified by comparison to predicted line energies. It was shown that core-excited states characterized by double K-shell vacancies are produced with considerable yield in the beam-foil interaction process. On the basis of recently calculated term values assignments of spectral lines were made in the prompt Li, Be and B spectra for autoionization transitions arising from doubly excited helium-like and triply excited lithium-like states. Specifically we identified two strong peaks in the beryllium spectrum as decays originating from triply excited $(2s^2 2p)\ ^2P^o$ and $(2s2p^2)\ ^2S$ states. This is the first time that such promptly decaying three-electron levels of positive ions for $Z \leq 6$ have been observed. Another important aspect of this work is the determination of relative production cross sections from the intensities of the observed autoionization structures. Information regarding single and double K-shell removal in 300 keV Li^+ → C-foil, Be^+ → C-foil and B^+ → C-foil collisions is summarized in Table 29. As can be seen, the difference in exci-

Table 29: Comparison of relative vacancy production cross sections for 300 keV Li^+, Be^+ and B^+ ions on carbon foils

Incident Ion	Beam Energy keV	Number of K-Shell Vacancies	Initial Configurations (n, n', n", n"' ≥ 2)	Relative Cross Section $\sigma_i / \sum_{j=1}^{n} \sigma_j$	const x σ_i
$^7Li^+$	300	1	1snln'l'	33.6 %	1
		2	nln'l'n"l"	64.4 %	1.97
		2	nln'l'		
$^9Be^+$	300	1	1snln'l'n"l"	69.0 %	1
		1	1snln'l'		
		2	nln'l'n"l"n"' l"'	31.0 %	0.45
		2	nln'l'n"l"		
		2	nln'l'		
$^{11}B^+$	300	1	1snln'l'n"l"n"' l"'	90.0 %	1
		1	1snln'l'n"l"		
		1	1snln'l'		
		2	nln'l'n"l"n"' l"' $n^{iv}l^{iv}$	10.0 %	0.11
		2	nln'l'n"l"n"' l"'		
		2	nln'l'n"l"		
		2	nln'l'		

tation of single and double K-hole states is very pronounced for Li^+ → C-foil and Be^+ → C-foil bombardment. The formation of K-shell vacancies in beam-foil excitation is of particular interest since numerous autoionizing or optically decaying ionic states may be populated via Auger cascades from levels of higher excitation and lower charge state. It is anticipated that many more lines due to the great number of possible autoionization transitions remained unresolved. For an unambiguous interpretation of the closely structures at higher energies the resolution of the apparatus must be improved. This can be realized by reducing the angular spread of the entrance aperture of the electron spectrometer to less than ±0.5 degrees and by using higher beam velocities (1 to 2 MeV) in conjunction with thinner foils (3 $\mu g/cm^2$). Furthermore, more exact theoretical values for transition energies, transition probabilities and branching ratios associated with two-to-six electron systems are urgently needed. In addition, more advanced experimental techniques, such as electron-ion, electron-electron and electron-photon coincidence measurements could help to classify presently unidentified lines.

b) Quartet-, Quintet-, and Sextet Terms

The principal feature of this work is the observation and identification of metastable autoionizing lithium-like quartet, beryllium-like quintet and boron-like sextet states. Thus we found evidence for appreciable population of

(i) three-electron ($1s2s2p$) $^4P^o$ terms in LiI, BeII, BIII and CIV,

(ii) four-electron ($1s2s2p^2$) ^5P terms in BeI, BII and CIII, and

(iii) five-electron ($1s2s2p^3$) $^6S^o$ terms in BI and CII.

The experimentally deduced term energies as indicated in Table 30 may be useful for further theoretical approximations of wave-

Table 30: Experimental and theoretical values for the energies of some metastable autoionizing states in beryllium, boron and carbon (energies in eV). The term energies are measured from the corresponding ionic ground state.

System	State	Energy
BeI	$(1s2s2p^2)\ ^5P$	115.7 0.5[a] 115.6[b]
BII	$(1s2s2p^2)\ ^5P$	194.2 0.5[a] 194[b]
BI	$(1s2s2p^3)\ ^6S^o$	189.8 0.5[a] 189.6[b]
CIII	$(1s2s2p^2)\ ^5P$	293.5 0.5[a] 293.4[b]
CII	$(1s2s2p^3)\ ^6S^o$	286.3 0.5[a] 286.4[b]
CI	$(1s2s2p^3 3s)\ ^7S^o$	293.7[b]

Table footnote: a = this work; b = Schwarz and Chang (Schwa 76, Schnei 76a, Br 76).

functions of three-to-five electron systems. The existence of long-lived autoionizing states of high spin and high excitation is of considerable importance, since as yet unidentified lines in the optical beam-foil spectra may arise from transitions among quintet and sextet terms. We studied also decay profiles of beryllium and carbon states by measuring the counting rate as a function of the target position. The prominent peaks in the delayed beryllium spectra were found to have complex decay curves, in the sense that more than one exponential was needed to fit the data. For the first time we succeeded in measuring the BeII $(1s2p^2)\ ^4P$ decay rate by detecting the Auger electron emission. In addition we studied the autoionization decay of the $(1s2s2p)\ ^4P^o$ term in BeII as a function of time of flight.

The decay curve indicates a pronounced growing-in cascade, most probably due to electric dipole transitions from higher lying quartet levels. For the $(1s2s2p^2)\ ^5P$ term in BeI an average mean life of the order of 132 nsec was estimated. For the cases of nonzero nuclear spin ($I \neq 0$) the hyperfine interaction mixes electron states of different total angular momentum J. This break-down of IJ coupling is evidently strong for states with unsaturated s electrons and should produce different lifetimes for the different hyperfine components F (differential metastability with respect to F). However, no such effects have been observed so far in the decays of metastable autoionizing states. Finally, beam-foil interaction generally leads to nonisotropically excited projectile states. The Auger electrons emitted in the subsequent decay will have a nonisotropic angular distribution depending on the relative population $\sigma|M_J|$ of magnetic substates M_J of the excited atomic system. It is also to be excepted, that such coherently excited, metastable autoionizing states (fine structure splitting << width of level IJF) give rise to interference effects due to decay to the adjacent continuum. This effect may cause superimposed osciallations in the time differential detection of the decay profiles. The frequencies of such "zero-field electron beats" would correspond to the fine- and hyperfine structure splittings of the long-lived autoionizing levels. An interesting extension of this work would be to measure the angular distribution of the emitted electrons and to study decay curves of metastable autoionizing states using higher time resolution.

c) Satellite Structures

Three electron Auger transitions of the type LL-MMM in which to M-electrons fill simultaneously two L-vacancies and a third M-electron is emitted, have been observed recently by Afrosimov et al. (Af 75). The possibility of such decay in triply excited lithium-like systems has first been suggested by Bruch et al. (Br 75b). In this work we studied three electron autoionization

transitions of the type $1s2s2p^2 \rightarrow 1s^2nsεs(εd)$, $1s2s2p^2 \rightarrow 1s^2npεp$ and $1s2s2p^2 \rightarrow 1s^2ndεs$ in which the energy released in the transition is distributed among two electrons, one of them being ejected and the other being transferred to an excited level. Thus two peaks on the low-energy side of the delayed boron spectrum were attributed to the initial $(1s2s2p^2)\ ^5P$ state in BII decaying to the $1s^231$ (l = 0, 1, 2) and the $1s^241$ (l = 0, 1, 2) final ionic levels. This is the first time that such three-electron transitions of long-lived beryllium-like states have been observed. We thus suspect that the presence of low-energy and high-energy satellite lines may be a general phenomenon in highly excited ion beams. It is particular interesting to note that spectroscopy of high energy satellite structures appearing on the high energy side of the normal lines may give valuable information about lithium-like and beryllium-like systems having double K-shell vacancies. Some predicted line energies corresponding to three electron autoionization transitions in LiI, BeII, BIII and CIV are summarized in Table 31. Finally, highly excited states can also decay via radiative Auger effect (radiative autoionization). In this process a photon and an electron are emitted simultaneously (Åb 75, Ris 75). The photons emitted have a continuous distribution of energies. To be specific the helium-like $(2p^2)\ ^3P$ term can either decay via the E1 transitions

$$(2p^3)\ ^3P \rightarrow (2s2p)\ ^3P + \hbar\omega$$

$$(2p^3)\ ^3P \rightarrow (1s2p)\ ^3P + \hbar\omega$$

or via radiative Auger effect, namely $(2p^2)\ ^3P \rightarrow (1sεp)\ ^3P^o + \hbar\omega$ (continuum distribution). It should be noted that no laboratory experiments have demonstrated the existence of the latter decay mode for doubly excited states in LiII, BeIII, BIV and CV.

Table 31: Predicted line energies for some three electron autoionization transitions in LiI, BeII, BIII and CIV.

System	Initial State	Final State	Transition Energy eV
LiI	$(2s^2 2p)\ ^2P^o$	$(1s^2 \varepsilon p)\ ^2P^o$	137.2[a]
LiI	$(2s2p^2)\ ^2S$	$(1s^2 \varepsilon s)\ ^2S$	142.1[a]
BeII	$(2s^2 2p)\ ^2P^o$	$(1s^2 \varepsilon p)\ ^2P^o$	251.1[b]
BeII	$(2s2p^2)\ ^2P^o$	$(1s^2 \varepsilon s)\ ^2S$	258.5[b]
BIII	$(2s^2 2p)\ ^2P^o$	$(1s^2 \varepsilon p)\ ^2P^o$	399.0[b]
BIII	$(2s2p^2)\ ^2S$	$(1s^2 \varepsilon s)\ ^2S$	408.7[b]
CIV	$(2s^2 2p)\ ^2P^o$	$(1s^2 \varepsilon P)\ ^2P$	581.1[b]
CIV	$(2s2p^2)\ ^2S$	$(1s^2 \varepsilon s)\ ^2S$	593.2[b]

Table footnote: a = Bruch et al. (Br 75b); b = this work.

X. CONCLUSION

1. Comments on the Beam-Foil Interaction Process

In summary, it was shown that a high fraction of projectiles emerge from the foil in highly excited states characterized by K-shell vacancies. These core-excited states then decay via Coulomb autoionization provided the [SLJπ] quantum numbers of the initial and final states are unchanged. The final stage of the autoionization process is not necessarily the ground state of the resultant ion. Thus in many instances Auger cascades lead to optically excited states which in turn spontaneously decay to lower lying states by radiative transitions. Such Auger cascades following beam-foil excitation can cause a drastic repopulation of the projectile states within some hundred Angstroms of flight path. Some general aspects of the beam-foil interaction mechanism (Gar 70, And 71, And 72, Da 73, Gar 73, Da 75) can be summarized in the four processes:

(i) Inner-shell excitation in the foil interiour and surface region.

(ii) Electron capture at the foil surface.

(iii) Cascade induced repopulation immediately beyond the foil surface.

(iv) Decay of long-lived states via magnetic autoionization or radiative transitions in the region far downstream.

The beam-foil interaction process is illustrated in Fig. 113. It is seen that moving ions within the foil are surrounded by many electrons. For projectiles with $Z \leq 6$ the ions remain stripped in their path through the foil, i.e. the outer shell electrons are shared with the foil atoms. In other words, the commonly discrete outer states are spread out by collective interaction processes, while inner-shell excitation can occur. When the projectiles reach the foil surface outer excited states are created. It is very likely that most of the outer

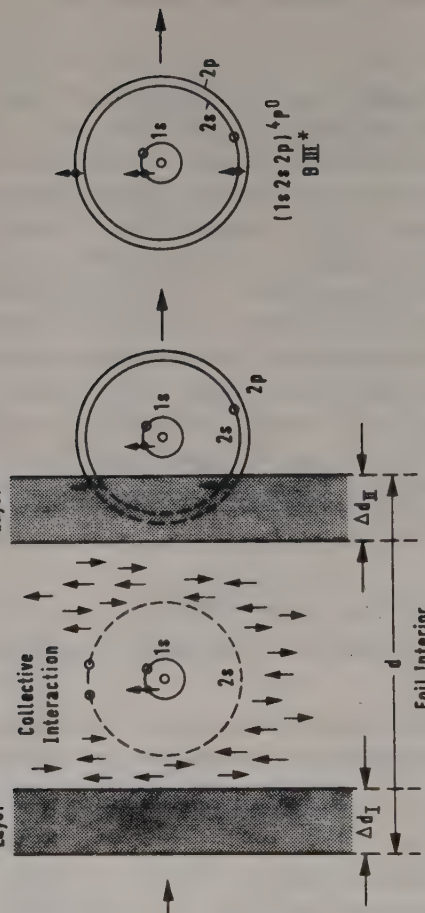

Fig. 113: Formation of beam-foil excited states with K-shell vacancies.

excited states are created. It is very likely that most of the outer excited states are produced by electron capture in the last monolayer of the foil. In particular, core-excited states may be produced predominantly from highly excited core ions as a result of capture of additional electrons into excited outer states (Dmi 76, Hve 76). In this way the strong population of core-excited states can be readily explained. Furthermore, multiply excited states with double K-shell vacancies may be produced by the same mechanism. For example, triply excited states in LiI characterized by double 1s-vacancies could be formed by attachement of three electrons to a bare lithium nucleus. In the vicinity of the foil surface such highly excited states will then release part of their excess energy via Coulomb autoionization and x-ray transitions. However, the deexcitation process is frequently complicated due to multi-stage cascade transitions. We note that for atomic systems with $Z \leq 6$ the autoionization rate is generally orders of magnitude greater than the radiative transition rate. Consequently, Auger decay should be in most cases the dominant cascade process. It is expected that Auger cascades strongly influence the production cross sections of a great number of excited states having lifetimes greater than 10^{-10} sec. Finally, we note that little is known experimentally or theoretically (McG 75) about the Auger cascade induced repopulation of highly excited states for projectiles with $Z \leq 6$.

2. Cascading via Autoionization and Transfer of Alignment

Another subject of current interest is the creation of alignment by beam-foil collisions. When electrons are captured from the last monolayer of the foil surface linear momentum is transferred in the direction of travel of the emerging particle. Let us take the incident beam axis as the axis of quantization. Then the linear momentum transfer has a component parallel to the quantization axis. This implies the population of $M_L = 0$ substates. There will be also a transverse component leading to the population of $M_L \neq 0$ substates. We note that the electron

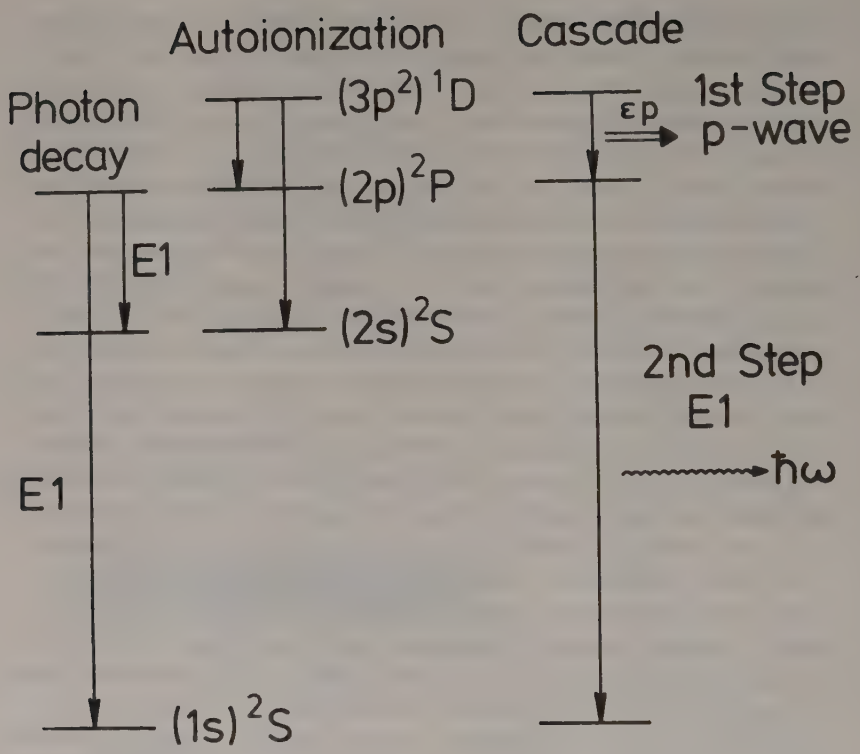

Fig. 114: Schematic representation of the $(3p^2)\ ^1D$ decay through a succession of an autoionization and E1 transition.

recombination process is independent of M_S since the relativistic interactions (e.g. spin-orbit, spin-other-orbit and spin-spin coupling) are assumed negligible when compared to the electrostatic forces. In general three physically processes can lead to an observable change of alignment:

(i) Alignment is transferred by collisions depending on the nature of the excitation process.

(ii) Alignment is exchanged between various internal degrees of freedom due to spin-orbit and hyperfine coupling, but

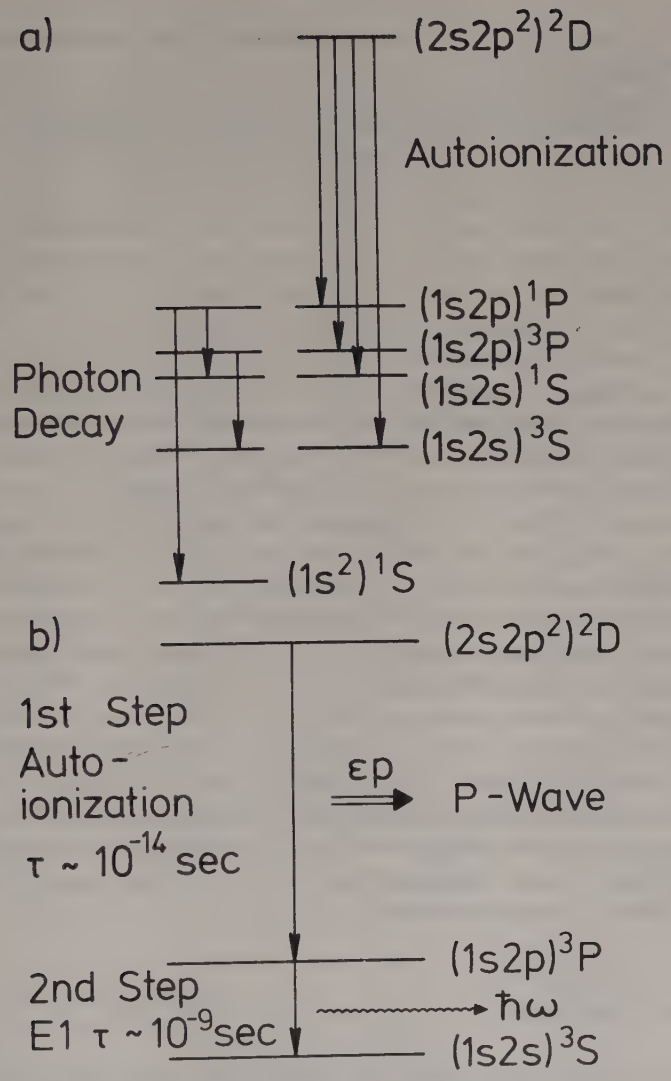

Fig. 115: Cascade scheme for the lithium-like $(2s2p^2)$ ^2D state. Fig. 1a indicates the cascade population of the $(1s2s)$ $^{3,1}S$ and $(1s2p)$ $^{3,1}P^o$ levels. Fig. 1b illustrates a two-step decay process.

the total alignment of the atomic system is conserved (Mac 76).

(iii) Alignment is carried away by radiative transitions (Be 72a, Du 73) and autoionization (Be 75, Mac 76).

In the following we restrict our attention to the deexcitation of the two-electron $(3p^2)\ ^1D$ and the three-electron $(2s2p^2)\ ^2D$ states (Fig. 114 and 115). It is seen from Fig. 114 that the $(3p^2)\ ^1D$ term decays via Coulomb autoionization to the hydrogen-like 2s and 2p levels. For example, in the $(3p^2)\ ^1D \rightarrow (2p\varepsilon p)\ ^1D$ Auger process a p electron is emitted, which carries away angular momentum, thus reducing the anisotropy in the following $(2p)\ ^2P^o \rightarrow (1s)\ ^2S$ or $(2p)\ ^2P^o \rightarrow (2s)\ ^2S$ radiative transitions. The cascade scheme for the triply excited $(2s2p^2)\ ^2D$ state is illustrated in Fig. 115. A typical two-step transition is depicted in Fig. 115b. As can be seen the $(2s2p^2)\ ^2D$ state decays via Coulomb autoionization to the $(1s2p\ ^3P^o\varepsilon p)\ ^2D$ continuum, while the residual $(1s2p)\ ^3P^o$ level is depleted via photon emission. From these examples it is clear that Auger cascades can produce a change in alignment. It is suggested that most beam-foil excited states are initially aligned but multiply excited. Much of the initial anisotropy is then carried away by Auger electron emission, thus reducing the anisotropy in the subsequent E1 transitions. From the viewpoint of planning future quantum beat experiments it is of considerable interest to know, which optically decaying levels are dominantly populated via Auger cascading.

3. Stark Quenching

It is suggested that capture of electrons on the last monolayer of the foil is responsible for most of the observed population of excited levels in beam-foil collisions. This mechanism may also explain the population of high angular momentum states having small energy separations. Such high angular momentum

levels are easily perturbed via Stark effect. It is very likely that electric fields near the foil surface induce redistribution of l states within a given n. For low l states,on the other hand,the quenching cross sections should be small. In conclusion, we note that the relative population of foil-excited states can be affected due to Stark quenching.

APPENDIX I: Some core excited configurations of 2-, 3-, 4-, 5-, and 6-electron atomic systems for $Z \leq 6$.

(i) One K-shell vacancy

m	$1s2s^2 2p^m$	$1s2s2p^{m+1}$	$1s2p^{m+2}$	Li	Be	B	C
0	$1s2s^2$	$1s2s2p$	$1s2p^2$	I	II	III	IV
1	$1s2s^2 2p$	$1s2s2p^2$	$1s2p^3$		I	II	III
2	$1s2s^2 2p^2$	$1s2s2p^3$	$1s2p^4$			I	II
3	$1s2s^2 2p^3$	$1s2s2p^4$	$1s2p^5$				I

(ii) Two K-shell vacancies

m	$2s^2 2p^{m+1}$	$2s2p^{m+2}$	$2p^{m+3}$	Li	Be	B	C
-1	$2s^2$	$2s2p$	$2p^2$	II	III	IV	V
0	$2s^2 2p$	$2s2p^2$	$2p^3$	I	II	III	IV
1	$2s^2 2p^2$	$2s2p^3$	$2p^4$		I	II	III
2	$2s^2 2p^3$	$2s2p^4$	$2p^5$			I	II
3	$2s^2 2p^4$	$2s2p^5$	$2p^6$				I

(iii) One K-shell vacancy, one outer nl-electron ($n \geq 3$)

m	$1s2s^2 2p^{m-1} nl$	$1s2s2p^m nl$	$1s2p^{m+1} nl$	Li	Be	B	C
0		$1s2snl$	$1s2pnl$	I	II	III	IV
1	$1s2s^2 nl$	$1s2s2pnl$	$1s2p^2 nl$		I	II	III
2	$1s2s^2 2pnl$	$1s2s2p^2 nl$	$1s2p^3 nl$			I	II
3	$1s2s^2 2p^2 nl$	$1s2s2p^3 nl$	$1s2p^4 nl$				I

(iv) Two K-shell vacancies, one outer nl-electron ($n \geq 3$)

m	$2s^2 2p^m nl$	$2s2p^{m+1} nl$	$2p^{m+2} nl$	Li	Be	B	C
0	$2s^2 nl$	$2s2pnl$	$2p^2 nl$	I	II	III	IV
1	$2s^2 2pnl$	$2s2p^2 nl$	$2p^3 nl$		I	II	III
2	$2s^2 2p^2 nl$	$2s2p^3 nl$	$2p^4 nl$			I	II
3	$2s^2 2p^3 nl$	$2s2p^4 nl$	$2p^5 nl$				I

(v) One K-shell vacancy, L-shell empty

m	$1s3s^2 3p^m$	$1s3s3p^{m+1}$	$1s3p^{m+2}$	Li	Be	B	C
0	$1s3s^2$	1s3s3p	$1s3p^2$	I	II	III	IV
1	$1s3s^2 3p$	$1s3s3p^2$	$1s3p^3$		I	II	III
2	$1s3s^2 3p^2$	$1s3s3p^3$	$1s3p^4$			I	II
3	$1s3s^2 3p^3$	$1s3s3p^4$	$1s3p^5$				I

(vi) K- and L-shell empty

m	$3s^2 3p^{m+1}$	$3s3p^{m+2}$	$3p^{m+3}$	Li	Be	B	C
-1	$3s^2$	3s3p	$3p^2$	II	III	IV	V
0	$3s^2 3p$	$3s3p^2$	$3p^3$	I	II	III	IV
1	$3s^2 3p^2$	$3s3p^3$	$3p^4$		I	II	III
2	$3s^2 3p^3$	$3s3p^4$	$3s3p^5$			I	II
3	$3s^2 3p^4$	$3s3p^5$	$3s3p^6$				I

APPENDIX II: The most prominent metastable autoionizing 2-, 3-, 4-, 5-, and 6-electron terms (LS coupling)

Isoelectronic Series	Number of Electrons	Ionic Configurations	Term Symbol	E 1 Transitions
helium-like	2	$2p^2$	$^3P^e$	yes
helium-like	2	2p3p	$^3P^e, ^1P^e$	yes
helium-like	2	2p3d	$^3D^o, ^1D^o$	yes
lithium-like	3	1s2s2p	$^4P^o$	no
lithium-like	3	$1s2p^2$	$^4P^e$	yes
lithium-like	3	$1s2p^2$	$^2P^e$	yes
lithium-like	3	$2p^3$	$^4S^o$	yes
beryllium-like	4	$1s2s2p^2$	$^5P^e$	no
beryllium-like	4	$1s2p^3$	$^5S^o$	yes
beryllium-like	4	$1s2p^3$	$^3S^o$	yes

Isoelectronic Series	Number of electrons	Ionic Configurations	Term Symbol	E 1 Transitions
beryllium-like	4	$1s2s2p(^4P)3s$	$^5P^o$	yes
beryllium-like	4	$1s2s2p(^4P)3p$	$^5S^e$, $^5P^e$, $^5D^e$	yes
beryllium-like	4	$1s2s2p(^4P)3d$	$^5P^o$, $^5D^o$, $^5F^o$	yes
beryllium-like	4	$1s2p^2(^4P)3s$	$^5P^e$	yes
beryllium-like	4	$1s2p^2(^4P)3p$	$^5S^o$, $^5P^o$, $^5D^o$	yes
beryllium-like	4	$1s2p^2(^4P)3d$	$^5P^e$, $^5D^e$, $^5F^e$	yes
boron-like	5	$1s2s2p^3$	$^6S^o$	no
boron-like	5	$1s2s2p^2(^5P)3s$	$^6P^e$	yes
boron-like	5	$1s2s2p^2(^5P)3p$	$^6S^o$, $^6P^o$, $^6D^o$	yes
boron-like	5	$1s2s2p^2(^5P)3d$	$^6P^e$, $^6D^e$, $^6F^e$	yes
boron-like	5	$1s2p^3(^5S)3s$	$^6S^o$	yes
boron-like	5	$1s2p^3(^5S)3p$	$^6P^e$	yes
boron-like	5	$1s2p^3(^5S)3d$	$^6D^o$	yes
carbon-like	6	$1s2s2p^3(^6S)3s$	$^7S^o$	no
carbon-like	6	$1s2s2p^3(^6S)3p$	$^7P^e$	yes
carbon-like	6	$1s2s2p^3(^6S)3d$	$^7D^o$	yes
carbon-like	6	$1s2s2p^2(^5P)3s3p$	$^7S^o$, $^7P^o$, $^7D^o$	likely
carbon-like	6	$1s2s2p2(^5P)3p^2$	$^7S^e$, $^7P^e$, $^7D^e$	yes

APPENDIX III: Magnetic Autoionization of the lowest quartet-, quintet-, sextet-, and septet terms for $Z \leq 6$.

Initial State	$^{2S+1}L_J$	Final State	$^{2S'+1}L'_{J'}$	ΔL	ΔS	ΔJ	Pure
1s2s2p	$^4P^o_{1/2}$	$1s^2\varepsilon p$	$^2P^o_{1/2}$	0	1	0	no
1s2s2p	$^4P^o_{3/2}$	$1s^2\varepsilon p$	$^2P^o_{3/2}$	0	1	0	no
1s2s2p	$^4P^o_{5/2}$	$1s^2\varepsilon p$	$^2P^o_{3/2}$	0	1	1	yes
1s2s2p	$^4P^o_{5/2}$	$1s^2\varepsilon f$	$^2F^o_{5/2}$	2	1	0	yes
$1s2s2p^2$	$^5P^e_1$	$1s^22p\varepsilon p$	$^3S^e_1$	1	1	0	no
$1s2s2p^2$	$^5P^e_1$	$1s^22p\varepsilon p$	$^3P^e_1$	0	1	0	no
$1s2s2p^2$	$^5P^e_1$	$1s^22p\varepsilon p$	$^1P^e_1$	0	2	0	no
$1s2s2p^2$	$^5P^e_1$	$1s^22p\varepsilon p$	$^3D^e_1$	1	1	0	no
$1s2s2p^2$	$^5P^e_1$	$1s^22s\varepsilon s$	$^3S^e_1$	1	1	0	no
$1s2s2p^2$	$^5P^e_1$	$1s^22s\varepsilon d$	$^3D^e_1$	1	1	0	no
$1s2s2p^2$	$^5P^e_2$	$1s^22p\varepsilon p$	$^3P^e_2$	0	1	0	no
$1s2s2p^2$	$^5P^e_2$	$1s^22p\varepsilon p$	$^3D^e_2$	1	1	0	no
$1s2s2p^2$	$^5P^e_2$	$1s^22p\varepsilon p$	$^1D^e_2$	1	2	0	no
$1s2s2p^2$	$^5P^e_2$	$1s^22s\varepsilon d$	$^3D^e_2$	1	1	0	no
$1s2s2p^2$	$^5P^e_2$	$1s^22s\varepsilon d$	$^1D^e_2$	1	2	0	no
$1s2s2p^2$	$^5P^e_3$	$1s^22p\varepsilon p$	$^3D^e_3$	1	1	0	no
$1s2s2p^2$	$^5P^e_3$	$1s^22s\varepsilon d$	$^3D^e_3$	1	1	0	no
$1s2s2p^3$	$^6S^o_{5/2}$	$1s^22p^2(^1D)\varepsilon p$	$^2D^o_{5/2}$	2	2	0	no
$1s2s2p^3$	$^6S^o_{5/2}$	$1s^22p^2(^3P)\varepsilon p$	$^4P^o_{5/2}$	1	1	0	no
$1s2s2p^3$	$^6S^o_{5/2}$	$1s^22p^2(^3P)\varepsilon p$	$^4D^o_{5/2}$	2	1	0	no
$1s2s2p^3$	$^6S^o_{5/2}$	$1s^22p^2(^3P)\varepsilon p$	$^2D^o_{5/2}$	2	2	0	no
$1s2s2p^3$	$^6S^o_{5/2}$	$1s^22s2p(^3P)\varepsilon s$	$^4P^o_{5/2}$	1	1	0	no
$1s2s2p^3$	$^6S^o_{5/2}$	$1s^22s2p(^3P)\varepsilon d$	$^4P^o_{5/2}$	1	1	0	no
$1s2s2p^3$	$^6S^o_{5/2}$	$1s2s2p(^3P)\varepsilon d$	$^4D^o_{5/2}$	2	1	0	no

Initial State	$^{2S+1}L_J$	Final State	$^{2S'+1}L'_{J'}$	ΔL	ΔS	ΔJ	Pure
$1s2s2p^3$	$^6S^o_{5/2}$	$1s^2 2s2p(^3P)\varepsilon d$	$^2D^o_{5/2}$	2	2	0	no
$1s2s2p^3$	$^6S^o_{5/2}$	$1s^2 2s2p(^1P)\varepsilon d$	$^2D^o_{5/2}$	2	2	0	no
$1s2s2p^3 3s$	$^7S^o_3$	$1s^2 2p^2 3s(^2D)\varepsilon p$	$^3D^o_3$	2	2	0	no
$1s2s2p^3 3s$	$^7S^o_3$	$1s^2 2p^2 3s(^4P)\varepsilon p$	$^5P^o_3$	1	1	0	no
$1s2s2p^3 3s$	$^7S^o_3$	$1s^2 2p^2 3s(^4P)\varepsilon p$	$^3D^o_3$	2	2	0	no
$1s2s2p^3 3s$	$^7S^o_3$	$1s^2 2p^2 3s(^4P)\varepsilon p$	$^5D^o_3$	2	1	0	no
$1s2s2p^3 3s$	$^7S^o_3$	$1s^2 2p^2 3s(^2P)\varepsilon p$	$^3D^o_3$	2	2	0	no
$1s2s2p^3 3s$	$^7S^o_3$	$1s^2 2p^3(^2D)\varepsilon s$	$^3D^o_3$	2	2	0	no
$1s2s2p^3 3s$	$^7S^o_3$	$1s^2 2s2p3s(^4P)\varepsilon s$	$^5P^o_3$	1	1	0	no
$1s2s2p^3 3s$	$^7S^o_3$	$1s^2 2s2p3s(^4P)\varepsilon d$	$^5P^o_3$	1	1	0	no
$1s2s2p^3 3s$	$^7S^o_3$	$1s^2 2s2p3s(^4P)\varepsilon d$	$^5D^o_3$	2	1	0	no
$1s2s2p^3 3s$	$^7S^o_3$	$1s^2 2s2p3s(^4P)\varepsilon d$	$^3D^o_3$	2	2	0	no
$1s2s2p^3 3s$	$^7S^o_3$	$1s^2 2s2p3s(^2P)\varepsilon d$	$^3D^o_3$	2	2	0	no
$1s2s2p^3 3s$	$^7S^o_3$	$1s^2 2s2p^2(^4P)\varepsilon p$	$^5P^o_3$	1	1	0	no
$1s2s2p^3 3s$	$^7S^o_3$	$1s^2 2s2p^2(^4P)\varepsilon p$	$^5D^o_3$	2	1	0	no
$1s2s2p^3 3s$	$^7S^o_3$	$1s^2 2s2p^2(^4P)\varepsilon p$	$^3D^o_3$	2	2	0	no
$1s2s2p^3 3s$	$^7S^o_3$	$1s^2 2s2p^2(^2D)\varepsilon p$	$^3D^o_3$	2	2	0	no
$1s2s2p^3 3s$	$^7S^o_3$	$1s^2 2s2p^2(^2P)\varepsilon p$	$^3D^o_3$	2	2	0	no

APPENDIX IV: Autoionization of some triply excited states

Initial State	Final State	Comment
$(2s^2 2p)\ ^2P^o$	$(1s2p(^{3,1}P)\varepsilon s)\ ^2P^o$	rapid
	$(1s2s(^{3,1}S)\varepsilon p)\ ^2P^o$	rapid
	$(1s^2(^1S)\varepsilon p)\ ^2P^o$	less likely
$(2s2p^2)\ ^4P^e$	$(1s2p(^3P)\varepsilon p)\ ^4P^e$	rapid
$(2s2p^2)\ ^2P^e$	$(1s2p(^{3,1}P)\varepsilon p)\ ^2P^e$	rapid
$(2s2p^2)\ ^2D^e$	$(1s2p(^{3,1}P)\varepsilon p)\ ^2D^e$	rapid
	$(1s2s(^{3,1}S)\varepsilon d)\ ^2D^e$	rapid
	$(1s^2\ (^1S)\varepsilon d)\ ^2D^e$	less likely
$(2s2p^2)\ ^2S^e$	$(1s2p(^{3,1}P)\varepsilon p)\ ^2S^e$	rapid
	$(1s2s(^{3,1}S)\varepsilon s)\ ^2S^e$	rapid
	$(1s^2\ (^1S)\varepsilon s)\ ^2S^e$	less likely
$(2p^3)\ ^4S^o$	$(1s2p(^{3,1}P)\varepsilon s)\ ^{4,2}P^o$	metastable
	$(1s2p(^{3,1}P)\varepsilon d)\ ^{4,2}P^o$	metastable
	$^{4,2}D^o,\ ^{4,2}F^o$	metastable
	$(1s2s(^{3,1}S)\varepsilon p)\ ^{4,2}P^o$	metastable
$(2p^3)\ ^2P^o$	$(1s2p(^{3,1}P)\varepsilon s)\ ^2P^o$	rapid
	$(1s2p(^{3,1}P)\varepsilon d)\ ^2P^o$	rapid
	$(1s2s(^{3,1}S)\varepsilon p)\ ^2P^o$	rapid
	$(1s^2\ (^1S)\varepsilon p)\ ^2P^o$	less likely
$(2p^3)\ ^2D^o$	$(1s2p(^{3,1}P)\varepsilon d)\ ^2D^o$	rapid

APPENDIX V: Coulomb autoionization of some state configurations with 4 electrons.

Initial state	Final state	$^{2s+1}L^{\pi}$	J
$1s2s^2 2p$	$1s^2 2p\varepsilon s$	$^3P^o$	0, 1, 2
$1s2s^2 2p$	$1s^2 2s\varepsilon p$	$^3P^o$	0, 1, 2
$1s2s^2 2p$	$1s^2 2p\varepsilon s$	$^1P^o$	1
$1s2s^2 2p$	$1s^2 2s\varepsilon p$	$^1P^o$	1
$1s2s2p^2$	$1s^2 2p\varepsilon p$	$^3S^e$	1
$1s2s2p^2$	$1s^2 2s\varepsilon s$	$^3S^e$	1
$1s2s2p^2$	$1s^2 2p\varepsilon p$	$^1S^e$	0
$1s2s2p^2$	$1s^2 2s\varepsilon s$	$^1S^e$	0
$1s2s2p^2$	$1s^2 2p\varepsilon p$	$^1P^e$	1
$1s2s2p^2$	$1s^2 2p\varepsilon p$	$^3_1P^e$	0, 1, 2
$1s2s2p^2$	$1s^2 2p\varepsilon p$	$^3_2P^e$	0, 1, 2
$1s2s2p^2$	$1s^2 2p\varepsilon p$	$^3D^e$	1, 2, 3
$1s2s2p^2$	$1s^2 2s\varepsilon d$	$^3D^e$	1, 2, 3
$1s2s2p^2$	$1s^2 2p\varepsilon p$	$^1D^e$	2
$1s2s2p^2$	$1s^2 2s\varepsilon d$	$^1D^e$	2
$1s2p^3$	$1s^2 2p\varepsilon s$	$^3P^o$	0, 1, 2
$1s2p^3$	$1s^2 2p\varepsilon d$	$^3P^o$	0, 1, 2
$1s2p^3$	$1s^2 2p\varepsilon s$	$^1P^o$	1
$1s2p^3$	$1s^2 2p\varepsilon d$	$^1P^o$	1
$1s2p^3$	$1s^2 2p\varepsilon d$	$^3D^o$	1, 2, 3
$1s2p^3$	$1s^2 2p\varepsilon d$	$^1D^o$	2
$1s2s2p(^4P)3s$	$1s^2 3s\varepsilon p$	$^3_1P^o$	0, 1, 2
$1s2s2p(^4P)3s$	$1s^2 2p\varepsilon s$	$^3_1P^o$	0, 1, 2
$1s2s2p(^4P)3s$	$1s^2 2s\varepsilon p$	$^3_1P^o$	0, 1, 2
$1s2s2p(^2P)3s$	$1s^2 3s\varepsilon p$	$^3_2P^o$	0, 1, 2
$1s2s2p(^2P)3s$	$1s^2 2p\varepsilon s$	$^3_2P^o$	0, 1, 2
$1s2s2p(^2P)3s$	$1s^2 2s\varepsilon p$	$^3_2P^o$	0, 1, 2

Initial state	Final state	$^{2s+1}L^{\pi}$	J
$1s2s2p(^2P)3s$	$1s^2 3s\epsilon p$	$^1P^o$	1
$1s2s2p(^2P)3s$	$1s^2 2p\epsilon s$	$^1P^o$	1
$1s2s2p(^2P)3s$	$1s^2 2s\epsilon p$	$^1P^o$	1
$1s2p^2(^2S)3s$	$1s^2 3s\epsilon s$	$^3S^e$	1
$1s2p^2(^2S)3s$	$1s^2 2s\epsilon s$	$^3S^e$	1
$1s2p^2(^2S)3s$	$1s^2 2p\epsilon p$	$^3S^e$	1
$1s2p^2(^2S)3s$	$1s^2 3s\epsilon s$	$^1S^e$	0
$1s2p^2(^2S)3s$	$1s^2 2s\epsilon s$	$^1S^e$	0
$1s2p^2(^2S)3s$	$1s^2 2p\epsilon p$	$^1S^e$	0
$1s2p^2(^4P)3s$	$1s^2 2p\epsilon p$	$^3P^e_1$	0, 1, 2
$1s2p^2(^2P)3s$	$1s^2 2p\epsilon p$	$^3P^e_2$	0, 1, 2
$1s2p^2(^2P)3s$	$1s^2 2p\epsilon p$	$^1P^e$	1
$1s2p^2(^2D)3s$	$1s^2 3s\epsilon d$	$^3D^e$	1, 2, 3
$1s2p^2(^2D)3s$	$1s^2 2s\epsilon d$	$^3D^e$	1, 2, 3
$1s2p^2(^2D)3s$	$1s^2 2p\epsilon p$	$^3D^e$	1, 2, 3
$1s2p^2(^2D)3s$	$1s^2 3s\epsilon d$	$^1D^e$	2
$1s2p^2(^2D)3s$	$1s^2 2s\epsilon d$	$^1D^e$	2
$1s2p^2(^2D)3s$	$1s^2 2p\epsilon p$	$^1D^e$	2

APPENDIX VI: Coulomb autoionization of some state configurations with 5 electrons

Initial state	Final state	$^{2s+1}L^{\pi}$	J
$1s2s^2 2p^2$	$1s^2 2s^2 \varepsilon s$	$^2S^e$	1/2
$1s2s^2 2p^2$	$1s^2 2s2p(^3P)\varepsilon p$	$^2S^e$	1/2
$1s2s^2 2p^2$	$1s^2 2s2p(^1P)\varepsilon p$	$^2S^e$	1/2
$1s2s^2 2p^2$	$1s^2 2p^2(^1S)\varepsilon s$	$^2S^e$	1/2
$1s2s^2 2p^2$	$1s^2 2s2p(^3P)\varepsilon p$	$^4P^e$	1/2, 3/2, 5/2
$1s2s^2 2p^2$	$1s^2 2p^2(^3P)\varepsilon s$	$^4P^e$	1/2, 3/2, 5/2
$1s2s^2 2p^2$	$1s^2 2s2p(^3P)\varepsilon p$	$^2P^e$	1/2, 3/2
$1s2s^2 2p^2$	$1s^2 2s2p(^1P)\varepsilon p$	$^2P^e$	1/2, 3/2
$1s2s^2 2p^2$	$1s^2 2p^2(^3P)\varepsilon s$	$^2P^e$	1/2, 3/2
$1s2s^2 2p^2$	$1s^2 2s^2 \varepsilon d$	$^2D^e$	3/2, 5/2
$1s2s^2 2p^2$	$1s^2 2s2p(^3P)\varepsilon p$	$^2D^e$	3/2, 5/2
$1s2s^2 2p^2$	$1s^2 2s2p(^1P)\varepsilon p$	$^2D^e$	3/2, 5/2
$1s2s^2 2p^2$	$1s2p^2(^1D)\varepsilon s$	$^2D^e$	3/2, 5/2
$1s2s2p^3$	$1s^2 2p^2(^3P)\varepsilon p$	$^4S^o_1$	3/2
$1s2s2p^3$	$1s^2 2p^2(^3P)\varepsilon p$	$^4S^o_2$	3/2
$1s2s2p^3$	$1s^2 2p^2(^3P)\varepsilon p$	$^4P^o$	1/2, 3/2, 5/2
$1s2s2p^3$	$1s^2 2s2p(^3P)\varepsilon s$	$^2P^o_{1,2}$	1/2, 3/2
$1s2s2p^3$	$1s^2 2s2p(^3P)\varepsilon d$	$^2P^o_{1,2}$	1/2, 3/2
$1s2s2p^3$	$1s^2 2s2p(^1P)\varepsilon s$	$^2P^o_{1,2}$	1/2, 3/2
$1s2s2p^3$	$1s^2 2s2p(^1P)\varepsilon d$	$^2P^o_{1,2}$	1/2, 3/2
$1s2s2p^3$	$1s^2 2p^2(^3P)\varepsilon p$	$^2P^o_{1,2}$	1/2, 3/2
$1s2s2p^3$	$1s^2 2p^2(^1D)\varepsilon p$	$^2P^o_{1,2}$	1/2, 3/2
$1s2s2p^3$	$1s^2 2p^2(^1S)\varepsilon p$	$^2P^o_{1,2}$	1/2, 3/2
$1s2s2p^3$	$1s^2 2s2p(^3P)\varepsilon d$	$^4D^o$	1/2, 3/2, 5/2, 7/2

Initial state	Final state	$^{2s+1}L^{\pi}$	J
$1s2s2p^3$	$1s^2 2p^2 (^3P) \varepsilon p$	$^4D^o$	1/2, 3/2, 5/2, 7/2
$1s2s2p^3$	$1s^2 2s2p (^3P) \varepsilon d$	$^{2}_{1,2}D^o$	3/2, 5/2
$1s2s2p^3$	$1s^2 2s2p (^1P) \varepsilon d$	$^{2}_{1,2}D^o$	3/2, 5/2
$1s2s2p^3$	$1s^2 2p^2 (^3P) \varepsilon p$	$^{2}_{1,2}D^o$	3/2, 5/2
$1s2s2p^3$	$1s^2 2p^2 (^1D) \varepsilon p$	$^{2}_{1,2}D^o$	3/2, 5/2
$1s2p^4$	$1s^2 2p^2 (^1D) \varepsilon d$	$^2S^e$	1/2
$1s2p^4$	$1s^2 2p^2 (^1S) \varepsilon s$	$^2S^e$	1/2
$1s2p^4$	$1s^2 2p^2 (^3P) \varepsilon s$	$^4P^e$	1/2, 3/2, 5/2
$1s2p^4$	$1s^2 2p^2 (^3P) \varepsilon d$	$^4P^e$	1/2, 3/2, 5/2
$1s2p^4$	$1s^2 2p^2 (^3P) \varepsilon s$	$^2P^e$	1/2, 3/2
$1s2p^4$	$1s^2 2p^2 (^3P) \varepsilon d$	$^2P^e$	1/2, 3/2
$1s2p^4$	$1s^2 2p^2 (^1D) \varepsilon d$	$^2P^e$	1/2, 3/2
$1s2p^4$	$1s^2 2p^2 (^3P) \varepsilon d$	$^2D^e$	3/2, 5/2
$1s2p^4$	$1s^2 2p^2 (^1D) \varepsilon s$	$^2D^e$	3/2, 5/2
$1s2p^4$	$1s^2 2p^2 (^1D) \varepsilon d$	$^2D^e$	3/2, 5/2
$1s2p^4$	$1s^2 2p^2 (^1S) \varepsilon d$	$^2D^e$	3/2, 5/2

APPENDIX VII: Energy values below total ionization estimated by the application of the quantum defect method (QDM)

Configuration	Energy Values (a.u.)			
	Z = 3	Z = 4	Z = 5	Z = 6
$1s2s(^3S)31$	- 5.166	- 9.52o	- 15.239	- 22.317
$1s2s(^3S)41$	- 5.142	- 9.423	- 15.o2o	- 21.928
$1s2s(^3S)51$	- 5.13o	- 9.378	- 14.919	- 21.748
$1s2s(^1S)31$	- 5.1o2	- 9.4o8	- 15.o83	- 22.117
$1s2s(^1S)41$	- 5.1oo	- 9.31o	- 14.864	- 21.728
$1s2s(^1S)51$	- 5.o89	- 9.266	- 14.763	- 21.548
$1s2p(^3P)31$	- 5.o83	- 9.398	- 15.o78	- 22.117
$1s2p(^3P)41$	- 5.o59	- 9.3o1	- 14.859	- 21.728
$1s2p(^3P)51$	- 5.o47	- 9.256	- 14.758	- 21.548
$1s2p(^1P)31$	- 5.o49	- 9.334	- 14.982	- 21.989
$1s2p(^1P)41$	- 5.o24	- 9.236	- 14.763	- 21.6oo
$1s2p(^1P)51$	- 5.o13	- 9.191	- 14.662	- 21.42o
$1s2s2p(^4P)31$		- 1o.118	- 16.485	- 24.464
$1s2s2p(^4P)41$		- 1o.o94	- 16.388	- 24.246
$1s2s2p(^4P)51$		- 1o.o83	- 16.343	- 24.144
$1s2p2p(^4P)31$		- 9.924	- 16.219	- 24.127
$1s2p2p(^4P)41$		- 9.9oo	- 16.122	- 23.9o8
$1s2p2p(^4P)51$		- 9.889	- 16.o77	- 23.8o7
$1s2s2p^2(^5P)31$			- 17.25o	- 25.972
$1s2s2p^2(^5P)41$			- 17.225	- 25.875
$1s2s2p^2(^5P)51$			- 17.214	- 25.83o
$1s2s2p^3(^6S)31$				- 26.923
$1s2s2p^3(^6S)41$				- 26.898
$1s2s2p^3(^6S)51$				- 26.887

APPENDIX VIII: Hartree-Fock energy values below total ionization (Fri 75)

Configuration	Energy Values (a.u.) Z = 3	Z = 4	Z = 5	Z = 6
$1s^2 2s$	- 7.4333	- 14.2795	- 23.3819	- 34.7394
$1s^2$	- 7.2369	- 13.6133	- 21.9918	- 32.3735
$1s2s2p^2$		- 1o.2335		
$1s2s^2$	- 5.3448			
1s2s2p	- 5.3o46	- 9.9688	- 16.1378	- 23.81o9
1s2s3p	- 5.161o	- 9.5266	- 15.2575	- 22.3533
1s2s4p	- 5.1279	- 9.4o7o	- 15.oo16	- 21.9118
1s2s5p	- 5.1138	- 9.3548	- 14.8882	- 21.7146
1s2s6p	- 5.1o65	- 9.3273	- 14.8281	- 21.6o94
1s2p3s	- 5.1oo3	- 9.4444	- 15.1536	- 22.2274
1s2p4s	- 5.o574	- 9.3o6o	- 14.87o5	- 21.75o6
1s2p5s	- 5.o4o4	- 9.2476	- 14.7479	- 21.5412
1s2p6s	- 5.o319	- 9.2175	- 14.6838	- 21.43o8
1s	- 4.5oo5	- 8.oo17	- 12.5o42	- 18.oo86
2s2p	- 1.83o1	- 3.4332		

APPENDIX IX: Energy values below total ionization as deduced from the work of Safronova et al. (Saf 69)

Configuration	State	Energy Values (a.u.) Z = 3	Z = 4	Z = 5	Z = 6
$1s2s^2$	$^2S^e$	- 5.3996	- 10.1181	- 16.3367	- 24.055
1s2s2p	$^2P^o_1$	- 5.2530	- 9.8776	- 16.0021	- 23.627
1s2s2p	$^2P^o_2$	- 5.3193	- 9.9652	- 16.1110	- 23.757
1s2s2p	$^4P^o$	- 5.3523	- 10.0558	- 16.2593	- 23.963
$1s2p^2$	^2S	- 5.1341	- 9.6820	- 15.7300	- 23.278
$1s2p^2$	^2P	- 5.2242	- 9.8075	- 15.8908	- 23.474
$1s2p^2$	^4P	- 5.2150	- 9.8495	- 15.9840	- 23.618
$1s2p^2$	^2D	- 5.2186	- 9.8149	- 15.9113	- 23.508
$1s2s^22p$	^3P		- 10.4525	- 17.268	- 25.834
$1s2s^22p$	^1P		- 10.4232	- 17.2048	- 25.736
$1s2s2p^2$	^5P		- 10.3883	- 17.194	- 25.750
$1s2s2p^2$	$^3P_1$		- 10.328	- 17.059	- 25.541
$1s2s2p^2$	^3D		- 10.289	- 17.027	- 25.515
$1s2s2p^2$	^1D		- 10.227	- 16.922	- 25.366
$1s2s2p^2$	^3S		- 10.209	- 16.916	- 25.373
$1s2s2p^2$	^1S		- 10.148	- 16.811	- 25.224
$1s2s2p^2$	$^3P_2$		- 10.165	- 16.862	- 25.309
$1s2s2p^2$	^1P		- 10.166	- 16.832	- 25.249
$1s2p^3$	^5S		- 10.126	- 16.832	- 25.287
$1s2p^3$	^3S		- 10.119	- 16.757	- 25.144
$1s2p^3$	^3D		- 10.106	- 16.763	- 25.169
$1s2p^3$	^1D		- 10.102	- 16.725	- 25.098
$1s2p^3$	^3P		- 10.032	- 16.658	- 25.035
$1s2p^3$	^1P		- 10.027	- 16.619	- 24.961

Configuration	State	Energy Values (a.u.) Z = 5	Z = 6
$1s2s^2 2p^2$	^2P	- 17.623	- 26.823
$1s2s^2 2p^2$	^4P	- 17.683	- 26.934
$1s2s^2 2p^2$	^2D	- 17.613	- 26.826
$1s2s^2 2p^2$	^2S	- 17.551	- 26.743
$1s2s2p^3$	^6S	- 17.623	- 26.867
$1s2s2p^3$	$^4S_1$	- 17.524	- 26.677
$1s2s2p^3$	^4D	- 17.463	- 26.63o
$1s2s2p^3$	$^2D_1$	- 17.387	- 26.495
$1s2s2p^3$	^4P	- 17.397	- 26.542
$1s2s2p^3$	$^2P_1$	- 17.321	- 26.4o8
$1s2s2p^3$	$^2D_2$	- 17.254	- 26.341
$1s2s2p^3$	$^4S_2$	- 17.231	- 26.336
$1s2s2p^3$	^2S	- 17.214	- 26.272
$1s2s2p^3$	$^2P_2$	- 17.188	- 26.254
$1s2p^4$	^2P	- 17.o77	- 26.o65
$1s2p^4$	^4P	- 17.o97	- 26.136
$1s2p^4$	^2D	- 17.o65	- 26.o65
$1s2p^4$	^2S	- 16.929	- 25.886

APPENDIX X: Matrix elements (a. u.) for some state configurations with 3 electrons as deduced from Goldsmith (Gol 74)

Li I

J = 1/2	$(1s2s2p)\,^2_1P^o$	$(1s2s2p)\,^2_2P^o$	$(1s2s2p)\,^4P^o$
$(1s2s2p)\,^2_1P^o$	- 5.25338	$8.486x10^{-5}$	$- 3.761x10^{-5}$
$(1s2s2p)\,^2_2P^o$	$8.485x10^{-5}$	- 5.319732	$- 1.393x10^{-5}$
$(1s2s2p)\,^4P^o$	$- 3.76ox10^{-5}$	$- 1.393x10^{-5}$	- 5.35265

Be II

J = 1/2	$(1s2s2p)\,^2_1P^o$	$(1s2s2p)\,^2_2P^o$	$(1s2s2p)\,^4P^o$
$(1s2s2p)\,^2_1P^o$	- 9.879o52	$1.5413x10^{-4}$	$- 6.414x10^{-5}$
$(1s2s2p)\,^2_2P^o$	$1.5412x10^{-4}$	- 9.966869	$- 5.527x10^{-5}$
$(1s2s2p)\,^4P^o$	$- 6.413x10^{-5}$	$- 5.527x10^{-5}$	- 1o.o57388

B III

J = 1/2	$(1s2s2p)\,^2_1P^o$	$(1s2s2p)\,^2_2P^o$	$(1s2s2p)\,^4P^o$
$(1s2s2p)\,^2_1P^o$	- 16.oo626	$2.o92x10^{-4}$	$- 7.644x10^{-5}$
$(1s2s2p)\,^2_2P^o$	$2.o92x10^{-4}$	- 16.11564	$- 1.514x10^{-4}$
$(1s2s2p)\,^4P^o$	$- 7.6436x10^{-5}$	$- 1.514x10^{-4}$	- 16.263776

Li I

J = 3/2	$(1s2s2p)\,^2_1P^o$	$(1s2s2p)\,^2_2P^o$	$(1s2s2p)\,^4P^o$
$(1s2s2p)\,^2_1P^o$	- 5.253457	$- 7.1o6x10^{-5}$	$1.525x10^{-5}$
$(1s2s2p)\,^2_2P^o$	$- 7.1o6x10^{-5}$	- 5.319739	$- 1.32ox10^{-5}$
$(1s2s2p)\,^4P^o$	$1.525x10^{-5}$	$- 1.32ox10^{-5}$	- 5.352723

Be II

J = 3/2	$(1s2s2p)\,^2P^o_1$	$(1s2s2p)\,^2P^o_2$	$(1s2s2p)\,^4P^o$
$(1s2s2p)\,^2P^o_1$	- 9.879211	-1.919×10^{-4}	-3.584×10^{-6}
$(1s2s2p)\,^2P^o_2$	-1.919×10^{-4}	- 9.966846	-6.646×10^{-5}
$(1s2s2p)\,^4P^o$	-3.584×10^{-5}	-6.646×10^{-5}	- 10.057542

B III

J = 3/2	$(1s2s2p)\,^2P^o_1$	$(1s2s2p)\,^2P^o_2$	$(1s2s2p)\,^4P^o$
$(1s2s2p)\,^2P^o_1$	- 16.00651	-6.886×10^{-3}	-8.461×10^{-5}
$(1s2s2p)\,^2P^o_2$	-6.886×10^{-3}	- 16.11551	-1.985×10^{-4}
$(1s2s2p)\,^4P^o$	-8.461×10^{-5}	-1.985×10^{-4}	- 16.2640

Li I $(1s2s2p)\,^4P_{5/2}$ = - 5.3526404

Be II $(1s2s2p)\,^4P_{5/2}$ = - 10.05718

B III $(1s2s2p)\,^4P_{5/2}$ = - 16.26298

Li I

J = 1/2	$(1s2s^2)\ ^2S$	$(1s2p^2)\ ^2S$	$(1s2p^2)\ ^2P$	$(1s2p^2)\ ^4P$
$(1s2s^2)\ ^2S$	- 5.400011	-1.208×10^{-5}	-1.509×10^{-5}	2.134×10^{-5}
$(1s2p^2)\ ^2S$	-1.208×10^{-5}	- 5.13446	2.995×10^{-5}	-4.235×10^{-5}
$(1s2p^2)\ ^2P$	-1.509×10^{-5}	2.995×10^{-5}	- 5.22481	-2.085×10^{-5}
$(1s2p^2)\ ^4P$	2.134×10^{-5}	-4.235×10^{-5}	-2.085×10^{-5}	- 5.215288

Be II

J = 1/2	$(1s2s^2)\ ^2S$	$(1s2p^2)\ ^2S$	$(1s2p^2)\ ^2P$	$(1s2p^2)\ ^4P$
$(1s2s^2)\ ^2S$	- 1o.12oo	- 7.o87x1o^{-5}	- 1.761x1o^{-5}	2.49ox1o^{-5}
$(1s2p^2)\ ^2P$	- 7.o87x1o^{-5}	- 9.68346	1.593x1o^{-5}	- 2.253x1o^{-5}
$(1s2p^2)\ ^2D$	- 1.761x1o^{-5}	1.593x1o^{-5}	- 9.8o9o93	1.624x1o^{-5}
$(1s2p^2)\ ^4P$	2.49ox1o^{-5}	- 2.253x1o^{-5}	1.624x1o^{-5}	- 9.85o8oo

B III

J = 1/2	$(1s2s^2)\ ^2S$	$(1s2p^2)\ ^2P$	$(1s2p^2)\ ^2D$	$(1s2p^2)\ ^4P$
$(1s2s^2)\ ^2S$	- 16.341682	- 2.2o93x1o^{-4}	1.o78x1o^{-6}	4.37o8x1o^{-6}
$(1s2p^2)\ ^2P$	- 2.2o93x1o^{-4}	- 15.733859	- 7.642x1o^{-5}	1.o8o6x1o^{-4}
$(1s2p^2)\ ^2D$	1.o78x1o^{-6}	- 7.642x1o^{-5}	- 15.895o6	- 6.441x1o^{-5}
$(1s2p^2)\ ^4P$	4.37o8x1o^{-6}	1.o8o6x1o^{-4}	- 6.441x1o^{-5}	- 15.987747

Li I

J = 3/2	$(1s2p^2)\ ^2P$	$(1s2p^2)\ ^2D$	$(1s2p^2)\ ^4P$
$(1s2p^2)\ ^2P$	- 5.22468	2.32ox1o^{-5}	- 1.469x1o^{-5}
$(1s2p^2)\ ^2D$	2.32ox1o^{-5}	- 5.21897	- 3.8o5x1o^{-5}
$(1s2p^2)\ ^4P$	- 1.469x1o^{-5}	- 3.8o5x1o^{-5}	- 5.2153o3

Be II

J = 3/2	$(1s2p^2)\ ^2P$	$(1s2p^2)\ ^2D$	$(1s2p^2)\ ^4P$
$(1s2p^2)\ ^2P$	- 9.8o91o8	9.164x1o^{-6}	- 6.128x1o^{-5}
$(1s2p^2)\ ^2D$	9.164x1o^{-6}	- 9.816297	- 6.969x1o^{-5}
$(1s2p^2)\ ^4P$	- 6.128x1o^{-5}	-6.969x1o^{-5}	- 9.85o8oo

B III

J = 3/2	$(1s2p^2)\ ^2P$	$(1s2p^2)\ ^2D$	$(1s2p^2)\ ^4P$
$(1s2p^2)\ ^2P$	- 15.894951	$- 7.161x1o^{-5}$	$- 1.7137x1o^{-4}$
$(1s2p^2)\ ^2D$	$- 7.161x1o^{-5}$	- 15.9145	$- 9.6o8x1o^{-5}$
$(1s2p^2)\ ^4P$	$- 1.714x1o^{-4}$	$- 9.6o8x1o^{-5}$	- 15.987676

Li I

J = 5/2	$(1s2p^2)\ ^2D$	$(1s2p^2)\ ^4P$
$(1s2p^2)\ ^2D$	- 5.219o86	$1.788x1o^{-5}$
$(1s2p^2)\ ^4P$	$1.788x1o^{-5}$	- 5.215411

Be II

J = 5/2	$(1s2p^2)\ ^2D$	$(1s2p^2)\ ^4P$
$(1s2p^2)\ ^2D$	- 9.816568	$7.821x1o^{-6}$
$(1s2p^2)\ ^4P$	$7.821x1o^{-6}$	- 9.85o997

B III

J = 5/2	$(1s2p^2)\ ^2D$	$(1s2p^2)\ ^4P$
$(1s2p^2)\ ^2D$	- 15.9155	$- 1.13339x1o^{-4}$
$(1s2p^2)\ ^4P$	$- 1.13339x1o^{-4}$	- 15.98795

APPENDIX XI: Energy values below total ionization as deduced from the work of Holøien and Geltman (Hol 67)

Configuration	State	Energy Values (a.u.) Z = 3	Z = 4	Z = 5	Z = 6
1s2s2p	$^4P^o(1)$	- 5.3659	- 1o.o628	- 16.263o	- 23.9643
(1s, 23sp+)	$^4P^o(2)$	- 5.224o	- 9.5586	- 15.3o34	- 22.4o95
(1s, 23sp-)	$^4P^o(3)$	- 5.1713	- 9.4557	- 15.17o3	- 22.2511
$1s2p^2$	$^4P^e(1)$	- 5.2459	- 9.8688	- 15.9968	- 23.6272
1s2p3p	$^4P^e(2)$	- 5.o939	- 9.4232	- 15.119o	- 22.1765
1s2p4p	$^4P^e(3)$	- 5.o6o7	- 9.2457	- 14.8o53	- 21.6724
1s2s3s	$^4S^e(1)$	- 5.211o	- 9.6177	- 15.3869	- 22.5176
1s2s4s	$^4S^e(2)$	- 5.1562	- 9.4592	- 15.1224	- 22.1762
1s2s5s	$^4S^e(3)$	- 5.1365	- 9.4117	- 15.o58o	- 21.9866

APPENDIX XII: Additional rules concerning transfer of orbital angular momentum

a) Coulomb autoionization

If we compute matrix elements of the Coulomb operator, then $\langle \gamma LSJM_J\pi | H_C | \gamma'L'S'J'M_J'\pi' \rangle$ must be diagonal in L, S, J, M_J, M_L, M_S and π. That is to say each set of quantum numbers $|LSJM_J\pi\rangle$ is not mixed with different sets. However, if one considers the coupling between orbital angular momenta $\vec{l}_\mu$, electrons participating in the autoionizing transition may alter their orbital quantum numbers. In computing Coulomb matrix elements we use the expansion of the electrostatic interaction in terms of scalar products. Thus

$$H_C = e^2 \sum_{i<j} \{\frac{1}{r_j} (C_i^{(0)} \cdot C_j^{(0)}) + \frac{r_i^1}{r_j^2} (C_i^{(1)} \cdot C_j^{(1)}) + \frac{r_i^2}{r_j^3} (C_i^{(2)} \cdot C_j^{(2)}) + \ldots\} \qquad \text{(XII-1)}$$

In particular we wish to study matrix elements of the Coulomb operator in the $[l_i l_j LM_L]$ representation. For a specific term of Eq. (XII-1) we have

$$\langle l_i l_j L || C_i^{(k)} \cdot C_j^{(k)} || l_i' l_j' L' \rangle \sim \delta(L, L') \begin{Bmatrix} L & l_j & l_i \\ k & l_i' & l_j' \end{Bmatrix}$$

$$\times \langle l_i || C_i^{(k)} || l_i' \rangle \langle l_j || C_j^{(k)} || l_j' \rangle$$

Examination of the 6j symbol discloses the following rules, as summarized in Table A. From Table A it is clear that for "monopole transitions" (k=0) the transfer of orbital angular momentum is zero. In the case of "dipole transitions" (k=1) interchange of orbital angular momentum is possible, but with the restrictions $\Delta l_i = 0, \pm 1$ and $\Delta l_j = 0, \pm 1$. In addition for "quadrupole transitions" (k=2) Δl_i

Table A: Transfer of orbital angular momentum for k=0, 1 and 2

k	Multipole	Δl_i	Δl_j
0	Monopole	0	0
1	Dipole	0, ±1	0, ±1
2	Quadrupole	0, ±1, ±2	0, ±1, ±2

and Δl_j can change by 0, ±1, ±2, etc. In summary we conclude that the matrix elements of H_C consist of a sum of terms corresponding to alternative transfer of orbital angular momentum. Assuming $r_i < r_j$ the terms $(r_i^k / r_j^{k+1}) \cdot (C_i^{(k)} \cdot C_j^{(k)})$ rapidly decrease with increasing k. Therefore, we expect that the term for zero transfer (k=0: screening interaction) is dominating.

b) Magnetic autoionization due to spin-other-orbit coupling

In order to find the conditions imposed on l_i and l_j we expand H_{SOO} in terms of sperical tensors. According to Judd (Ju 63) H_{SOO} can be written as

$$H_{SOO} \sim \sum_{i<j} \sum_k (-1)^k [(2k+1)\cdot(2k-1)^{1/2} \frac{r_i^{k-2}}{r_j^{k+1}} \times \{C_j^{(k)} \times \{C^{(k)} \times l^{(1)}\}_i^{(k-1)}\}^{(1)} \qquad \text{(XII-2}$$

$$- (2k+1)\cdot(2k+3)^{1/2} \frac{r_j^k}{r_i^{k+3}} \{C_j^{(k)} \times \{C^{(k)} \times l^{(1)}\}_i^{(k+1)}\}^{(1)}] \cdot (\vec{s}_i + 2\vec{s}_j)$$

where i, j runs over all unpaired electrons of the atom. Let us consider, for instance, matrix elements of the second part of

H_{SOO} in the $[l_i l_j L M_L]$ representation. It is sufficient to study reduced matrix elements of the type

$$\langle l_i l_j L || \{c_j^{(k)} \times \{c^{(k)} \times l^{(1)}\}_i^{(k+1)}\}^{(1)} || l_i' l_j' L' \rangle$$

$$\sim \begin{Bmatrix} l_i & l_j & L \\ l_i' & l_j' & L' \\ k+1 & k & 1 \end{Bmatrix} \langle l_i || \{c^{(k)} \times l^{(1)}\}_i^{(k+1)} || l_i' \rangle \langle l_j || c_j^{(k)} || l_j' \rangle$$

By inspecting the above 9j symbol we find that magnetic autoionization due to H_{SOO} has to satisfy the following conditions.

Table B: Transfer of orbital angular momentum for the leading terms (k=0, k=1 and k=2) of the spin-other-orbit interaction

k	Δl_i	Δl_j
0	0, ±1	0
1	0, ±1, ±2	0, ±1
2	0, ±1, ±2, ±3	0, ±1, ±2

We see from Table B that even for the dominating term (k=0) the angular momentum of the i-th electron can change by $\Delta l_i = \pm 1$. In addition for k=1 both interacting electrons can change orbital angular momentum at least by 1 and for k=2 at least by 2 units.

c) Magnetic autoionization due to spin-spin coupling

In close analogy to Section (XII-b) we may now deduce rules for the spin-spin interaction. We recall that the spin-spin opera-

tor can be expanded in a sum of terms with decreasing factors r_i^k/r_j^{k+2}, namely

$$H_{SS} \sim \Sigma \frac{r_i^k}{r_j^{k+2}} \{C_i^{(k)} \times C_j^{(k+2)}\}^{(2)} \{s_i^{(1)} \times s_j^{(1)}\}^{(2)} \qquad \text{(XII-3)}$$

$$r_j > r_i$$

In this case it is sufficient to study reduced matrix elements of the type

$$\langle l_i l_j L || \{C_i^{(k)} \times C_j^{(k+2)}\}^{(2)} || l_i' l_j' L' \rangle$$

$$\sim \begin{Bmatrix} l_i & l_j & L \\ l_i' & l_j' & L' \\ k & k+2 & 2 \end{Bmatrix}$$

The non-vanishing of the above reduced matrix element follows from the properties of the 9j symbol. The various rules imposed on two interacting orbital electrons, e.g. l_i and l_j can be seen from Table C.

Table C: Transfer of orbital angular momentum for the leading terms (k=0, k=1 and k=2) of the spin-spin interaction

k	Δl_i	Δl_j
0	0	0,±1,±2
1	0,±1	0,±1,±2,±3
2	0,±1,±2	0,±1,±2,±3,±4

When k=0, Δl_i=0 and Δl_j can only be 0, ±1 or ±2. When k=1, both l_i and l_j can change at least by 1, etc. We emphasize that autoionizing transitions induced by the k=0 term are most probable.

Appendix XIII: Determination of the $|(1s2s2p)\ ^4P^o\rangle$ wave functions

A basic problem is to calculate the $(1s2s2p)\ ^4P^o_{5/2,3/2,1/2}$ states. The method used is to expand the wave function $|\tilde{\Psi}_i\rangle$ of the total Hamiltonian in terms of the eigenstates of a zero-order Hamiltonian. We define

$$(H^o + H_C)|\Psi_i\rangle = E_i|\Psi_i\rangle \qquad \text{(XIII-1)}$$

To proceed further we use the eigenfunctions defined by Eq. (XIII-1) as a set of basis functions for expanding the complete wave function $|\tilde{\Psi}_i\rangle$. Thus we can write

$$|\tilde{\Psi}_i\rangle = \sum_{j=1}^{\infty} C_j|\Psi_j\rangle \qquad \text{(XIII-2)}$$

The coefficients C_j are now determined by diagonalizing the complete Hamiltonian, where $H = H^o + H_C + H_{SO} + H_{SOO} + H_{SS} + H_{HF}$. This procedure is approximately equivalent to the application of first-order perturbation theory, giving the result

$$|\tilde{\Psi}_i\rangle = |\Psi_i\rangle + \sum_{\substack{j \\ (i\neq j)}} \frac{\langle\Psi_i|H_{INT}|\Psi_j\rangle}{E_i - E_j}|\Psi_j\rangle \qquad \text{(XIII-3)}$$

where the perturbation operator is

$$H_{INT} = H - (H^o + H_C) = H_{SO} + H_{SOO} + H_{SS} + H_{HF}$$

and the summation is over all intermediate states $|\Psi_j\rangle$. In this connection we note that there is no mixing between various J states so long as the nuclear spin I is equal to zero. The problem of solving the energy matrix with respect to the complete Hamiltonian is complicated and lies outside the scope of this work. Instead, we present a qualitative discussion of the physical effects involved by examining the general behaviour of the $(1s2s2p)\ ^4P^o$ wave functions.

a) Break-down of LS coupling

When the spin-orbit, spin-other-orbit and spin-spin interactions are included in the Hamiltonian, the resulting break-down of LS coupling causes a mixing of the doublet and quartet states of the same total angular momentum and parity. The most significant spin-dependent perturbations are expected between the (1s2s2p) $^4P^o_{3/2,1/2}$ and the 1s(2s2p ^{3,1}P) $^2P^o_{3/2,1/2}$ states. Thus the (1s2s2p) $^4P^o_{3/2,1/2}$ states are no longer pure quartet states but contain admixtures of $^2P^o_{3/2,1/2}$ states.

$$|5/2\rangle \simeq |^4P^o_{5/2}\rangle$$

$$|3/2\rangle \simeq |^4P^o_{3/2}\rangle + a_1|^2_1P^o_{3/2}\rangle + a_2|^2_2P^o_{3/2}\rangle \qquad \text{(XIII-4)}$$

$$|1/2\rangle \simeq |^4P^o_{1/2}\rangle + a_1'|^2_1P^o_{1/2}\rangle + a_2'|^2_2P^o_{1/2}\rangle$$

where

$$|(1s2s2p)\ ^4P^o_{5/2}\rangle = |^4P^o_{5/2}\rangle$$

$$|(1s2s2p)\ ^4P^o_{3/2}\rangle = |^4P^o_{3/2}\rangle$$

$$|(1s2s2p)\ ^4P^o_{1/2}\rangle = |^4P^o_{1/2}\rangle$$

$$|1s(2s2p\ ^1P)\ ^2P^o_{3/2}\rangle = |^2_1P^o_{3/2}\rangle$$

$$|1s(2s2p\ ^1P)\ ^2P^o_{1/2}\rangle = |^2_1P^o_{1/2}\rangle$$

$$|1s(2s2p\ ^3P)\ ^2P^o_{3/2}\rangle = |^2_2P^o_{3/2}\rangle$$

$$|1s(2s2p\ ^3P)\ ^2P^o_{1/2}\rangle = |^2_2P^o_{3/2}\rangle$$

and a_1, a_2, a_1' and a_2' denote the mixing coefficients, defined as follows

$$\frac{\langle {}^4P^o_{3/2}|H_{RL}|{}^2_1P^o_{3/2}\rangle}{E({}^4P^o_{3/2}) - E({}^2_1P^o_{3/2})} = a_1 \qquad \frac{\langle {}^4P^o_{3/2}|H_{RL}|{}^2_2P^o_{3/2}\rangle}{E({}^4P^o_{3/2}) - E({}^2_2P^o_{3/2})} = a_2$$

$$\frac{\langle {}^4P^o_{1/2}|H_{RL}|{}^2_1P^o_{1/2}\rangle}{E({}^4P^o_{1/2}) - E({}^2_1P^o_{1/2})} = a_1' \qquad \frac{\langle {}^4P^o_{1/2}|H_{RL}|{}^2_2P^o_{1/2}\rangle}{E({}^4P^o_{1/2}) - E({}^2_2P^o_{1/2})} = a_2'$$

Here H_{RL} refers to $H_{SO} + H_{SOO} + H_{SS}$. For example the fine-structure expansion coefficients a_1, a_2, a_1' and a_2' may be estimated using the non-diagonal matrix elements listed in Appendix X. In particular for the (1s2s2p) $^4P^o$ states in BeII we obtain

$$|5/2\rangle \simeq |{}^4P^o_{5/2}\rangle$$

$$|3/2\rangle \simeq |{}^4P^o_{3/2}\rangle + 2.0\times10^{-5}|{}^2_1P^o_{3/2}\rangle + 7.3\times10^{-4}|{}^2_2P^o_{3/2}\rangle$$

$$|1/2\rangle \simeq |{}^4P^o_{1/2}\rangle + 3.6\times10^{-4}|{}^2_1P^o_{1/2}\rangle + 6.1\times10^{-4}|{}^2_2P^o_{1/2}\rangle$$

b) Break-down of IJ coupling

We adopt for H_{INT} the general form, namely $H_{INT} = H_{SO} + H_{SOO} + H_{SS} + H_{FC} + H_O + H_D + H_Q$ where H_{FC}, H_O, H_D and H_Q represent the Fermi contact, the orbital, the dipole-dipole and the quadrupole interactions, respectively. We note that in the presence of hyperfine coupling different J states are mixed, i.e. J is no longer a constant of motion. We recall that for core-excited states with unsaturated s electrons the Fermi contact interaction is about two orders of magnitude larger than the orbital, dipole-dipole and the quadrupole terms. Therefore H_O, H_D and H_Q may be neglected. We further note that the non-diagonal matrix elements of H_{FC} if not to vanish must satisfy the condition $\Delta J = \pm 1$. Moreover these matrix elements are diagonal in L and S. In addition only those admixtures of J states lying close together will be taken into account.

Assuming I = 3/2, the (1s2s2p) $^4P^o$ states in ^{7}LiI and ^{9}BeII can be expressed in terms of |J, F> eigenfunctions. We have

$$|5/2,\ 4\rangle \simeq |^4P^o_{5/2,4}\rangle$$

$$|5/2,\ 3\rangle \simeq |^4P^o_{5/2,3}\rangle + b_{5/2,3/2}|^4P^o_{3/2,3}\rangle$$

$$|5/2,\ 2\rangle \simeq |^4P^o_{5/2,2}\rangle + b_{5/2,3/2}|^4P^o_{3/2,2}\rangle \qquad \text{(XIII-5)}$$

$$|5/2,\ 1\rangle \simeq |^4P^o_{5/2,1}\rangle + b_{5/2,3/2}|^4P^o_{3/2,1}\rangle$$

$$|3/2,\ 3\rangle \simeq |^4P^o_{3/2,3}\rangle + b_{3/2,5/2}|^4P^o_{5/2,3}\rangle$$

$$|3/2,\ 2\rangle \simeq |^4P^o_{3/2,2}\rangle + b_{3/2,5/2}|^4P^o_{5/2,2}\rangle + b_{3/2,1/2}|^4P^o_{1/2,2}\rangle$$

$$|3/2,\ 1\rangle \simeq |^4P^o_{3/2,1}\rangle + b_{3/2,5/2}|^4P^o_{5/2,1}\rangle + b_{3/2,1/2}|^4P^o_{1/2,1}\rangle$$

$$|3/2,\ 0\rangle \simeq |^4P^o_{3/2,0}\rangle$$

$$|1/2,\ 2\rangle \simeq |^4P^o_{1/2,2}\rangle + b_{1/2,3/2}|^4P^o_{3/2,2}\rangle$$

$$|1/2,\ 1\rangle \simeq |^4P^o_{1/2,1}\rangle + b_{1/2,3/2}|^4P^o_{3/2,1}\rangle$$

where $b_{J,J'}$ symbolizes the hyperfine coupling due to H_{FC}. We emphasize that the expansion coefficients $b_{J,J'}$ are independent of F. For example, to estimate $b_{5/2,3/2}$ and $b_{3/2,1/2}$ we must evaluate

$$\frac{\langle ^4P^o_{5/2}|H_{FC}|^4P^o_{3/2}\rangle}{E(^4P^o_{5/2}) - E(^4P^o_{3/2})} \simeq b_{5/2,3/2}$$

$$\frac{\langle ^4P^o_{3/2}|H_{FC}|^4P^o_{1/2}\rangle}{E(^4P^o_{3/2}) - E(^4P^o_{1/2})} \simeq b_{3/2,1/2}$$

However, it should be noted that the diagonal and non-diagonal matrix elements of H_{FC} can be of the same order. Then perturbation theory is not adequate and the $b_{J,J'}$ coefficients must be optimized by diagonalization of the energy matrix. One further comment concerning the coupling of discrete $|J, F\rangle$ states with the adjacent continuum is in order. It is assumed that autoionization of the (1s2s2p) $^4P^o$ states proceeds via the fine-structure Hamiltonian, which is diagonal in J and independent of F. Consequently differing F states, but originating from the same J value, will have the same coupling to the continuum. Therefore the F quantum numbers may be dropped. Finally, if the results of Eq. (XIII-4) are inserted into Eq. (XIII-5) we obtain

$$|5/2,\ 4\rangle = |^4P^o_{5/2}\rangle$$

$$|5/2,\ 3\rangle \simeq |^4P^o_{5/2}\rangle + b_{5/2,3/2}|^4P^o_{3/2}\rangle + b_{5/2,3/2}\cdot a_1|^2_1P^o_{3/2}\rangle + b_{5/2,3/2}\cdot a_2|^2_2P^o_{3/2}\rangle$$

$$|5/2,\ 3\rangle = |5/2,\ 2\rangle = |5/2,\ 1\rangle \qquad \text{(XIII-6)}$$

$$|3/2,\ 2\rangle = |^4P^o_{3/2}\rangle + a_1|^2_1P^o_{3/2}\rangle + a_2|^2_2P^o_{3/2}\rangle + b_{3/2,5/2}|^4P^o_{5/2}\rangle + b_{3/2,1/2}|^4P^o_{1/2}\rangle + b_{3/2,1/2}\cdot a_1'|^2_1P^o_{1/2}\rangle + b_{3/2,1/2}\cdot a_2'|^2_2P^o_{1/2}\rangle$$

$$|3/2,\ 2\rangle = |3/2,\ 1\rangle$$

$$|3/2,\ 0\rangle \simeq |^4P^o_{3/2}\rangle + a_1|^2_1P^o_{3/2}\rangle + a_2|^2_2P^o_{3/2}\rangle$$

$$|1/2,\ 2\rangle \simeq |^4P^o_{1/2}\rangle + a_1'|^2_1P^o_{1/2}\rangle + a_2'|^2_2P^o_{1/2}\rangle + b_{1/2,3/2}|^4P^o_{3/2}\rangle + b_{1/2,3/2}\cdot a_1|^2_1P^o_{3/2}\rangle$$

$$+ b_{1/2,3/2} \cdot a_2 |^2P^o_{3/2}\rangle$$

$$|1/2,\ 2\rangle = |1/2,\ 1\rangle$$

This result has to be compared with Eq. (XIII-4), where the hyperfine coupling was ignored. From Eq. (XIII-6) it is seen that the fine- and hyperfine structure coupling of core-excited states is sensitive to non-diagonal matrix elements with respect to L, S and J.

APPENDIX XIV: Autoionization Rates

The number of radiationless transitions occuring in time dt is given by first-order perturbation theory as

$$W_A \cdot dt = (2\pi/\hbar)|\langle\Psi_f|H_{INT}|\Psi_i\rangle|^2\delta(E_f-E_i)dt \qquad \text{(XIV-1)}$$

provided the continuous wave function $|\Psi_f\rangle$ is normalized to represent one ejected electron per unit time per unit energy range. The wave functions of Appendix XIII are now applied to study autoionization rates. Making use of Eq. (XIII-3) we find

$$W_A(i) = (2\pi/\hbar)\left|\langle\Psi_f|H_{INT}|\Psi_i\rangle + \sum_{\substack{j \\ (i\neq j)}} \frac{\langle\Psi_f|H_{INT}|\Psi_j\rangle\langle\Psi_j|H_{INT}|\Psi_i\rangle}{E_j - E_i}\right|^2 \qquad \text{(XIV-2)}$$

where $H_{INT} = H_C + H_{SO} + H_{SOO} + H_{SS} + H_{FC}$

and the summation is over the intermediate states $|\Psi_j\rangle$. For example, inserting Eq. (XIII-4) into (XIV-2) we can write

$$W_A(5/2) \simeq (2\pi/\hbar)[\langle(1s^2\varepsilon f)\ {}^2F^o_{5/2}|H_{SS}|{}^4P^o_{5/2}\rangle]^2$$

$$\begin{aligned} W_A(3/2) \simeq (2\pi/\hbar)[&\langle(1s^2\varepsilon p)\ {}^2P^o_{3/2}|H_{SO}+H_{SOO}+H_{SS}|{}^4P^o_{3/2}\rangle \\ &+ a_1\langle(1s^2\varepsilon p)\ {}^2P^o_{3/2}|H_C|{}^2_1P^o_{3/2}\rangle \\ &+ a_2\langle(1s^2\varepsilon p)\ {}^2P^o_{3/2}|H_C|{}^2_2P^o_{3/2}\rangle]^2 \end{aligned} \qquad \text{(XIV-3)}$$

$$\begin{aligned} W_A(1/2) \simeq (2\pi/\hbar)[&\langle(1s^2\varepsilon p)\ {}^2P^o_{1/2}|H_{SO}+H_{SOO}+H_{SS}|{}^4P^o_{1/2}\rangle \\ &+ a'_1\langle(1s^2\varepsilon p)\ {}^2P^o_{1/2}|H_C|{}^2_1P^o_{1/2}\rangle \\ &+ a'_2\langle(1s^2\varepsilon p)\ {}^2P^o_{1/2}|H_C|{}^2_2P^o_{1/2}\rangle]^2 \end{aligned}$$

From Eq. (XIV-3) it is seen that the autoionization amplitudes add up coherently and hence give rise to interference effects.

In addition the $(1s2s2p)\ {}^4P_{3/2,1/2}$ decay probabilities depend upon how much of the perturbed wave functions have doublet character.

For sufficiently large Z, for which a hydrogenic approximation is appropriate, we may deduce scaling laws. Thus the autoionization rate of the $(1s2s2p)\ {}^4P^o_{5/2}$ state, namely

$W_A(5/2) \sim |\langle 1s^2\varepsilon f)\ {}^2F^o_{5/2}|H_{SS}|{}^4P^o_{5/2}\rangle|^2 \sim (\alpha^2Z^3/Z)^2 = \alpha^2Z^4$ scales approximately as α^2Z^4. We note that the Coulomb matrix elements such as $\langle (1s^2\varepsilon p)\ {}^2P^o_{3/2}|H_C|{}^2_1P^o_{3/2}\rangle$ are independent of the atomic number, whereas the doublet-quartet energy separation in the denominator of a_1, a_2, a_1' and a_2' (see Appendix XIII) scales as Z. Moreover we assume that the doublet-quartet mixing is mainly due to spin-orbit interaction. Then, it follows that the a_1, a_2, a_1' and a_2' coefficients scale as α^2Z^3. Consequently second-order autoionization processes of the type

$$|a_1\langle (1s^2\varepsilon p)\ {}^2P^o_{3/2}|H_C|{}^2_1P^o_{3/2}\rangle|^2 \sim (\alpha^2Z^4/Z)^2 = \alpha^4Z^6$$

scale as α^4Z^6. We recall that the magnetic hyperfine constant for a hydrogen-like atom is proportional to $\alpha^2Z^3(m_e/M_p)$ and the energy difference between adjacent J levels, i.e. $E({}^4P^o_{5/2}) - E({}^4P^o_{3/2})$ scales approximately as α^2Z^4. Therefore the hyperfine coupling coefficients $b_{J,J'}$ (see Appendix XIII) are proportional to $Z^{-1}\ (m_e/M_p)$ and second-order rates due to hyperfine mixing are proportional to

$$|a_1b_{5/2,3/2}\langle (1s^2\varepsilon p)\ {}^2P^o_{3/2}|H_C|{}^2_1P^o_{3/2}\rangle|^2$$

$$\sim[\alpha^2Z^3Z^{-1}(m_e/M_p)]^2 = \alpha^4Z^4(m_e/M_p)^2 \text{ and}$$

scale as $\alpha^4Z^4(m_e/M_p)^2$. To conclude autoionization rates arising from the $(1s2s2p)\,{}^4P^o$ term scale approximately as:

spin-spin coupling: $W_A(5/2) \sim \alpha^4Z^4$

spin-orbit coupling: $W_A(3/2) \sim \alpha^4 Z^6$

$W_A(1/2) \sim \alpha^4 Z^6$

hyperfine coupling: $W_A(J) \sim \alpha^4 Z^4 (m_e/M_p)^2$

where Z is the effective nuclear charge, α is the Sommerfeld fine-structure constant, m_e is the electron mass and M_p the proton mass, respectively. In general, it is supposed that autoionization rates due to spin-spin coupling scale as Z^6, whereas spin-orbit and hyperfine coupling might lead to a Z^4 scaling law.

APPENDIX XV

PHYSICAL REVIEW A VOLUME 12, NUMBER 5 NOVEMBER 1975

Autoionization of foil-excited states in Li I and Li II

R. Bruch, G. Paul, and J. Andrä
Freie Universität Berlin, Institut für Atom- und Festkörperphysik A, 1 Berlin 33, Boltzmannstrasse 20, West Germany

Lester Lipsky
University of Nebraska, Department of Computer Science, Lincoln, Nebraska, 68508
(Received 10 December 1973; revised manuscript received 23 June 1975)

We have used the beam-foil interaction mechanism to populate highly excited states in lithium by passing 300-keV Li^+ ions through 8-$\mu g/cm^2$-thick carbon foils. The energies of the electrons emitted via autoionization were analyzed. By moving the foil along the beam axis, prompt and delayed electrons due to decays of Li I and Li III states were identified. These spectra are interpreted with the help of detailed theoretical calculations. The excitation energies of the Li I $(1s2s^2)^2S^e$ and Li II $(2s2p)^{1,3}P^o$ terms were determined to 0.5% accuracy. We have observed decays of doubly excited Li III states above the $n = 2$ threshold. On the basis of our theoretical estimates, we assign a peak in the high-energy portion of the spectra as due to deexcitation of triply excited Li I $2s^22p$ and $2s2p^2$ configurations.

I. INTRODUCTION

The study of doubly excited autoionization states of low-Z atoms, particularly He, has yielded considerable information on two-electron correlations.[1] Despite the fundamental importance of these resonances in two-electron atoms, with the exception of H^- and He, no systematic experimental investigation of autoionizing transitions in the isoelectronic He series has been reported in the literature. We present here measurements and interpretations of energies of electrons emitted in the decay of some doubly and triply excited states in Li I and Li II.

Observation of the decay of two- and three-electron states in ions requires an efficient means for their excitation. Sellin and co-workers[2] have shown that beam-foil excitation is a powerful method for producing highly charged ions in highly excited states. Among the methods commonly used to excite autoionizing states (elastic and inelastic electron scattering,[3,4] uv absorption,[5] electron or proton impact,[6] and heavy-ion bombardment of gases[7] and vapors[8]) beam-foil excitation[9,10] resembles heavy-ion excitation most closely. There are certain advantages in heavy-ion excitations, such as (a) observation of electrons emitted from the projectile as well as the target, and (b) multiple excitation of electrons. In addition, beam-foil excitation also allows the production of highly excited ionic states over a wide energy range with the mean ionic charge controllable to some degree. Futhermore, both the prompt electron spectra and the delayed spectra from long-lived metastable states can be observed in the same experiment by moving the foil in and out of the focus of a spectrometer along the beam axis.

II. METHOD AND RESULTS

When a fast Li^+ ion beam with a velocity of about 2.8×10^8 cm/sec (300 keV) passes through a 8-$\mu g/cm^2$-thick carbon foil, a high fraction of Li and Li^+ projectiles in doubly and triply excited states emerges from the back surface of the foil. These multiply excited Li I**, Li I***, and Li II** states, having excitation energies in excess of the first ionization limit, then decay via Coulomb autoionization provided the parity, spin, and orbital angular momenta of the initial and final states are unchanged.[11] Such highly excited lithium states (decaying by Coulomb autoionization with mean lives of typically 10^{-14} sec) have decay lengths $L = v\tau$ of the order of 280 Å at 300 keV beam energy. Thus in a foil-excitation experiment (foil thickness $d \simeq 300$ Å) there is a certain probability for the unperturbed observation of such short-lived ions in flight after the particles leave the foil. Therefore, we have chosen an experimental setup (Fig. 1) which allows the foil to be moved in the focus of our cylindrical electrostatic electron spectrometer, which is similar in design to the one used by Sellin and co-workers.[2] The foil can be moved up to 8 cm downstream (tunable time delay: 0–30 nsec) out of the focus of our cylindrical analyzer. In this manner we are able to separate the less probable delayed electron decays caused by spin-orbit (H_{so}), spin-other-orbit (H_{soo}), spin-spin (H_{ss}), and hyperfine coupling (H_{hf}) from the prompt decays.

The electron spectrometer views the beam at an angle of $\Theta = 42.3°$ and is provided with two pairs of continuously variable entrance and exit slits in order to reduce the viewing region of the beam to a length (l) of about 1.8 mm at 1-mm beam diam-

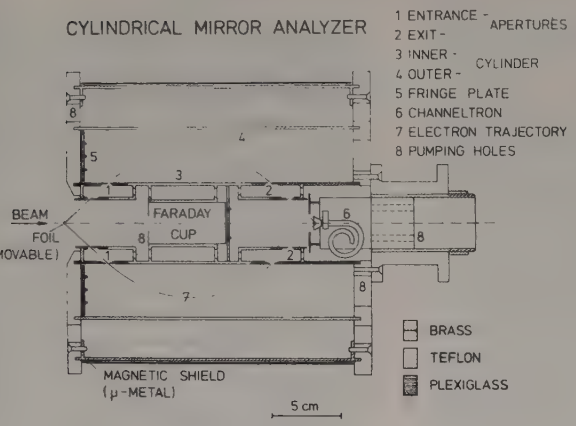

FIG. 1. Electrostatic analyzer used for measurements of energy distributions of electrons ejected after beam-foil excitation.

eter, corresponding to an angular spread $2\Delta\Theta = 2°$ and a transmission $T = 1\%$. This finite extension of the beam length viewed by the spectrometer causes a time uncertainty of the observation $t = l/v = 0.6$ nsec.

For calibration of the analyzer a monochromatic point-electron source[12] was used. Above 50 eV we achieved a 0.3% full width at half-maximum (FWHM) resolution and an absolute energy calibration ±0.1% with slit widths of 0.5 mm. To avoid any influence of Earth's magnetic field on the resolution and calibration of the spectrometer, both the target chamber and the analyzer were shielded with μ metal.

However, the kinematic transformation[7,13] from the rest frame of the emitting ion ($E_{c.m.}$) to the laboratory frame (E_{lab}) causes a considerable line spread arising from (i) the energy straggling of the projectiles in the target, (ii) the angle scattering of the ion beam by the foil, and (iii) the finite angular divergence ($\Delta\Theta = 1°$) defined by the acceptance of the spectrometer. We thus obtain an effective energy resolution by convoluting these dynamical contributions with the spectrometer window function. For Li^+ ions (300 keV) passing through 8-μg/cm^2 carbon foils, we measured an effective resolution of about 1.7% FWHM.

With this experimental arrangement, prompt and delayed electron spectra of incident 300–310-keV $^7Li^+$ ions on carbon foils were recorded at beam currents of a few nAmp. Typical results of the lithium electron spectra are shown in Figs. 2 and 3. The Li spectrum is presented here because it is the simplest system we studied, and even at this stage it permits a rather complete interpretation. In Fig. 2 we have displayed the energy distribution (lab system) of the prompt electron ejection after $^7Li^+$ – C-foil collisions. This spectrum exhibits two distinct autoionization line structures superimposed on a continuous electron background. Because of the fast motion of the Li projectiles during deexcitation, the autoionization lines are doppler shifted by about 50 eV. This allows discrimination against the slowly varying low-energy background. This paper will be concerned with the high-energy portion of the prompt and delayed electron spectra which are shown in Figs. 3(a) and 3(b), respectively. The intensities of the data, (a) the prompt and (b) the delayed spec-

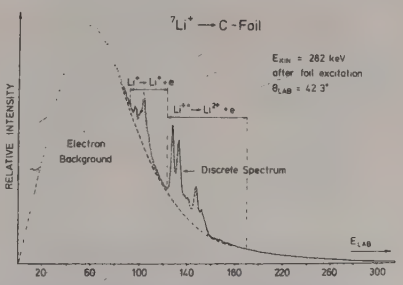

FIG. 2. Prompt electron energy spectrum from lithium produced by foil excitation. Discrete peaks are due to Coulomb autoionization of highly excited Li I and Li II states. Energies are in eV.

tra, differ by a factor of about one hundred and are therefore not directly comparable.

III. METASTABLE AUTOIONIZING QUARTET LEVELS

Study of autoionization of Li I $(1s2lnl')^4L$ states to the $(1s^2\epsilon l)^2l$ continuum ($\Delta S=1$) via spin-orbit, spin-other-orbit, and spin-spin mixing reveals information on the strength of relativistic interactions in high-lying quartet levels. Such metastable "weak" autoionizing states are of interest for several reasons. The most important reasons are the following: (i) Autoionization rates due to relativistic mixings are of the order 10^4–10^9 sec^{-1}. Hence electric dipole transitions can compete as deexcitation mechanisms.[14,15] (ii) Because of the narrow inherent widths, metastable autoionizing levels allow precision measurements of the fine- and even hyperfine-structure splitting.[16] (iii) The different strength of configuration interaction within a given fine-structure multiplet (differential metastability[16]) provides a mechanism to produce polarized electrons[17] and nuclei.[16]

In Fig. 4 we have shown a level diagram of the most prominent odd- and even-parity quartet states in Li I converging to the $(1s2s)^3S$ and $(1s2p)^3P$ series limits. The excitation energies indicated in the level scheme are based on theoretical estimates[18] and on optical line identifications.[9,10,14] From the $(1s2snl)^4l$ and $(1s2pnl)^4l$, $^4(l\pm1)$ levels, those lying below the $(1s2s)^3S$ ionization threshold can undergo nonradiative transitions only to the $(1s^2\epsilon l)^2l$ continuum, whereas $(1s2pnl)$ configurations with $n\geq3$ are coupled alternatively to the $(1s^2\epsilon l)^2l$ and the $(1s2s^3S\epsilon l)^{2,4}l$ continua. According to Garcia and Mack[19] the members of the series $(1s2p^3Pnl)^4l$ with $n\geq3$ and $l\geq1$ are metastable with respect to Coulomb autoionization (see Fig. 4). The odd-parity configurations $(1s2snp)$, $(1s2pns)$, and $(1s2pnd)$ as well as the even parity configurations $(1s2sns)$ and $(1s2pnp)$ are strongly mixed. The perturbation of the quartet states lose significance for the higher n values, because of the nondegeneracy of the thresholds $(1s2s)^3S$ and $(1s2p)^3P$, respectively. Holøien and Geltman[18] have suggested classification of the lowest $^4P^o$ states in the following way: $(1s,2s2p+)^4P^o(1)$, $(1s,23sp+)^4P^o(2)$, $(1s,23sp-)\times{}^4P^o(3)$, etc., where the (±) classification has been introduced.

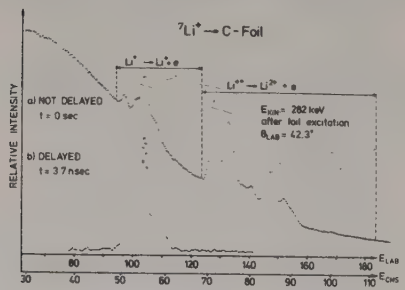

FIG. 3. Prompt and delayed Li I and Li II electron emission spectrum plotted both in the lab frame (E_{lab}) and in the rest frame of the emitting projectiles ($E_{c.m.}$). Energies are in eV.

The experimental electron spectrum ($t=3.7$ nsec) due to decays of some metastable Li I quartet states to the doublet continuum is displayed in Fig. 5. The quartet energies as indicated in this plot have been calculated by Holøien and Geltman.[18] We have assigned the first strong peak in the spectrum at about 51.1 eV due to metastable autoionization of the $(1s2s2p)^4P^o=^4P^o(1)$ level. The excitation energy of the Li I $^4P^o(1)$ state has been measured by threshold electron excitation[20] (57.3 ± 0.3 eV). A crucial point in our experiments is the velocity determination of the beam after the foil. In order to avoid this difficulty, the value[4] 57.442 ± 0.004 eV for $^4P^o(1)$ has been adopted as an energy calibration point for all the Li spectra,

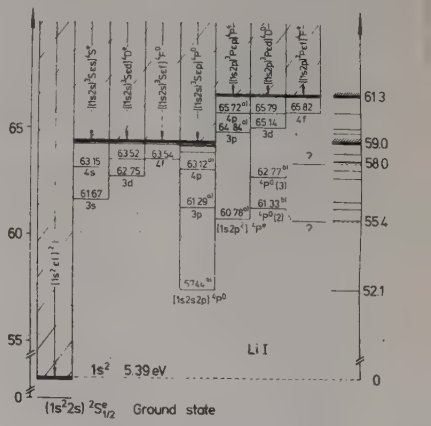

FIG. 4. Energy-level diagram for metastable autoionizing ^4L states in Li I. Experimental values (a) are deduced from dipole transitions (Refs. 9 and 10). Theoretical values (b) are taken from Holøien and Geltman (Ref. 18). The remainder have been estimated using the quantum-defect method (Ref. 7). The energy scale on the right-hand side of the figure represents possible transition energies of Li I quartet states decaying to the adjacent $(1s^2\epsilon l)^2l$ continuum. Energies are in eV.

since the prompt and the delayed spectra could be obtained successively with the same foil. Thus it is possible, in principle, to determine the transition energies of the most prominent features in the prompt and delayed Li electron spectra to an accuracy of ±0.1 eV.

The second strong line in the spectrum at about 55.4 eV could be composed of four lines due to autoionization of the states $^4P^e$ (1), $^4P^o$ (2), $^4S^e$ (1), and $(1s2p^2)\,^2P^e$, respectively. However, the $(1s2p^2)\,^2P^e$ level decays by photon emission to the low-lying $(1s^22p)\,^2P^o$ level in about 0.015 nsec.[21] Therefore, the peak at 55.4 eV is essentially an admixture of at least two transitions associated with autoionization of the $^4P^e$ (1) and $^4P^o$ (2) levels which should nearly coincide in energy. This is justified by the agreement of the energy separation of the two strongest peaks in this experiment (3.33 eV) as compared to the optical $^4P^e$ (1)-$^4P^o$ (1) transition energy of 3.34 eV.[15]

The third peak at about 1 eV below the $(1s2s)\,^3S$ series limit is surprisingly sharp, although several transitions (see Fig. 5) should overlap in this energy region. Above $(1s2s)\,^3S$, two unresolved peaks appear which might originate from metastable Li I levels of the kind $(1s2pnl)\,^4l$ decaying to the $(1s^2\epsilon l)\,^2l$ continuum.

Recent beam-foil studies of Li^+ ions using grazing incidence spectrometers[9,10] have revealed dipole transitions arising from Li II levels which are metastable with respect to Coulomb autoionization. However, no delayed electrons owing to decays of doubly excited Li II states have been recognized in our spectra. We thus conclude that these levels decay mainly by radiation and not by electron emission.

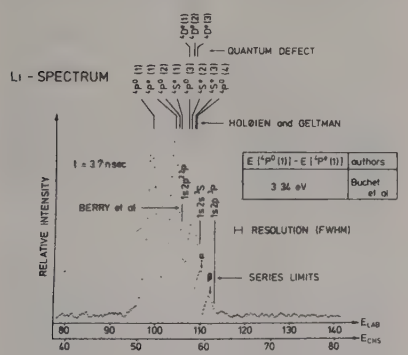

FIG. 5. Electron energy spectrum for decay of autoionizing quartet states in Li I. The notation of Holøien and Geltman (Ref. 18) has been adopted. Energies are in eV.

IV. PROMPT AUTOIONIZING DOUBLET LEVELS

The energy-level diagram as displayed in Fig. 6 is devoted to Coulomb autoionization of odd- and even-parity Li I states of the kind $1s2lnl'$ with $n>2$. The Li I resonances of the type $(1s2lnl')\,^2L$ converge to four distinct series limits $(1s2s)\,^{1,3}S$ and $(1s2p)\,^{1,3}P$, respectively. There is a strong mixing in the $(1s2s)\,^1Snl$ and $(1s2p)\,^3Pnl$ configurations owing to the narrow spacing of the $(1s2s)\,^1S$ and $(1s2p)\,^3P$ thresholds (Fig. 6). The odd-parity Li I $^2P^o$ resonances are known from uv absorption[5] to better than 0.1 eV accuracy, whereas the even-parity states such as $(1s2s^2)\,^2S^e$, $(1s2p^2)\,^2S^e$, and $^2D^e$, etc., cannot be excited optically from the Li I ground state $(1s^22s)\,^2S^e$. In order to classify resonant structures above the $(1s2s)\,^3S$ threshold, Cooper *et al.*[22] have performed close-coupling calculations. Some of their results are plotted in Fig. 6. For Li I $1s2lnl'$ states above the onset of the $(1s2s)\,^3S$ series limit at least two continua are adjacent, namely, $(1s^2\epsilon l)\,^2l$ and $(1s2s\,^3S\epsilon l)\,^2l$. Owing to the fact that autoionization is strongest near threshold,[23] we would expect that transitions to the $(1s2s\,^3S\epsilon l)\,^2l$ continuum to be favored.

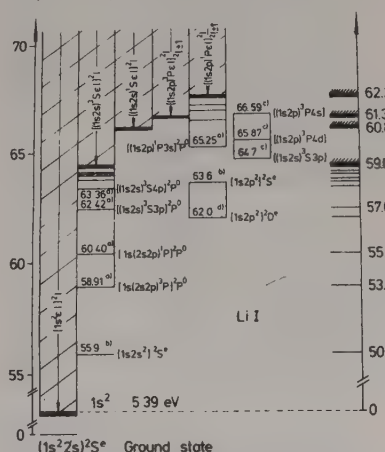

FIG. 6. Energy-level diagram for Coulomb autoionizing ^2L states in Li I as derived from (a) uv-absorption measurements (Ref. 4), (b) present work, (c) close-coupling calculations (Ref. 22), and (d) variational minimum principle (Ref. 39). The energy ladder on the right predicts peak positions of possible decays of ^2L states to the $(1s^2\epsilon l)^2l$ continuum.

The low-energy group of lines in the prompt spectrum (Fig. 7) can be assigned to Li I doublet configurations. An analysis of this part of the spectrum has been attempted. The main group of lines which occur at about 55 eV coincide with three $^2P^o$ states from uv-absorption experiments[5] to within 0.2 eV. It is apparent from the level diagram that the first peak in the spectrum at 50.5 ± 0.5 eV cannot be associated to Coulomb autoionization of odd-parity levels. Therefore, we have interpreted this line as the transition $(1s2s^2)\,^2S^e \rightarrow (1s^2\epsilon s)\,^2S^o$ giving an excitation energy of 55.9 ± 0.5 eV for the $(1s2s^2)\,^2S^e$ level. This interpretation is consistent with Fricke's Hartree-Fock calculation[24] which predicts the $(1s2s^2)\,^2S^e$ excitation energy 0.6 eV above our experimental value. The higher-lying even-parity states of the kind $(1s2p^2)\,^2S^e$ and $^2D^e$ could not be verified experimentally.

Possible charging up of the foil during heavy-ion bombardment would tend to slow down the prompt electrons, but not the delayed ones. This effect contributes an unknown uncertainty in the calibration of the prompt spectra. Comparison of our Li $^2P^o$ energies with those obtained by uv absorption, however, shows no discernible shift in the prompt spectra.

V. THEORETICAL CALCULATIONS

Extensive experimental investigations[7,11] and theoretical calculations[7,11,25] have been performed to identify the resonant states in helium due to double-electron excitation. Since two-electron atoms are the simplest systems that can autoionize, our interest has been to extend these studies to higher members of the He isoelectronic series. In particular, this allows the study of two-electron correlations in highly excited states as a function of the atomic number. Our experimental data are explained here in terms of complete calculations of doubly excited states in Li II and triply excited states in Li I.

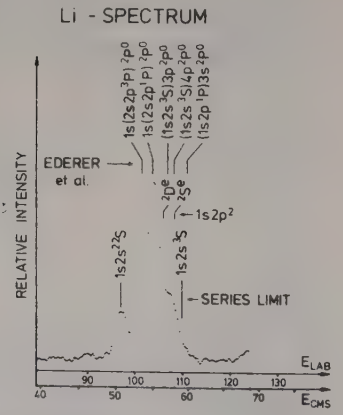

FIG. 7. Li I autoionization spectrum between 40 and 60 eV (background subtracted).

The doubly excited states for Li^+ have been calculated using the truncated diagonalization method (TDM) of Lipsky and Russek,[25] or Altick and Moore.[26] For resonances below the $n = 2$ threshold, all possible hydrogenic product functions have been included in which one of the electrons is represented by a $2s$, $2p$, $3s$, $3p$, or $3d$ function, and the other electron can have any radial quantum number from 2 to 10. No $1s$ configurations were used, although other states through $5g5g$ were. In order to calculate resonances below the $N = 3$ threshold, all configurations with N or n equal 2 were eliminated, and the reduced matrix diagonalized. The full details are given by Lipsky, Conneely, and Anania.[27]

The triply excited states were calculated using an extension of the TDM as described by Ahmed and Lipsky.[28] Here, only configurations up through $n = 5$ were included, while (as in doubly excited states) all ($1s$) states were excluded. Furthermore, the wave functions are expanded in terms of doubly excited states, so the resultant energy levels are upper bounds to the true levels.

All the calculated doubly and triply excited levels come from *ab initio* calculations, and therefore do not depend on any experimental constants when expressed in atomic units below total ionization (1 a.u. = 27.21 eV). In converting to electron volts, we used

$$E\ (\text{eV above } 1s) = 2 \times 13.605 \times (\tfrac{3}{2} - |E(\text{a.u.})|)\,. \qquad (1)$$

The doubly excited states for Li^+ (as with all other two-electron systems with nuclear charge $Z \geq 2$) can be classified into different Rydberg series which converge to the $N = 2$ and 3 levels of Li^{++}. When the energy levels are expressed as effective quantum numbers (n^*), i.e.,

$$E\ (\text{a.u.}) = -(3)^2/2N^2 - (2)^2/2(n^*)^2\,, \qquad (2)$$

then, in most cases, the identities of the different series become apparent, since the fractional parts of the n^*'s should differ only slightly from one member of a series to another member of the same series. The series classifications are based partly on this relationship and partly on a detailed examination of the wave functions, which was carried out to compare the configuration mixings of the

TABLE I. Doubly excited states below the $N = 2$ threshold in Li^+. See Eq. (3) of the text for explanation of the classifications. An (*) marks each state which is the lowest member of its series. Energy in a.u. is total energy below double ionization. The column marked eV lists the energy above the 1s threshold of Li^{++}.

Classification	Effective quantum number	Energy (a.u.)	(eV)	Classification	Effective quantum number	Energy (a.u.)	(eV)
$(2,2a)100^*$	1.604 259	1.902 106	70.6887	$(2,4c)111$	4.182 206	1.239 345	88.7224
$(2,2a)311^*$	1.633 379	1.874 644	71.4359	$(2,4b)100$	4.224 985	1.237 041	88.7851
$(2,2a)310^*$	1.733 333	1.790 680	73.7206	$(2,5a)300$	4.531 818	1.222 383	89.1889
$(2,2a)120^*$	1.773 660	1.760 753	74.5349	$(2,5b)111$	4.582 310	1.220 248	89.2420
$(2,2a)111^*$	1.792 699	1.747 321	74.9004	$(2,5a)100$	4.639 533	1.217 914	89.3055
$(2,2b)100^*$	2.022 883	1.613 751	78.5348	$(2,5a)311$	4.683 824	1.216 165	89.3531
$(2,3a)300^*$	2.522 386	1.439 344	83.2804	$(2,5a)320$	4.714 098	1.214 997	89.3849
$(2,3b)111^*$	2.562 720	1.429 527	83.5475	$(2,5a)110$	4.743 378	1.213 890	89.4150
$(2,3a)100$	2.641 231	1.411 693	84.0328	$(2,5b)311$	4.762 351	1.213 183	89.4342
$(2,3a)320^*$	2.677 374	1.404 004	84.2420	$(2,5a)331$	4.843 406	1.210 257	89.5139
$(2,3a)311$	2.682 455	1.402 948	84.2707	$(2,5a)120$	4.873 517	1.209 206	89.5425
$(2,3a)110^*$	2.695 314	1.400 303	84.3427	$(2,5a)121$	4.874 990	1.209 155	89.5438
$(2,3b)311^*$	2.710 716	1.397 183	84.4276	$(2,5a)310$	4.878 016	1.209 050	89.5467
$(2,3a)331^*$	2.835 735	1.373 713	85.0662	$(2,5b)320$	4.919 013	1.207 656	89.5847
$(2,3a)121^*$	2.853 693	1.370 592	85.1511	$(2,5a)321$	4.960 595	1.206 276	89.6222
$(2,3a)310$	2.856 890	1.370 043	85.1661	$(2,5a)111$	4.962 954	1.206 199	89.6243
$(2,3a)120$	2.867 171	1.368 289	85.2139	$(2,5a)130$	4.965 235	1.206 123	89.6263
$(2,3b)320^*$	2.906 634	1.361 728	85.3923	$(2,5a)330$	4.966 748	1.206 075	89.6277
$(2,3b)300^*$	2.925 479	1.358 687	85.4751	$(2,5b)300$	4.974 803	1.205 812	89.6348
$(2,3a)111$	2.939 003	1.356 542	85.5335	$(2,5b)331$	4.994 279	1.205 183	89.6519
$(2,3a)321^*$	2.945 590	1.355 507	85.5616	$(2,5b)131$	4.996 069	1.205 126	89.6535
$(2,3a)131^*$	3.020 945	1.344 151	85.8706	$(2,5b)120$	5.032 199	1.203 979	89.6847
$(2,3b)120^*$	3.021 059	1.344 134	85.8711	$(2,5a)131$	5.036 745	1.203 836	89.6886
$(2,3c)311^*$	3.088 426	1.334 679	86.1283	$(2,5c)331^*$	5.039 818	1.203 740	89.6912
$(2,3c)111^*$	3.178 053	1.323 019	86.4456	$(2,5c)131^*$	5.040 104	1.203 732	89.6914
$(2,3b)100$	3.206 373	1.319 536	86.5404	$(2,5c)320$	5.070 369	1.202 794	89.7169
$(2,4a)300$	3.527 069	1.285 769	87.4592	$(2,5c)120$	5.076 944	1.202 593	89.7224
$(2,4b)111$	3.574 533	1.281 528	87.5746	$(2,5c)311$	5.081 129	1.202 465	89.7259
$(2,4a)100$	3.637 290	1.276 173	87.7203	$(2,5c)111$	5.183 908	1.199 424	89.8086
$(2,4a)311$	3.680 926	1.272 610	87.8172	$(2,5b)100$	5.230 927	1.198 092	89.8449
$(2,4a)320$	3.701 707	1.270 957	87.8622	$(2,6a)300$	5.536 384	1.190 249	90.0583
$(2,4a)110$	3.727 963	1.268 909	87.9180	$(2,6b)111$	5.588 162	1.189 046	90.0910
$(2,4b)311$	3.745 984	1.267 527	87.9555	$(2,6a)100$	5.642 308	1.187 822	90.1243
$(2,4a)331$	3.838 759	1.260 721	88.1407	$(2,6a)311$	5.686 599	1.186 848	90.1508
$(2,4a)121$	3.867 235	1.258 730	88.1949	$(2,6a)320$	5.721 407	1.186 097	90.1712
$(2,4a)310$	3.870 770	1.258 486	88.2016	$(2,6a)110$	5.752 100	1.185 447	90.1889
$(2,4a)120$	3.871 001	1.258 470	88.2020	$(2,6b)311$	5.771 410	1.185 043	90.1999
$(2,4b)320$	3.913 693	1.255 573	88.2808	$(2,6a)331$	5.846 538	1.183 510	90.2416
$(2,4a)321$	3.955 510	1.252 828	88.3555	$(2,6a)120$	5.874 480	1.182 955	90.2568
$(2,4a)111$	3.956 001	1.252 795	88.3564	$(2,6a)121$	5.879 453	1.182 857	90.2594
$(2,4b)300$	3.960 549	1.252 502	88.3644	$(2,6a)310$	5.881 724	1.182 812	90.2606
$(2,4a)130^*$	3.963 221	1.252 331	88.3690	$(2,6b)320$	5.922 110	1.182 026	90.2820
$(2,4a)330^*$	3.964 352	1.252 257	88.3710	$(2,6a)321$	5.963 176	1.181 243	90.3033
$(2,4b)331^*$	3.992 804	1.250 450	88.4202	$(2,6a)111$	5.965 801	1.181 194	90.3047
$(2,4b)131^*$	3.994 130	1.250 367	88.4225	$(2,6a)130$	5.966 672	1.181 177	90.3051
$(2,4b)120$	4.029 120	1.248 199	88.4815	$(2,6a)330$	5.968 345	1.181 146	90.3060
$(2,4a)131$	4.032 302	1.248 005	88.4867	$(2,6b)300$	5.981 894	1.180 892	90.3129
$(2,4c)320^*$	4.070 227	1.245 724	88.5488	$(2,6b)331$	5.995 311	1.180 642	90.3197
$(2,4c)120^*$	4.074 559	1.245 466	88.5558	$(2,6b)131$	5.997 295	1.180 605	90.3207
$(2,4c)311$	4.082 131	1.245 020	88.5680	$(2,6b)120$	6.033 372	1.179 943	90.3387

TABLE I *(continued)*

Classification	Effective quantum number	Energy (a.u.)	Energy (eV)	Classification	Effective quantum number	Energy (a.u.)	Energy (eV)
(2, 6*a*)31	6.038 168	1.179 855	90.3411	(2, 7*a*)100	6.643 619	1.170 312	90.6007
(2, 6*c*)31	6.040 273	1.179 816	90.3421	(2, 7*a*)11	6.687 761	1.169 716	90.6170
(2, 6*c*)31	6.040 999	1.179 804	90.3425	(2, 7*a*)20	6.725 186	1.169 220	90.6305
(2, 6*c*)20	6.070 688	1.179 269	90.3571	(2, 7*a*)10	6.756 776	1.168 807	90.6417
(2, 6*c*)10	6.078 375	1.179 132	90.3608	(2, 7*b*)11	6.776 184	1.168 556	90.6486
(2, 6*c*)11	6.080 793	1.179 089	90.3619	(2, 7*a*)31	6.848 045	1.167 648	90.6733
(2, 6*c*)11	6.184 581	1.177 288	90.4109	(2, 7*a*)10	6.874 125	1.167 324	90.6820
(2, 6*b*)10	6.233 455	1.176 472	90.4332	(2, 7*a*)11	6.881 708	1.167 232	90.6846
(2, 7*a*)00	6.539 535	1.171 766	90.5612	(2, 7*a*)10	6.883 150	1.167 213	90.6851
(2, 7*b*)11	6.591 753	1.171 028	90.5813	(2, 7*b*)20	6.923 556	1.166 722	90.6984

different states.

In Table I, all doubly excited states which are less than 91 eV above the 1*s* threshold, and with total orbital angular momentum 0, 1, 2, and 3, are included. As mentioned before, the energies (in atomic units) below total ionization come directly from the TDM calculations so they are included in this table for comparison with other calculations. The effective quantum numbers, calculated from Eq. (2), and the energies in eV from Eq. (1) are also contained in the table.

Whenever there is more than one series for a given S, L, and π, the mixings between the different configurations are so great that traditional classifications based on single products of orbitals are useless.[29] Therefore, the letters a, b, c, etc., are used instead to label the different series. When $Z>1$, there exists a one-to-one correspondence between the radial quantum numbers (N and n) of the single-particle states and the true states, and these are used in our classification scheme. The letters a, b, etc., are assigned according to the energy of the lowest member of each series. We use the following notation:

$$(N, n\alpha)\,(2S+1)\,L,\,\pi, \qquad (3)$$

where N is the inner-electron quantum number (also the level of Li^{++} below which this state lies), n is the outer-electron radial quantum number, and $\alpha = a, b, c, \ldots$ (member of αth series).

Table II contains a description of all the series represented in Table I. The column called "approximate mixings," except where otherwise noted, lists descriptions which account for at least 90% of each wave function in the series. Since few calculations have been made of Li^-, the column labeled "width" is to be taken only as a guide as to what one might expect after considering information about other atoms or other series. It seems clear, though, that widths are as characteristic of a series as are the configuration mixings, so we guess that the following rules are generally true: (i) Series for which configurations add (plus states) are broader than those for which configurations subtract[1] (minus states). (ii) Series with configurations of smaller orbital quantum numbers will be broader than those with larger orbital quantum numbers. (iii) Lower lettered series are usually broader than higher lettered ones. (iv) Series which have no adjacent open channels of like configuration mixings to couple to, will be very narrow. This rule is strictly true for the metastable states such as $(2p2p)\,^3P^e$ which cannot decay at all through electron-electron interactions, but must either photodecay, or decay via one of L, S, and parity-violating perturbations such as the spin-orbit interaction.

These rules are not independent, but may be interrelated in one way or another.

Tables III and IV display data similar to Tables I and II, but for doubly excited states above $N=2$, and below the $N=3$ threshold. Here, since most states can decay through more than one channel (the bound electron can drop to either the 1*s*, or the 2*s* or 2*p* states), estimates of the widths are even less reliable, so they have been omitted.

Table V displays the results of Ahmed and Lipsky[28] for triply excited states with $^2S^e$ and $^2P^o$ symmetries. No attempt has been made to describe the configuration mixings, and so it has not been possible as yet to classify the states into series (except for the lowest states of each symmetry).

Table VI summarizes the possible decay modes for the various doubly excited configurations.

VI. Li II STATES BELOW THE $N=2$ SERIES LIMIT

In Fig. 8 we have displayed the higher-energy portion of the prompt lithium spectrum between 60

TABLE II. Classification of different series for Li^+ below the $N = 2$ state of Li^{++}.

Series classification	Lowest n	Approximate mixings	Probable widths	Comments
$^1S^e$, two series involving configurations: $2snS$, $2pnp$				
$(2,na)\,^1S^e$	2	$(2snS + 2pnp)$	Broad	
$(2,nb)\,^1S^e$	2	$(2snS - 2pnp)$	Narrow	$(2,2b)$ contains 1.6% $3d3d$
$^3S^e$, two series involving configurations: $2snS$, $2pnp$				
$(2,na)\,^3S^e$	3	$(2snS + 2pnp)$	Narrow?	
$(2,nb)\,^3S^e$	3	$(2snS - 2pnp)$	Very narrow?	
$^1P^o$, three series involving configurations: $2snp$, $ns2p$, $2pnd$				
$(2,na)\,^1P^o$	2	$(2snp + ns2p)$	Broad	All except $(2,2a)$, contain over 10% $2pnd$
$(2,nb)\,^1P^o$	3	$(2snp - ns2p)$	Narrow	Have about 10% $2pnd$
$(2,nc)\,^1P^o$	3	$2pnd$	Very narrow	Have 20% sp
$^3P^o$, three series involving configurations: $2snp$, $ns2p$, $2pnd$				
$(2,na)\,^3P^o$	2	$(2snp + ns2p)$	Broad	
$(2,nb)\,^3P^o$	3	$(2snp - ns2p) + 2pnd$	Narrow	
$(2,nc)\,^3P^o$	3	$(2snp - ns2p) - 2pnd$	Very narrow	
$^1P^e$, one series involving configuration: $2pnp$				
$(2,na)\,^1P^e$	3	$2pnp$	Metastable	
$^3P^e$, one series involving configuration: $2pnp$				
$(2pnp)\,^3P^e$	2	$2pnp$	Metastable	
$^1D^o$, one series involving configuration: $2pnd$				
$(2,na)\,^1D^o$	3	$2pnd$	Metastable	
$^3D^o$, one series involving configuration: $2pnd$				
$(2,na)\,^3D^o$	3	$2pnd$	Metastable	
$^1D^e$, three series involving configurations: $2pnp$, $2snd$, $2pnf$				
$(2,na)\,^1D^e$	2	$(2pnp - 2snd$	Narrow?	The $(2,2a)$ state is mostly $2p\,2p$
$(2,nb)\,^1D^e$	3	$(2pnp + 2snd)$	Broad?	
$(2,nc)\,^1D^e$	4	$2pnf$	Very narrow?	
$^3D^e$, three series involving configurations: $2pnp$, $2snd$, $2pnf$				
$(2,na)\,^3D^e$	3	$(2pnp - 2snd)$	Narrow?	2:1 ratio pp to sd.
$(2,nb)\,^3D^e$	3	$(2pnp + 2snd)$	Broad?	1:2 ratio pp to sd; up to 10% pf
$(2,nc)\,^3D^e$	4	$2pnf$	Very narrow?	10% other
$^1F^o$, three series involving configurations: $2snf$, $2pnd$, $2png$				
$(2,na)\,^1F^o$	3	$2pnd$		25% others
$(2,nb)\,^1F^o$	4	$2snf$		a and c are crossing above $n = 6$
$(2,nc)\,^1F^o$	5	$2png$		
$^3F^o$, three series involving configurations: $2snf$, $2pnd$, $2png$				
$(2,na)\,^3F^o$	3	$2pnd$		15% other
$(2,nb)\,^3F^o$	4	$2snf$		15% other
$(2,nc)\,^3F^o$	5	$2png$		
$^1F^e$, one series involving configuration: $2pnf$				
$(2,na)\,^1F^e$	4	$2pnf$	Metastable	
$^3F^e$, one series involving configuration: $2pnf$				
$(2,na)\,^3F^e$	4	$2pnf$	Metastable	

TABLE III. Doubly excited states below the $N = 3$ threshold in Li^+. See Eq. (3) of the text for explanation of the classifications. An (*) marks each state which is the lowest member of its series. Energy in a.u. is total energy below double ionization. The column marked eV lists the energy above the 1s threshold of Li^{++}.

Classification	Effective quantum number	Energy (a.u.)	Energy (eV)	Classification	Effective quantum number	Energy (a.u.)	Energy (eV)
(3, 4*b*)330*	3.848 669	0.635 023	105.1660	(3, 5*c*)130*	5.044 549	0.578 593	106.7014
(3, 4*a*)131	3.904 760	0.631 172	105.2708	(3, 5*c*)330*	5.045 078	0.578 577	106.7019
(3, 4*d*)331*	3.951 238	0.628 104	105.3542	(3, 5*e*)320	5.073 602	0.577 696	106.7259
(3, 4*c*)121*	3.962 439	0.627 381	105.3739	(3, 5*c*)321	5.078 919	0.577 533	106.7303
(3, 4*c*)120	4.016 859	0.623 953	105.4672	(3, 5*e*)131*	5.107 665	0.576 663	106.7540
(3, 4*b*)310	4.018 856	0.623 830	105.4705	(3, 5*e*)331*	5.107 934	0.576 655	106.7542
(3, 4*c*)321*	4.069 728	0.620 753	105.5543				
(3, 4*e*)320*	4.078 543	0.620 232	105.5684	(3, 3*a*)100*	2.355 671	0.860 413	99.0331
(3, 4*c*)300*	4.126 824	0.617 435	105.6445	(3, 3*a*)311*	2.370 379	0.855 954	99.1544
(3, 4*d*)131*	4.143 932	0.616 467	105.6709	(3, 3*a*)120*	2.412 464	0.843 644	99.4894
				(3, 3*a*)310*	2.454 094	0.832 084	99.8040
(3, 4*b*)111	4.164 094	0.615 342	105.7015	(3, 3*a*)111*	2.467 751	0.828 418	99.9037
(3, 4*e*)120*	4.197 557	0.613 511	105.7513	(3, 3*a*)331*	2.486 609	0.823 456	100.0387
(3, 5*a*)300	4.237 407	0.611 386	105.8092	(3, 3*a*)131*	2.502 490	0.819 363	100.1501
(3, 5*c*)111	4.261 830	0.610 113	105.8438	(3, 3*a*)320*	2.525 504	0.813 569	100.3077
(3, 4*e*)311*	4.300 321	0.608 150	105.8972	(3, 3*a*)321*	2.597 784	0.796 363	100.7759
(3, 5*b*)320	4.316 852	0.607 324	105.9197	(3, 3*b*)120*	2.604 412	0.794 856	100.8169
(3, 5*a*)100	4.323 992	0.606 970	105.9293				
(3, 5*a*)311	4.348 654	0.605 760	105.9622	(3, 3*b*)100*	2.606 461	0.794 393	100.8295
(3, 4*e*)111*	4.384 070	0.604 058	106.0085	(3, 3*a*)330*	2.636 122	0.787 805	101.0088
(3, 5*a*)110	4.398 467	0.603 378	106.0270	(3, 3*b*)311*	2.643 316	0.786 241	101.0513
				(3, 3*a*)131*	2.720 094	0.770 310	101.4848
(3, 5*c*)311	4.402 746	0.603 177	106.0325	(3, 3*b*)310*	2.806 190	0.753 978	101.9292
(3, 5*b*)131	4.418 806	0.602 428	106.0529	(3, 3*c*)120*	2.857 374	0.744 960	102.1746
(3, 5*a*)120	4.422 271	0.602 268	106.0572	(3, 3*b*)111*	2.948 693	0.730 023	102.5810
(3, 5*b*)321	4.471 510	0.600 028	106.1182	(3, 4*a*)300*	3.251 126	0.689 218	102.6913
(3, 4*c*)100	4.483 692	0.599 485	106.1330	(3, 4*c*)111*	3.270 620	0.686 969	103.7525
(3, 5*d*)120	4.485 655	0.599 398	106.1353	(3, 4*b*)320*	3.315 399	0.681 953	103.8890
(3, 5*a*)310	4.521 118	0.597 845	106.1776				
(3, 5*a*)331	4.528 520	0.597 525	106.1863	(3, 3*c*)100*	3.322 360	0.681 191	103.9097
(3, 5*a*)111	4.550 003	0.596 606	106.2113	(3, 4*a*)100	3.356 666	0.677 506	104.0100
(3, 5*a*)121	4.578 688	0.595 400	106.2441	(3, 4*a*)110*	3.376 221	0.675 456	104.0658
				(3, 4*a*)311	3.377 701	0.675 302	104.0700
(3, 5*b*)300	4.587 292	0.595 042	106.2539	(3, 4*c*)311*	3.380 754	0.674 986	104.0786
(3, 5*c*)320	4.587 827	0.595 020	106.2545	(3, 4*b*)131*	3.401 962	0.672 811	104.1378
(3, 5*b*)121	4.594 721	0.594 735	106.2622	(3, 4*b*)321*	3.441 341	0.668 878	104.2448
(3, 5*a*)130	4.615 439	0.593 887	106.2853	(3, 4*a*)120	3.445 167	0.668 504	104.2550
(3, 5*a*)320	4.622 393	0.593 604	106.2930	(3, 4*d*)120*	3.453 702	0.667 672	104.2776
(3, 5*d*)111	4.644 111	0.592 731	106.3168	(3, 4*b*)300*	3.533 074	0.660 223	104.4803
(3, 5*b*)331	4.651 984	0.592 417	106.3253				
(3, 5*a*)330	4.701 480	0.590 482	106.3779	(3, 4*a*)310	3.527 621	0.660 719	104.4668
(3, 5*c*)331	4.748 149	0.588 712	106.4261	(3, 4*c*)320*	3.540 072	0.659 590	104.4975
(3, 5*b*)130	4.752 835	0.588 537	106.4309	(3, 4*b*)121*	3.540 907	0.659 515	104.4996
				(3, 4*a*)331	3.546 557	0.659 007	104.5134
(3, 5*a*)321	4.754 378	0.588 479	106.4324	(3, 4*a*)111	3.553 077	0.658 424	104.5292
(3, 5*c*)131	4.759 041	0.588 306	106.4371	(3, 4*a*)130*	3.576 699	0.656 338	104.5860
(3, 5*b*)120	4.769 366	0.587 924	106.4475	(3, 4*a*)121	3.586 816	0.655 457	104.6100
(3, 5*d*)320	4.793 380	0.587 045	106.4714	(3, 4*d*)111*	3.589 605	0.655 216	104.6165
(3, 5*b*)100	4.807 164	0.586 547	106.4850	(3, 4*b*)331*	3.607 930	0.653 643	104.6593
(3, 5*b*)311	4.818 072	0.586 156	106.4957	(3, 4*a*)320	3.622 332	0.652 424	104.6925
(3, 5*b*)110	4.839 493	0.585 395	106.5164				
(3, 5*b*)330	4.863 430	0.584 556	106.5392	(3, 4*a*)330	3.707 024	0.645 539	104.8798
(3, 5*d*)311	4.877 417	0.584 072	106.5524	(3, 4*c*)331*	3.723 344	0.644 266	104.9145
(3, 5*a*)131	4.921 801	0.582 562	106.5934	(3, 4*b*)130*	3.728 520	0.643 866	104.9254
(3, 5*d*)331	4.948 313	0.581 680	106.6174	(3, 4*d*)320*	3.742 45	0.642 797	104.9545
				(3, 4*a*)321	3.743 317	0.642 730	104.9563
(3, 5*c*)121	4.973 987	0.580 839	106.6403	(3, 4*b*)120	3.755 444	0.641 810	104.9813
(3, 5*c*)120	5.024 704	0.579 215	106.6845	(3, 4*c*)131*	3.759 163	0.641 530	104.9889
(3, 5*b*)310	5.040 031	0.578 734	106.6976	(3, 4*b*)110*	3.779 222	0.640 031	105.0297

TABLE III *(continued)*

Classification	Effective quantum number	Energy (a.u.)	Energy (eV)	Classification	Effective quantum number	Energy (a.u.)	Energy (eV)
(3, 4*b*)100	3.786 420	0.639 499	105.0442	(3, 6*f*)131*	6.131 236	0.553 203	107.3923
(3, 4*b*)311	3.804 180	0.638 200	105.0795	(3, 6*f*)331*	6.131 924	0.553 191	107.3926
(3, 4*d*)311*	3.812 884	0.637 570	105.0967	(3, 6*d*)131	6.162 879	0.552 658	107.4071
(3, 5*d*)131	5.156 034	0.575 231	106.7929	(3, 6*e*)120	6.182 800	0.552 319	107.4164
(3, 5*c*)300	5.166 800	0.574 918	106.8014	(3, 6*c*)300	6.190 456	0.552 190	107.4199
(3, 5*e*)120	5.182 586	0.574 462	106.8138	(3, 6*f*)320	6.199 789	0.552 033	107.4241
(3, 5*b*)111	5.191 949	0.574 194	106.8211	(3, 6*b*)111	6.202 114	0.551 994	107.4252
(3, 5*f*)320*	5.195 904	0.574 081	106.8242	(3, 7*a*)300	6.226 016	0.551 595	107.4360
(3, 5*f*)120*	5.219 994	0.573 399	106.8428	(3, 6*f*)120	6.228 992	0.551 546	107.4374
(3, 6*a*)300	5.229 228	0.573 140	106.8498	(3, 7*c*)111	6.254 794	0.551 122	107.4489
(3, 6*c*)111	5.256 422	0.572 385	106.8704	(3, 6*e*)311	6.274 243	0.550 805	107.4575
(3, 5*e*)311	5.276 161	0.571 845	106.8851	(3, 7*a*)100	6.301 519	0.550 366	107.4695
(3, 6*a*)100	5.308 764	0.570 965	106.9090	(3, 7*b*)320	6.318 347	0.550 098	107.4768
(3, 6*b*)320	5.316 965	0.570 746	106.9150	(3, 7*a*)311	6.328 366	0.549 940	107.4811
(3, 6*a*)311	5.334 856	0.570 272	106.9278	(3, 6*e*)111	6.382 732	0.549 093	107.5041
(3, 5*e*)111	5.378 273	0.569 142	106.9586	(3, 7*a*)120	6.406 397	0.548 731	107.5140
(3, 6*a*)110	5.410 067	0.568 332	106.9806	(3, 7*a*)110	6.417 382	0.548 564	107.5185
(3, 6*a*)120	5.411 658	0.568 292	106.9817	(3, 7*c*)311	6.422 225	0.548 491	107.5205
(3, 6*c*)311	5.414 688	0.568 215	106.9838	(3, 7*b*)131	6.431 515	0.548 351	107.5243
(3, 6*b*)131	5.426 483	0.567 919	106.9919	(3, 7*b*)321	6.494 984	0.547 410	107.5499
(3, 6*b*)321	5.486 502	0.566 441	107.0321	(3, 7*d*)120	6.510 189	0.547 189	107.5559
(3, 6*d*)120	5.501 321	0.566 084	107.0418	(3, 7*a*)331	6.515 181	0.547 117	107.5579
(3, 5*c*)100	5.506 077	0.565 970	107.0449	(3, 7*a*)310	6.518 220	0.547 073	107.5591
(3, 6*a*)310	5.519 267	0.565 655	107.0535	(3, 6*c*)100	6.519 465	0.547 055	107.5596
(3, 6*a*)331	5.519 927	0.565 639	107.0539	(3, 7*a*)111	6.547 161	0.546 658	107.5704
(3, 6*a*)111	5.548 564	0.564 963	107.0723	(3, 7*a*)121	6.579 881	0.546 195	107.5830
(3, 6*a*)121	5.580 117	0.564 231	107.0922	(3, 7*a*)320	6.608 728	0.545 792	107.5939
(3, 6*a*)320	5.604 959	0.563 663	107.1077	(3, 7*b*)300	6.626 457	0.545 548	107.6006
(3, 6*b*)300	5.613 390	0.563 472	107.1129	(3, 7*b*)121	6.627 797	0.545 529	107.6011
(3, 6*b*)121	5.616 235	0.563 407	107.1146	(3, 7*c*)320	6.634 505	0.545 437	107.6036
(3, 6*c*)320	5.627 760	0.563 148	107.1217	(3, 7*a*)130	6.641 494	0.545 342	107.6062
(3, 6*a*)130	5.632 986	0.563 031	107.1249	(3, 7*b*)331	6.679 697	0.544 825	107.6203
(3, 6*d*)111	5.669 706	0.562 217	107.1470	(3, 7*d*)111	6.681 882	0.544 795	107.6211
(3, 6*b*)331	5.670 644	0.562 196	107.1476	(3, 7*a*)330	6.700 573	0.544 546	107.6279
(3, 6*a*)330	5.701 229	0.561 531	107.1657	(3, 7*a*)321	6.758 698	0.543 783	107.6486
(3, 6*a*)321	5.758 563	0.560 312	107.1989	(3, 7*c*)131	6.759 274	0.543 775	107.6488
(3, 6*c*)131	5.759 986	0.560 282	107.1997	(3, 7*c*)331	6.769 991	0.543 637	107.6526
(3, 6*c*)331	5.762 761	0.560 224	107.2013	(3, 7*b*)130	6.773 548	0.543 591	107.6538
(3, 6*b*)130	5.766 648	0.560 143	107.2035	(3, 7*b*)120	6.775 890	0.543 561	107.6547
(3, 6*b*)120	5.775 180	0.559 965	107.2083	(3, 7*b*)100	6.813 942	0.543 076	107.6679
(3, 6*b*)100	5.813 842	0.559 170	107.2299	(3, 7*b*)311	6.822 816	0.542 964	107.6709
(3, 6*d*)320	5.817 001	0.559 106	107.2317	(3, 7*d*)320	6.827 594	0.542 904	107.6725
(3, 6*b*)311	5.823 160	0.558 981	107.2351	(3, 7*b*)330	6.869 939	0.542 376	107.6869
(3, 6*b*)110	5.867 736	0.558 088	107.2594	(3, 7*b*)110	6.879 434	0.542 260	107.6901
(3, 6*b*)330	5.869 243	0.558 059	107.2602	(3, 7*d*)311	6.920 339	0.541 761	107.7036
(3, 6*d*)311	5.907 285	0.557 313	107.2805	(3, 7*a*)131	6.925 504	0.541 699	107.7053
(3, 6*a*)131	5.926 307	0.556 946	107.2905	(3, 7*d*)331	6.954 737	0.541 349	107.7148
(3, 6*d*)331	5.952 875	0.556 439	107.3043	(3, 7*c*)121	6.988 408	0.540 952	107.7257
(3, 6*c*)121	5.985 090	0.555 833	107.3208	(3, 7*c*)120	7.020 629	0.540 577	107.7359
(3, 6*c*)120	6.024 590	0.555 103	107.3406	(3, 7*c*)130	7.050 348	0.540 235	107.7451
(3, 6*b*)310	6.049 717	0.554 646	107.3530	(3, 7*c*)330	7.050 574	0.540 233	107.7452
(3, 6*c*)130	6.049 939	0.554 642	107.3531	(3, 7*b*)310	7.050 861	0.540 230	107.7453
(3, 6*c*)330	6.050 642	0.554 629	107.3535	(3, 7*e*)320	7.076 178	0.539 942	107.7531
(3, 6*e*)320	6.076 334	0.554 168	107.3660	(3, 7*c*)321	7.089 240	0.539 795	107.7571
(3, 6*c*)321	6.087 556	0.553 969	107.3715	(3, 7*e*)131	7.102 884	0.539 642	107.7613
(3, 6*e*)331	6.105 965	0.553 644	107.3803	(3, 7*e*)331	7.103 466	0.539 636	107.7615
(3, 6*e*)131	6.105 974	0.553 644	107.3803	(3, 7*f*)131	7.131 714	0.539 323	107.7700
				(3, 7*f*)331	7.132 942	0.539 309	107.7704

TABLE IV. Classification of different series for Li^+ below the $N = 3$ state of Li^{++}.

Series classification	Lowest n	Approximate mixings	Comments
$^1S^e$, three series involving configurations: $3sns$, $3pnp$, $3dnd$			
$(3,na)\ ^1S^e$	3	$(3sns + 3pnp)$	
$(3,nb)\ ^1S^e$	3	$(3sns - 3pnp) - 3dnd$	
$(3,nc)\ ^1S^e$	3	$(3sns - 3pnp) + 3dnd$	$(3,3c)$ contains 5% $4f4f$
$^3S^e$, three series involving configurations: $3sns$, $3pnp$, $3dnd$			
$(3,na)\ ^3S^e$	4	$(3sns + 3pnp)$	
$(3,nb)\ ^3S^e$	4	$(3sns - 3pnp) - 3dnd$	
$(3,nc)\ ^3S^e$	4	$(3sns - 3pnp) + 3dnd$	
$^1P^o$, five series involving configurations: $3snp$, $ns3p$, $3pnd$, $np3d$, $3dnf$			
$(3,na)\ ^1P^o$	3	$(3snp + ns3p) + (3pnd + np3d)$	
$(3,nb)\ ^1P^o$	3	$(3snp + ns3p) - (3dnf + np3d)$	
$(3,nc)\ ^1P^o$	4	$(3snp - ns3p) + (3pnd - np3d)$	
$(3,nd)\ ^1P^o$	4	$(3pnd - np3d) - (3snp - ns3p) + 3dnf$	
$(3,ne)\ ^1P^o$	4	$(3pnd - 3dnf)$	10% mixture of other states
$^3P^o$, five series involving configurations: $3snp$, $ns3p$, $3pnd$, $np3d$, $3dnf$			
$(3,na)\ ^3P^o$	3	$(3snp + ns3p) + (3pnd + np3d)$	$(3,4a)$ and $(3,4c)$ are mixed because series a and c are crossing in that energy range
$(3,nb)\ ^3P^o$	3	$(3snp + ns3p) + 3dnf$	
$(3,nc)\ ^3P^o$	4	$(3snp - ns3p) - (3pnd - np3d)$	
$(3,nd)\ ^3P^o$	4	$(3snp - ns3p) + np3d - 3dnf$	
$(3,ne)\ ^3P^o$	4	$(3snp - ns3p) - 3pnd + 3dnf$	
$^1P^e$, two series involving configurations: $3pnp$, $3dnd$			
$(3,na)\ ^1P^e$	4	$(3pnp + 3dnd)$	both series decay only to $2p$ plus a p-continuum electron
$(3,nb)\ ^1P^e$	4	$(3pnp - 3dnd)$	
$^3P^e$, two series involving configurations: $3pnp$, $3dnd$			
$(3,na)\ ^3P^e$	3	$(3pnp + 3dnd)$	both series decay only to $2p$ plus a p-continuum electron. Mixings are not 1:1 (more like 2:1 for a, and 1:2 for b)
$(3,nb)\ ^3P^e$	3	$(3pnp - 3dnd)$	
$^1D^o$, three series involving configurations: $3pnd$, $np3d$, $3dnf$			
$(3,na)\ ^1D^o$	3	$(3pnd + np3d)$	contain 15%df. Series a and b are crossing at $(3,5a)$ and $(3,5b)$
$(3,nb)\ ^1D^o$	4	$(3pnd + np3d)$	contain 15% df
$(3,nc)\ ^1D^o$	4	$3pnf$	contain 20% pd
$^3D^o$, three series involving configurations: $3pnd$, $np3d$, $3dnf$			
$(3,na)\ ^3D^o$	3	$(3pnd + np3d)$	contain 8% $3dnf$
$(3,nb)\ ^3D^o$	4	$(3pnd - np3d)$	contain 8% $3dnf$
$(3,nc)\ ^3D^o$	4	$3dnf$	contain 20% pd
$^1D^e$, six series involving configurations: $3pnp$, $3snp$, $ns3d$, $3dnd$, $3pnf$, $3dng$			
$(3,na)\ ^1D^e$	3	$(3snd + ns3d) - 3pnp$	
$(3,nb)\ ^1D^e$	3	$(3snd + ns3d) - 3dnd$	
$(3,nc)\ ^1D^e$	3	$ns3d + 3pnp - 3pnf - (3dnd - 3dng)$	difficult to classify
$(3,nd)\ ^1D^e$	4	$(3snd - ns3d) + 3pnf$	2:1 sd-to-pf ratio
$(3,ne)\ ^1D^e$	4	$3snd + 3pnp - 3pnf - 3dnd - 3dng$	difficult to classify
$(3,nf)\ ^1D^e$	5	$3dng$	35% other

TABLE IV *(continued)*

Series classification	Lowest n	Approximate mixings	Comments
$^1D^e$, six series involving configurations: $3pnp$, $3snd$, $ns3d$, $3dnd$, $3pnf$, $3dng$			
$(3,na)\,^1D^e$	3	$(3snd+ns3d)$	a and c cross near $n=6$
$(3,nb)\,^1D^e$	4	$(3snd-ns3d)-3pnp$	
$(3,nc)\,^3D^e$	4	$(3snd-ns3d)+3pnf-3dnd$	Above $n=5$ crossing causes breakdown of classifications
$(3,nd)\,^1D^e$	4	$3pnp+3pnf-3pnf$	
$(3,ne)\,^3D^e$	4	$(3snd+ns3d)+3pnp-3pnf+3dng$	
$(3,nf)\,^3D^e$	5	$3dng-3pnf$	
$^1F^o$, six series involving configurations: $3snf$, $3pnd$, $np3d$, $3png$, $3dnf$, $3dnh$			
$(3,na)\,^1F^o$	3	$3pnd-np3d+3dnf$	
$(3,nb)\,^1F^o$	4	$3pnd-npsd$	10–15% $3snf$
$(3,nc)\,^1F^o$	4	$3snf+(3png+3dnf-np3d)$	
$(3,nd)\,^1F^o$	4	$3pnd+3png-3dnf$	15% other
$(3,ne)\,^1F^o$	5	$3snf-3png$	25% other
$(3,nf)\,^1F^o$	6	$3dnf$	15% other
$^3F^o$, six series involving configurations: $3snf$, $3pnd$, $np3d$, $3png$, $3dnf$, $3dnh$			
$(3,na)\,^3F^o$	3	$3pnd+np3d$	10% $3snf$
$(3,nb)\,^3F^o$	4	$3snf+np3d$	
$(3,nc)\,^3F^o$	4	$3snf+3dnf$	12% other
$(3,nd)\,^3F^o$	4	$(3pnd-np3d)+(3png-3dnf)$	$(3,4d)$ has 20% $3snf$
$(3,ne)\,^3F^o$	5	$3snf-3png$	20% other
$(3,nf)\,^3F^o$	6	$3dnh$	10% other
$^1F^e$, three series involving configurations: $3pnf$, $3dnd$, $3dng$			
$(3,na)\,^1F^e$	4	$3pnf-3dnd$	
$(3,nb)\,^1F^e$	4	$3pnf+3dnd$	10% $3dng$
$(3,nc)\,^1F^e$	5	$3dng$	15% $3pnf$
$^3F^e$, three series involving configurations: $3pnf$, $3dnd$, $3dng$			
$(3,na)\,^3F^e$	3	$3pnf-3dnd$	
$(3,nb)\,^3F^e$	4	$3pnf+3dnd$	
$(3,nc)\,^3F^e$	5	$3dng$	10% $3pnf$

and 110 eV (c.m. system). The peaks in this spectrum are arbitrarily numbered 1–7. The identifications of these line structures are based on the comparison of the peak energies with the transition energies listed in Tables I, III, and V, respectively. We have assigned the main peaks to transitions of doubly excited Li II states decaying via Coulomb autoionization to the $(1s\epsilon l)^{1,3}l$ continua. This is consistent with the calculations of Balashov *et al.*[30] and Stewart *et al.*[31–33] The experimental autoionization structures are shown in Fig. 8 along with comparisons with the following calculations: (a) the six lowest transition energies of $^1P^o$ resonances deduced from Balashov's calculation[30]; (b) Stewart and co-worker's[31–33] energy values of the configurations $(2s^2)\,^1S$, $(2s2p)^{1,3}P$, and $(2p^2)\,^1S,^1D$ (traditional classification); and (c) the main Li II $^{1,3}S^e$, $^{1,3}P^o$, $^{1,3}D^e$, and $^{1,3}F^o$ energy values above the Li III $1s$ ground state as presented in this paper (see Tables I and III). We have excluded from the figure the $^{1,3}P^e$ and $^{1,1}D^o$ states since they would not produce prompt electrons.

The energy resolution of our apparatus was not sufficient to resolve variations in the cross section of the order of the natural width ($\Gamma < 0.2$ eV), hence the observed Li II autoionization peak heights for transitions to single final states depend only on the excitation cross sections.[13] This is important when relative intensities of lines stemming from different initial levels such as Li II $(2,2a)\,^3P^o$ and Li II $(2,2a)\,^1P^o$, etc., are compared.

From Table I it can be seen that the lowest prompt autoionizing Li II states are $(2,2a)\,^1S^e$, $(2,2a)\,^3P^o$, $(2,2a)\,^1D^e$, and $(2,2a)\,^1P^o$ in order of increasing energy. The theoretical transition en-

TABLE V. Triply excited states in Li. with configurations $^2S^e$ and $^2P^o$.

Classification	No. of Electrons	Energy (a.u.) below total ionization	Energy (eV) above Li ground state	Energy (eV) above 1s threshold	Energy (eV) above $(1s2s)\,^1S$
$1(2s^2\,2p)\,^2P^o$	3	2.237 332	142.552	61.567	78.181
$1(2s\,2p^2)\,^2S^e$	3	2.059 242	147.398	66.413	83.026
2 $^2S^e$	3	2.000 671	148.992	68.007	84.621
$2(2p^3)\,^2P^o$	3	1.992 823	149.206	68.220	84.833
3 $^2P^o$	3	1.977 296	149.628	68.643	85.256
4 $^2P^o$	3	1.957 597	150.164	69.179	85.792
3 $^2S^e$	3	1.946 582	150.464	69.479	86.092
4 $^2S^e$	3	1.935 286	150.771	69.786	86.381
5 $^2P^o$	3	1.930 839	150.892	69.907	86.520
6 $^2P^o$	3	1.924 614	151.062	70.076	86.689
7 $^2P^o$	3	1.906 205	151.562	70.577	87.190
$(2, 2a)\,^1S^e$	2	1.902 107	151.674	70.689	87.302
5 $^2S^e$	3	1.876 317	152.376	71.390	88.003
$(2, 2a)\,^3P^o$	2	1.874 645	152.421	71.436	88.049
8 $^2P^o$	3	1.863 538	152.723	71.738	88.351
9 $^2P^o$	3	1.856 891	152.904	71.919	88.532
10 $^2P^o$	3	1.853 743	152.990	72.005	88.618
6 $^2S^e$	3	1.835 791	153.478	72.493	89.106
11 $^2P^o$	3	1.821 748	153.861	72.875	89.488
7 $^2S^e$	3	1.801 004	154.425	73.440	90.053
12 $^2P^o$	3	1.800 661	154.434	73.449	90.062
13 $^2P^o$	3	1.798 138	154.503	73.518	90.131
$(2p)^2\,^3P^e$	2	1.790 680 6	154.706	73.721	90.334
Continuum	•••	0	203.4303	122.445	139.058

ergies associated with these states deviate less than 0.5 eV from the centroid of the two strongest peaks (1) and (2), respectively. The strongest peak in the spectrum (1) and about 70 eV can be attributed to decay of the $^1S^e$ and $^3P^o$ states which are predicted at 70.69 and 71.44 eV, respectively. These two levels ($\Delta E = 0.75$ eV) cannot be resolved in our experiments. The positions of the $(2, 2a)\,^1D^e$ and $(2, 2a)\,^1P^o$ states (Table I) coincide closely with the position of the 2nd strong peak. The correct identification of this peak is also supported by the theoretical estimate of Stewart *et al.* and Balashov *et al.* who predict the transition $(2s2p)\,^1P^o - (1s\epsilon p) \times {}^1P^o$ slightly above the experimental line center. The energy separation of the peaks (1) and (2) is 3.3 eV which is very close to the energy separation of 3.46 eV for the $(2, 2a)\,^3P^o$ and $(2, 2a)\,^1P^o$ levels (see Table I).

We conclude that this measurement gives the first experimental observation of Li II $(2, 2a)\,^{1,3}P^o$ states. These results are summarized in Table VII. The uncertainties of our data are purely systematic and include the possible error of the analysis of the spectra due to the underlying $(2, 2a)\,^1S^e - (1s\epsilon s)\,^1S^e$ and $(2, 2a)\,^1D^e - (1s\epsilon d)\,^1D^e$ unresolved lines. The observation of the transitions $(2, 2a) \times {}^3P^o - (1s\epsilon p)\,^3P^o$ and $(2, 2a)\,^1P^o - (1s\epsilon p)\,^1P^o$ in Li^+

TABLE VI. Decay modes for doubly excited states. States below the $n = 2$ threshold decay only to the 1s continuum. States between the $n = 2$ and $n = 3$ thresholds can decay through all channels listed below.

Initial Configuration	Final decay channels	
$^{1,3}S^e$	$1s\epsilon s$	$2s\epsilon s$
		$2p\epsilon p$
$^{1,3}P^o$	$1s\epsilon p$	$2s\epsilon p$
		$2p\epsilon s$
		$2p\epsilon d$
$^{1,3}P^e$		$2p\epsilon p$
$^{1,3}D^o$		$2p\epsilon d$
$^{1,3}D^e$	$1s\epsilon d$	$2s\epsilon d$
		$2p\epsilon p$
		$2p\epsilon f$
$^{1,3}F^o$	$1s\epsilon f$	$2s\epsilon f$
		$2p\epsilon d$
		$2p\epsilon g$
$^{1,3}F^e$		$2p\epsilon f$

demonstrates that the collective foil excitation populates these states with considerable cross-section. This is of particular interest for measurements on Be (Ref. 34) and B (Ref. 35), since experimental data for doubly excited P states are available only for H^- and He.

For the higher-lying Li II transitions below the $n=2$ series limit a unique interpretation of the experimental features is not possible, in general. However, a small hump just below peak (3) might be associated with the decay of $(2,2B)\,^1S$ at 78.53 eV. Peak (3) cannot be identified on the basis of autoionizing Li II states and will be discussed later. The peak (4) at about 86 eV should not be assigned to a single decay, since many closely spaced transitions (see Table I) are overlapping in this region. Similarly, the peak (5) near 88 eV could be a cumulative effect of many decaying states with effective quantum number $n^* \simeq 4$ (Table I). A multitude of autoionizing levels with effective quantum numbers $n^* \simeq 5$ and $n^* \simeq 6$ (Table I) might be responsible for the shoulder (6) on peak (5).

VII. Li II STATES BETWEEN THE $N=2$ AND $N=3$ SERIES LIMITS

In a nonrelativistic approximation the $N=2$ and $N=3$ levels of Li III are degenerate. As a result of this degeneracy the configuration mixing is strong whenever there are more than one series of equal parity and J values (Tables II and IV). Some exceptions occur for F states. One would expect that these deviations from the independent particle model become even more pronounced when one goes from the $N=2$ to the $N=3$ threshold. For example, for $^1P^o$ states below $N=2$, three series exist (Table II), whereas for $^1P^o$ states between $N=2$ and $N=3$ (Table IV) there are five distinct series, corresponding to heavy configuration interaction of the five configurations: $3snp$, $ns3p$, $3pnd$, $np3d$, $3dnf$.

Figure 9 shows the discrete decay modes of the lowest $^1P^o$ state above $N=2$ specifically $(3,3a)\,^1P^o$. Fano has pointed out that the autoionization channel requiring the least energy transfer is most likely.[23] Thus autoionization of $3\ell n\ell'(n \geq 3)$ levels leads principally to the $2\ell\epsilon\ell'$ continuum. Nevertheless, a small fraction of these Li II states decay to the final ionic state Li III $1s$ (second column of Table VI). In the case of $(3,3a)\,^1P$ (see Fig. 9), the channels leading to the $(2s\epsilon p)\,^1P^o$, $(2p\epsilon s)\,^1P^o$, and $(2p\epsilon d)\,^1P^o$ final states are favored. One expects such low-energy electrons to be ejected by fast moving Li projectiles only in forward directions. The "kinematical cutoff" is defined by[13, 36]

$$E_{\text{c.m.}} + \epsilon \sin^2\Theta_{\text{lab}} = 0\,, \tag{4}$$

where $\epsilon = (m/M)E$ is the reduced projectile energy and Θ_{lab} is the maximum angle of observation (beam axis: $\Theta_{\text{lab}}=0^\circ$). For our geometry Θ_{lab} is 42.3°. Substituting this value in the above equation, one can show that all electrons arising from decays of Li projectiles (E: 282 keV) with transition energies less than 10 eV ($E_{\text{lab}} < 12$ eV) are outside the range of our spectrometer. Consequently, autoionization of Li II levels below $(3,3a)\,^1F^o$ states (see Table II) decaying into the $2\ell\epsilon\ell'$ continuum fall below the kinematic threshold of our electron analyzer. However, those Li II levels positioned above $(3,3a)\,^1F^o$ could contribute to the

TABLE VII. Excitation energies in eV for $(2,2A)\,^{1,3}P^o$ states in Li II (measured from the Li III $1s^2$ ground state).

Experiment $(2,2A)\,^3P$	Theory $(2,2A)\,^3P$	Experiment $(2,2A)\,^1P$	Theory $(2,2A)\,^1P$
146.9±0.5 [a]	147.07 [a]	150.3±0.5 [a]	150.54 [a]
	146.95 [b]		150.31 [b]
			150.59 [c]

[a] This work.
[b] See Chan and Stewart (Ref. 31).
[c] See Balashov *et al.* (Ref. 30).

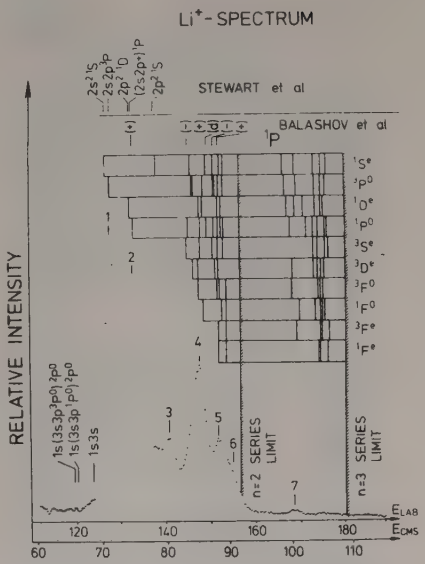

FIG. 8. Li II autoionization spectrum between 60 and 110 eV (background subtracted).

spectrum at low energies. A hump appearing in the prompt spectrum at about $E_{lab} = 12$ eV (Fig. 2) might therefore be attributed to such low-energy decays. In addition a small structure (peak 7) above the noise level occurs in the high-energy portion at about 100 eV (Fig. 8) which coincides with several Li II $(3, 3a)$, $(3, 3b)$, and $(3, 3c)$ levels decaying to the $1s\epsilon l$ continuum (Table III). Thus the existence of beam-foil excited Li II levels lying at energies between the second and third ionization limit of Li^{2+} is indicated. An equivalent structure has been seen in the H^- spectrum by Risley and co-workers[13] who identified these narrow peaks as corresponding to autodetachment of $3lnl'$ $(n \geq 3)$ levels.

VIII. TRIPLY EXCITED STATES IN Li I

Recently some work[37,38] has been carried out to investigate the formation and decay of short-lived negative helium ions of the kind $2s^2 2p$, $2s2p^2$, and $2p^3$. For monoenergetic electrons interacting with a helium gas, Fano and Cooper[38] have predicted the formation of the following triply excited He^- resonances: $(2s^2 2p)\,^2P^o$, $(2s2p^2)\,^2S^e$, $^2D^e$, and $(2p^3)\,^2P^o$. Kuyatt, Simpson, and Mielczarek[4] were the first who identified the $(2s^2 2p)\,^2P^o$ and $(2s2p^2)\,^2D^e$ He^- compound states using a transmission experiment. The beam-foil technique has the advantage over elastic electron scattering of being able to produce these states much more abundantly in positive ions. Hence triply excited Li I levels isoelectronic with He^- might contribute to the prompt electron emission after $^7Li^+$ → C-foil collisions. In fact, the high-energy portion of our prompt lithium spectrum (Fig. 8) has revealed an unidentified peak labeled 3 at about 80 eV. We assign this peak as due to Coulomb autoionization

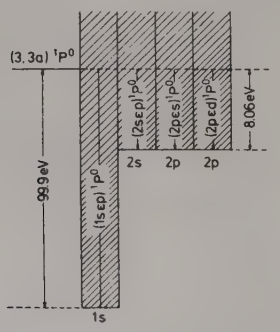

FIG. 9. Decay channels of the Li II $(3, 3a)\,^1P^o$ level.

of triply excited Li I states for the following reasons: (a) Apparently no transition energies of Li II levels lie between 78.53 and 83.28 eV (see Table I). Therefore peak (3) cannot arise from decays of Li II states. (b) The overlap with Li I transitions as originating from autoionization of the kind $1s3snl$ $(n \geq 3) - 1s^2\epsilon l$ must be excluded because these levels are converging at lower energies (68.8 eV) towards the series limit $(1s3s)^3S \infty l - 1s^2\epsilon l$ and because these states are decaying predominantly to the final Li II states $(1s2s)^{1,3}S$ and $(1s2p) \times ^{1,3}P$, respectively. (c) Finally, this feature at about 80 eV is consistent with energies of triply excited Li I states decaying via Coulomb autoionization to the $(1s2s)^{1,3}S\epsilon l$ and $(1s2p)^{1,3}P\epsilon l$ continua (Table V).

Figure 10 shows the resulting decay scheme for the $(2s^2 2p)\,^2P^o$ and $(2s2p^2)\,^2S^e$ states in Li I where dashed lines are used to represent lower intensity transitions due to shake-down processes. We have compared the experimental lithium spectrum (Fig. 11) around 80 eV with (i) transition energies associated with the levels $(2s^2 2p)\,^2P^o$ and $(2s2p^2)\,^2S$ as derived from Ahmed and Lipsky's TDM calculations[28] (Table V), and (ii) with energy positions of $(2s^2 2p)\,^2P^o$ and $(2s2p^2)\,^2D^e$ decays calculated by the application of a variational method.[39] All transition energies indicated in Fig. 11 are upper limits. We suggest that the structure near 80 eV

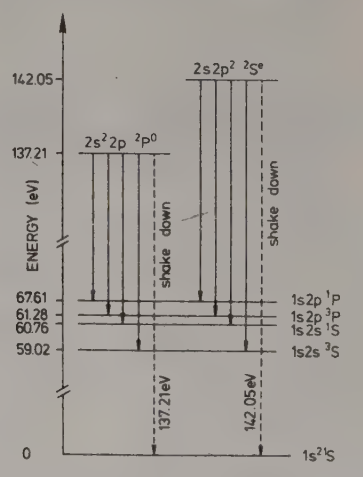

FIG. 10. Schematic drawing of the different competing decay channels of the $(2s^2 2p)\,^2P^o$ and $(2s2p^2)\,^2S^e$ states in Li^+ (not to scale).

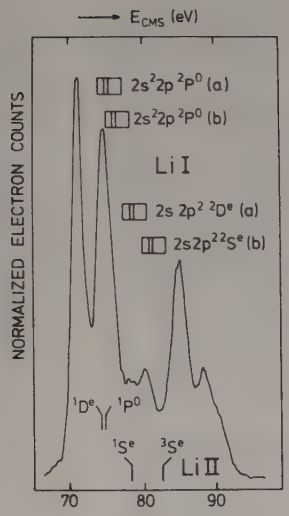

FIG. 11. Comparison of the high-energy portion of the Li spectrum with computed transition energies from autoionizing states of doubly excited Li II and triply excited Li I. (a) Nicolaides (Ref. 39), (b) this paper (Table V) (Ref. 28).

is best assigned to decays of triply excited states. We cannot exclude the possibility that decays of Li I are partially overlapping the decays from Li II levels. For example, the Li II transition $(2, 2\alpha)\,^1P^o$ $-(1s\epsilon p)\,^1P^o$ might coincide with decays of triply excited Li I levels.

IX. CONCLUSION

Using the beam-foil method and observing electrons rather than photons, the decay of short-lived autoionizing states can be studied. We have shown that doubly and triply excited Li I and doubly excited Li II levels are produced with considerable cross sections in $^7Li^+$ – C-foil collisions. This is of particular interest since Li II and Li III levels decaying via dipole transitions might be populated due to cascades of autoionizing states in Li I and Li II.

Because of the insufficient resolution at about 300 keV beam energy a unique interpretation of the observed line structures is difficult except for the most prominent peaks. However, by using thinner foils or gas targets and higher beam energies it is expected that the resolution can be improved. Furthermore, by measuring electrons in coincidence with ions it is hoped that the charge state coordination of the lithium spectra might be obtained.

ACKNOWLEDGMENTS

The authors are indebted to Professor E. Matthias for suggesting the study of electron spectra from foil-excited beams. We should like to thank Professor J. H. Macek for discussing the results with us. We are especially grateful to W. Wittman for his capable assistance in the experimental work. We thank the Deutsche Forschungsgemeinschaft for financial support. The computational work for this paper was carried out at the University of Nebraska's Computing Facility.

[1] J. W. Cooper, U. Fano, and F. Prats, Phys. Rev. Lett. 10, 518 (1963).
[2] I. A. Sellin, Nucl. Instrum. Methods 110, 477 (1973), and references quoted therein.
[3] J. A. Simpson, S. R. Mielczarek, and J. W. Cooper, J. Opt. Soc. Am. 54, 269 (1964).
[4] C. E. Kuyatt, J. A. Simpson, and S. R. Mielczarek, Phys. Rev. 138, A385 (1965).
[5] D. L. Ederer, T. Lucatorto, and R. P. Madden, Phys. Rev. Lett. 25, 1537 (1970).
[6] W. Mehlhorn, Phys. Lett. 21, 155 (1966).
[7] M. E. Rudd and J. H. Macek, Case Studies At. Phys. 3, 47 (1972).
[8] P. Ziem, thesis (1974) (unpublished).
[9] I. Martinson and A. Gaupp, Phys. Rep. 15C, (1974).
[10] I. Martinson, Phys. Scr. 9, 281 (1974).
[11] K. D. Sevier, *Low Energy Electron Spectrometry* (Wiley-Interscience, 1972).
[12] E. B. Bas, U. Banninger, and P. Keller, J. Vac. Sci. Technol. 2, 306 (1972).
[13] J. S. Risley, A. K. Edwards, and R. Geballe, Phys. Rev. A 9, 1115 (1974).
[14] H. G. Berry, J. Desesquelles, and M. Dufay, Nucl. Instrum. Methods 110, 43 (1973).
[15] J. P. Buchet, A. Denis, J. Desesquelles, and M. Dufay, Phys. Lett. 28A, 529 (1969).
[16] M. Levitt, R. Novick, and P. D. Feldman, Phys. Rev. A 3, 130 (1971).
[17] S. T. Manson, Phys. Rev. A 3, 147 (1971).
[18] E. Holøien and S. Geltman, Phys. Rev. 153, 81 (1967).
[19] J. D. Garcia and J. E. Mack, Phys. Rev. 138, A987 (1965).

[20]P. Feldman and R. Novick, Phys. Rev. 160, 143 (1967).
[21]J. P. Buchet, M. C. Buchet-Poulizac, H. G. Berry, and G. W. F. Drake, Phys. Rev. A 7, 922 (1973).
[22]J. W. Cooper, M. J. Conneely, K. Smith, and S. Ormonde, Phys. Rev. Lett. 25, 1540 (1970).
[23]U. Fano and J. W. Cooper, Phys. Rev. 137, A1364 (1965).
[24]B. Fricke (private communication).
[25]L. Lipsky and A. Russek, Phys. Rev. 142, 59 (1966).
[26]P. L. Altick and E. N. Moore, Phys. Rev. Lett. 15, 100 (1965).
[27]L. Lipsky, M. J. Conneely, and R. Anania (unpublished); L. Lipsky, M. J. Conneely, and S. Ormonde, in *Proceedings of the Sixth International Conference on the Physics of Electronic and Atomic Collisions* (MIT, Cambridge, Mass., 1969), p. 1026.
[28]M. Ahmed and L. Lipsky, Phys. Rev. A 12, 1176 (1975); M. Ahmed, Ph.D. thesis (University of Nebraska, 1974) (unpublished).
[29]L. Lipsky, M. Ahmed, and M. J. Conneely, in *Proceedings of the Seventh International Conference on the Physics of Electronic and Atomic Collisions* (North-Holland, Amsterdam, 1971), Vol. 2, p. 917.
[30]V. V. Balashov, S. J. Grishanova, H. M. Kruglowa, and V. Senashenko, Opt. Spectrosc. 28, 466 (1970).
[31]Y. M. C. Chan and A. L. Stewart, Proc. Phys. Soc. Lond. 90, 619 (1967).
[32]R. H. Perrott and A. L. Stewart, J. Phys. B 1, 381 (1968).
[33]R. H. Perrott and A. L. Stewart, J. Phys. B 1, 1226 (1968).
[34]R. Bruch, G. Paul, J. Andrä, and B. Fricke (unpublished).
[35]R. Bruch, G. Paul, and J. Andrä (unpublished).
[36]D. J. Pegg, I. A. Sellin, R. Peterson, J. R. Mowat, W. W. Smith, M. D. Brown, and J. R. MacDonald, Phys. Rev. A 8, 1350 (1973).
[37]G. J. Schulz, Rev. Mod. Phys. 45, 378 (1973).
[38]U. Fano and J. W. Cooper, Phys. Rev. 138, A400 (1965).
[39]C. Nicolaides, Nucl. Instrum. Methods 110, 231 (1973).

XII. BIBLIOGRAPHY

(Åb 75) T. Åberg, Atomic Inner-Shell Processes Vol. I, Edited by B. Crasemann, Academic Press (1975) 353

(Af 75) V.V. Afrosimov, Yn. S. Gordeev, A.N. Zinoviev, D.H. Rasulov, A.P. Shergin, Abstracts of Papers of the IXth International Conference on the Physics of Electronic and Atomic Collisions, Edited by J.S. Risley and R. Geballe, Seattle 1975

(Ahm 75) M. Ahmed and L. Lipsky, Phys. Rev. A 12 (1975) 1176, M. Ahmed, Thesis, University of Nebraska, (1974)

(Ak 70) S. Aksela, M. Karras, M. Pessa, and E. Suoninen, Rev. Sci. Instr. 41 (1970) 351; S. Aksela, M. Pessa, and M. Karras, Z. Physik 237 (1970) 381

(Al 65) P.L. Altick and E.N. Moore, Phys. Rev. Lett. 15 (1965) 100

(Al 67) P.L. Altick and E.N. Moore, Proc. Phys. Sco. 92 (1967) 853

(An 70) H.J. Andrä, Nucl. Instr. and Meth. 90 (1970) 343; Phys. Rev. Lett. 25 (1970) 325

(And 72) N. Andersen, G.W. Carriveau, A.F. Glinsky, K. Jensen, J. Melskens and E. Veje, Z. Physik 253 (1972) 53

(And 71) N. Andersen, W.S. Bickel, R. Bolen, K. Jensen and E. Veje, Physica Scripta 3 (1971) 255

(Arm 71) L. Armstrong, Theory of the Hyperfine Structure of Free Atoms, Wiley-Interscience (1971)

(Au 25) P. Auger, J. Phys. Radium 6 (1925) 205

(Ax 73) A. Axmann, Appl. Phys. Lett. 23 (1973) 645

(B 70) H. Betz and L. Grodzins, Phys. Rev. Lett. 25 (1970) 211

(B 72) H.D. Betz, Rev. Mod. Phys. 44 (1972) 465

(Ba 71) E.B. Bas, U. Bänninger and P.Keller, The Journal of Vacuum Science and Technology 9 (1972) 306

(Ba 72) W. Bambynek, B. Crasemann, R.W. Fink, H.-U. Freund, H. Mark, C.D. Swift, R.E. Price and P. Venugopala Rao, Rev. Mod. Phys. 44 (1972) 716; W. Bambynek, Proc. International Conference on Inner-Shell Ionization Phenomena, Atlanta, Vol. 1 (1972) 80

(Bal 67) V.V. Balashov, V.S. Senashenko and B. Tekou, Phys. Lett. 25A (1967) 487

(Bal 70) V.V. Balashov, S.I. Grishanova, I.M. Kruglova, and V.S. Senashenko, Opt. and Spectrosc. 28 (1970) 466

(Bar 72) M. Barat and W. Lichten, Phys. Rev. A 6 (1972) 211

(Bash 64) S. Bashkin, Nucl. Instr. and Meth. 28 (1964) 88

(Bash 68) S. Bashkin, Applied Optics 7 (1968) 2341

(Be 72) H.G. Berry, Phys. Rev. A 6 (1972) 514

(Be 72a) H.G. Berry, L.J. Curtis, and J.L. Subtil, J. Opt. Soc. Am. 62 (1972) 771

(Be 73) H.G. Berry, J. Desesquelles and M. Dufay, Nucl. Instr. and Meth. 110 (1973) 43

(Be 74) H.G. Berry, E.H. Pinnington, and J.L. Subtil, Phys. Rev. A 10 (1974) 1065

(Be 75) H.G. Berry, Physica Scripta 12 (1975) 5

(Be 76) H.G. Berry, Beam-Foil Spectroscopy 2, Edited by I.A. Sellin and D.J. Pegg, Plenum Press (1976) 755

(Beck 74) D.R. Beck and C.A. Nicolaides, International Journal of Quantum Chemistry Symp. 8 (1974) 17

(Beck 75) D.R. Beck, C.A. Nicolaides, Journal of Electron Spectroscopy and Related Phenomena, 5 (1975) 1, Elsevier Scientific Publishing Company

(Beth 57) H.A. Bethe and E.E. Salpeter, Quantum Mechanics of One-And Two-Electron Atoms, Springer Verlag (1957)

(Ben 72) C. Benazeth, L. Viel et N. Colombie, Surface Sci. 32 (1972) 618

(Ber 62) H.W. Berry, Phys. Rev. 127 (1962) 1634

(Beu 35) H. Beutler, Z. Phys. 93 (1935) 177

(Bha 67) A.K. Bhatia, A. Temkin and J.F. Perkins, Phys. Rev. 153 (1967) 177

(Bha 76) A.K. Bhatia and A. Temkin, Phys. Rev. A 13 (1976) 2322

(Bick 68) W.S. Bickel, Applied Optics 7 (1968) 2367

(Bick 69) W.S. Bickel, I. Bergström, R. Buchta, B. Lundin, and I. Martinson, Phys. Rev. 178 (1969) 118

(Bick 70) W.S. Bickel, K. Jensen, C.S. Newton and E. Veje, Nucl. Instr. and Meth. 90 (1970) 309

(Bier 68) J.P. Biersack, Z. Physik 211 (1968) 495

(Bier 75) J.P. Biersack, HMI-Bericht 75 (1975)

(Bl 62) M. Blume and R.E. Watson, Proc. Roy. Soc. (London) A 270 (1972) 127

(Bl 70) L.M. Blau, R. Novick, and D. Weinflash, Phys. Rev. Lett. 23 (1970) 1268

(Blau 57) E. Blauth, Z. Phys. 147 (1957) 228

(Bo 54) N. Bohr and J. Lindhard, Kgl. Dan. Vidensk. Selsk., Mat.-Fys. Medd. 28 (1954)

(Bouch 74) C.C. Bouchiat and M.A. Bouchiat, Phys. Lett. 48 B (1974) 111

(Br 68) R. Bruch, K. Heilig, D. Wendlandt, Proceedings of the International Conference on Optical Pumping and Atomic Line Shape, Warsaw (1968) 299

(Br 69) R. Bruch, K. Heilig, D. Kaletta, A. Steudel, D. Wendlandt, Journal de Physique, Colloque C1, supplément au n° 1 (1969) C1-51

(Br 70) R. Bruch, Diplom-Thesis (1970)

(Br 74) R. Bruch, G. Paul, J. Andrä and B. Fricke, International Symposium on Electron and Photon Interactions with Atoms, University of Stirling, Scotland, Abstracts of Contributed Papers (1974) 45

(Br 74) R. Bruch, Verhandlungen der DPG 9 (1974) 903

(Br 75a) R. Bruch, G. Paul, J. Andrä and B. Fricke, Phys. Lett. 53A (1975) 293

(Br 75b) R. Bruch, G. Paul, J. Andrä and L. Lipsky, Phys. Rev. A 12 (1975) 1808

(Br 75c) R. Bruch, G. Paul and J. Andrä, J. Phys. B 8 (1975) L 253

(Br 75d) R. Bruch, J. Andrä, G. Paul, Beam-Foil Spectroscopy 1, Edited by I.A. Sellin and D.J. Pegg, Plenum Press (1976) 437

(Br 76a) R. Bruch, G. Paul, J. Andrä and B. Fricke, Electron And Photon Interactions With Atoms, Edited by H. Kleinpoppen and M.R.C. McDowell, Plenum Publishing Corporation (1976) 621

(Br 76b) R. Bruch, Proceedings of the 2nd International Conference on Inner-Shell Ionization Phenomena, Freiburg (1976)

(Br 76c) R. Bruch, D. Schneider, W.H.E. Schwarz, T.C. Chang, C.F. Moore, to be published; D. Schneider, R. Bruch, W.H.E. Schwarz, T.C. Chang, C.F. Moore, to be published

(Bra 54) D.E. Bradley, Brit. J. Appl. Phys. 5 (1954) 65

(Breu 76) E. Breuckmann, B. Breuckmann, W. Schmitz, and W. Mehlhorn, Proceedings of the 2nd International Conference on Inner-She-l Ionization Phenomena Freiburg (1976)

(Brod 76) S.J. Brodsky and G. Karl, Comments Atom. Mol. Phys. 5 (1976) 63

(Bu 63) P.G. Burke and D.D. McVicar, Phys. Rev. Lett. 11 (1963) 559

(Bu 65) P.G. Burke and D.D. McVicar, Proc. Phys. Soc. 86 (1965) 989

(Bu 72) T.M. Buck and G.H. Wheatley, Surface Sci. 33 (1972) 35

(Buch 69) J.P. Buchet, A. Denis, J. Desesquelles, and M. Dufay, Phys. Lett. 28 A (1969) 529

(Cha 71) R.L. Chase and H.P. Kelly and H.S. Köhler, Phys. Rev. A 3 (1971) 1550

(Chan 67) Y.M.C. Chan and A.L. Stewart, Proc. Phys. Soc. Lond. 90 (1967) 619

(Che 74) K.T. Cheng, C.P. Lin and W.R. Johnson, Phys. Lett. A 48 (1974) 437

(Cle 69) B. Cleff and W. Mehlhorn, Z. Phys. 219 (1969) 311

(Co 63) J.W. Cooper, U. Fano, and F. Prats, Phys. Rev. Lett. 10 (1963) 518

(Co 67) J.W. Cooper, S. Ormonde, C.H. Humphrey and P.G. Burke, Proc. Phys. Soc. 91 (1967) 285

(Co 70) J.W. Cooper, M.J. Conneely, K. Smith, and S. Ormonde, Phys. Rev. Lett. 25 (1970) 1540)

(Cock 72) C.L. Cocke, B. Curnutte, and J.R. MacDonald, Phys. Rev. Lett. 28 (1972) 1233

(Cock 74) C.L.B. Cocke, J.R. Macdonald, and R. Randall, Phys. Rev. A 9 (1974) 57

(Com 28) K.T. Compton and J.C. Boyce, J. Franklin Inst. 205 (1928) 497

(Cur 70) L.J. Curtis, R.M. Schectman, J.L. Kohl, D.A. Chojnacki and D.R. Shoffstall, Nucl. Instr. and Meth. 90 (1970) 207

(Da 73) J. Davidson and W. Bickel, Nucl. Instr. and Meth. 110 (1973) 253

(Da 75) J. Davidson, Phys. Rev. A 12 (1975) 1350

(Das 73) T.P. Das, Relativistic Quantum Mechanics of Electrons, New York, Harper and Row (1973)

(De 60) G. Dearnaley, Rev. Sci. Instr. 31 (1960) 197

(Der 69) H. Dertinger and H. Jung, Molekulare Strahlenbiologie, Springer-Verlag Berlin (1969)

(Der 71) R. Der, R. Fortner, T. Kavanagh, and J. Garcia, Phys. Rev. Lett. 27 (1971) 1631

(Des 75) J.P. Desclaux, Comp. Phys. Comm. 9 (1975) 31

(Dh 73) P. Dhez and D.L. Ederer, J. Phys. B 6 (1973) L 59

(Die 72) E. Dietz, K.O. Groeneveld, R. Spohr and R. Staudte, Nucl. Instr. and Meth. 105 (1972) 1

(Dmi 68) I.S. Dmietriev, V.S. Nikolaev, and Ya.A. Teplova, Phys. Lett. 26 A (1968) 122

(Dmi 72) I.S. Dmitriev, Ya.A. Teplova and V.S. Nikolaev, Sov. Phys. JETP 34 (1972) 723

(Dmi 76) I.S. Dmitriev, Beam-Foil Spectroscopy 2, Edited by I.A. Sellin and D.J. Pegg, Plenum Press (1976)

(Do 74) P. Dobberstein and L. Henke, Nucl. Instr. and Meth. 119 (1974) 611

(Don 71) B. Donally, W.W. Smith, D.J. Pegg, M. Brown and I.A. Sellin, Phys. Rev. A 4 (1971) 122

(Du 70) M. Dufay, Nucl. Instr. and Meth. 90 (1970) 15

(Du 73) M. Dufay, Nucl. Instr. and Meth. 110 (1973) 79

(Dyn 75) B. Dynefors, I. Martinson and E. Veje, Physica Scripta 12 (1975) 58

(Ed 70) D.L. Ederer, T. Lucatorto, and R.P. Madden, Phys. Rev. Lett. 25 (1970) 1537

(Erm 72) A.M. Ermalaev and M. Jones, J. Phys. B 5 (1972) L 225

(Est 68) G.N. Estberg and R.W. LaBahn, Phys. Lett. 28A (1968) 420

(Est 70) G.N. Estberg and R.W. LaBahn, Phys. Rev. Lett. 24 (1970) 1265

(Fa 61) U. Fano, Phys. Rev. 124 (1961) 1866

(Fa 64) U. Fano and J.W. Cooper, Phys. Rev. 137 (1964) A 1364

(Fa 65) U. Fano and J.W. Cooper, Phys. Rev. 138 (1965) A 400

(Fa 65) U. Fano and W. Lichten, Phys. Rev. Lett. 14 (1965) 627

(Fa 75) U. Fano and C. Lin, Atomic Physics 4, Editors G. zu Putlitz, E.W. Weber and A. Winnacker, Plenum Press (1975) 47

(Fein 74) G. Feinberg and M.Y. Chen, Phys. Rev. D 10 (1974) 190

(Fel 67) P. Feldman and R. Novick, Phys. Rev. 160 (1967) 143

(Fel 68) P. Feldman, M. Levitt, and R. Novick, Phys. Rev. Lett. 21 (1968) 331

(Fol 75) F. Folkmann, K.O. Groeneveld, R. Mann, G. Nolte, S. Schumann, and R. Spohr, Z. Physik A 275 (1975) 229

(For 73) R.J. Fortner and J.D. Garcia, UCRL-75094 (1973)

(For 74) R. Fortner, Phys. Rev. A 10 (1974) 2218

(For 74a) R.J. Fortner, J.D. Garcia and H. Oona, Phys. Lett. 47 A (1974) 93

(For 75) R.J. Fortner, J.D. Garcia, Phys. Rev. A 12 (1975) 856

(Fri 75) B. Fricke, private communication

(Fu 27) E. Fues, Z. Phys. 43 (1927) 726

(Ga 72) A.H. Gabriel and T.M. Paget, J. Phys. B 5 (1972) 673

(Gar 65) J.D. Garcia and J.E. Mack, Phys. Rev. 138 (1965) A 987

(Gar 70) J.D. Garcia, Nucl. Instr. and Meth. 90 (1970) 295

(Gar 73) J.D. Garcia, Nucl. Instr. and Meth. 110 (1973) 245

(Gar 73) J.D. Garcia, R.J. Fortner and T.M. Kavanagh, Rev. Mod. Phys. 45 (1973) 111

(Gau 75) A. Gaupp, SFB Report 1974/75, Freie Universität Berlin

(Ger 30) H. Geiger und K. Scheel, Handbuch der Physik, Band XXII, zweiter Teil (and references quoted therein)

(Gol 74) S. Goldsmith, J. Phys. B 7 (1974) 2315

(Gre 51) R. Gremmelmaier, Thesis, Technische Hochschule Karlsruhe (1951)

(Groe 75a) K.O. Groeneveld, R. Mann, G. Nolte, S. Schumann, R. Spohr and B. Fricke, Z. Physik A 274 (1975) 191

(Groe 75) K.O. Groeneveld, R. Mann, G. Nolte, S. Schumann and R. Spohr, Phys. Lett. 54 A (1975) 335

(Groe 76) K.O. Groeneveld, Beam-Foil Spectroscopy 2, Edited by I.A. Sellin and D. Pegg, Plenum Press (1976) 593

(Ha 75) H.H. Haselton, R.S. Thoe, J.R. Mowat, P.M. Griffin, D.J. Pegg, and I.A. Sellin, Phys. Rev. A 11 (1975) 468

(Har 71) K.G. Harrison and M.W. Lucas, Phys. Lett. 35 A (1971) 402

(Har 72) K.G. Harrison, H. Tawara, F.J. de Heer and F.W. Saris, Proc. International Conference on Inner-Shell Ionization Phenomena, Atlanta, Vol. 1 (1972) 414

(Her 59) G. Herzberg and H.R. Moore, Can. J. Phys. 37 (1959) 1293

(Hol 67) E. Holøien and S. Geltman, Phys. Rev. 153 (1967) 81

(Hol 70) E. Holøien, Nucl. Instr. and Meth. 90 (1970) 229

(Hol 71) E. Holøien and J. Midtdal, J. Phys. B 4 (1971) 1243

(Hon 73) S. Hontzeas, I. Martinson, P. Erman and R. Buchta, Nucl. Instr. and Meth. 110 (1973) 51

(Hve 76) P. Hvelplund, J. Phys. B 9 (1976) 1555

(Hy 30) E.A. Hylleraas, B. Undheim, Z. Physik 65 (1930) 759

(Ja 71) K. Jacobi and Holzmann, Surface Sci. 26 (1971) 54

(Ja 71) K. Jacobi and J. Hölzl, Surface Sci. 26 (1971) 54

(Jet 74) A. Norman Jette, T. Lee and T.P. Das, Phys. Rev. A 9 (1974) 2337

(Ju 62) B.R. Judd, Lecture Notes, Sorbonne, Paris (1962)

(Ju 63) B.R. Judd, Operator Techniques in Atomic Spectroscopy, McGraw-Hill (1963)

(Junk 73) B.J. Junker and J.N. Bardsley, Phys. Rev. A 8 (1973) 1345

(Ka 59) E. Kashy, R.R. Perry and J.R. Risser, Nucl. Instr. and Meth. 4 (1959) 167

(Kay 63) L. Kay, Phys. Lett. 5 (1963) 36

(Ke 75) H.P. Kelly, Atomic Inner-Shell Processes Vol. I, Edited by B. Crasemann, Academic Press (1975), 331

(Ke 76) H.P. Kelly, private communication

(Kess 74) Q.C. Kessel and B. Fastrup, Case Studies in Atomic Physics 3 (1974) 137

(Ki 71) D. King and G.R. Hoffman, Journal of Physics E Scientific Instruments 4 (1971) 993

(Ko 56) H. Kopfermann, Kernmomente, Akademische Verlagsgesellschaft, Frankfurt (1956)

(Kob 70) E.J. Kobetich and R. Katz, Phys. Rev. 170 (1970) 391

(Kö 66) H. Körber und W. Mehlhorn, Z. Phys. 191 (1966) 217

(Kny 76) E.J. Knystautas and R. Drouin, Beam-Foil Spectroscopy 1, Edited by I.A. Sellin and D.J. Pegg, Plenum Press (1976) 377

(Kr 75) M.O. Krause, Atomic Inner-Shell Processes Vol. II, Edited by B. Crasemann, Academic Press (1975) 33

(Kru 30) P.G. Kruger, Phys. Rev. 36 (1930) 855

(Lan 53) J.J. Lander, Phys. Rev. 91 (1953) 1382

(Land 69) L.D. Landau and E.M. Lifschitz, Lehrbuch der Theoretischen Physik Band I, Friedr. Vieweg, Braunschweig (1969)

(Lar 75) F.P. Larkins, Atomic Inner-Shell Processes Vol. I, Edited by B. Crasemann, Academic Press (1975) 377

(Leo 71) M. Levitt, R. Novick and P.D. Feldman, Phys. Rev. A 3 (1971) 130

(Lich 67) W. Lichten, Phys. Rev. 164 (1967) 131

(Lip 66) L. Lipsky and A. Russek, Phys. Rev. 142 (1966) 59

(Lip 75) L. Lipsky, private communication

(Luc 72) M.W. Lucas and K.G. Harrison, J. Phys. B 5 (1972) L 20

(Ma 65) T.F. O'Malley and S. Geltman, Phys. Rev. 137 (1965) A 1344

(Ma 66) S.T. Manson, Phys. Lett. 23 (1966) 315, Phys. Rev. 145 (1966) 35

(Ma 71) S.T. Manson, Phys. Rev. A 3 (1971) 147

(Mac 67) J. Macek, Phys. Rev. 160 (1967) 170

(Mac 68) J. Macek, J. Phys. B 1 (1968) 831

(Mac 74) J. Macek, private communication

(Mac 76) J. Macek, Beam-Foil Spectroscopy 2, Edited by I.A. Sellin and D.J. Pegg, Plenum Press (1976) 781

(MacD 33) J.C.L. MacDonald, Phys. Rev. 43 (1933) 830

(Mad 65) R.P. Madden and K. Codling, Astrophys. J. 141 (1965) 364

(Mar 68) J.B. Marion, F.C. Yound, Nuclear Reaction Analysis, North-Holland Publishing Company, Amsterdam (1968)

(Mar 70) I. Martinson, Nucl. Instr. and Meth. 90 (1970) 81

(Mar 70) I. Martinson, W.S. Bickel, and A. Ölme, J. Opt. Soc. Am. 60 (1970) 1213

(Mar 74) I. Martinson and A. Gaupp, Physics Reports 15 C (1974) 113

(Mat 68) E. Matthias and D.A. Shirley, Hyperfine Structure and Nuclear Radiations, Nord-Holland Publishing Company, Amsterdam (1968)

(Max 67) S.H. Maxman, Nucl. Instr. and Meth. 50 (1967) 53

(McG 75) E.J. McGuire, Phys. Rev. A 11 (1975) 1889

(Me 60) W. Mehlhorn, Z. Phys. 160 (1960) 247

(Me 65) W. Mehlhorn, Z. Phys. 187 (1965) 21

(Me 68) W. Mehlhorn und D. Stalherm, Z. Phys. 217 (1968) 294

(Mey 73) W.E. Meyerhof, Phys. Rev. Lett. 31 (1973) 1341

(Moa 76) C.D. Moak, TEEE Transactions on Nuclear Science NS-23 (1976) 1126

(Mo 46) C.E. Moore, Atomic Energy Levels, Nat. Bur. Stds. Circ. 467, Vol. I (1946)

(Mo 67) D.L. Moores, Proc. Phys. Soc. 91 (1967) 830

(Mo 76) C. Fred Moore, D. Schneider, B.M. Johnson, L.E. Smith, and W. Hodge, Beam-Foil Spectroscopy 1, Edited by I.A. Sellin and D.J. Pegg, Plenum Press (1976) 445

(Mus 72) R.G. Musket and W. Bauer, Appl. Phys. Letters 20 (1972) 455

(Nic 73) C.A. Nicolaides, Nucl. Instr. and Meth. 110 (1973) 231

(Nic 76) C.A. Nicolaides and D.R. Beck, J. Chem. Phys. (1976) in press

(Nic 76) C.A. Nicolaides, private communication

(On 75) J.S. Onello and L. Ford, Phys. Rev. A 11 (1975) 749

(Oon 67) H. Oona and D.G. Bickel, Rev. Sci. Instr. 38 (1967) 980

(Or 67) S. Ormonde, W. Whitaker and L. Lipsky, Phys. Rev. Lett. 19 (1967) 1161

(Pau 75) G. Paul, Diplom-Thesis, Freie Universität Berlin (1975)

(Pe 72) D.J. Pegg, I.A. Sellin, P.M. Griffin, and W.W. Smith, Phys. Rev. Lett. 28 (1972) 1229

(Pe 73) D.J. Pegg, I.A. Sellin, R. Peterson, and J.R. Mowat, W.W. Smith, M.D. Brown and J.R. MacDonald, Phys. Rev. A 8 (1973) 1350

(Pe 75) D.J. Pegg, H.H. Haselton, R.S. Thoe, P.M. Griffin, M.D. Brown and I.A. Sellin, Phys. Rev. A 12 (1975) 1330

(Pea 69) N.J. Peacock, R.J. Speer and M.G. Hobby, J. Phys. B 2 (1969) 798

(Per 68) R.H. Perrott and A.L. Stewart, J. Phys. B 1 (1968) 381

(Per 68) R.H. Perrott and A.L. Stewart, J. Phys. B 1 (1968) 381, J. Phys. B 1 (1968) 1226

(Pfe 75) K.E. Pferdekämper and H.G. Clerc, Z. Phys. A 275 (1975) 223

(Pop 73) K.R. Popper, Logik der Forschung, J.C.B. Mohr (Paul Siebeck) Tübingen (1973), Fünfte Auflage

(Pro 61) R.Kh. Propin, Opt. and Spectrosc. 10 (1961) 155

(Rich 73) P. Richard, C.F. Moore, and D.K. Olsen, Phys. Lett. A 43 (1973) 519

(Ris 72) J.S. Risley, Rev. Sci. Instrum. 43 (1972) 95

(Ris 74) J.S. Risley, A.K. Edwards, and R. Geballe, Phys. Rev. A 9 (1974) 1115

(Ris 75) J.S. Risley, Atomic Physics 4, Editors G. zu Putlitz, E.W. Weber and A. Winnacker, Plenum Press (1975)

(Ru 64) M.E. Rudd, Phys. Rev. Lett. 13 (1964) 503

(Ru 74) M.E. Rudd and J.H. Macek, Case Studies in Atomic Physics 3 (1974) 47

(Saf 69) U.I. Safronova and V.N. Kharitonova, Opt. Spectrosc. 27 (1969) 300

(Sar 67) H.Z. Sar-El, Rev. Sci. Instrum. 38 (1967) 1210

(Sar 71) H.Z. Sar-El, Rev. Sci. Instrum. 42 (1971) 1601

(Sch 31) H. Geiger und K. Scheel, Handbuch der Physik, Band XXII, zweiter Teil (and references quoted therein)

(Schnei 76) D. Schneider, C.F. Moore and B.M. Johnson, J. Phys. B 9 (1976) L 153

(Schnei 76a) D. Schneider, R. Bruch, W.H.E. Schwarz, T.C. Chang, C.F. Moore, to be published

(Schwa 76) W.H.E. Schwarz, private communication

(Sel 71) I.A. Sellin, D.J. Pegg, M. Brown, W.W. Smith and B. Donnally, Phys. Rev. Lett. 27 (1971) 1108

(Sel 72) I.A. Sellin, D.J. Pegg, P.M. Griffin, and W.W. Smith, Phys. Rev. Lett. 28 (1972) 1229

(Sel 73) I.A. Sellin, Nucl. Instr. and Meth. 110 (1973) 477

(Sav 72) K.D. Sevier, Low Energy Electron Spectrometry, Wiley-Interscience (1972)

(She 31) A.G. Shenstone, Phys. Rev. 37 (1931) 1701 and 38 (1931) 873

(Sin 68) O. Sinanoglu and J. Öksüz, Phys. Rev. Lett. 21 (1968) 507

(Sin 70) O. Sinanglu and K.A. Brueckner, Three Approaches to Electron Correlation in Atoms, New Haven, Yale University Press (1970)

(Sm 73) W. Smith, B. Donally, D.J. Pegg, M. Brown, and I.A. Sellin, Phys. Rev. A (1973) 487

(Smi 71) K. Smith, The Calculation of Atomic Collision Processes, Wiley-Interscience (1971)

(So 72) I.I. Sobel'man, Introduction to the Theory of Atomic Spectra, Pergamon Press (1972)

(Sto 69) J.O. Stoner, Jr.J. Appl. Phys. 40 (1969) 707

(Stol 71) N. Stolterfoht, Thesis, Freie Universität Berlin (1971)

(Stol 71) N. Stolterfoht and U. Leithäuser, Phys. Rev. Lett. 36 (1976) 186

(Stol 76) N. Stolterfoht, Report given at the 2nd International Conference on Inner-Shell Ionization Phenomena, Freiburg (1976)

(Stre 69) C. Streffer, Strahlen-Biochemie, Springer-Verlag Berlin (1969)

(Su 72) A. Sureau, Proceedings of the International Conference on Inner-Shell Ionization Phenomena, Atlanta, Vol. 1 (1972) 430

(Tem 66) A. Temkin, Autoionization, Mono Book Corp. (1966)

(Tra 72) J.C. Tracy, Lecture Notes, Nato Summer School on "Electron Emission Spectroscopy", Gent, Belgium (1972)

(To 76) K.X. To, E.J. Knystautas, R. Drouin, and H.G. Berry, Beam-Foil Spectroscopy 1, Edited by I.A. Sellin and D.J. Pegg, Plenum Press (1976) 385

(Vou 63) P. Vouros, J.I. Masters and R.J. Starble, Rev. Sci. Instr. 39 (1963) 741

(Wa 71) A.B.C. Walker, Jr., and H.R. Rugge, Astroph. Journal 164 (1971) 181

(We 27) G. Wentzel, Z. Phys. 43 (1927) 524

(Wei 61) A.W. Weiss, Phys. Rev. 122 (1961) 1826

(Wei 70) A.W. Weiss, quoted in: D.L. Ederer, T. Lucatorto, and R.P. Madden, Phys. Rev. Lett. 25 (1970)

(Wei 71) A.W. Weiss, quoted in: H.G. Berry, J. Bromander, I. Martinson and R. Buchta, Phys. Scripta 3 (1971) 63

(Wie 16) W. Wien, Ann. d. Physik 49 (1916) 843

(Wit 73) W. Wittmann, K. Tillmann and H.J. Andrä, Nucl. Instr. and Meth. 110 (1973) 305

(Wit 75) W. Wittmann, private communication (1975)

(Wit 76) W. Wittmann, Thesis, Freie Universität Berlin (1976) and private communication

(Whi 34) R. Whiddington and H. Priestly, Proc. Roy. Soc. (London) A 145 (1934) 462

(Whi 35) R. Widdington and H. Priestly, Proc. Leeds Phil. Soc. 3 (1935) 81

(Ya 67) T. Yamaya, T. Tohei and S. Morita, Nucl. Instr. and Meth. 49 (1967) 173

(Yn 76) J.L. Yntema, TEEE Transactions on Nuclear Science NS-23 (1976) 1133

(Za 66) V.V. Zashkvara, M.I. Korsunskii, and O.S. Kosmachev, Soviet Phys. Tech. Phys. 11 (1966) 96

(Za 69) V.V. Zashkvara and V.S. Redkin, Soviet Phys. Tech. Phys. 14 (1969) 1089

(Za 70) V.V. Zashkvara, M.I. Korsunskii, V.S. Redkin and V.P. Lavrov, Soviet Phys. 15 (1970) 2033

(Za 71) V.V. Zashkvara, M.I. Korsunskii, V.P. Lavrov and V.S. Redkin, Soviet Phys. Tech. Phys. 16 (1971) 141

(Zie 74) P. Ziem, Thesis, Technische Universität Berlin (1974)

(Zie 75) P. Ziem, R. Bruch and N. Stolterfoht, J. Phys. B 8 (1975) L 480

XIII. LEBENSLAUF (VITA)

Geboren wurde ich am 28.11.1941 in Berlin als Sohn des Ingenieurs Walter Bruch und seiner Ehefrau Ruth. Von 1948 bis 1950 war ich Schüler der Rudolf-Steiner-Schule in Berlin-Dahlem. Nach der Übersiedlung meiner Eltern nach Hannover besuchte ich von Ostern 1953 bis Ostern 1963 den mathematisch-naturwissenschaftlichen Zweig der Tellkampfschule. Die Reifeprüfung bestand ich im März 1963. Nach dem Abitur begann ich mit dem Studium der Fächer Mathematik und Physik für das Höhere Lehramt an der Technischen Universität Hannover. Im Oktober 1965 wechselte ich zur Fachrichtung Physik über und bestand im April 1966 die Diplom-Physiker-Vorprüfung. Die Diplom-Physiker-Hauptprüfung legte ich im Juli 1970 ab. Meine Diplomarbeit mit dem Thema "Isotopieverschiebung im Ti I Spektrum" führte ich am Institut für Experimentalphysik A der TU Hannover aus. Anschließend bewarb ich mich um eine Assistentenstelle an der Freien Universität Berlin am Institut für Atom- und Festkörperphysik A und wurde dort mit Wirkung vom 1. Februar 1971 zum Beamten auf Widerruf ernannt. Neben der Durchführung meiner Doktorarbeit habe ich in Berlin an dem Aufbau des Beschleunigerlabors der Gruppe Ionenstrahlspektroskopie (Prof. Dr. J. Andrä) mitgearbeitet. Außerdem gehöre ich dem dortigen Sonderforschungsbereich 161 für Hyperfeinwechselwirkung an.

F. Höpfner - Dissertationsdruck - 1 Berlin 12 - Pestalozzistraße 106
Tel.: 3128885 - 3138198